Autonomous and Responsive Surveillance Network Management for Adaptive Space Situational Awareness

Kevin M. Nastasi

Dissertation submitted to the Faculty of the
Virginia Polytechnic Institute and State University
in partial fulfillment of the requirements for the degree of

Doctor of Philosophy
in
Aerospace Engineering

APPROVED:
Jonathan T. Black, Chair
Eric G. Paterson
Robert A. Canfield

NOT APPROVED:
Mark L. Psiaki

June 8, 2018
Blacksburg, Virginia

Keywords: Sensor Network Management, Remote Sensing, Adaptive Estimation, Astrodynamics, Space Situational Awareness, Autonomy

Autonomous and Responsive Surveillance Network Management for Adaptive Space Situational Awareness

Kevin M. Nastasi

(ABSTRACT)

As resident space object populations grow, and satellite propulsion capabilities improve, it will become increasingly challenging for space-reliant nations to maintain space situational awareness using current human-in-the-loop methods. This dissertation develops several real-time adaptive approaches to autonomous sensor network management for tracking multiple maneuvering and non-maneuvering satellites with a diversely populated Space Object Surveillance and Identification network. The proposed methods integrate suboptimal Partially Observed Markov Decision Processes (POMDPs) with covariance inflation or multiple model adaptive estimation techniques to task sensors and maintain viable orbit estimates for all targets. The POMDPs developed in this dissertation use information-based and system-based metrics to determine the rewards and costs associated with tasking a specific sensor to track a particular satellite. Like in real-world situations, the population of target satellites vastly outnumbers the available set of sensors. Robust and adaptable tasking algorithms are needed in this scenario to determine how and when sensors should be tasked. The strategies developed in this dissertation successfully track 207 non-maneuvering and maneuvering spacecraft using only 24 ground and space-based sensors. The results show that multiple model adaptive estimation coupled with a multi-metric, suboptimal POMDP can effectively and efficiently task a diverse network of sensors to track multiple maneuvering spacecraft, while simultaneously monitoring a large number of non-maneuvering objects. Overall, this dissertation demonstrates the potential for autonomous and adaptable sensor network command and control for real-world space situational awareness.

This research was supported by the Virginia Tech New Horizons Graduate Scholar Program, the Ted and Karyn Hume Center for National Security and Technology, the DARPA Hallmark program, and the U.S. Joint Warfare Analysis Center.

Autonomous and Responsive Surveillance Network Management for Adaptive Space Situational Awareness

Kevin M. Nastasi

(GENERAL AUDIENCE ABSTRACT)

As the number of spacecraft in orbit increase, and satellite propulsion capabilities improve, it will become increasingly difficult for space-reliant nations to keep track of every object orbiting earth using human-in-the-loop methods. Already, the population of target satellites vastly outnumbers the available set of sensors. At any given time, a given network of sensors cannot observe every satellite in orbit, and must manage the available sensors effectively to keep track of every object of interest. The ability to maintain actionable knowledge of every orbiting object of interest is known as space situational awareness. Conventional tracking processes have generally not changed for decades, and were designed when there were far fewer satellites in orbit with little or no ability to maneuver. These methods involve large numbers of operators and engineers who schedule a network of sensors under the assumption that the satellites will not unexpectedly change their orbits for long periods of time. In the near future, traditional space surveillance approaches will become insufficient at maintaining space situational awareness, particularly if more satellites conduct unanticipated maneuvers. This dissertation develops several real-time approaches for controlling a diverse network of ground and space-based sensors that remove the need for human intervention. These fully computer-based command and control processes adapt to dynamic situations and automatically task sensors to rapidly track multiple maneuvering and non-maneuvering satellites. The decision processes used to determine which sensors should be tasked to observe a particular spacecraft compare the amount of information that can be collected in a single observation and the workload a sensor must execute to collect the observation. The command and control strategies developed in this dissertation successfully track 207 non-maneuvering and maneuvering spacecraft using only 24 ground and space-based sensors. The results show that adaptive, fully autonomous sensor network control processes can effectively and efficiently task a diverse set of sensors to track multiple maneuvering spacecraft, while simultaneously monitoring a large number of non-maneuvering objects. Overall, this dissertation demonstrates the potential for adaptive, computer-based sensor network command and control for real-world space situational awareness.

This research was supported by the Virginia Tech New Horizons Graduate Scholar Program, the Ted and Karyn Hume Center for National Security and Technology, the DARPA Hallmark program, and the U.S. Joint Warfare Analysis Center.

Acknowledgments

First and foremost, I cannot thank enough my smart and beautiful wife, Jessie, for joining me on this crazy journey since we met in 2008. Military life is especially hard on spouses to begin with, and adding a three-year PhD program on top of that has made this assignment particularly burdensome. Jessie has overcome every new personal and professional challenge with diligence and poise. She is my rock and inspiration.

Next, I dedicate this dissertation to my beautiful baby girl, Aria, who was born two years into my three-year PhD program. She won't understand the content of this dissertation for at least a couple years, but my hope is that the work presented here will contribute to operational systems that will ensure the economic, civil, and military utility of space for decades to come. If Aria's generation can take the critical space capabilities for granted, my professional and academic experience will have been proven worthwhile.

I owe a great debt of gratitude to Dr. Jon Black for all of the support he has provided over the past seven years. Dr. Black and I did great work at the Air Force Institute of Technology, and I was eager to work with him again. When he moved to Virginia Tech, and asked if I wanted to join his research group, there was only one answer. Absolutely! Without his help I would not have had the opportunity to attend Virginia Tech while continuing to serve as an active duty USAF officer.

Over the past three years, I've had the privilege to work with many brilliant students and staff. I'd like to specifically thank Dr. Andrew Rogers, Dylan Thomas, Sonya Rowe, and Dr. Kevin Schroeder, with whom I've collaborated, vented about setbacks, and celebrated successful pursuits. Virginia Tech's security managers, Tim Leake, Chris Phelps, T.J. Beckett, and John Talerico have been incredibly supportive, and have enabled interesting extensions to the research. Virginia Tech has a robust ability to conduct national security research because of their dedication and patriotism.

Lastly, I'd like to thank the Hume Center, the Virginia Tech New Horizon Graduate Scholar program, and the U.S. Air Force for funding my PhD program and giving me the opportunity to attend Virginia Tech.

Contents

List of Figures

List of Tables

List of Algorithms

List of Acronyms

ASAT anti-satellite.

CIF Covariance Inflation Filter.

DOT Degrees of Transport.

ECEF Earth-Centered, Earth-Fixed.
ECI Earth-Center, Inertial.
EKF Extended Kalman Filter.
EOIR electro-optical/infrared.

FIG Fisher Information Gain.

GEO Geosynchronous Earth Orbit.
GMST Greenwich Mean Sidereal Time.
GPB1 Generalized Pseudo-Bayesian of First Order Multiple Model.
GSSAP Geosynchronous Space Situational Awareness Program.

HEO Highly Elliptical Orbit.
HMM Hidden Markov Model.

IMM Interacting Multiple Model.
ISON International Scientific Optical Network.

JSTO Joint Space Tasking Order.

LEO Low Earth Orbit.
LKF Linear Kalman Filter.
LPAR Large Phased Array Radar.

MEO Medium Earth Orbit.
MLEA maximal Lyapunov exponent approximation.
MMAE Multiple Model Adaptive Estimation.

NTW Normal-Tangential Body-Fixed.

POMDP Partially Observed Markov Decision Process.

RMS root mean squared.
RPO Rendezvous and Proximity Operations.
RSO Resident Space Object.

SBSS Space Based Space Surveillance.
SEZ Topocentric-Horizon.
SMM Static Multiple Model.
SOSI Space Object Surveillance & Identification.
SSA Space Situational Awareness.
SSN U.S. Space Surveillance Network.

UKF Unscented Kalman Filter.

List of Symbols

Architecture

$\mathcal{O}$	Constellation Agent Set
$\mathcal{O}_{\text{mnvr}}$	Subset of Maneuvering Targets
$\mathcal{O}_{\text{static}}$	Subset of Non-Maneuvering Targets
$\mathcal{S}$	SOSI Network Agent Set
$\mathcal{S}_{\text{ARF}}$	Subset of Advanced Radar Sensors
$\mathcal{S}_{\text{EO}}$	Subset of EOIR Sensors
$\mathcal{S}_{\text{RF}}$	Subset of Radar Sensors
o_n	Target Satellite n
s_m	Sensor Agent m
M	Total Number of Sensors
N	Total Number of Targets

Covariance Inflation

$\mathcal{L}$	Binar Search Lower Bound
a	Binary Search Lower Interval Limit
b	Binary Search Upper Interval Limit
$f(\cdot)$	Binary Search Function
p	Binary Search Intremediate Point

Dynamics

$\boldsymbol{w}$	Process Noise
$\boldsymbol{\sigma}_w$	Process Noise Disturbance
Δt	Time Interval per Step
λ	Longitude
$\mathbf{r}$	Position Vector
$\mathbf{u}$	Control Input (Thrust)
$\mathbf{v}$	Velocity Vector
$\mathbf{x}$	Kinematic State Vector
ϕ_{gd}	Geodetic Latitude
h_{ellp}	Height above the ellipsoidal Earth
t	Time
t_0	Initial Time
t_f	Final Time
t_k	Time at Step k

Estimation

α	UKF Tuning Factor
β	UKF Tuning Factor
$\boldsymbol{\sigma}_{\boldsymbol{v}}$	Measurement Noise Standard Deviation
$\boldsymbol{\sigma}_{\boldsymbol{w},k}$	Process Noise Standard Deviation
$\boldsymbol{\varepsilon}$	True Error

ℓ	Number of State Dimensions
$\hat{\mathbf{C}}$	Cross Covariance
$\hat{\mathbf{K}}$	Kalman Gain Matrix
$\hat{\mathbf{P}}$	Covariance Estimate
$\hat{\mathbf{S}}$	Innovations Covariance
$\hat{\mathbf{x}}$	State Estimate
$\hat{\Psi}$	Maneuver Detection Threshold
$\hat{\psi}$	Maneuver Detection Metric
κ	UKF Tuning Factor
Λ	UKF Scaling Factor
$\mathbf{Q}$	Process Noise Covariance
$\mathbf{R}$	Measurement Noise Covariance
$\mathbf{W}_{\mathrm{P}}$	UKF Covariance Weights
$\mathbf{W}_{\mathrm{x}}$	UKF State Estimate Weights
$\tilde{\boldsymbol{\varepsilon}}$	Residual Error

Model Parameters

$\mu_{\oplus}$	Earth's Gravitational Parameter
$\omega_{\oplus}$	Earth's Angular Rotation Rate
θ_{GMST_0}	ECI to ECEF Rotation Angle
$F_{\odot}$	Solar Power Flux Density
$r_{\oplus}$	Radius of Earth
t_{mvr}	Maneuver Time

Decision Processes

α	maximal Lyapunov exponent approximation (MLEA) vs. Fisher Information Gain (FIG) Weight
β	FIG vs. Degrees of Transport (DOT) Weight
$\boldsymbol{\mathcal{F}}$	FIG Metric Matrix
$\boldsymbol{\mathcal{F}}^{\mathrm{eff}}$	Modified FIG Metric Matrix
$\boldsymbol{\mathcal{J}}$	Objective Function
$\boldsymbol{\mathcal{L}}$	MLEA Metric Matrix
$\boldsymbol{\mathcal{S}}$	Slew Time Metric Matrix
$\boldsymbol{\mathcal{T}}$	DOT Metric Matrix
$\boldsymbol{\mathfrak{F}}$	Fisher Information Matrix
$\boldsymbol{u}$	Partially Observed Markov Decision Process (POMDP) Action Set
$\boldsymbol{\Omega}$	Fisher Information Gain
δ	Slew Time vs. FIG Weight
γ	DOT vs. MLEA Weight
$\hat{\phi}$	Fisher Information Gain Metric
λ^1	Maximal Lyapunov Exponent
λ^{eff}	Maximal Lyapunov Exponent Approximation
τ	Distance Of Travel Metric
t_{ω}	Slew Time Metric

Remote Sensing

$\boldsymbol{v}$	Measurement Noise Vector
$\boldsymbol{\varrho}$	Boresight Unit Vector
$\dot{\rho}$	Range-Rate
κ	Overall Sensor Efficiency
λ	Wavelength
$\mathbf{y}$	Observation Output Vector
ω	Sensor Slew Rate

ρ Range

ρ_{max} Maximum Detectable Range

σ Cross Sectional Area

σ_{RF} Radar Cross Section

φ Elevation Angle

ϑ Azimuth Angle

d Dish/Telescope Aperture

$P_{\odot}$ Incident Solar Power

$P_{rx,min}$ Minimum Detectable Power

P_{tx} Radar Transmit Power

Sub/Superscripts & Notation

$(\cdot)$ True Value

$(\cdot)^{(\text{ECEF})}$ Value in the Earth-Centered, Earth-Fixed (ECEF) Frame

$(\cdot)^{(\text{ECI})}$ Value in the Earth-Center, Inertial (ECI) Frame

$(\cdot)^{(\text{NTW})}$ Value in the Normal-Tangential Body-Fixed (NTW) Frame

$(\cdot)^{(\text{SEZ})}$ Value in the Topocentric-Horizon (SEZ) Frame

$\hat{(\cdot)}$ Estimated Value

$\mathfrak{j}$ Multiple Model Adaptive Estimation (MMAE) model number

$\tilde{(\cdot)}$ Measured Value

k Time Step Designator

k' Previously Observed Step

m Sensor Number Designator

n Target Number Designator

Adaptive Estimation

$\boldsymbol{\mathcal{N}}$ Set of Multiple Models

χ Universal Variable

ΔT Satellite Time-Of-Flight

$\hat{\mathbf{X}}$ Matrix of MMAE State Estimates

$\hat{\mathbf{x}}^{+}$ Post-Maneuver State Estimate

$\hat{\mathbf{x}}^{-}$ Pre-Maneuver State Estimate

$\mathbf{w}$ Array of Modal Weights

$\mathfrak{N}$ Total Number of Multiple Models

ψ Auxiliary Universal Variable

c_2, c_3 Universal Variable Functions

Chapter 1

Introduction

1.1 Research Objectives

The space domain is a complex, dynamic, and critically important environment, which must be closely monitored to ensure its continued usability. Unfortunately, increased accessibility to space, and developments in satellite propulsion continue to outpace advances in the space community's ability to maintain actionable Space Situational Awareness (SSA). In the 2011 National Security Space Strategy, the U.S. Department of Defense and the U.S. Director of National Intelligence famously characterized the space domain as "congested, contested, and competitive" [1]. That assertion is more true today than it was just seven years ago. Using predominantly human-in-the-loop command and control systems, Space Object Surveillance & Identification (SOSI) networks are straining to keep track of a rapidly growing catalog of Resident Space Objects (RSOs). Incorporating automation into the sensor network command and control process can alleviate the challenges placed on space operators, as asserted by the National Academies [2].

With a globally-distributed and diverse array of sensors, how might a centralized SOSI network autonomously track a much larger population of non-maneuvering and maneuvering RSOs? This dissertation addresses this principal question with three research objectives:

1. Develop a set of decision processes that enable responsive and efficient SOSI network command and control
2. Develop a set of adaptive estimation algorithms to track maneuvering spacecraft
3. Within the defined scenario, assess how effectively decision processes and adaptive estimation algorithms interact to track a large RSO population

Responsive decision processes are needed to autonomously task sensors to maintain actionable SSA. Adaptive estimation is required to rapidly acquire a viable orbit estimate when a

satellite maneuvers. How efficiently these processes interact to control a global SOSI network ultimately determines the degree to which SSA of the entire space domain is maintained.

1.2 Motivation

1.2.1 Space Situational Awareness

U.S. Strategic Command, which is the dominant provider of satellite tracking information for the global space community, defines Space Situational Awareness as, "the requisite current and predictive knowledge of the space environment and the [operational environment] upon which space operations depend" [3]. Through various means of detection, tracking, and identification, SSA operations enable:

1. Continued availability of critical space-based services, to include communications, and precision navigation and timing [3]
2. Spaceflight safety via collision prediction and avoidance [3]
3. Protection of space-based services through attribution and diplomatic deterrence [3]

Continued and effective SSA facilitates much of modern civilization, and the space community has invested significant resources to establish and operate large SOSI networks to track RSOs of interest. Figure 1.1 depicts the general geographic distribution of three important networks, based on [4] and [5]: the U.S. Space Surveillance Network (SSN), the European Space Agency's Space Surveillance System, and the International Scientific Optical Network (ISON). Several generalities of current SOSI Networks can be gleaned from Figure 1.1. First,

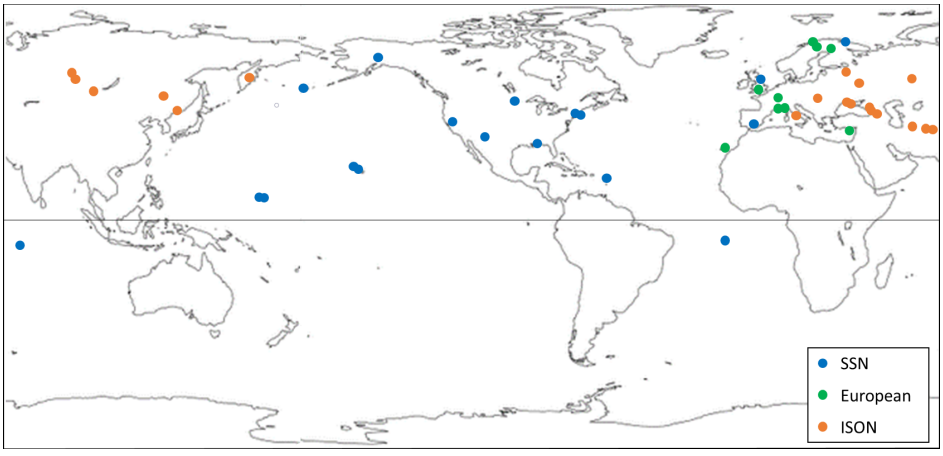

Figure 1.1: SOSI Network Map

ground-based sensors tend to be distributed hemispherically, in that almost all of the sensors are in the northern hemisphere. Second, the network topologies appear to be more influenced by geopolitical relationships than by an optimized distribution for space surveillance. In addition to a few sensors in allied nations, the SSN is located in the United States and its territories. The ISON, which is led by the Russian Academy of Sciences, is located primarily in Russia and neighboring countries [4]. The United States, among others, is augmenting these ground-based networks with space-based sensors, such as the Space Based Space Surveillance (SBSS) system [6] and the Geosynchronous Space Situational Awareness Program (GSSAP) [7]. It's also important to note that many of these SOSI networks, especially the U.S. owned ones, contain a diverse set of sensors, to include large phased array radar, mechanical radar, and EOIR systems. Lastly, as will be seen in Section 1.2.2, the number of sensors available in any one SOSI network is many orders of magnitude smaller than the total RSO population. With only a few sensors, the United States and others must maintain SSA of thousands or hundreds of thousands of orbiting objects.

Currently, efficient sensor management in these SOSI networks is achieved through careful, human-in-the-loop planning. As an example, SSN operations are part of a larger process known as the Joint Space Tasking Order (JSTO) Process. Figure 1.2 depicts the complex

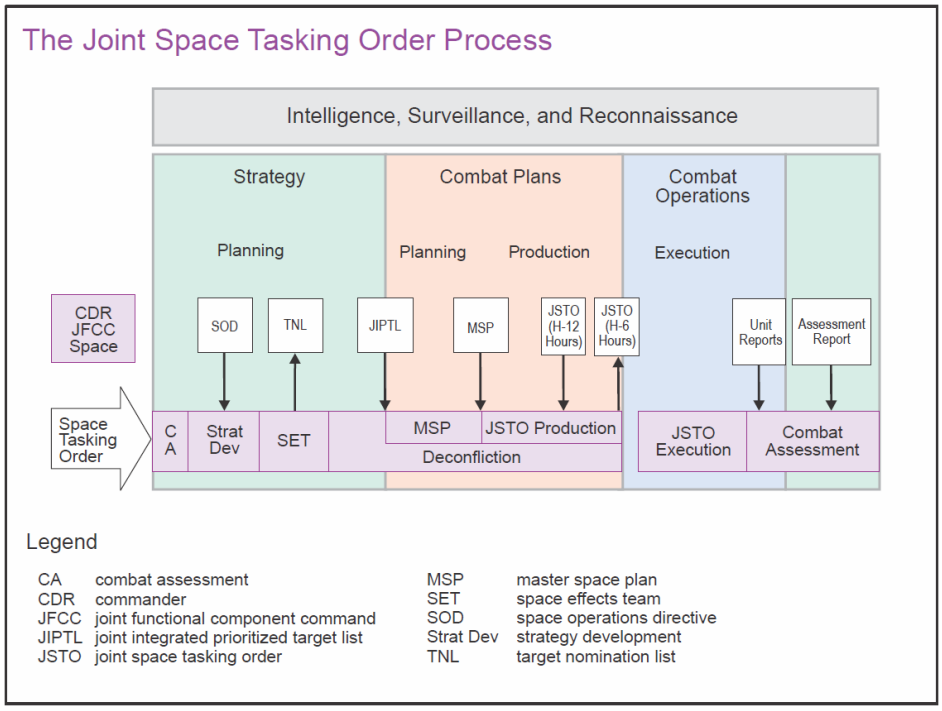

Figure 1.2: The Joint Space Tasking Order Process [3]

chain of events through which a JSTO is developed, executed, and assessed. While it is ultimately adaptable to unforeseen events, the JSTO process can be slow to respond in rapidly evolving situations, often taking many hours, or possibly even days, to determine

an appropriate course of action. [8] states that collision risks are assessed for operational spacecraft every 24 hours. [9] reveals that published state information for active satellites is updated every 1.4 to 3 days. Orbit estimates for debris, on the other hand, can go upwards of 10 days without an update. [9] also notes that the time to detect a change in an RSO's state or dynamics can take between seven to thirty days. Many programs are attempting to improve all or some of this process, by introducing varying degrees of automation. The U.S. Air Force's Joint Space Operations Center Mission System (JMS) and the DARPA HALLMARK program are two such initiatives.

1.2.2 The Congested Space Domain

Not only must SOSI networks monitor an enormous population of space objects with a comparatively small number of sensors, but the number of RSOs is rapidly growing. Multiple trends in space technology are contributing to the population growth. The fundamental factor is the seemingly relentless reduction in electronics size, weight, and power that often comes with technological advancement. A capability that would have once required a complex, bus-sized spacecraft, can now be accommodated on a satellite the size of a shoebox. Figure 1.3 shows how commercial remote sensing satellites are shrinking with little or no reduction in mission performance [10].

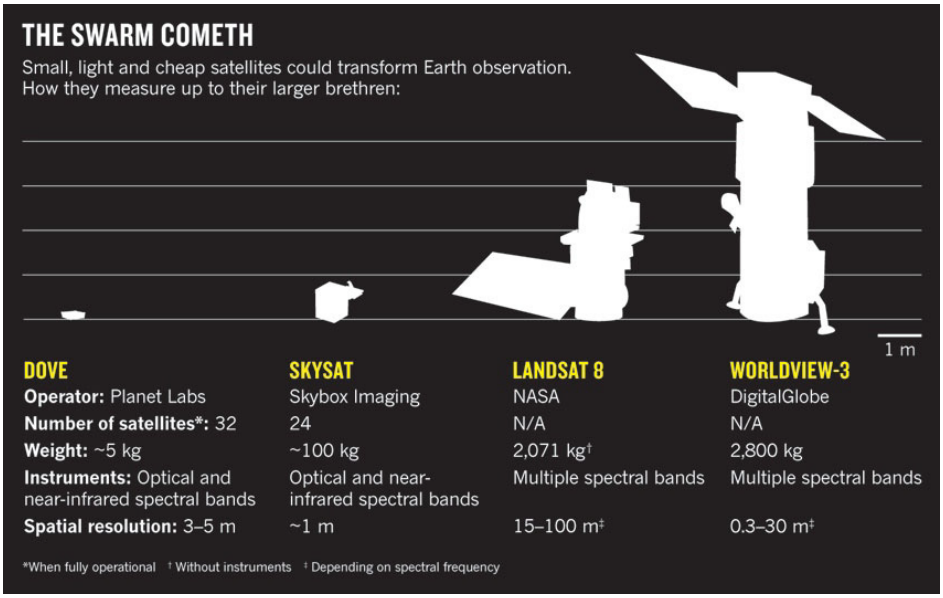

Figure 1.3: Commercial Remote Sensing Satellite Size, Weight, & Power [10]

Consequently, space-based systems are becoming financially viable options for more non-government organizations and nations. The 2011 U.S. National Security Strategy noted that in 2009 there were roughly 57 space-faring nations and non-government consortia [1]. At

the time, however, these entities still served largely military or civil institutions. As the commercial viability for space-based services, like global broadband internet, have started to outweigh the associated risks, multiple concepts for mega-constellations with 100+ small satellites have gained traction with investors. In 2016, the National Academy of Science predicted exponential growth in commercial satellite communications and remote sensing over the next decade, as shown in Figure 1.4.

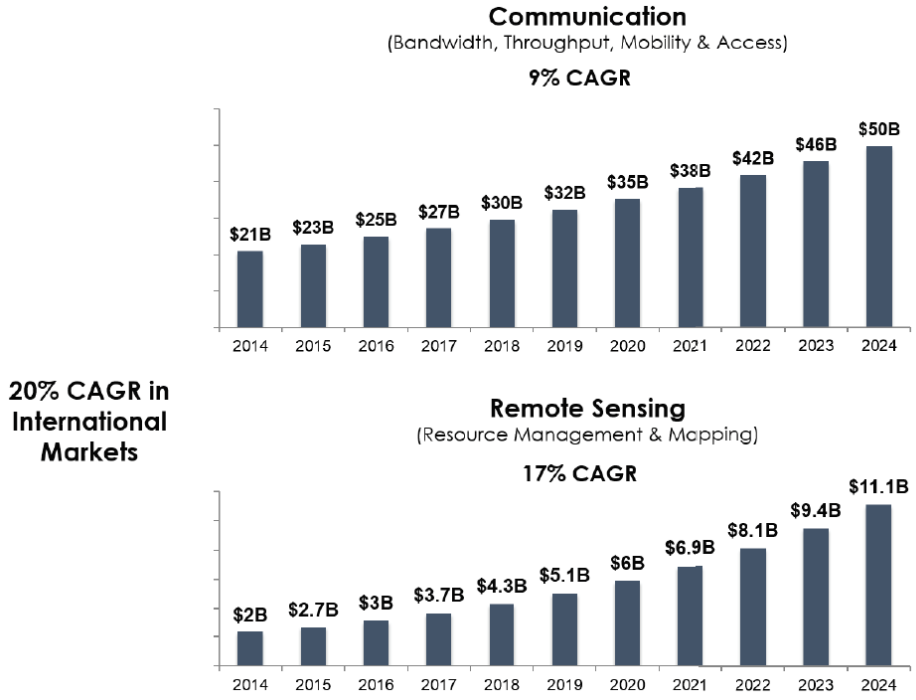

Figure 1.4: Compound Annual Growth Rate [10]

From a U.S. national security perspective, the reduction in satellite form factors has produced new options for mission assurance and satellite resiliency. Under the old paradigm, a few large spacecraft with multiple capabilities were deployed to facilitate a wide variety of missions. This strategy was partly due to the technological limitations described earlier, but it was also the result of a belief that space assets were untouchable by a potential adversary. This invulnerability is simply not the case any longer. An increasingly popular concept is known as disaggregation. [11] described how disaggregated architectures, where multiple small satellites provide a distributed capability, are being considered as a means for mitigating threats and reducing costs.

The commercial and national security advantages of reduced satellite form factors are clear, but this trend places nuanced challenges on SOSI network command and control. Primarily, and most obviously, with more RSOs to track, a SOSI network must spend less time observing any one single target. The time between observations of a single target is also potentially

longer. Additionally, smaller spacecraft are often harder to detect and track than their larger counterparts. For example, a telescope may be able to observe a van-sized spacecraft in geosynchronous orbit, but not a basketball-sized satellite. As a result, the number of potentially available sensors for a particular target can be significantly smaller than it would have historically been. These trends make observational data for a specific target increasingly sporadic, decreasing the confidence in the orbit estimate and increasing the risk of collisions.

Congestion in the space domain has so far been attributed to increased interest in space-based assets; however, most RSOs are debris and defunct satellites. Figure 1.5 demonstrates the exponential growth in the RSO population from 1958 to 2010, which results primarily from several collision events [1].

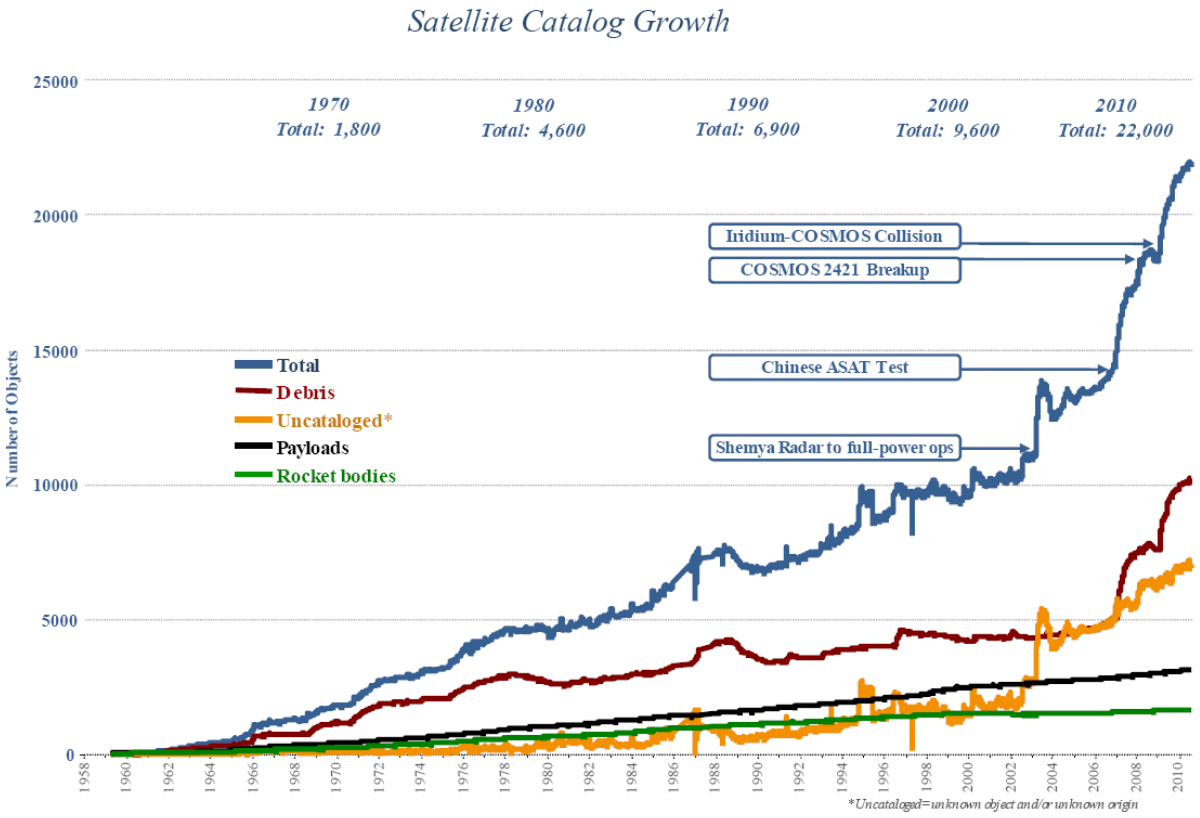

Figure 1.5: Resident Space Object Population Growth [1]

A vicious cycle thus becomes evident. A larger RSO population decreases a SOSI network's ability to track all targets. Decreased orbit estimate accuracy and precision increase the risk and frequency of on-orbit collisions. The debris generated during such events dramatically increases the RSO population, and the cycle begins again. If autonomous SOSI network command and control can streamline or quicken the sensor tasking process, more RSOs

could be tracked than are currently possible, and the vicious cycle would be slowed, if not stopped. Indeed, autonomous and adaptive surveillance network command and control may be the only solution for tracking the proposed mega-constellations now in development.

1.2.3 The Contested & Competitive Space Domain

The developing challenges on SOSI networks and their operators are only partly due to the growing RSO population. Developments in space technology are also making advanced propulsion systems available to a larger array of spacecraft. High thrust, hydrazine systems are now available for shoebox-size satellites known as CubeSats [12]. Hydrazine, however, is a hypergolic and very toxic fuel, making it too expensive and dangerous for most small satellite providers. More recently, comparatively safer alternatives to hydrazine propulsion systems have been developed, which employ AF-M315E mono-propellant [13]. These systems can provide significant maneuverability in a small form factor, and can be cost-effectively accommodated on CubeSats and other small spacecraft [14].

These high thrust propulsion systems can be used to augment already advanced space systems to enable a slew of new missions. Constellations, or groups of satellites, may soon be able to rapidly reconfigure to achieve new operational requirements. A large body of academic research now exists, and continues to grow, investigating various uses for highly maneuverable satellites. [15] produced methods for developing and executing responsive orbital maneuvers using electric propulsion. [16] used particle swarms, and [17] used a linearized state transition matrix, to develop optimization methods for navigation in multi-satellite formations.

Perhaps the most revolutionary concept is cost-effective Rendezvous and Proximity Operations (RPO), where one satellite maneuvers to meet another and remain nearby. RPO can enable a variety of capabilities, particularly on-orbit maintenance. [18] used onboard model predictive control to optimize maneuver planning in eccentric orbits. [19] and [20] demonstrated how a 6U (10cm $\times$ 20cm $\times$ 30cm) CubeSat could conduct RPO starting at hundreds of kilometers from the secondary spacecraft. DARPA is pursuing a larger variation, which is known as the Robotic Servicing of Geosynchronous Satellites (RSGS) Program [21], and shown in Figure 1.6.

These evolving RPO capabilities have significant utility in extending operational lifespans of high value satellites, but they could also have considerable military value. RPO is a necessary capability for co-orbital anti-satellite (ASAT) systems. [22] describes Chinese and Russian interest in deploying RPO systems that could be lead directly to a co-orbital ASAT capability. [22] also identifies several instances when supposed Russian debris began conducting RPO around nearby objects. RPO technology is advancing so rapidly that public policy and internationally agreed upon definitions of appropriate use have yet to be established [23].

How might current SSA capabilities handle such a rapidly changing domain? [24] charac-

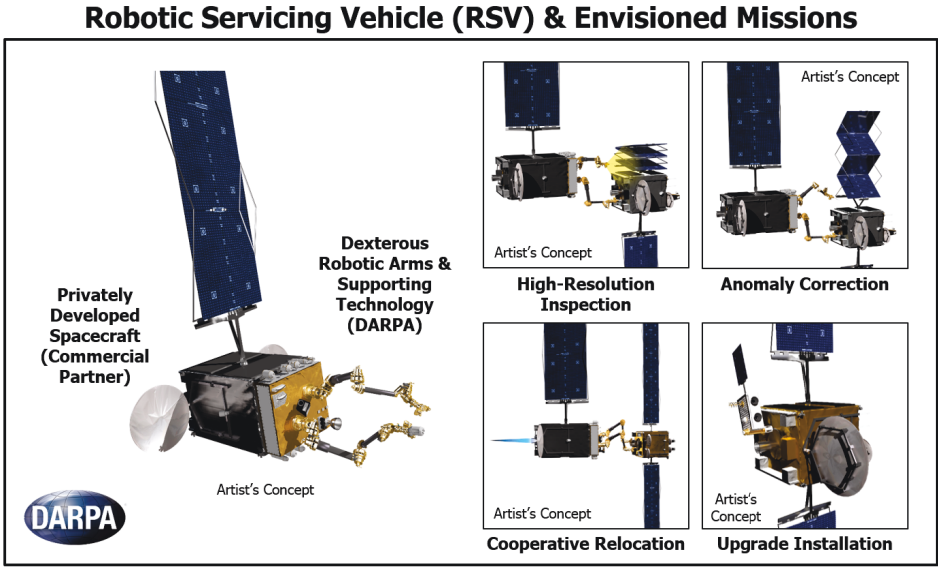

Figure 1.6: Robotic Servicing of Geosynchronous Satellites System (Courtesy: DARPA)

.

terizes the current SOSI network command and control framework as designed for "routine catalog maintenance", and calls for an ability to rapidly detect, track, and characterize threats. Autonomous command and control of a SOSI network combined with adaptive estimation techniques is a viable option to achieve this goal.

1.2.4 Complexities in SOSI Network Command and Control

The command and control of a SOSI network is an incredibly complex process. As such, research into multi-sensor network management is often highly simplified to address a specific aspect of the overall framework. [25] explains how the multi-sensor network management problem can be broken into distinct aspects: estimation, data association, sensor registration, data fusion, and decision processes. Each element is a research area in itself.

Estimation refers to the dynamics used to model sensors and target objects, as well as the processes used to update state estimates when new observational data becomes available. Not surprisingly, estimation research, particularly in the area of space surveillance, is extensive. More information on previous and relevant estimation research is discussed in Chapter 2, Section 2.4.

Data Association describes the process by which one object is distinguished from another in an observation that contains multiple targets. How does a SOSI network determine which illuminated pixel in an image is the satellite-of-interest and not a piece of nearby debris? How are illuminated pixels from one image to the next determined to be the same satellite?

If observational data and a target object are incorrectly correlated, the resulting state estimate may diverge from the truth, leading to track loss. At the very least, additional error is injected into the estimation process, which could have been mitigated with a rigorous data association process. When research focuses on the sensor tasking strategies themselves, as this dissertation does, data association becomes an additional layer of fidelity that contributes to, but isn't required to design and compare decision-making strategies. Thus, in this dissertation, it is assumed that observations are always correlated with the correct target satellite.

Sensor registration refers to processes used to determine the sensor's kinematic state and capabilities. Sensor uncertainties need to be mitigated to reduce estimation error and correctly correlate observations and targets. The sensor's kinematic state can be incorporated into the estimation process so that the target and sensor states are estimated with each observation. When multiple sensors simultaneously observe one target, methods exist to determine and correct relative sensor biases. Effectively, this aspect of the sensor network management problem addresses the trustworthiness of the sensors and their observations. In sensor network management research, it is often assumed that sensor states are known with absolute certainty, and that their observation noise is within expected limits. Like data association, including sensor registration capabilities isn't required to determine how efficiently or effectively a sensor network management process tasks sensors. As this dissertation focuses on the integration of adaptive estimation and decision processes, it is assumed that the sensor states are known with certainty, and that the actual measurement noise is white and uncorrelated between individual sensors.

Data fusion describes the processes by which independent observational data from multiple sources are fused to update a target's state estimate. This aspect of the sensor network management problem is critically important when multiple sensors are used to track targets, particularly if those sensors have different observational capabilities (e.g. radar versus EOIR). As explained in [26], data fusion can occur at multiple levels, on a scale of zero to five. High level processing occurs at or close to the human operator interface, while lower level processing takes place at a hardware or raw data-processing level. Level one processing, which integrates observational data in the estimation process, is used in this dissertation to enable simultaneous observations from independent, but centrally controlled sensors.

Lastly, decision processes describe how sensors are tasked either centrally or at the individual system level. How sensors are managed can vary widely to account for the advantages and disadvantages associated with a specific network topology. In a centralized network, command and control is executed from one or two nodes, requiring large computational resources, but also avoiding many of the data integrity complexities associated with decentralized control. In a decentralized network, command and control is executed at each sensor, or among local clusters of sensors. Decentralized control distributes the computational load across the network, but the chain of custody of observational data and target estimates must be rigorously managed.

1.3 Architecture Framework & General Nomenclature

The real-time, multi-sensor command and control problem can be posed as a suboptimal POMDP that controls the interaction between two independent networks: a constellation of maneuvering and non-maneuvering spacecraft, and a SOSI network. Actors in this dissertation, whether they are a satellite in the constellation or a sensor in the SOSI network, are broadly defined as agents.

The constellation is defined by a set, $\mathcal{O}$, of N Earth-orbiting spacecraft, or more generally targets.

$$\mathrm{o}_n \in \mathcal{O} \quad \forall \quad n = [1, N] \tag{1.1}$$

The term constellation in this context is used loosely, as the satellites are not necessarily similar in size, purpose, or capability. Additionally, the constellation spans multiple inclinations in Low Earth Orbit (LEO), Medium Earth Orbit (MEO), and Geosynchronous Earth Orbit (GEO) to comprehensively assess the tasking strategy's robustness.

A number of spacecraft, $\mathcal{O}_{\text{mnvr}}$, may execute an impulsive maneuver at any time during a particular scenario. The remaining subset of non-maneuvering satellites, $\mathcal{O}_{\text{static}}$, constitutes the majority of the constellation.

$$\mathcal{O}_{\text{static}} \cup \mathcal{O}_{\text{mnvr}} = \mathcal{O} \quad | \quad \mathcal{O}_{\text{static}} \cap \mathcal{O}_{\text{mnvr}} = \emptyset \tag{1.2}$$

The maneuvering satellites in this study only perform unknown maneuvers. These burns will occur when the spacecraft are out of view of the network, and no observation is possible. This approach simulates real world situations, such as an unforeseen anomaly like propulsive out-gassing or system failure.

The SOSI network is defined by a set $\mathcal{S}$ of M ground and space-based nodes.

$$\mathrm{s}_m \in \mathcal{S} \quad \forall \quad m = [1, M] \tag{1.3}$$

Each node in the SOSI network holds a sensor, the capabilities of which vary from one node to another. In this study, sensors may be advanced radar ($\mathcal{S}_{\text{ARF}}$), radar ($\mathcal{S}_{\text{RF}}$), or EOIR ($\mathcal{S}_{\text{EO}}$), which provide 4D, 3D, or 2D observational data, respectively, as described in Section 2.3.1. Each node of the SOSI network hosts one type of sensor, which is described mathematically as:

$$\mathcal{S}_{\text{ARF}} \cup \mathcal{S}_{\text{RF}} \cup \mathcal{S}_{\text{EO}} = \mathcal{S} \quad | \quad \mathcal{S}_{\text{ARF}} \cap \mathcal{S}_{\text{RF}} = \emptyset, \quad \mathcal{S}_{RF} \cap \mathcal{S}_{\text{EO}} = \emptyset, \quad \mathcal{S}_{\text{ARF}} \cap \mathcal{S}_{\text{EO}} = \emptyset \tag{1.4}$$

Advanced radar are assumed to be Large Phased Array Radar (LPAR), which to have rigidly constrained fields of regard and very fast electronically steered beams. Radar are assumed to be mechanical radar, which have much slower slew rates, but generally wider fields of regard than LPAR. EOIR sensors are assumed to be conventional electro-optical telescopes. They're called EOIR sensors because electro-optical/infrared capabilities often require similar technologies and have similar constraints.

An important detail of this framework is that $N \gg M$. As a result, sensors always have more targets in view than can be observed at a given time step. The SOSI network command and control strategy must choose one observation per sensor while neglecting a significant number of possible observations. How the tasking algorithm accomplishes this task will determine how well SSA is maintained of the entire constellation.

In this dissertation there are a number of variables that are denoted by the same symbol, but have different values based on which sensor or target they are associated with and whether they refer to the actual, measured, or estimated value. The terms n and m, are used to denote the target and sensor element, respectively. To distinguish actual, measured, and estimated values this dissertation uses the notation described in [27]. A true value is given no accent $(\cdot)$. A measured value is given a tilde $\tilde{(\cdot)}$. A circumflex $\hat{(\cdot)}$ denotes an estimated value. A predicted state or covariance in the estimation process is distinguished with a conditional subscript $\hat{(\cdot)}_{k+1|k}$, while an updated variable has a single step subscript $\hat{(\cdot)}_{k+1}$. Three examples of commonly used variables are presented to demonstrate the described subscript notation.

$$\mathbf{x}_{m,k} = \text{Actual state vector for sensor } m \text{ at time, } t_k \tag{1.5}$$

$$\hat{\mathbf{x}}_{n,k} = \text{Estimated state vector for target } n \text{ at time, } t_k \tag{1.6}$$

$$\tilde{\mathbf{y}}_{(n,m),k} = \text{Measured observation vector for the target-sensor pair, } (n,m), \text{ at time, } t_k \tag{1.7}$$

1.4 Summary of Contributions

As described in Section 1.2, Space Situational Awareness is a critically important and complex component of national security space and the larger space community. The current SOSI network command and control infrastructure will be significantly challenged by future growth in the RSO catalog and by the increasing availability of RPO capabilities for all satellite sizes.

To date, adaptive estimation and autonomous network management have been independent research areas, particularly with regard to SSA. Previous adaptive estimation research has focused on a single maneuvering target, or continuously available observations of a few maneuvering targets. Additionally, observations have tended to be consistent across sensors. In the SSA realm, there would likely be multiple maneuvering, with large gaps in observational availability, and a variety of observational data from various sources. New research needs to develop and assess adaptive estimation algorithms that are tailored to the challenges associated with SSA. This dissertation seeks to address this need.

Sensor network management research, as it pertains to SSA, has focused exclusively on optimizing an observation schedule over a time window for multiple non-maneuvering satellites. [28] is perhaps the only instance where a sensor tasking strategy was developed specifically

to track a single maneuvering satellite. There is a clear need for sensor network management research that focuses on responsive tasking to track multiple maneuvering satellites. This dissertation and its precursors [29, 30, 31] seek to develop an integrated SOSI network command and control strategy for monitoring a large number of non-maneuvering and maneuvering spacecraft.

This dissertation's primary contribution is the development and assessment of responsive SOSI network command and control algorithms using suboptimal POMDPs and MMAE to track a large number of non-maneuvering and maneuvering satellites with a diverse set of sensors. By achieving the research objectives delineated in Section 5.3, the specific novel contributions of this dissertation are as follows:

1. The development and assessment of a real-time, continuous observation suboptimal POMDP algorithm that uses Fisher Information Gain, maximal Lyapunov exponent approximation, and Distance of Travel (DOT) reward metrics to task radar and EOIR sensors

2. The development and assessment of a real-time, cost-constrained suboptimal POMDP algorithms that uses Fisher Information Gain, maximal Lyapunov exponent approximation, and slew time cost to task radar and EOIR sensors

3. The development of a real-time, baseline suboptimal POMDP using only Fisher Information Gain to task radar and EOIR sensors

4. The development and assessment of a "Shotgun" Static Multiple Model algorithm to detect and track through unknown tangential maneuvers

5. The development and assessment of a Lambert Targeter Static Multiple Model algorithm to detect and track through unknown maneuvers in any direction

6. The development and assessment of a Lambert Targeter Generalized Pseudo-Bayesian of First Order Multiple Model algorithm to detect and track through unknown maneuvers in any direction

7. The development of a baseline Covariance Inflation algorithm that uses the bisection method to determine an optimal covariance inflation to detect and track through unknown maneuvers in any direction

8. The integration of the aforementioned suboptimal POMDPs and adaptive estimation algorithms, and assessment of the combined algorithms in a globally-distributed, diversely populated SOSI network that is tasked to track a large number of maneuvering and non-maneuvering spacecraft

The term assessment in this dissertation denotes the comparison of the selected algorithm against the baseline or nominal (non-adaptive) cases. The baseline and nominal approaches emulate other research, but are formatted to function

1.5 Dissertation Structure

In pursuit of the research objectives described in Section 5.3, this dissertation is organized into seven chapters.

Chapter 1 outlines the research objectives to clearly define the scope of the research and provide an overall structure to the dissertation. Section 1.2 gives this dissertation in context within the Space Situational Awareness mission, and explains why the research is valuable to ongoing efforts within the space community. Section 1.3 introduces the general nomenclature used to describe the relevant SSA scenario and the research's overall framework. Lastly, Section 1.4 delineates the value of this dissertation and the specific contributions to the SSA research community.

Chapter 2 provides the mathematical framework upon which the research is built. Section 2.2 introduces and briefly explains the kinematic models used throughout the dissertation. Section 2.3 describes how observations are calculated and structured. Section 2.4 gives a brief overview of sequential estimation, and reviews the Unscented Kalman Filter (UKF), which is the selected estimation method used throughout the research. Section 2.5 introduces the POMDP, and describes the two information-based decision metrics used in this dissertation.

Chapter 3 introduces the architectural framework and modeling environment that was developed to facilitate the research. In Section 3.1, the baseline SOSI network, which is used to assess each command and control protocol, is described. A command and control protocol is a combination of a specific decision process and a particular adaptive estimation technique. Section 3.2 defines the preliminary and full RSO catalogs that the SOSI network is tasked to track. The preliminary RSO catalog is used to determine how well each decision process tracks a population of non-maneuvering satellites. The full RSO catalog is twice the size of the preliminary catalog, and includes several maneuvering spacecraft in each orbital regime. The full catalog provides a comprehensive test for each command and control protocol.

Chapter 4 presents the adaptive estimation algorithms that were developed for this dissertation. Section 4.3 describes the Covariance Inflation algorithm that uses a bisection method to optimally inflate the process noise covariance, based on the detected maneuver. Section 4.5 describes a Static Multiple Model (SMM) Adaptive Estimation algorithm that uses a shotgun approach to characterize an unknown maneuver and converge quickly on a new orbit estimate. Section 4.6 describes a SMM Adaptive Estimation technique that uses a Universal Variable Lambert Targeter to characterize an unknown maneuver and reestablish a viable orbit estimate. Section 4.7 describes a GPB1 Adaptive Estimation algorithm that also uses a Universal Variable Lambert Targeter to characterize and mitigate an unknown maneuver.

Chapter 5 presents the developed decision processes and metrics. Section 5.3.1 describes the baseline POMDP algorithm that emulates previous research, but is adapted for this research to provide an apples-to-apples comparison. Section 5.3.2 describes the continuous tasking, suboptimal POMDP that implements multiple decision metrics, and assumes each sensor

must make an observation at every time step, as long as a target satellite is visible. Section 5.3.3 describes a cost-constrained, suboptimal POMDP approach that also implements multiple decision metrics, but only tasks a sensor to observe a target satellite if the rewards outweigh the costs.

Chapter 6 integrates each of the POMDP approaches from Chapter 5 with each adaptive estimation technique from Chapter 4, and assesses each resulting command and control protocol. The assessment is executed using the SOSI network and RSO catalog defined in Chapter 3. The resulting analyses are used to compare and contrast the command and control algorithms.

Chapter 7 summarizes the decision processes and adaptive estimation algorithms developed in this dissertation. The results generated in Chapter 6 are also reviewed. Finally, this dissertations overall objectives and contributions are restated to reinforce the value of this work to the larger SSA body of knowledge.

Chapter 2

Foundational Concepts

2.1 Introduction

In this chapter the mathematical foundations upon which the processes in later chapters are developed are presented. Fundamental concepts in astrodynamics, remote sensing, sequential estimation, and partially observed Markov decision processes are described within the scope of the dissertation. It is assumed that the reader has familiarity with dynamics and statistics, particularly those concepts that apply to orbital mechanics.

2.2 Dynamics

2.2.1 General Dynamics Formulation

The model dynamics and geometries used in this dissertation are based on two-body orbital mechanics and a rotating, ellipsoidal Earth. All dynamic systems follow the standard format for equations of motion.

$$\dot{\mathbf{x}}(t) = \mathbf{f}(\mathbf{x}(t), \mathbf{u}(t)) + \boldsymbol{w}(t), \quad \boldsymbol{w}(t) \sim \mathcal{N}(\mathbf{0}, \mathbf{Q}(t)) \tag{2.1}$$

$\mathbf{u}(t)$ refers to the thrust in a maneuvering spacecraft. There are no control inputs to ground-based sensors that would change the kinematic states of the host facilities. All satellite maneuvers are impulsive in this dissertation. Because control inputs are defined as an acceleration, impulsive maneuvers are modeled as one second continuous, constant thrusts. In continuous time, $\boldsymbol{w}(t)$ denotes additional unmodeled noise in the agent's state, and is zero mean Gaussian with spectral density matrix $\mathbf{Q}(t)$, such that $E\left[\boldsymbol{w}(t)\boldsymbol{w}^T(\tau)\right] = \mathbf{Q}(t)\delta(t-\tau)$ [32].

The kinematic state, $\mathbf{x}$, of each agent is defined as a six dimensional vector consisting of the agent's position and velocity, relative to the ECI reference frame, unless otherwise specified.

$$\mathbf{x} = \begin{bmatrix} \mathbf{r} & \mathbf{v} \end{bmatrix}^T \tag{2.2}$$

where

$$\mathbf{r} = \begin{bmatrix} x_1 & x_2 & x_3 \end{bmatrix} \qquad \text{and} \qquad \mathbf{v} = \dot{\mathbf{r}} = \begin{bmatrix} \dot{x}_1 & \dot{x}_2 & \dot{x}_3 \end{bmatrix} \tag{2.3}$$

2.2.2 Continuous & Discrete Time

Two forms of time are used in this dissertation: continuous and discrete. Because of the simplifying assumptions described in later sections, continuous time t is defined as Greenwich Mean Sidereal Time (GMST) and measured in seconds. t_0 denotes the initial scenario time, or epoch time, and is always set as $t_0 = 0$.

$$t = [0, t_f] \quad | \quad t \in \mathbb{R} \quad \& \quad t_f = (0, \infty] \tag{2.4}$$

While kinematic states are propagated in continuous time, observational data are only available at uniform, discrete intervals.

$$t_k = k\Delta t \quad | \quad k \in \mathbb{Z} \quad \& \quad k = \left[1, \frac{t_f}{\Delta t}\right] \tag{2.5}$$

Therefore, state estimates and their associated covariances are calculated and reported at each step, k, regardless of the duration between steps, denoted as Δt. For brevity, a commonly used step notation is implemented where the subscript k connotes the associated variable at time t_k. That is, $\mathbf{x}(t_k) = \mathbf{x}_k$.

2.2.3 Reference Frames

First, a brief summary of the relevant coordinate systems used frequently in this dissertation. Figure 2.1 depicts each of these reference frames and how they relate to one another.

Earth-Centered Coordinate Systems

The foundational reference frame for astrodynamics and orbit estimation is the Earth-Center, Inertial (ECI) reference frame (depicted in green in Figure 2.1). An inertial reference frame, by definition, is one that is not accelerating with respect to any other inertial origin. Most importantly, the ECI reference frame does not rotate with the Earth, and is therefore ideal for describing orbital equations of motion. The principal axis, $\hat{\mathrm{x}}_1^{\mathrm{ECI}}$, is often defined at specific time and date, known as an epoch. The third axis, $\hat{\mathrm{x}}_3^{\mathrm{ECI}}$, is aligned with the Earth's spin axis. The second axis completes the triad, and forms the fundamental plane with the

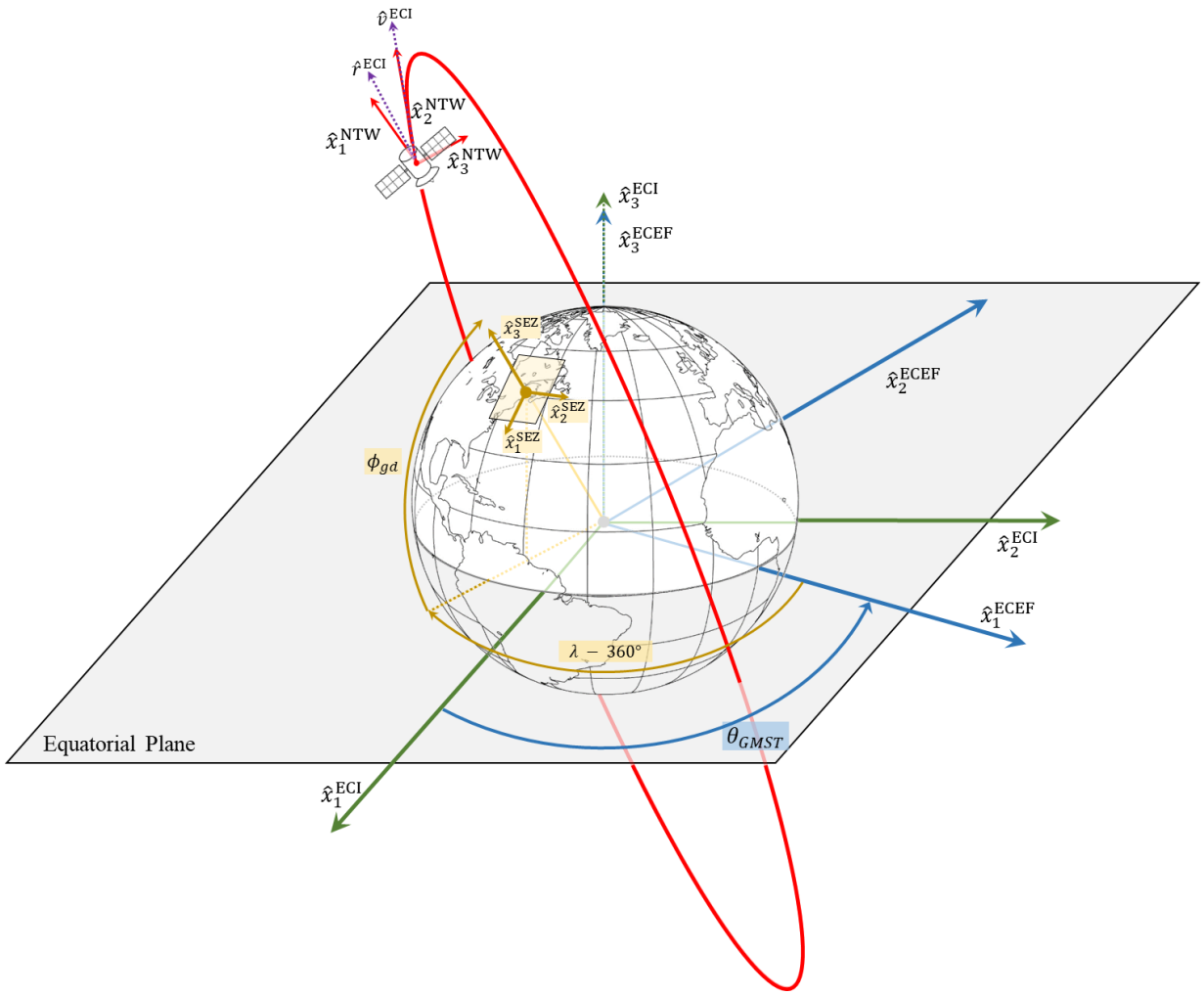

Figure 2.1: Pertinent Reference Frames

principal axis, which coincides with the equatorial plane. The details of how the ECI frame is defined are complex and well documented, particularly in [33].

The other critical reference frame is the ECEF reference frame (depicted in blue in Figure 2.1). This coordinate system aligns with the ECI frame on the epoch date and time, but rotates, precesses, and nutates with the Earth. The principal axis is defined by a unit vector extending from the center of the Earth through (0° N, 0° E). The third axis is aligned with the Earth's spin axis. The second axis completes the triad.

In a two-body model (defined in Section 2.2.4), the relationship between the ECI and ECEF frames is straightforward; defined by a single, third axis rotation matrix. In reality, when geopotential perturbations and temporal variations are introduced to the two-body system,

the transformation between the ECI and ECEF frames becomes very complex. While the transformation fundamentally remains a single third axis rotation, the calculation becomes a very laborious process. There are multiple international organizations that are tasked with measuring, monitoring, and calculating the diverse set of variables that go into determining the rotation. [33] gives a brief, but comprehensive discussion of this complex process.

Given the two-body model assumptions, the rotation angle, θ_{GMST_0}, which is depicted in Figure 2.1, is defined by Equation 2.6.

$$\theta_{\text{GMST}} = \theta_{\text{GMST}_0} + \omega_{\oplus} t \tag{2.6}$$

where $\omega_{\oplus}$ is the Earth's angular rotation rate, and θ_{GMST_0} is an initial GMST. Because the ECI and ECEF reference frames are aligned at the epoch time, t_0, $\theta_{\text{GMST}_0} = 0$.

Using the notation in [33], the transformation between the ECI and the ECEF reference frames is:

$$\left[\tfrac{\mathbf{ECEF}}{\mathbf{ECI}}\right] = \begin{bmatrix} \mathbf{R}_3(\theta_{\text{GMST}}) & \mathbf{0} \\ \dot{\mathbf{R}}_3(\theta_{\text{GMST}}) & \mathbf{R}_3(\theta_{\text{GMST}}) \end{bmatrix} \tag{2.7}$$

Such that,

$$\mathbf{x}^{(\text{ECEF})} = \left[\tfrac{\mathbf{ECEF}}{\mathbf{ECI}}\right] \mathbf{x}^{(\text{ECI})} \tag{2.8}$$

Topocentric-Horizon Reference Frame

While there are many topocentric reference frames from which to define sensor observations, this dissertation implements the SEZ coordinate system (depicted in Yellow in Figure 2.1). With an origin centered at the observer, the first axis, $\hat{\mathrm{x}}_1^{\text{SEZ}}$ points due south. The second axis points due east, and the third axis is normal to the horizontal plane, pointing towards zenith.

The transformation between the ECI and SEZ requires rotations about the third axis and the second axis.

$$\left[\tfrac{\mathbf{SEZ}}{\mathbf{ECI}}\right] = \left[\tfrac{\mathbf{SEZ}}{\mathbf{ECEF}}\right] \left[\tfrac{\mathbf{ECEF}}{\mathbf{ECI}}\right] \tag{2.9a}$$

$$\left[\tfrac{\mathbf{SEZ}}{\mathbf{ECEF}}\right] = \begin{bmatrix} \mathbf{R}_2(\frac{\pi}{2} - \phi_{gd})\mathbf{R}_3(\lambda) & \mathbf{0} \\ \mathbf{0} & \mathbf{R}_2(\frac{\pi}{2} - \phi_{gd})\mathbf{R}_3(\lambda) \end{bmatrix} \tag{2.9b}$$

such that,

$$\mathbf{x}^{(\text{SEZ})} = \left[\tfrac{\mathbf{SEZ}}{\mathbf{ECEF}}\right] \left[\tfrac{\mathbf{ECEF}}{\mathbf{ECI}}\right] \mathbf{x}^{(\text{ECI})} \tag{2.10}$$

Body-Fixed Reference Frame

A spacecraft-fixed coordinate system known as the NTW frame (depicted in red in Figure 2.1) is used in this dissertation to define some of the satellite maneuvers. The N-axis, $\hat{\mathrm{x}}_1^{\text{NTW}}$, lies

in the orbital plane and is normal to the ECI velocity vector. The T-axis is aligned with the ECI velocity vector. The W-axis is normal to the orbital plane, and parallel to the orbit's angular momentum vector. The NTW reference frame is a useful system for defining satellite maneuvers because the most fuel-efficient, impulsive maneuvers occur in the tangential, or in-track, direction.

The rotation matrix required to incorporate thrust vectors that are described in the NTW frame with the numerically integrated kinematic state vector in the ECI frame is described in Equation 2.11.

$$\left[\tfrac{\mathbf{ECI}}{\mathbf{NTW}}\right] = \mathbf{R}_{\mathbf{x}(t)} = \left[\hat{\mathbf{N}} \quad \vdots \quad \hat{\mathbf{T}} \quad \vdots \quad \hat{\mathbf{W}}\right] \tag{2.11}$$

where

$$\hat{\mathbf{T}} = \frac{\mathbf{v}(t)}{||\mathbf{v}(t)||_2} \tag{2.12a}$$

$$\hat{\mathbf{W}} = \frac{\mathbf{r}(t) \times \mathbf{v}(t)}{||\mathbf{r}(t) \times \mathbf{v}(t)||_2} \tag{2.12b}$$

$$\hat{\mathbf{N}} = \hat{\mathbf{T}} \times \hat{\mathbf{W}} \tag{2.12c}$$

Therefore a thrust in the ECI frame, $\mathbf{a}_{thrust}^{(\text{ECI})}(t)$, is calculated using Equation 2.13

$$\mathbf{a}_{thrust}^{(\text{ECI})}(t) = \left[\tfrac{\mathbf{ECI}}{\mathbf{NTW}}\right]_{\mathbf{x}(t)} \mathbf{a}_{thrust}^{(\text{NTW})}(t) \tag{2.13}$$

2.2.4 Two-Body Orbital Dynamics

In this dissertation two types of agents are subject to two-body orbital dynamics: spacecraft, and the estimates thereof. The two-body model is sufficient to describe satellite dynamics within the scope of the research objectives. Because of the assumptions made in the two-body model [33], the equations of motion for satellites and their state estimates are described by Equation (2.14), in the ECI reference frame.

$$\dot{\mathbf{x}}(t) = \begin{bmatrix} \mathbf{v}(t) \\ -\frac{\mu_\oplus}{r^3}\mathbf{r}(t) \end{bmatrix} + \boldsymbol{w}(t) \tag{2.14}$$

where r is the distance to the satellite from the center of the Earth, $r = \|\mathbf{r}(t)\|_2$. The spacecraft's state at each time step, $\mathbf{x}_k$, is determined either using a state transition matrix or through direct numerical integration (Equation (2.15)).

$$\mathbf{x}_{k+1} = \int_{t_k}^{t_{k+1}} f(\mathbf{x}(t), \mathbf{u}(t))dt \tag{2.15}$$

As discussed in Chapter 1, Section 1.2.4, $\mathbf{w}(t) = \mathbf{0}$ for spacecraft in the SOSI network, but is nonzero for target satellites.

2.2.5 Ellipsoidal Earth Dynamics

A facility's kinematic state is first calculated in the ECEF reference frame, using the site's geodetic latitude (ϕ_{gd}), longitude (λ), and height above the ellipsoidal Earth (h_{ellp}). Algorithm 2.1 specifies this conversion, based on formulas in [33].

Algorithm 2.1 Geodetic Coordinates to the Earth-Centered, Earth Fixed Frame

1: Calculate the Radius of Curvature in the Prime Vertical $C_\oplus$

$$C_\oplus = \frac{R_\oplus}{\sqrt{1 - {e_\oplus}^2}} \tag{2.16}$$

where $R_\oplus$ is the Earth's equatorial radius, and $e_\oplus$ is the Earth's eccentricity.

2: Calculate auxiliary variable $S_\oplus$

$$S_\oplus = C_\oplus(1 - {e_\oplus}^2) \tag{2.17}$$

3: Calculate the equatorial component of the position vector r_δ

$$r_\delta = (C_\oplus + h_{ellp})\cos(\phi_{gd}) \tag{2.18}$$

4: Calculate the vertical component of the position vector r_k

$$r_k = (S_\oplus + h_{ellp})\sin(\phi_{gd}) \tag{2.19}$$

5: Calculate the facility's position vector in the ECEF frame $r_{site}^{(ECEF)}$

$$\mathbf{r}_{site}^{(ECEF)} = \begin{bmatrix} r_\delta \cos(\lambda) \\ r_\delta \sin(\lambda) \\ r_k \end{bmatrix} \tag{2.20}$$

The equations of motion for ground-based objects are described by Equation (2.21).

$$\dot{\mathbf{x}}(t) = \begin{bmatrix} \mathbf{v}(t) \\ -\omega_\oplus^2 \mathbf{r}(t) \end{bmatrix} \tag{2.21}$$

Per the two-body model, the Earth's rotation in this dissertation is not subject to precession or nutation effects, and spins about the third axis in both the ECI and ECEF frames. The resulting equations of motion, in the ECI frame, have a closed form solution, Equation (2.22), using the facility's ECEF position vector $\mathbf{r}_{site}^{(\mathrm{ECEF})} = \begin{bmatrix} x_\mathrm{X} & x_\mathrm{Y} & x_\mathrm{Z} \end{bmatrix}^T$. Because facilities are

stationary in this dissertation, $\mathbf{r}_{site}^{(\text{ECEF})}$ does not change with time.

$$\mathbf{x}^{(\text{ECI})}(t) = \begin{bmatrix} x_{\text{X}}\cos(\omega_{\oplus}t) - x_{\text{Y}}\sin(\omega_{\oplus}t) \\ x_{\text{Y}}\cos(\omega_{\oplus}t) + x_{\text{X}}\sin(\omega_{\oplus}t) \\ x_{\text{Z}} \\ -\omega_{\oplus}x_{\text{Y}}\cos(\omega_{\oplus}t) - \omega_{\oplus}x_{\text{X}}\sin(\omega_{\oplus}t) \\ \omega_{\oplus}x_{\text{X}}\cos(\omega_{\oplus}t) - \omega_{\oplus}x_{\text{Y}}\sin(\omega_{\oplus}t) \\ 0 \end{bmatrix} \tag{2.22}$$

The locations and velocities of ground-based sensors are assumed to be known with absolute certainty. Hence, $\boldsymbol{w}(t) = \mathbf{0}$ in Equation (2.21).

2.2.6 Continuous Process Noise

Continuous process noise, $\boldsymbol{w}(t)$, is assumed to be a zero-mean Gaussian with spectral density matrix $\mathbf{Q}(t)$. Process noise simulates random, unmodeled disturbances in the spacecraft's nominal equations of motion. In this dissertation $\boldsymbol{w}(t)$ is assumed to be purely additive. $\boldsymbol{w}(t)$ injects noise solely as accelerative disturbances, as defined in Equation (2.23).

$$\boldsymbol{w}(t) = \begin{bmatrix} \mathbf{0} & \boldsymbol{\sigma}_w \end{bmatrix}^T \tag{2.23}$$

where $\mathbf{0}$ and $\boldsymbol{\sigma}_{w(t)}$ are each 1×3 vectors.

The continuous process noise is also reduced with altitude to simulate the decreasing potency of random disturbances due to variations in Earth's gravitational field. The continuous process noise in Equation (2.23) is scaled using Equation (2.24).

$$\boldsymbol{w}(t) = \boldsymbol{w}(t)e^{\frac{r_{\oplus}+250-r_k}{100000}} \tag{2.24}$$

The scaled process noise is equal to the baseline when the object's altitude is 250km.

2.3 Remote Sensing

The "interactions" between a Resident Space Object and the sensor observing it are characterized by observations, which are based on the kinematic states of the particular target satellite and the sensor, as well as the sensor's capabilities and limitations. These observations are passive in that the observed spacecraft does not cooperatively provide information to support the surveillance process. In a cooperative scenario target satellites may have transponders or other devices with which a sensor can interface to glean additional information. In a passive scenario the observation data from a particular sensor is limited to what is detectable and measurable at a given time step.

2.3.1 Observation Formulation

Observational data are represented by an observation output vector, which is derived from the observation state vector. In state space notation the measured observation output vector is given by Equation (2.25).

$$\tilde{\mathbf{y}}_{(n,m),k} = \mathbf{h}_(\mathbf{x}_{n,k}, \mathbf{x}_{m,k}) + \boldsymbol{v}_{m,k}, \quad \boldsymbol{v}_{m,k} \sim \mathcal{N}(\mathbf{0}, \mathbf{R}_{m,k}) \tag{2.25a}$$

$$\hat{\mathbf{y}}_{(n,m),k} = \mathbf{h}_(\hat{\mathbf{x}}_{n,k}, \hat{\mathbf{x}}_{m,k}) \tag{2.25b}$$

$\boldsymbol{v}_{m,k}$ is the measurement noise vector, which is assumed to be a zero-mean Gaussian with variance $\mathbf{R}_{m,k}$. The measurement noise covariance matrix characterizes the uncertainty in the associated observation and is often predefined through rigorous sensor testing and characterization. In this dissertation $\mathbf{R}_{m,k}$ is defined as a diagonal matrix.

$$\mathbf{R}_{m,k} = \boldsymbol{\sigma}_{\boldsymbol{v},m,k} \tag{2.26}$$

The nonlinear measurement function $\mathbf{h}_(\mathbf{x}_{n,k}, \mathbf{x}_{m,k})$ produces measurement data based on the observation state vector in the Topocentric-Horizon Reference Frame (SEZ).

$$\boldsymbol{\rho}^{(\text{SEZ})}_{(n,m),k} = \begin{bmatrix} \mathbf{r}^{(\text{SEZ})}_k & \mathbf{v}^{(\text{SEZ})}_k \end{bmatrix}^T \tag{2.27}$$

$$\boldsymbol{\rho}^{(\text{SEZ})}_{(n,m),k} = \begin{bmatrix} x_\text{s} & x_\text{e} & x_\text{z} & \dot{x}_\text{s} & \dot{x}_\text{e} & \dot{x}_\text{z} \end{bmatrix}^T \tag{2.28}$$

$$\boldsymbol{\rho}^{(\text{SEZ})}_{(n,m),k} = \left[\frac{\mathbf{SEZ}}{\mathbf{ECI}}\right] \left(\mathbf{x}^{(\text{ECI})}_{n,k} - \mathbf{x}^{(\text{ECI})}_{m,k}\right) \tag{2.29}$$

where $\left[\frac{\mathbf{SEZ}}{\mathbf{ECI}}\right]$ is the ECI to SEZ coordinate transformation defined in Equation (2.9).

In this dissertation observations are combinations of up to four measurements depending on the sensor type: azimuth, elevation, range, and range-rate. These measurement data are derived from the observation state vector to form the observation output vector. Azimuth ϑ is defined as the angle from due north $-\hat{x}^{(\text{SEZ})}_1$ clockwise to the observation state vector, projected onto the sensor-centered, horizontal plane. Elevation φ is defined as the angle from the horizontal plane to the observation state vector. Range ρ is the magnitude of the observation state vector, and range-rate $\dot{\rho}$ is the associated time-rate of change. These measurements are calculated using Equations (2.30a), (2.30b), (2.30c), and (2.30d), respectively.

$$h_\vartheta(\mathbf{x}_{n,k}, \mathbf{x}_{m,k}) = \tan^{-1}\left(\frac{-x_\text{e}}{x_\text{s}}\right) \tag{2.30a}$$

$$h_\varphi(\mathbf{x}_{n,k}, \mathbf{x}_{m,k}) = \sin^{-1}\left(\frac{x_\text{z}}{||\mathbf{r}_{\text{SEZ},k}||_2}\right) \tag{2.30b}$$

$$h_\rho(\mathbf{x}_{n,k}, \mathbf{x}_{m,k}) = ||\mathbf{r}_{\text{SEZ},k}||_2 \tag{2.30c}$$

$$h_{\dot{\rho}}(\mathbf{x}_{n,k}, \mathbf{x}_{m,k}) = \frac{\mathbf{r}^{(\text{SEZ})}_k \cdot \mathbf{v}^{(\text{SEZ})}_k}{||\mathbf{r}^{(\text{SEZ})}_k||_2} \tag{2.30d}$$

Equation (2.30) describes ideal observations [34] because they are instantaneous geometric measurements that do not take into account the physics behind a real-world observation, such as the travel time for a microwave pulse to propagate to a target and return to the radar.

The SOSI Network developed for this dissertation is notional and contains a diverse set of ground and space-based advanced radar, radar, and EOIR sensors. Advanced radar provide the most data per observation with a 4×1 observation output vector. If $\mathrm{s}_m \in \mathcal{S}_{ARF}$, then

$$\mathbf{h}(\mathbf{x}_{n,k}, \mathbf{x}_{m,k}) = \begin{bmatrix} h_\vartheta(\mathbf{x}_{n,k}, \mathbf{x}_{m,k}) \\ h_\varphi(\mathbf{x}_{n,k}, \mathbf{x}_{m,k}) \\ h_\rho(\mathbf{x}_{n,k}, \mathbf{x}_{m,k}) \\ h_{\dot{\rho}}(\mathbf{x}_{n,k}, \mathbf{x}_{m,k}) \end{bmatrix} \tag{2.31}$$

Radar produce a 3×1 observation output vector. If $\mathrm{s}_m \in \mathcal{S}_{RF}$, then

$$\mathbf{h}(\mathbf{x}_{n,k}, \mathbf{x}_{m,k}) = \begin{bmatrix} h_\vartheta(\mathbf{x}_{n,k}, \mathbf{x}_{m,k}) \\ h_\varphi(\mathbf{x}_{n,k}, \mathbf{x}_{m,k}) \\ h_\rho(\mathbf{x}_{n,k}, \mathbf{x}_{m,k}) \end{bmatrix} \tag{2.32}$$

Lastly, the observation output for an electro-optical sensor is a 2×1 vector containing only angular information. If $\mathrm{s}_m \in \mathcal{S}_{EO}$, then

$$\mathbf{h}(\mathbf{x}_{n,k}, \mathbf{x}_{m,k}) = \begin{bmatrix} h_\vartheta(\mathbf{x}_{n,k}, \mathbf{x}_{m,k}) \\ h_\varphi(\mathbf{x}_{n,k}, \mathbf{x}_{m,k}) \end{bmatrix} \tag{2.33}$$

2.4 Estimation

This section combines and summarizes information from [27] and [32]. Estimation is the process by which the state of an indirectly observed, stochastically-driven target can be determined using noisy measurements. Sequential estimation originated with Carl Friedrich Gauss, who devised the normal probability distribution function (PDF) and the linear least squares principle as a means of minimizing estimation error. The univariate normal, or Gaussian PDF of x, with mean μ and variance σ^2, is defined in Equation (2.34) where $x \in \mathbb{R}$.

$$p(x; \mu, \sigma^2) = \frac{1}{\sigma\sqrt{2\pi}} e^{\frac{-(x-\mu)^2}{2\sigma^2}} \tag{2.34}$$

Orbit estimation, however, is inherently a multivariate instance where $\mathbf{x} \in \mathbb{R}^\ell$ with mean $\hat{\mathbf{x}}$ and covariance $\hat{\mathbf{P}}$. The multivariate Gaussian PDF is thus defined in Equation 2.35.

$$p(\mathbf{x}; \hat{\mathbf{x}}, \hat{\mathbf{P}}) = \frac{1}{\sqrt{(2\pi)^\ell |\hat{\mathbf{P}}|}} e^{-\frac{1}{2}(x-\hat{\mathbf{x}})^T \hat{\mathbf{P}}^{-1}(x-\hat{\mathbf{x}})} \tag{2.35}$$

The covariance $\hat{\mathbf{P}}$ in Equation (2.35) is a symmetric positive definite matrix with diagonal elements σ_i^2 where $i \in [1, \ell]$. Additionally, if the true error is defined as the difference between the estimate and the actual target state, as in Equation (2.36),

$$\boldsymbol{\varepsilon} = \hat{\mathbf{x}} - \mathbf{x} \tag{2.36}$$

then $\hat{\mathbf{P}} = E\{\boldsymbol{\varepsilon}\boldsymbol{\varepsilon}^T\}$. This property lets us minimize the true error through the estimation process without ever knowing the true error.

2.4.1 The Linear Least Squares Principle

Gauss' principle of linear least squares [27] seeks to find the state estimate $\hat{\mathbf{x}}$ that minimizes the summed squares of the residual errors $\tilde{\boldsymbol{\varepsilon}}$.

$$J = \frac{1}{2}\tilde{\boldsymbol{\varepsilon}}^T\tilde{\boldsymbol{\varepsilon}} \tag{2.37}$$

Given a set of observations, their associated times, and a set of independent basis functions that map a kinematic state vector to an observation:

$$\tilde{\mathbf{y}} = [\tilde{y}_1 \ \tilde{y}_2 \ \cdots \ \tilde{y}_\kappa]^T \tag{2.38}$$

$$\mathbf{t} = [t_1 \ t_2 \ \cdots \ t_\kappa]^T \tag{2.39}$$

$$\mathbf{H} = \begin{bmatrix} h_1(t_1) & h_2(t_1) & \cdots & h_\ell(t_1) \\ h_1(t_2) & h_2(t_2) & \cdots & h_\ell(t_2) \\ \vdots & \vdots & \vdots & \vdots \\ h_1(t_\kappa) & h_2(t_\kappa) & \cdots & h_\ell(t_\kappa) \end{bmatrix} \tag{2.40}$$

a set of state estimates can be determined

$$\hat{\mathbf{x}} = [\hat{x}_1 \ \hat{x}_2 \ \cdots \ \hat{x}_\kappa]^T \tag{2.41}$$

such that

$$\hat{\mathbf{y}} = \mathbf{H}\hat{\mathbf{x}} \tag{2.42}$$

$$\tilde{\boldsymbol{\varepsilon}} = \tilde{\mathbf{y}} - \hat{\mathbf{y}} \tag{2.43}$$

Therefore, Equation (2.37) can be rewritten the multidimensional quadratic function in Equation 2.44.

$$\mathbf{J}(\hat{\mathbf{x}}) = \frac{1}{2}\left(\tilde{\mathbf{y}}^T\tilde{\mathbf{y}} - 2\tilde{\mathbf{y}}^T\mathbf{H}\hat{\mathbf{x}} + \hat{\mathbf{x}}^T\mathbf{H}^T\mathbf{H}\hat{\mathbf{x}}\right) \tag{2.44}$$

The global minimum of Equation 2.44 occurs where the Jacobian of J is zero (Equation 2.45)

$$(\nabla_{\hat{\mathbf{x}}}\mathbf{J})^T = \mathbf{H}^T\mathbf{H}\hat{\mathbf{x}} - \mathbf{H}^T\tilde{\mathbf{y}} = \mathbf{0} \tag{2.45}$$

given that the Hessian of $\mathbf{J}$ with respect to $\hat{\mathbf{x}}$ is positive definite (Equation 2.46).

$$\nabla^2_{\hat{\mathbf{x}}}\mathbf{J} = \mathbf{H}^T\mathbf{H} \tag{2.46}$$

$\mathbf{H}^T\mathbf{H}$ is positive definite if $\mathbf{H}$ is of maximum rank (that is, ℓ).

From Equation (2.45) the appropriate state estimate can be found.

$$\hat{\mathbf{x}} = \left(\mathbf{H}^T\mathbf{H}\right)^{-1}\mathbf{H}^T\tilde{\mathbf{y}} \tag{2.47}$$

For the inverse of $\mathbf{H}^T\mathbf{H}$ to exist the number of independent observations must be equal to or greater than the dimensions of $\mathbf{x}$. In other words, $m \geq \ell$.

Thus, without ever directly observing the actual target state or knowing the noise injected into each observation an accurate state estimate can be determined. For additional information see [27] and [32].

2.4.2 Linear Least Squares Sequential Estimation

The linear list squares principle in Section 2.4.1 inherently assumes that all observations are available simultaneously and then incorporated to define an estimate at a desired epoch time. This approach works well in data sparse scenarios, such as orbit estimation, when observations may be few and far between. Indeed, many SOSI networks employ what is known as Batch Least Squares to create an orbit estimate after a sufficient number of observations have been collected. A significant disadvantage to this approach, however, is that a potentially large number of observations must be continuously carried forward in time. This issue can be mitigated by sequentially incorporating new observations into the estimate as they become available [27].

Suppose an initial set of observations $\tilde{\mathbf{y}}_1$ is available followed later by a second set of observations $\tilde{\mathbf{y}}_2$, as defined in Equation (2.38). Each observation set comes with the associated times ($\mathbf{t}_1$ and $\mathbf{t}_2$), from Equation (2.39), and independent basis functions ($\mathbf{H}_1$ and $\mathbf{H}_2$), from Equation (2.40). Additionally, two diagonal matrices are provided ($\mathbf{W}_1$ and $\mathbf{W}_2$), which defined how each observation should be weighted compared to the other observations in the set.

The original linear least squares approach from Section 2.4.1 would suggest that both sets of observations are combined to determine the final state estimate, per Equation (2.47).

$$\hat{\mathbf{x}}_2 = \left(\mathbf{H}^T\mathbf{W}\mathbf{H}\right)^{-1}\mathbf{H}^T\mathbf{W}\tilde{\mathbf{y}} \tag{2.48}$$

where

$$\tilde{\mathbf{y}} = \begin{bmatrix}\tilde{\mathbf{y}}_1 \\ \tilde{\mathbf{y}}_2\end{bmatrix} \qquad \mathbf{H} = \begin{bmatrix}\mathbf{H}_1 \\ \mathbf{H}_2\end{bmatrix} \qquad \mathbf{W} = \begin{bmatrix}\mathbf{W}_1 & \mathbf{0} \\ \mathbf{0} & \mathbf{W}_2\end{bmatrix} \tag{2.49}$$

Equation (2.48) can be expanded to delineate each set of observations.

$$\hat{\mathbf{x}}_2 = \left(\mathbf{H}_1^T\mathbf{W}_1\mathbf{H}_1 + \mathbf{H}_2^T\mathbf{W}_2\mathbf{H}_2\right)^{-1}\left(\mathbf{H}_1^T\mathbf{W}_1\tilde{\mathbf{y}}_1 + \mathbf{H}_2^T\mathbf{W}_2\tilde{\mathbf{y}}_2\right) \tag{2.50}$$

Equation (2.50) does not save any computational resources over the original linear least squares approach, but it does infer a means by which an efficient update process can be developed. To devise such an estimate update procedure to efficiently go from $\hat{\mathbf{x}}_1$ to $\hat{\mathbf{x}}_2$, the covariance matrices, $\hat{\mathbf{P}}_1$ and $\hat{\mathbf{P}}_2$, are first introduced.

$$\hat{\mathbf{P}}_1 = \left(\mathbf{H}_1^T\mathbf{W}_1\mathbf{H}_1\right)^{-1} \tag{2.51}$$

$$\hat{\mathbf{P}}_2 = \left(\mathbf{H}_1^T\mathbf{W}_1\mathbf{H}_1 + \mathbf{H}_2^T\mathbf{W}_2\mathbf{H}_2\right)^{-1} \tag{2.52}$$

$\hat{\mathbf{P}}_1$ and $\hat{\mathbf{P}}_2$ are covariance matrices if $\mathbf{W}_1$ and $\mathbf{W}_2$ are the inverse covariance matrices of random errors associated with $\tilde{\mathbf{y}}_1$ and $\tilde{\mathbf{y}}_2$, respectively. Additionally, $\tilde{\mathbf{y}}_1$ and $\tilde{\mathbf{y}}_2$ are not correlated with one another.

First, an equation to update $\hat{\mathbf{P}}_2$ based on $\hat{\mathbf{P}}_1$ is readily available.

$$\hat{\mathbf{P}}_2^{-1} = \hat{\mathbf{P}}_1^{-1} + \mathbf{H}_2^T\mathbf{W}_2\mathbf{H}_2 \tag{2.53}$$

Through matrix manipulation an update equation for $\hat{\mathbf{x}}_2$ can be defined.

$$\hat{\mathbf{x}}_2 = \hat{\mathbf{x}}_1 + \hat{\mathbf{P}}_2\mathbf{H}_2^T\mathbf{W}_2\left(\tilde{\mathbf{y}}_2 - \mathbf{H}_2\hat{\mathbf{x}}_1\right) \tag{2.54}$$

Equations (2.53) and (2.54) can be rewritten and generalized.

$$\hat{\mathbf{P}}_{k+1}^{-1} = \hat{\mathbf{P}}_k^{-1} + \mathbf{H}_{k+1}^T\mathbf{W}_{k+1}\mathbf{H}_{k+1} \tag{2.55}$$

$$\hat{\mathbf{x}}_{k+1} = \hat{\mathbf{x}}_k + \mathbf{K}_{k+1}\left(\tilde{\mathbf{y}}_{k+1} - \mathbf{H}_{k+1}\hat{\mathbf{x}}_k\right) \tag{2.56}$$

where,

$$\mathbf{K}_{k+1} = \hat{\mathbf{P}}_{k+1}\mathbf{H}_{k+1}^T\mathbf{W}_{k+1} \tag{2.57}$$

Equation (2.56) is known as the Kalman Update Equation. Equation (2.57) is known as the Kalman Gain Matrix, which specifies how heavily new observations should be weighted compared to the original state estimate during the update process. Equation (2.55) is known as the information matrix recursion form of the covariance update equation. This process should be simplified further, however, because the matrix inverse of Equation (2.55) must be computed repeatedly whenever the state estimate is updated.

Using the Sherman-Morrison-Woodbury matrix inversion lemma (Reference [27]), Equations (2.55) and (2.57) can be rearranged into the covariance recursion form.

$$\mathbf{K}_{k+1} = \hat{\mathbf{P}}_k\mathbf{H}_{k+1}^T\left(\mathbf{H}_{k+1}\hat{\mathbf{P}}_k\mathbf{H}_{k+1}^T + \mathbf{W}_{k+1}^{-1}\right)^{-1} \tag{2.58}$$

$$\hat{\mathbf{P}}_{k+1} = \left(\mathbf{I} - \mathbf{K}_{k+1}\mathbf{H}_{k+1}\right)\hat{\mathbf{P}}_k \tag{2.59}$$

Several terms are introduced to facilitate comparisons with later estimation algorithms. First, the numerator of Equation (2.58) is redefined as the cross covariance, $\hat{\mathbf{C}}_k$. The cross covariance relates how the state estimate varies compared to how the residual error, or innovation, varies.

$$\hat{\mathbf{C}}_k = \hat{\mathbf{P}}_k \mathbf{H}_{k+1}^T \tag{2.60}$$

Second, the denominator of Equation (2.58) is defined as the innovations covariance, $\hat{\mathbf{S}}_k$. The innovations covariance characterizes how the residual error varies.

$$\hat{\mathbf{S}}_k = \left(\mathbf{H}_{k+1} \hat{\mathbf{P}}_k \mathbf{H}_{k+1}^T + \mathbf{W}_{k+1}^{-1} \right) \tag{2.61}$$

Thus, the Kalman Gain Matrix calculation in Equation (2.58) can be written as,

$$\mathbf{K}_{k+1} = \hat{\mathbf{C}}_k \left(\hat{\mathbf{S}}_k \right)^{-1} \tag{2.62}$$

Equations (2.56), (2.58), and (2.59) are the fundamental equations for many different sequential estimation processes, particularly those based on the Linear Kalman Filter (LKF). More information can be found in [27].

2.4.3 The Continuous-Time Discrete Observation Kalman Filter

The linear least squares principle and sequential estimation approach discussed in Sections 2.4.1 and 2.4.2, respectively, were devised for algebraic, but not dynamic systems [27]. While the underlying mathematics remain valid, the equations developed in Section 2.4.2 must be modified to accommodate changes in the state that occur between the last estimate and the next observation. In 1960, Rudolf E. Kalman developed what would become known as the Linear Kalman Filter (LKF) to adapt the linear least squares principle to dynamic systems [35]. The fundamental difference between the linear least squares sequential estimation and the Kalman Filter is that from t_k to t_{k+1} the state estimate, $\hat{\mathbf{x}}_k$ must be propagated before it can be updated based on new observations.

First, the LKF, as shown in Algorithm 2.2, was created to directly apply linear least squares sequential estimation to a dynamic system. The presented LKF is derived for a continuous-time, linear dynamics system, and a discrete observation model, as defined in Equation (2.63).

$$\dot{\mathbf{x}}(t) = \mathbf{F}(t)\mathbf{x}(t) + \mathbf{B}(t)\mathbf{u}(t) + \mathbf{G}(t)\boldsymbol{w}(t), \quad E\left[\boldsymbol{w}(t)\boldsymbol{w}^T(\tau)\right] = \mathbf{Q}(t)\delta(t-\tau) \tag{2.63a}$$

$$\tilde{\mathbf{y}}_k = \mathbf{H}_k \mathbf{x}_k + \boldsymbol{v}_k, \quad \boldsymbol{v}_k \sim \mathcal{N}(\mathbf{0}, \mathbf{R}_k) \tag{2.63b}$$

The LKF is initialized with a state estimate $\hat{\mathbf{x}}_0$ and covariance $\hat{\mathbf{P}}_0$ at $t_k = t_0$. While $t_k < t_f - \Delta t$, Algorithm 2.2 is used to propagate and update the estimate from one time step to the next.

Algorithm 2.2 Continuous-Time, Discrete Observation Linear Kalman Filter

procedure PREDICTION PHASE($\hat{\mathbf{x}}_{n,k}$, $\hat{\mathbf{P}}_{n,k}$, t_k, t_{k+1})

Propagate the state estimate to t_{k+1} to find the predicted state estimate, $\hat{\mathbf{x}}_{n,k+1|k}$

$$\dot{\hat{\mathbf{x}}} = \mathbf{F}(t)\hat{\mathbf{x}}(t) + \mathbf{B}(t)\mathbf{u}(t) \tag{2.64}$$

Propagate the covariance to t_{k+1} to determine the predicted covariance, $\hat{\mathbf{P}}_{n,k+1|k}$

$$\dot{\hat{\mathbf{P}}} = \mathbf{F}(t)\hat{\mathbf{P}}(t) + \hat{\mathbf{P}}(t)\mathbf{F}^T(t) + \mathbf{G}(t)\mathbf{Q}(t)\mathbf{G}^T(t) \tag{2.65}$$

procedure UPDATE PHASE($\hat{\mathbf{x}}_{n,k+1|k}$, $\hat{\mathbf{P}}_{n,k+1|k}$, $\tilde{\mathbf{y}}_{(n,m),k+1}$, t_{k+1})

Calculate the cross covariance, $\hat{\mathbf{C}}_{n,k+1|k}$

$$\hat{\mathbf{C}}_{(n,m),k+1|k} = \hat{\mathbf{P}}_{n,k+1|k}\mathbf{H}^T_{m,k+1} \tag{2.66}$$

Calculate the innovations covariance, $\hat{\mathbf{S}}_{n,k+1|k}$

$$\hat{\mathbf{S}}_{(n,m),k+1|k} = \mathbf{H}_{m,k+1}\hat{\mathbf{P}}_{n,k+1|k}\mathbf{H}^T_{m,k+1} + \mathbf{R}_{m,k+1} \tag{2.67}$$

Calculate the Kalman Gain Matrix, $\mathbf{K}_{(n,m),k+1}$, at t_{k+1}

$$\mathbf{K}_{(n,m),k+1} = \hat{\mathbf{C}}_{(n,m),k+1|k}\left(\hat{\mathbf{S}}_{(n,m),k+1|k}\right)^{-1} \tag{2.68}$$

Update the state estimate

$$\hat{\mathbf{x}}_{n,k+1} = \hat{\mathbf{x}}_{n,k+1|k} + \mathbf{K}_{(n,m),k+1}\left(\tilde{\mathbf{y}}_{(n,m),k+1} - \mathbf{H}_{m,k+1}\hat{\mathbf{x}}_{n,k+1|k}\right) \tag{2.69}$$

Update the covariance

$$\hat{\mathbf{P}}_{n,k+1} = \left(\mathbf{I} - \mathbf{K}_{(n,m),k+1}\mathbf{H}_{m,k+1}\right)\hat{\mathbf{P}}_{n,k+1|k} \tag{2.70}$$

It's useful to note that the measurement noise covariance matrix $\mathbf{R}_k$ replaces the inverse of the weighting matrix $\mathbf{W}^{-1}_{k+1}$ from the linear least squares sequential estimation process in Section 2.4.2. This substitution indicates that the observational information from more accurate sensors is weighted more heavily than the data from less capable sensors.

Additionally, similar to Equation (2.55), the information form of Equation (2.70) can be written as Equation (2.71).

$$\hat{\mathbf{P}}^{-1}_k = \hat{\mathbf{P}}^{-1}_{k|k-1} + \mathbf{H}^T_k\mathbf{R}^{-1}_k\mathbf{H}_k \tag{2.71}$$

A key drawback of the LKF is that it does not work well for nonlinear dynamic systems,

like the two-body model [27, 33]. Since the inception of the Kalman Filter, numerous variants have been developed to facilitate estimation of nonlinear systems. Unsurprisingly, the key trade-off for nonlinear estimation is between accuracy and computational power. R.E. Kalman developed one of the first, known as the Extended Kalman Filter (EKF), which was first used during NASA's Apollo program to calculate lunar trajectories [36]. The Extended Kalman Filter (EKF) is still widely used because it is incurs a relatively small computational cost over the LKF, compared to more modern, and more complex approaches.

The key differences between a continuous-time, discrete observation EKF and the LKF are in how the state estimate and covariance are propagated Lines 2 and 3 in Algorithm 2.2. First, a nonlinear system is defined in Equation (2.72).

$$\dot{\mathbf{x}}(t) = \mathbf{f}(\mathbf{x}(t), \mathbf{u}(t), t) + \mathbf{G}(t)\boldsymbol{w}(t), \quad E\left[\boldsymbol{w}(t)\boldsymbol{w}^T(\tau)\right] = \mathbf{Q}(t)\delta(t-\tau) \tag{2.72a}$$

$$\tilde{\mathbf{y}}_k = \mathbf{h}(\mathbf{x}_k) + \boldsymbol{v}_k, \quad \boldsymbol{v}_k \sim \mathcal{N}(\mathbf{0}, \mathbf{R}_k) \tag{2.72b}$$

The state estimate is directly propagated using the nonlinear dynamics by numerically integrating Equation (2.73).

$$\dot{\hat{\mathbf{x}}}(t) = \mathbf{f}(\hat{\mathbf{x}}(t), \mathbf{u}(t), t) \tag{2.73}$$

The plant matrix $\mathbf{F}(t)$ in Algorithm 2.2, would be defined by Equation (2.74), for a nonlinear system.

$$\mathbf{F}(t) = \left.\frac{\partial \mathbf{f}}{\partial \mathbf{x}}\right|_{\hat{\mathbf{x}}_0, \mathbf{u}_0} \tag{2.74}$$

In the EKF, however, the plant matrix is recalculated with $\mathbf{x}(t)$, as shown in Equation (2.75).

$$\mathbf{F}(t) = \left.\frac{\partial \mathbf{f}}{\partial \mathbf{x}}\right|_{\hat{\mathbf{x}}(t), \mathbf{u}(t)} \tag{2.75}$$

Similarly, the output matrix $\mathbf{H}_k$ in Algorithm 2.2 that is used to calculate the Kalman Gain and update the covariance in Equations (2.68) and (2.70), is replaced by Equation (2.76).

$$\mathbf{H}_k = \left.\frac{\partial \mathbf{h}}{\partial \mathbf{x}}\right|_{\hat{\mathbf{x}}_{k|k-1}} \tag{2.76}$$

Finally, the state update equation in Equation (2.69) is slightly modified, as shown in Equation (2.77).

$$\hat{\mathbf{x}}_k = \hat{\mathbf{x}}_{k|k-1} + \mathbf{K}_k\left(\tilde{\mathbf{y}}_k - \mathbf{h}(\hat{\mathbf{x}}_{k|k-1})\right) \tag{2.77}$$

2.4.4 Unscented Kalman Filter

The EKF is a useful tool for orbit estimation, but fails to provide the level of covariance propagation accuracy that is needed for this dissertation. The estimated covariance is an important component of both the adaptive estimation algorithm and decision process. Therefore, accurately modeling the covariance is a critical component of the overall framework. There are multiple alternatives that more closely capture the true covariance, to include the Unscented Kalman Filter (UKF) [37, 38], and the Particle Filter.

A useful and commonly presented illustration of the capability differences between the EKF, UKF, and particle filter is captured in how the filters model the covariance. A Gaussian distribution of orbital states, shown in Figure 2.2, is propagated through the two-body orbital dynamics. The resulting distribution, shown in Figure 2.3, stretches out in the in-

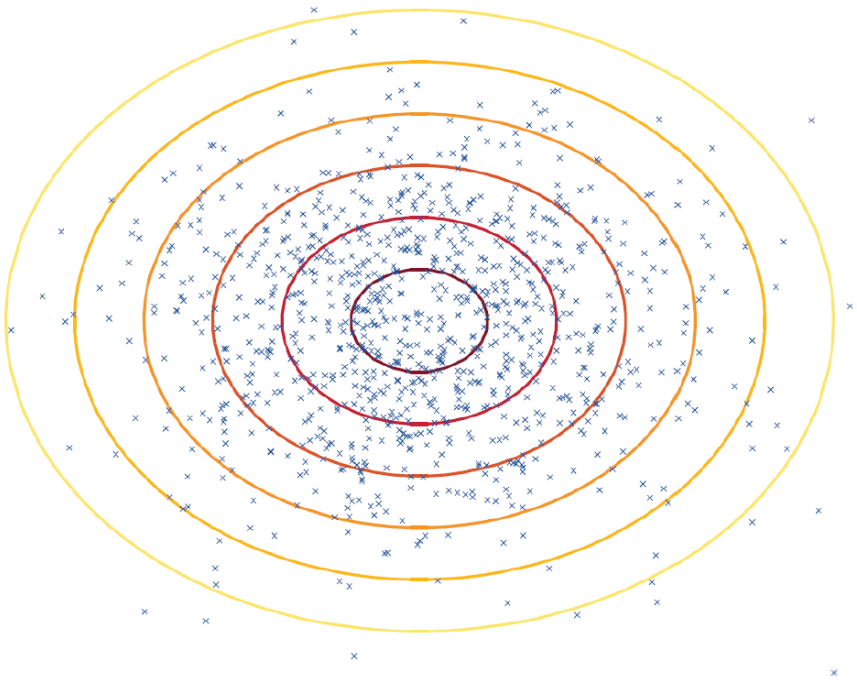

Figure 2.2: Initial Gaussian Distribution of Orbital States [2]

track direction and curves with the orbital path. In Figure 2.3 the estimated covariance from the EKF clearly only captures a fraction of the total distribution and extends out in the "along-track" direction, not curving with the orbit. The UKF captures more of the distribution, but also doesn't reflect the propagated distribution's non-ellipsoidal shape. It should be noted that the mean (the state estimate) is offset from the most likely state, in the radial direction, towards the Earth. The propagated particle distribution in a particle filter would more closely resemble the real distribution uncertainty in Figure 2.3 depending on the number of particles used. As previously mentioned, greater covariance estimation accuracy

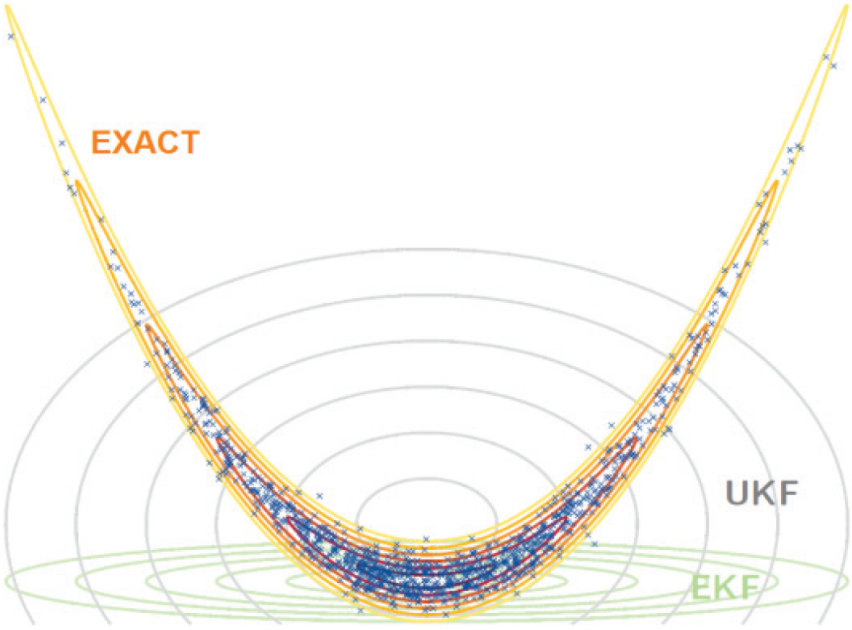

Figure 2.3: Propagated Distribution Comparison of Orbital States [2]

incurs a greater computational burden. In [39] a nonlinear scenario was devised that could be used to test various filters. For that particular scenario an EKF ran for an average of 0.08 seconds, while the two UKF algorithms took 1.18 seconds to run on average. Two particle filters were also assessed: one with 3,000 particles, and the second with 10,000. The former ran for and average of 249.7 seconds, while the latter took 680.9 seconds. Similarly, [40] compared the EKF and the UKF in an orbit estimation scenario, and concluded that the UKF was more robust to the initial estimate selection and therefore easier to tune than the EKF. [40] also confirmed that the UKF provides generally superior results over the EKF in the orbit estimation case. Therefore, the UKF was selected for this dissertation because it better accounts for the nonlinear propagation of the covariance while not dramatically increasing the computational workload.

The UKF process used in this dissertation is divided into four algorithms to facilitate later sensor tasking discussions and generally follows the process described in [41]. Additionally, it is assumed that the process and measurement noise is additive. This assumption is a common one in orbit estimation [42, 43, 44], and improves computation time by reducing the number of dimensions in the state and covariance estimates. [45] showed that in an additive noise case not incorporating process and measurement noise covariances in the state and covariance estimates yields similar results to the incorporated case, as long the number of dimensions in the state estimate remains constant. Like numerous other orbit estimation research efforts cited in this dissertation, an additive noise variation of the UKF is used in this research.

The continuous-time nonlinear system, and discrete observation model used in the UKF

are given in Equation (2.72). The UKF must be initialized at $t_k = t_0$ with an initial state estimate $\hat{\mathbf{x}}_0$, of dimension ℓ, and a corresponding covariance $\hat{\mathbf{P}}_0$. First, a scaling factor, Λ, is calculated in Equation (2.78), based on several parameters.

$$\Lambda = \alpha^2(\ell + \kappa) - \ell \tag{2.78}$$

These parameters characterize the number and distribution of the sigma points. The scaling factor Λ in Equation (2.78) determines the spread of the sigma point distribution based on ℓ and three tuning parameters: α, β, and κ. As previously mentioned, $\ell = 6$ in this dissertation, because the UKF used in this dissertation assumes additive noise. Additive noise is a common assumption in orbit estimation [43, 44, 46, 47, 33, 48], and significantly reduces the computational load incurred with each UKF. α is limited to the range $[0, 1]$. For this work $\alpha = 0.001$ based on previous sensor tasking research using a UKF [49]. β, is used to further characterize the covariance weighting scheme. $\kappa = 3 - \ell$ and $\beta = 2$ for Gaussian distributions.

At a given time step the UKF works by constructing a set of sigma points based on the current covariance estimate and Λ, the first of which is the current state estimate. These sigma points are variations on the current state estimate. The sigma points are distributed such that their mean remains the original state estimate. This process is shown in Equations (2.83) and (2.84).

A set the state and covariance weights are then determined using Equations (2.79) and (2.80). These weights are used to integrate sigma point information to form the final state estimate and covariance for a given time step.

$$\boldsymbol{\mathcal{W}}_{\mathrm{x}} = \begin{cases} \frac{\Lambda}{\ell+\Lambda} & \text{if } \gamma = 0 \\ \frac{1}{2(\ell+\Lambda)} & \text{if } \gamma = 1 \dots 2\ell \end{cases} \tag{2.79}$$

$$\boldsymbol{\mathcal{W}}_{\mathrm{P}} = \mathbf{W}_{\mathrm{x}} + \begin{bmatrix} (1 - \alpha^2 + \beta) \\ \mathbf{0}_{2\ell \times 1} \end{bmatrix} \tag{2.80}$$

where γ is a column number in the $\ell \times (2\ell + 1)$ sigma point matrix.

It is important to note that $\mathbf{W}_{\mathrm{x}}$ and $\mathbf{W}_{\mathrm{P}}$ used in the UKF prediction and forecast phases (Algorithms 2.3 and 2.4, respectively) are diagonal matrices of the column vectors calculated in Equations (2.79) and (2.80).

$$\mathbf{W}_{\mathrm{x}} = \mathrm{DIAG}\left(\boldsymbol{\mathcal{W}}_{\mathrm{x}}\right) \tag{2.81}$$

$$\mathbf{W}_{\mathrm{P}} = \mathrm{DIAG}\left(\boldsymbol{\mathcal{W}}_{\mathrm{P}}\right) \tag{2.82}$$

This minor change facilitates writing the UKF algorithms in matrix notation rather than the traditional summation notation.

The UKF begins with the prediction phase at the first time step, $k = 0$, and follows Algorithm 2.3 while $t_{k+1} \leq t_f$. The UKF differs from previously developed filters in that the

Algorithm 2.3 Unscented Kalman Filter: Prediction Phase

1: **procedure** PREDICTION PHASE($\hat{\mathbf{x}}_{n,k}$, $\hat{\mathbf{P}}_{n,k}$, t_k, t_{k+1})

2: Determine the Cholesky Decomposition of $\hat{\mathbf{P}}_{n,k}$ such that,

$$\hat{\mathbf{P}}_{n,k} = \hat{\mathbf{P}}_{n,k}^{CH} \left(\hat{\mathbf{P}}_{n,k}^{CH}\right)^T \tag{2.83}$$

3: Calculate the sigma points

$$\hat{\boldsymbol{\mathcal{X}}}_{n,k} = \hat{\mathbf{X}}_{n,k}\mathbf{1}_{(1\times 2\ell+1)} + \sqrt{\ell+\Lambda}\begin{bmatrix}\mathbf{0}_{(\ell\times 1)} & \hat{\mathbf{P}}_{n,k}^{CH} & -\hat{\mathbf{P}}_{n,k}^{CH}\end{bmatrix} \tag{2.84}$$

4: Propagate the sigma points without adding process noise.

$$\dot{\boldsymbol{\mathcal{X}}}_{n,i,k+1|k} = \mathbf{f}(\hat{\boldsymbol{\mathcal{X}}}_{n,i,t}) \qquad \text{for } i = 1\ldots 2\ell+1 \tag{2.85}$$

5: Calculate the predicted state estimate, $\hat{\mathbf{x}}_{n,k+1|k}$

$$\hat{\mathbf{x}}_{n,k+1|k} = \hat{\boldsymbol{\mathcal{X}}}_{n,k+1|k}\mathbf{W}_{\mathrm{x}} \tag{2.86}$$

6: Calculate the predicted covariance, $\hat{\mathbf{P}}_{n,k+1|k}$

$$\hat{\mathbf{P}}_{n,k+1|k} = \left[\Delta\hat{\boldsymbol{\mathcal{X}}}\right]\mathbf{W}_{\mathbf{P}}\left[\Delta\hat{\boldsymbol{\mathcal{X}}}\right]^T + \mathbf{Q}_{n,k} \tag{2.87}$$

$$\Delta\hat{\boldsymbol{\mathcal{X}}} = \hat{\boldsymbol{\mathcal{X}}}_{n,k+1|k} - \hat{\mathbf{x}}_{n,k+1|k}\mathbf{1}_{(1\times 2\ell+1)} \tag{2.88}$$

7: Redraw the sigma points to incorporate process noise effects

$$\hat{\boldsymbol{\mathcal{X}}}_{n,k+1|k} = \hat{\mathbf{x}}_{n,k+1|k}\mathbf{1}_{(1\times 2\ell+1)} + \sqrt{\ell+\Lambda}\begin{bmatrix}\mathbf{0}_{(\ell\times 1)} & \hat{\mathbf{P}}_{n,k+1|k}^{CH} & -\hat{\mathbf{P}}_{n,k+1|k}^{CH}\end{bmatrix} \tag{2.89}$$

where $\hat{\mathbf{P}}_{n,k+1|k}^{CH}$ follows the relationship defined in Equation 2.83.

state and covariance estimates are predicted by propagating the sigma points and essentially taking the weighted sum. Calculating the predicted covariance requires an additional step (Equation 2.88), but the general concept is still valid. The propagated sigma points take on the non-ellipsoidal distribution displayed in Figure 2.3, but it is this "weighted sum" that gives the predicted covariance estimate the ellipsoidal, somewhat offset shape seen in the figure.

The Forecast Phase, shown in Algorithm 2.4, is used to determine which sensors to task and to update the estimated covariance for a selected target-sensor pair.

When an observation is collected the state estimate is updated using Algorithm 2.5 and the maneuver detection metric is calculated.

Algorithm 2.4 Unscented Kalman Filter: Forecast Phase

1: **procedure** FORECAST PHASE($\hat{\boldsymbol{\mathcal{X}}}_{n,i,k+1|k}$, $\hat{\mathbf{P}}_{n,k+1|k}$, t_{k+1})

2: Calculate the predicted observations for each sigma point

$$\hat{\boldsymbol{\mathcal{Y}}}_{(n,m),k+1|k} = \mathbf{h}(\hat{\boldsymbol{\mathcal{X}}}_{n,i,k+1|k}, \mathbf{x}_{m,k+1}) \qquad \text{for } i = 1 \dots 2\ell+1 \quad \& \quad m = 1 \dots M' \tag{2.90}$$

3: Combined the predicted sigma point observations to form the predicted observation

$$\hat{\mathbf{y}}_{(n,m),k+1|k} = \hat{\boldsymbol{\mathcal{Y}}}_{(n,m),k+1|k} \mathbf{W}_{\mathrm{x}} \tag{2.91}$$

4: Calculate the cross covariance matrix, $\hat{\mathbf{C}}_{(n,m),k+1|k}$

$$\hat{\mathbf{C}}_{(n,m),k+1|k} = \left[\Delta\hat{\boldsymbol{\mathcal{X}}}\right] \mathbf{W}_{\mathbf{P}} \left[\Delta\hat{\boldsymbol{\mathcal{Y}}}\right]^T \tag{2.92}$$

$$\Delta\hat{\boldsymbol{\mathcal{Y}}} = \hat{\boldsymbol{\mathcal{Y}}}_{(n,m),k+1|k} - \hat{\mathbf{y}}_{(n,m),k+1|k} \mathbf{1}_{(1\times 2\ell+1)} \tag{2.93}$$

5: Calculate the innovations covariance matrix, $\hat{\mathbf{S}}_{(n,m),k+1|k}$

$$\hat{\mathbf{S}}_{(n,m),k+1|k} = \left[\Delta\hat{\boldsymbol{\mathcal{Y}}}\right] \mathbf{W}_{\mathbf{P}} \left[\Delta\hat{\boldsymbol{\mathcal{Y}}}\right]^T + \mathbf{R}_{m,k+1} \tag{2.94}$$

6: Calculate the Kalman gain matrix

$$\hat{\mathbf{K}}_{(n,m),k+1|k} = \hat{\mathbf{C}}_{(n,m),k+1|k} \hat{\mathbf{S}}^{-1}_{(n,m),k+1|k} \tag{2.95}$$

7: Update the covariance

$$\hat{\mathbf{P}}_{n,k+1} = \hat{\mathbf{P}}_{n,k+1|k} - \hat{\mathbf{K}}_{(n,m),k+1|k} \hat{\mathbf{S}}_{(n,m),k+1|k} \hat{\mathbf{K}}^T_{(n,m),k+1|k} \tag{2.96}$$

Because the filter must accommodate simultaneous observations from disparate sensors, several variables must be specifically structured to facilitate concurrent observations with potentially different measurement types. In Algorithms 2.4 and 2.5 all observation output vectors in the same time step are stacked vertically. Thus, for S observations from S sensors the combined observation output vector is given in Equation (2.100).

$$\tilde{\mathbf{y}}_{(n,1),k+1} = \left[\tilde{\mathbf{y}}^T_{k+1,1} \cdots \tilde{\mathbf{y}}^T_{(n,S),k+1}\right]^T \tag{2.100}$$

The sigma point observation output vector and the estimated observation output vector must be similarly structured. Additionally, the measurement covariance matrices for each sensor

Algorithm 2.5 Unscented Kalman Filter: Update Phase

1: **procedure** UPDATE PHASE($\hat{\mathbf{x}}_{n,k+1|k}$, $\tilde{\mathbf{y}}_{(n,m),k+1}$, $\hat{\mathbf{y}}_{(n,m),k+1|k}$, $\hat{\mathbf{S}}_{(n,m),k+1|k}$, $\hat{\mathbf{K}}_{(n,m),k+1|k}$, t_{k+1})

2: Calculate the innovations vector, $\tilde{\boldsymbol{\nu}}_{(n,m),k+1}$

$$\tilde{\boldsymbol{\varepsilon}}_{(n,m),k+1} = \tilde{\mathbf{y}}_{(n,m),k+1} - \hat{\mathbf{y}}_{(n,m),k+1|k} \tag{2.97}$$

3: Update the state estimate, $\hat{\mathbf{x}}_{n,k+1}$

$$\hat{\mathbf{x}}_{n,k+1} = \hat{\mathbf{x}}_{n,k+1|k} + \hat{\mathbf{K}}_{(n,m),k+1|k}\tilde{\boldsymbol{\varepsilon}}_{(n,m),k+1} \tag{2.98}$$

4: Calculate the Maneuver Detection Metric, $\hat{\psi}_{(n,m),k+1}$

$$\hat{\psi}_{(n,m),k+1} = \tilde{\boldsymbol{\varepsilon}}^{T}_{(n,m),k+1}\hat{\mathbf{S}}^{-1}_{(n,m),k+1|k}\tilde{\boldsymbol{\varepsilon}}_{(n,m),k+1} \tag{2.99}$$

associated with the observations must be combined into a single block diagonal matrix.

$$\mathbf{R}_{m,k+1} = \begin{bmatrix} \mathbf{R}_{1,k+1} & \cdots & \mathbf{0} \\ \vdots & \ddots & \vdots \\ \mathbf{0} & \cdots & \mathbf{R}_{S,k+1} \end{bmatrix} \tag{2.101}$$

If no observations are collected at t_{k+1}, the predicted state and covariance estimates are stored as the updated estimates.

$$\hat{\mathbf{x}}_{k+1} = \hat{\mathbf{x}}_{k+1|k} \tag{2.102}$$

$$\hat{\mathbf{P}}_{k+1} = \hat{\mathbf{P}}_{k+1|k} \tag{2.103}$$

2.4.5 Maneuver Detection

The ability to rapidly detect an unobserved maneuver is a critical component of the tasking algorithm's ability to maintain a viable orbit estimate for the maneuvering satellite. A number of methods are available (References [50], [51] and [52]), but this work implements the normalized innovations squared value, as described in [32], to serve as a maneuver detection metric. [28] demonstrated the utility of the normalized innovations squared metric for initiating adaptive estimation techniques when maneuvers are detected. The innovations vector and the Innovations Covariance Matrix are used to calculate the normalized innovations squared value using Equation 2.99.

$\hat{\psi}_{(n,m),k+1}$ is a chi-squared distributed variable with p degrees of freedom, or simply the dimension of the observation output vector. The detection threshold for $\hat{\psi}_{(n,m),k+1}$ is constant when all sensors output the same size observation output vector. In this dissertation the degrees of freedom can change for a particular target at each time step. Therefore, the chi-squared distribution associated with $\hat{\psi}_{(n,m),k+1}$ must be derived. Like in [29] and [30], the tasking strategy developed in this dissertation sets the maneuver detection threshold as the inverse chi-squared cumulative distribution function, shown in Equation (2.104).

$$\Psi_{m,k+1} = \left\{ \Psi : \int_0^{\Psi} \frac{t^{\frac{p-2}{2}} e^{-\frac{t}{2}}}{2^{\frac{p}{2}} \Gamma(\frac{p}{2})} dt = 1 - 1e^{-10} \right\} \tag{2.104}$$

where $\Gamma(\cdot)$ is the Gamma function. A maneuver is detected when the threshold is surpassed.

$$\psi_{(n,m),k+1} \geq \Psi_{m,k+1} \tag{2.105}$$

The threshold is set sufficiently high to reduce the risk of false detection. An important assumption associated with using the normalized innovations squared value as a maneuver detection metric is that the observational data from the sensors is trustworthy. In other words, the measurement noise injected into each observation is characterized by the measurement noise covariance matrix. This assumption would be violated if sensor malfunctions or unknown additional noise, like jamming, were modeled. This is not the case in this dissertation.

The maneuver detection metric is calculated at the current time step, and initializes the MMAE process over a prescribed time window.

2.4.6 Previous Adaptive Estimation Research

Adaptive estimation is the process by which a sequential estimation process is modified or augmented to account for unknown or new dynamics. There is a wide array of adaptive estimation techniques that have been developed over the last few decades for a variety of situations. For the sake of this discussion, many adaptive estimation techniques can be binned into two categories:

1. Modification of the nominal filter to accommodate abrupt changes in the dynamics (e.g. input estimation, and variable state dimension filters)
2. MMAE to capture a sufficient set of possible dynamics

[53] developed a method, using input estimation, where the thrust acceleration and the non-thrusting state are estimated concurrently. The estimated thrust acceleration is only incorporated into the state estimate when a bias threshold is reached, thus signaling that a maneuver has occurred and mitigating the resulting error. [54] later applied input estimation to orbit estimation of a maneuvering spacecraft. Known maneuver reconstruction techniques were integrated with a neural network to more accurately estimate the thrust input. [55] introduced the Variable Dimension Filter where, after a maneuver is detected, the non-maneuvering dynamics are augmented with the thrust acceleration dynamics, and the state estimate is reassessed over the time window defined by the maneuver detection metric. [56] demonstrated the use of a fading memory Kalman filter where the covariance estimate is adaptively expanded to essentially "forget" older observations. In doing so, a fading memory filter may accept new observations more readily after the target maneuvers than a nominal filter with a longer history of observations. [57] refined the fading memory approach with a UKF for a maneuvering vehicle, and demonstrated the method's utility over other adaptive UKF algorithms. Several other methods have been proposed for modifying the process and measurement noise covariances to account for unknown, nonlinear dynamics. [58] developed adaptive approaches for a UKF and a Divided Difference Filter, while [59] described two UKF-based approaches, similar to the input estimation method, to control a model helicopter in the presence of unknown rotor noise.

A popular alternative to the augmented filters described previously is Multiple Model Adaptive Estimation (MMAE), which was first proposed in the 1960s [60]. [61] later formulated the Interacting Multiple Model (IMM), which serves as an efficient means of conducting dynamic multiple model estimation. The IMM enabled the partial mixing of estimates from a set of models to enable rapid switching between modes when system dynamics change. [62] was one of the first to demonstrate the advantages of the IMM approach over Input Estimation. In that paper, it was shown that an IMM could detect a maneuver and mitigate the resulting errors faster than the input estimation approach. The IMM also required fewer computational resources. [63] assessed the use of an IMM to fuse observations from multiple sensors when tracking a maneuvering target, noting that more data didn't necessarily imply better estimates if the filter isn't consistent. [63] concluded that, barring additional complexities and biases in the sensor network, an IMM could be used to detect inconsistencies, such as when a maneuver occurs, and help mitigate those inconsistencies.

Since then, MMAE methods have been applied to a wide array of situations, to include orbit estimation. [64] used scalar covariance inflation within an IMM to rapidly filter through an unobserved maneuver. [65] integrated variable state dimension filters with the multiple-model approach to produce a robust method of tracking a continuously thrusting spacecraft. [47] and [66] used an IMM to detect and characterize the duration of a finite thrust. [67] used

an IMM to rapidly determine a guided missile's trajectory to enable avoidance maneuver planning, and estimate the resulting miss distance. Most recently, [68] used two types of UKFs in an IMM. The first set of UKFs varied the process noise covariance, while the second set varied the measurement noise covariance. The result was an IMM that produced a more accurate estimate over time than either filter could independently, once again demonstrating the value of multiple model adaptive estimation over other approaches. [2] noted the utility of MMAE techniques to converge on new orbit estimates after an unobserved maneuver was detected, and recommended that the U.S. government pursue MMAE to improve SSA. As such, this dissertation focuses on using MMAE within the decision making process to detect and mitigate unobserved maneuvers.

2.5 Decision Processes

This section introduces the concept of a partially observed Markov decision process and derives the two information-based metrics that are used in this dissertation.

2.5.1 Partially Observed Markov Decision Processes

The concept of a Partially Observed Markov Decision Process (POMDP) provides framework for determining which actions should be taken for a given situation based on noisy indirect measurements of a dynamic system. Figure 2.4 graphically lays out thePOMDP process. A Hidden Markov Model (HMM) is a noisy stochastic system that is observed with noisy

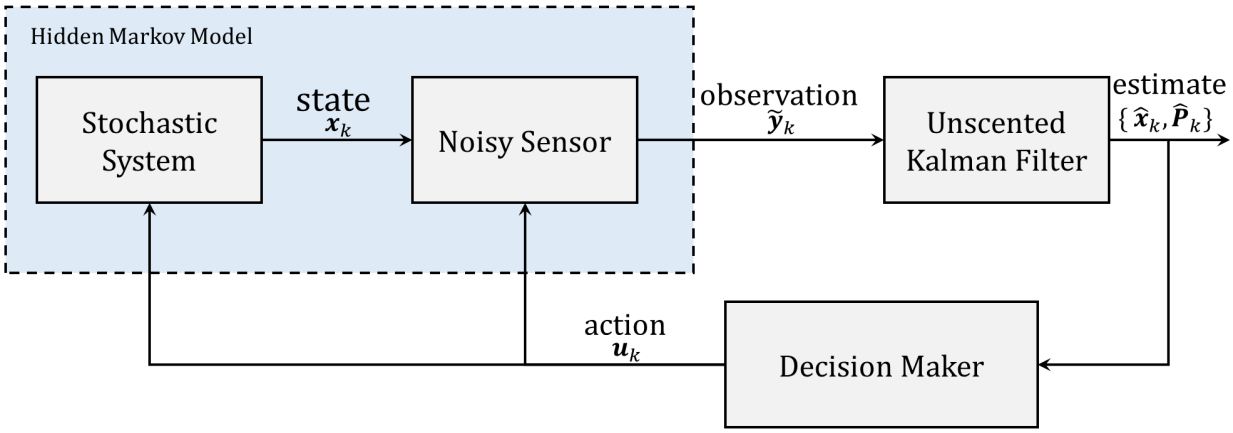

Figure 2.4: Applied Partially Observed Markov Decision Process

measurements. In this dissertation the HMM is comprised of the underlying deterministic, two-body and terrestrial dynamics, the boresight direction of the sensors, and the continuous-

time process noise $\boldsymbol{w}_{n,k}$, discussed in Section 2.2.6. The stochastic system is a Markov Chain because the boresight direction of each sensor is the result of a series of previous decisions, which were themselves stochastically driven. The observations of the stochastic system are indirect measurements because they do not specifically measure position and velocity. Instead, observations consist of the azimuth, elevation, range, and range-rate measurements, described in Section 2.3, with measurement noise $\boldsymbol{v}_{m,k}$, which further obscures the system model.

As depicted in Figure 2.4, the HMM informs the estimation process, which is a UKF in this dissertation. The state estimates for the targets $\hat{\mathbf{x}}_{1..N,k}$, and the associated covariance $\hat{\mathbf{P}}_{1..N,k}$ are together defined as the belief state. The belief state at t_k propagates forward to t_{k+1} and is used to determine a set of actions, u_k. In this dissertation, the actions dictate where each sensor should point on the next time step, and which target it should observe.

Optimization of the POMDP would take place over a time horizon $t_k \rightarrow t_{k+\tau}$ using linear or dynamic programming, depending on the scenario [69]. Optimization in this manner assumes that the underlying dynamics in the HMM do not change within the time window. As noted in Section 2.5.4, much of the previous research into POMDPs for sensor network management has investigated various methods for optimizing actions over a time horizon. Indeed, part of why the current sensor tasking process takes hours or days to assess anomalous activity is because underlying decision process is an optimized POMDP over a 12-24 hour time horizon [70, 9]. The current framework is designed for routine observations.

If the monitored target maneuvered during the time window, the system becomes a jump Markov linear/nonlinear system and the remaining set of actions would no longer be optimal. Instead, a suboptimal and myopic decision policy can be used that determines the optimal set of actions for the given time step only [69]. If the presence of maneuvering, but unknown targets over a time period is assumed, then a suboptimal POMDP process can be used to responsively mitigate unknown jump Markov systems.

2.5.2 Fisher Information Gain

The Fisher Information Matrix represents the amount of accumulated information present in an unbiased filter. Most importantly, the inverse of the Fisher Information Matrix is directly related to the Cramer-Rao limit, which characterizes the lower bound of the mean-squared error between the estimated and true states. Therefore, if the Fisher Information is high, the variance, or uncertainty in the estimate, will be low. The Fisher Information Matrix is defined in Equation (2.106) [44].

$$\mathfrak{F}_k = \mathrm{E}\left\{\left[\frac{\partial}{\partial \mathbf{x}_k}\log_e\left(p\left(\tilde{\mathbf{y}}_k|\mathbf{x}_k\right)\right)\right]\left[\frac{\partial}{\partial \mathbf{x}_k}\log_e\left(p\left(\tilde{\mathbf{y}}_k|\mathbf{x}_k\right)\right)\right]^T\right\} \tag{2.106a}$$

$$\mathfrak{F}_k = \mathrm{E}\left\{\frac{\partial^2}{\partial \mathbf{x}_k \partial \mathbf{x}_k^T}\log_e\left(p\left(\tilde{\mathbf{y}}_k|\mathbf{x}_k\right)\right)\right\} \tag{2.106b}$$

The Cramer-Rao Lower Bound states that the estimation error covariance must be greater than or equal to the inverse of the Fisher Information Matrix [32, 27].

$$\hat{\mathbf{P}}_k \geq \mathfrak{F}_k^{-1} \tag{2.107}$$

[71] describes a recursive method for calculating the Fisher Information Matrix for estimation of nonlinear systems with purely additive and invertible process and measurement noise covariances. Using this process, the Fisher Information Matrix at t_{k+1} can be related to the previous value at t_k, as shown in Equation (2.108).

$$\mathfrak{F}_{k+1} = \mathbf{Q}_k^{-1} + \mathbf{H}_{k+1}^T \mathbf{R}_{k+1}^{-1} \mathbf{H}_{k+1} - \mathbf{Q}_k^{-1} \mathbf{F}_k \left(\mathfrak{F}_k + \mathbf{F}_k^T \mathbf{Q}_k^{-1} \mathbf{F}_k \right)^{-1} \mathbf{F}_k^T \mathbf{Q}_k^{-1} \tag{2.108}$$

As discussed in Section 2.4, the substitution $\mathfrak{F}_k = \hat{\mathbf{P}}_k^{-1}$ can be made to get a recursive information matrix form for the covariance update equation.

$$\hat{\mathbf{P}}_{k+1}^{-1} = \left(\mathbf{Q}_k + \mathbf{F}_k \hat{\mathbf{P}}_k \mathbf{F}_k^T \right)^{-1} + \mathbf{H}_{k+1}^T \mathbf{R}_{k+1}^{-1} \mathbf{H}_{k+1} \tag{2.109}$$

$$\hat{\mathbf{P}}_{k+1}^{-1} = \hat{\mathbf{P}}_{k+1|k}^{-1} + \mathbf{H}_{k+1}^T \mathbf{R}_{k+1}^{-1} \mathbf{H}_{k+1} \tag{2.110}$$

The term $\mathbf{H}_{k+1}^T \mathbf{R}_{k+1}^{-1} \mathbf{H}_{k+1}$ represents the information gained from the observations at t_{k+1} and is thus referred to as the Fisher Information Gain (FIG), which will be referred to as $\mathbf{\Omega}_{k+1}$.

$$\hat{\mathbf{\Omega}}_{k+1} = \mathbf{H}_{k+1}^T \mathbf{R}_{k+1}^{-1} \mathbf{H}_{k+1} \tag{2.111}$$

Equations (2.110) and (2.71) are equivalent for estimation of a linear system, but for nonlinear estimation, particularly in the UKF, an approximation of $\mathbf{H}_k$ must be made. The necessary approximation can be derived using the definition of the cross covariance in Equation (2.66) or (2.92).

$$\boldsymbol{\eta}_{k+1} = \hat{\mathbf{C}}_{k+1|k}^T \hat{\mathbf{P}}_{k+1|k}^{-1} \approx \mathbf{H}_{k+1} \tag{2.112}$$

The Fisher Information Gain can then be written as

$$\hat{\mathbf{\Omega}}_{k+1} = \hat{\boldsymbol{\eta}}_{k+1}^T \left(\mathbf{R}_{k+1} \right)^{-1} \hat{\boldsymbol{\eta}}_{k+1} \tag{2.113}$$

A very useful characteristic of the FIG is that the values from multiple simultaneous observations of a specific target from independent sensors can be summed to find the total FIG at a particular time step. Given a subset of sensors $\{\mathrm{s}_1 \ldots \mathrm{s}_{m'}\} \subset \mathcal{S}$,

$$\{\hat{\mathbf{P}}_{n,k}\}^{-1} = \{\hat{\mathbf{P}}_{n,k|k-1}\}^{-1} + \sum_{j=1}^{m'} \hat{\mathbf{\Omega}}_{n,j,k} \tag{2.114}$$

where n is the element number in the set of target estimates and m is the element number in the set of sensors.

Because the FIG is a matrix, it's necessary to find a scalar representation that can be used as a metric. Previous studies have used the trace of the FIG matrix to accommodate linear filters, like the Extended Kalman Filter [72]. This practice admittedly limits the metric's realism. Because this dissertation uses the UKF, the determinant can be used instead, as in Equation (2.115).

$$\hat{\phi}_{(n,m),k} = \left|\det\left(\hat{\mathbf{\Omega}}_{n,m,k}\right)\right| \tag{2.115}$$

2.5.3 Maximal Lyapunov Exponent Approximation

A second information-based metric, referred to as the maximal Lyapunov exponent approximation (MLEA), takes inspiration from Lyapunov stability analysis to roughly approximate the stability of a target estimate over time based on a set of stochastic data. The approximation of the maximal Lyapunov exponent was introduced as a metric for space surveillance network management in [49]. Whereas Fisher Information Gain is an instantaneous metric, based solely on the information available at a single time step, MLEA offers less myopic insight into the rate at which the estimate covariance converges or diverges.

In Lyapunov stability analysis the Lyapunov Spectrum refers to a set of exponents that characterize how a trajectory is converging or diverging in each dimension. Suppose two data points, $x_{i,0}$ and $x_{j,0}$, at an initial time, t_0 with an initial separation defined as

$$\left|\left|x_{i,0} - x_{j,0}\right|\right|_2 = \delta_0 \ll 1 \tag{2.116}$$

The separation between the two points after some time $\delta_{\Delta t}$ can be described as

$$\delta_{\Delta t} = \left|\left|x_{i,\Delta t} - x_{j,\Delta t}\right|\right|_2 \approx \delta_0 e^{\lambda_i \Delta t} \tag{2.117}$$

given that $\delta_{\Delta t} \ll 1$, and $\Delta t \gg 1$ [73]. A positive λ_i indicates exponential divergence and an unstable system. When $\lambda_i = 0$, the system is marginally stable in that dimension. A negative λ_i indicates exponential convergence in a stable system.

Stability, however, can only be conclusively determined in a deterministic system. Such assertions are much more difficult in stochastic systems, particularly those that are observed indirectly with noisy measurements. Lyapunov stability analysis of a time series data set, however, can still be used to approximately characterize the stability of a system based on the indirect observations [73]. Lyapunov exponents are invariant with respect to transformations from state to observations and back. An "instability" in a time series of observations, particularly over a long period of time, *may* indicate an instability in the observed system.

[74] was the first to use the maximal Lyapunov exponent $\lambda^1_{n,k+1}$ to assess system stability with a time series of measurement data, as shown in Equation (2.118).

$$\lambda^1_n = \frac{1}{t_f - t_0} \sum_{\kappa=0}^{K} \log_2\left(\frac{\delta_{n,\kappa+1}}{\delta_{n,\kappa}}\right) \tag{2.118}$$

where K is the total number of time steps in a scenario.

When $t_0 = 0$, as is the case in this dissertation, Equation (2.118) simplifies to Equation (2.119) for a given time step to form the effective maximal Lyapunov exponent [75].

$$\lambda_{n,k+1}^{\text{eff}} = \frac{1}{t_{k+1}} \log_2 \left(\frac{\delta_{n,k+1}}{\delta_{n,0}} \right) \tag{2.119}$$

In orbit estimation the two points of interest are the estimated state and the true state. In this case, $\delta_{n,k}$ is the RMS true error of estimate n, associated with target n, as defined in Equation (2.36).

$$\lambda_{n,k+1}^{\text{eff}} = \frac{1}{t_{k+1}} \log_2 \left(\frac{||\boldsymbol{\varepsilon}_{n,k+1}||_2}{||\boldsymbol{\varepsilon}_{n,0}||_2} \right) \tag{2.120}$$

As discussed in Section 2.4.1, the distance between the estimated and the true states (i.e. the true error) cannot be known. However, it can be approximated by the covariance estimate. Therefore, let

$$||\boldsymbol{\varepsilon}_{n,k+1}||_2 = \sqrt{\text{trace}\left(\hat{\mathbf{P}}_{n,k+1|k} \right)} \tag{2.121}$$

and associate the initial distance with the prescribed initial covariance estimate,

$$||\boldsymbol{\varepsilon}_{n,0}||_2 = \sqrt{\text{trace}\left(\hat{\mathbf{P}}_{n,0} \right)} \tag{2.122}$$

Therefore, the maximal Lyapunov exponent approximation metric for a POMDP can be defined as Equation (2.123), as per [44].

$$\lambda_{n,k+1}^{\text{eff}} = \frac{1}{t_{k+1}} \log_2 \sqrt{\frac{\text{trace}\left(\hat{\mathbf{P}}_{n,k+1|k} \right)}{\text{trace}\left(\hat{\mathbf{P}}_{n,0} \right)}} \tag{2.123}$$

2.5.4 Previous Sensor Management Research

Investigations into sensor management, and the decision processes therein, cover a wide range of areas from single system control to large scale network management. Sensor management becomes particularly important when multiple sensors are tasked to track multiple targets. The general concept of using information gain, derived from the estimation process, to task sensors was first fleshed out in [76]. [77] explicitly applied the concept to a sequential estimation problem involving a single vehicle with a diverse set of sensors and multiple targets to track. [78] presented a decentralized sensor network management approach where sensors decided independently if they would contribute to the overall tracking mission, based on communications with the sensors in the immediate vicinity (i.e. one-hop communications).

[79] used FIG to optimize how an unmanned aerial vehicle should configure its sensors to track multiple moving targets. [80] investigated how to manage several network topologies using latency, interference, and information gain metrics. The inclusion of a delay metric that sought to minimize the travel time of information from the sensor to a central hub was used in place of a more direct energy cost metric.

[81] and [82] formally defined the sensor management process as a Partially Observed Markov Decision Process process, and introduced cost metrics that accounted for the impact on the sensor hardware. [83] investigated the utility of Partially Observed Markov Decision Processes for tracking a generalized non-maneuvering target with multiple sensors using energy consumption metrics. [84] developed a POMDP approach that sought to reduce estimation error while also limiting the sensors' operational durations. In other words sensors could "sleep" when it was deemed appropriate. [85] created a POMDP algorithm to manage multiple unmanned aerial vehicles that are tasked to track multiple targets with visual sensors. In that paper, observational data are fused at a central level to enable centralized command and control of the sensor network.

Sensor management research for space surveillance has often attempted to address a specific aspect of the overall SOSI network command and control problem, as described in 1.2.4. Over a single orbital period, [86] showed how a set of four sensors (two radar, and two eletro-optical space-based sensors) could be optimally tasked to track 26 non-maneuvering, low earth orbit satellites. This paper also gave some consideration to sensor observability constraints. [87] used a centralized EKF with measurement-level data fusion, and a FIG metric to track non-maneuvering spacecraft. The sensors in [87] were ground and space-based, but provided the same types of two-dimensional observations. [88] and [89] directly used elements of the covariance estimate to determine multiple metrics with which to task three ground-based sensors to track non-maneuvering, medium Earth orbit satellites. [72] and [49], as successors to [87], introduced Shannon Information Gain and MLEA as decision metrics for space surveillance network management. [72] and [49] used the same set of ground and space-based sensors as [87], but tested the surveillance network against a set of 100 non-maneuvering satellites. To help manage error, [72] and [49] implemented the UKF, instead of the previously used EKF. [44] would later replace the UKF with an adaptive entropy-based Gaussian-mixture information synthesis (AEGIS) filter for additional nonlinear fidelity in the estimation process. [48] and [90] provided a similar network management algorithm that used a UKF and Fisher Information Gain to inform the decision-making process in a scenario much like the one used in [87]. [91, 92, 70] collectively provide a comprehensive characterization of the many aspects related to optimal satellite range scheduling, which is the term used to optimize sensor observations over a period of time. As with the previous research, an important assumption with optimal satellite range scheduling is that the monitored spacecraft do not maneuver unexpectedly within the time window. [69] describes a suboptimal POMDP approach that enables the responsiveness needed to autonomously manage a sensor network to track maneuvering targets. [28] was one of the first attempts to autonomously control a global sensor network to track a maneuvering satellite. In that

paper, a heuristics-based, suboptimal tasking strategy was developed and integrated with a simple adaptive estimation approach to track a single maneuvering spacecraft.

[87, 72, 49, 90, 48] demonstrated multi-sensor network management in a two dimensional model. Though only two dimensions are necessary to develop tasking algorithms for space domain awareness, the overall effectiveness of such algorithms cannot be thoroughly assessed without a three dimensional model. [28] and this dissertation's forerunners [29, 30, 31] used a 3D dynamics model with spacecraft at various altitudes and inclinations. Generally, the frequency and duration of satellites passes over a particular sensor vary greatly with orbit inclination, which cannot be modeled in a 2D simulation environment. For example, a polar or sun-synchronous spacecraft will have fewer and shorter passes over an equatorial, ground-based sensor, than a satellite in a 60° inclination orbit. Additionally, a satellite in a 60° inclination orbit is viewable to more sensors in a globally distributed sensor network than a satellite in an equatorial orbit. To facilitate the aforementioned research objectives, and to thoroughly assess the proposed tasking strategies, this dissertation develops and implements a higher fidelity simulation environment than those used in previous space surveillance network management investigations.

2.6 Summary

This chapter provided the foundational concepts upon which the research presented in this dissertation is developed. An overview of dynamics and relevant coordinate frames was provided to provide context and present the standardized notation used throughout the research. Relevant concepts in estimation and decision processes were also explained. Previous research in the areas of adaptive estimation and decision processes was described to delineate the current breadth and limitations of SSA command and control research.

Chapter 3

Model Development

3.1 Surveillance Network

3.1.1 Sensor Modeling & Constraints

As shown in Section 2.3.1, advanced radar provide the most information per observation and EOIR sensors provide the least. While radar provide more information than EOIR sensors, a robust sensor network consists of both because of the unique advantages and disadvantages associated with each. Radar, even powerful ones, often do not have the detection range of EOIR sensors. However, EOIR sensors are often more limited by environmental constraints like weather and solar illumination. EOIR sensors are generally more compact than radar, which makes them more viable options for space-based platforms. The SOSI network model used in this work is diversely populated, because many real-world global SOSI networks have a combination of ground and space-based sensors.

Radar Modeling

The advanced radar and radar sensor types are defined by transmit power ($P_{tx|m}$), wavelength (λ_m), dish diameter (d_m), and an overall efficiency (κ_m) specification. An example target with a known cross sectional area and range, as defined in Equation (3.1), is included to characterize the smallest detectable target at a particular range.

$$o_0 = \{\sigma_0, \rho_0\} \tag{3.1}$$

From this data the minimum detectable power at the sensor can be derived, using Algorithm 3.1, and then applied to any target. This method is used to facilitate the use of available real-world radar specifications. While characteristics like dish size, wavelength,

and even transmit power are often publicly available, the specifications that directly describe the radar's capabilities, such as minimum detectable power at the sensor, are often proprietary or classified. In place of these technical specifications, many organizations will advertise, "Radar A can track a basketball at 5,000 nautical miles" [93, 94, 95, 96].

Algorithm 3.1 Calculating Radar Power Received

1: Calculate the transmitted power for the given sensor s_m directed towards the example target o_n

$$P_{out|m} = \frac{\pi^2 P_{tx|m} d_m^2 \kappa_m}{\lambda_m^2} \tag{3.2}$$

2: Determine the power flux density at the target

$$F_{m|\rho_n,tx} = \frac{P_{out|m}}{4\pi\rho_n^2} \tag{3.3}$$

3: Calculate the power reflected from the target back to the radar

$$P_{back} = F_{m|\rho_n,tx}\sigma_{\mathrm{RF}|(n,m)} \tag{3.4}$$

$$\sigma_{\mathrm{RF}|(n,m)} = \frac{4\pi\sigma_n^2}{\lambda_m^2} \tag{3.5}$$

4: Calculate the power flux density at the radar aperture

$$F_{m|\rho_n,rx} = \frac{P_{back}}{4\pi\rho_n^2} \tag{3.6}$$

5: Determine the received power at the sensor

$$P_{rx} = \frac{\pi P_{tx|m} d_m^4 \kappa_m^2 \sigma_{\mathrm{RF}|(n,m)}}{64\lambda_m^2 \rho_n^4} \tag{3.7}$$

Equation (3.5) is used to determine the radar cross section of the target with σ_n representing the physical cross section. Equation (3.4) assumes the target is a perfectly conductive flat plate and surface normal to the observation state vector. Equation (3.7) is a variation of the widely documented standard Radar Equation [97, 98]. If the example target in Equation (3.1) is substituted into Algorithm 3.1, Equation (3.7) yields the minimum detectable power at the sensor for the given radar, $P_{rx,min|(m,n)}$.

With the minimum detectable power determined, the maximum detectable range for any target satellite can be calculated, as shown in Equation 3.8.

$$\rho_{max|(n,m)} = \sqrt[4]{\frac{\pi P_{tx|m} d_m^4 \kappa_m^2 \sigma_{\mathrm{RF}|(n,m)}}{64\lambda_m^2 P_{rx,min|(m,n)}}} \tag{3.8}$$

Electro-Optical/Infrared Modeling

Electro-optical/infrared (EOIR) sensors are modeled based on their aperture diameter and an overall efficiency specification. Because the EOIR sensors used here are strictly passive, the target satellite must be illuminated by the Sun. The reflected solar power off a satellite is defined in Equation (3.9).

$$P_{\odot|(n,k)} = F_{\odot}\sigma_n \tag{3.9}$$

where $F_{\odot} = 1440$ W/m^2 if the object is illuminated, and $F_{\odot} = 0$ W/m^2 if the object is in eclipse. The Earth's umbra is modeled as a cylinder with no penumbra. Thus, the spacecraft is illuminated if it does not fall within the umbra, per Equation (3.10). Additionally, because the scenarios run in this dissertation are relatively short, the Sun's position remains fixed in the $\hat{x}_1^{(\mathrm{ECI})}$ direction.

$$\Theta = \arccos \frac{\hat{\mathbf{x}}_1^{(\mathrm{ECI})} \cdot \mathbf{r}_k}{r_k} \leq \frac{\pi}{2} \qquad \text{or} \qquad r_k \cos\left(\Theta - \frac{\pi}{2}\right) > r_{\oplus} \tag{3.10}$$

This eclipse condition is depicted in Figure 3.1.1.

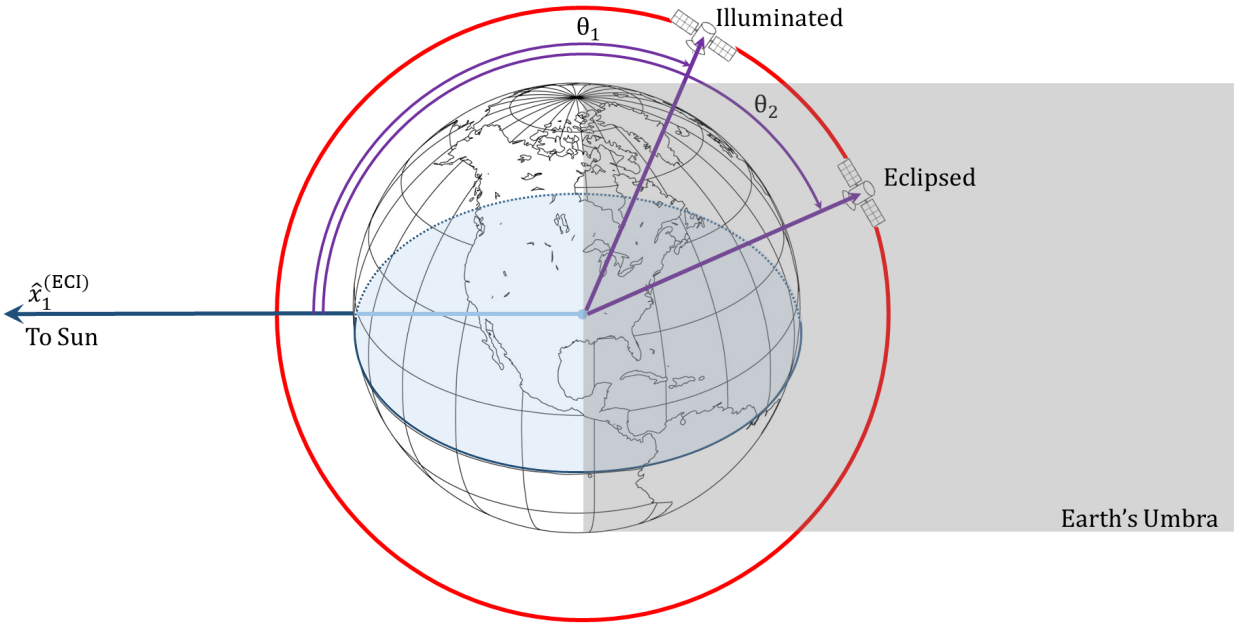

Figure 3.1: Earth's Eclipse Model

Like with radar, an exemplar, defined by a range and cross section from Equation (3.1), is used to characterize the smallest detectable target at a particular range. A minimum detectable power at the detector is then derived in Equation (3.11). Exemplars, from which the sensor's minimum detectable power is calculated, are based in part on [6, 7, 99, 100, 101,

102].

$$P_{rx,min|m} = \frac{P_{\odot|(0,0)} d_m^2 \kappa_m}{16 \rho_0^2} \tag{3.11}$$

The maximum range for a particular target is the calculated using Equation (3.12).

$$\rho_{max|(n,m)} = \sqrt{\frac{P_{\odot|(n,k)} d_m^2 \kappa_m}{16 P_{rx,min|m}}} \tag{3.12}$$

This formulation assumes the visible portion of the target has a flat, perfectly reflective cross sectional area. In this dissertation, the visible cross sectional area is equal to the physical cross section.

Observation Constraints

Each sensor's ability to observe the target constellation is constrained to increase the model's fidelity. The angular field of regard for a sensor can be limited to emulate rigidly pointed sensors, like LPARs, or terrain obstructions. The fields of view for sensors hosted on spacecraft are limited by the Earth's limb, which is defined as a disk of radius $r_\oplus + 100km$ from the center of the Earth. Expressed another way, a space-based sensor cannot observe a target if the Earth or the atmosphere are in the background.

A specific sensor's ability to observe a particular target is further constrained by the maximum detectable range, as calculated in Equation (3.8) and Equation (3.12) for radar and EOIR sensors, respectively. The range to the target must be less than or equal to the sensor's maximum detectable range for the target to be observable.

$$\rho_k^{(\text{SEZ})} \leq \rho_{max|(n,m)} \tag{3.13}$$

EOIR sensors have visibility constraints that depend on whether they are hosted on a facility or a spacecraft. Ground-based EOIR sensors must be in darkness, as determined using Equation (3.14), with the target still illuminated for an observation to be possible [33].

$$\hat{\mathbf{x}}_1^{(\text{ECI})} \cdot \mathbf{r}_k > 0 \tag{3.14}$$

In addition to the other relevant constraints described in this section, a space-based telescope can observe a target as long as the targeted spacecraft is illuminated.

A sensor's slew rate is also taken into consideration when determining whether a target is in-view. A sensor is not in view of a particular target if it cannot slew to the target's predicted position in the time allotted. The sensor's current boresight vector is based on the observation state vector associated with the last observation. k' refers to the time step

associated with the last observation, $t_{k'}$.

$$\boldsymbol{\varrho}_{m,k} = \frac{\boldsymbol{\rho}_{k'}^{(\mathrm{SEZ})}}{||\boldsymbol{\rho}_{k'}^{(\mathrm{SEZ})}||_2} \tag{3.15}$$

A target is in-view at t_{k+1} if

$$\cos^{-1}\left(\frac{\boldsymbol{\varrho}_{m,k} \cdot \boldsymbol{\rho}_{k+1}^{(\mathrm{SEZ})}}{||\boldsymbol{\rho}_{k+1}^{(\mathrm{SEZ})}||_2}\right) \leq \omega_m \left(t_{k+1} - t_{k'}\right) \tag{3.16}$$

where ω_m is the sensor's angular slew rate. In this study, the azimuthal and elevation slew rates are equal, though this is not necessarily true in reality.

The locations, types, capabilities, and constraints for each sensor in the SOSI Network developed for this study are provided in the following sections.

The Test SOSI Network

The SOSI network model is intended to emulate modern globally distributed networks, like the U.S. Space Surveillance Networks, but the code can accommodate any network design. Global SOSI networks tend to reside in a single hemisphere, based on [4]. Spacecraft are added to emulate developing trends in SSA [103, 104]. The space-based EOIR sensors are described in Table 3.1. The σ values provided in the tables in this section refer to the sensor's measurement noise characteristics. As mentioned in Section 2.3.1, a space-based sensor's observable azimuth and elevation are limited only by the Earth's limb. Azimuth and elevation angles are calculated for space-based sensors, instead of right ascension and declination, by determining the satellite's local "horizon" at the given time step using the equations outlined in Section 2.3.1. For this dissertation, space-based sensors in Highly Elliptical Orbit (HEO) replaced traditionally LEO spacecraft. The intent was to introduce additional differences in the geometry between space-based sensors and targets, in an effort to increase information gain. The so-called HEOSats have a perigee in LEO and an apogee that extends above GEO. The HEOSats can detect a small vehicle with $\sigma_{vis} = \pi$ m^2 at $\rho_0 = 36000$ km. The GEOSats can detect a basketball with $\sigma_{vis} = 0.0491$ m^2 at $\rho_0 = 10000$ km. All space-based sensors have a 4π steradian field of regard, with $d_m = 0.5$ m, $\kappa_m = 0.99$, and $\omega_m = 2\ ^\circ/s$. These values are based on a generalization of publicly available space-based telescope information [6, 7, 10].

Ground-based sensors in the Test SOSI Network are located in the Northern Hemisphere, and there are an equal number of advanced radar, radar, and electro-optical sensors. Advanced radar are assumed to be Large Phased Array Radar (LPAR) with fixed azimuthal fields of regard. The LPAR site and sensor specifications are detailed in Tables 3.2 and 3.3, respectively. All LPAR can detect a baseball with $\sigma_{vis} = 0.004371$ m^2 at $\rho_0 = 5500$ km. LPAR use electronically steered beams so it is assumed that they can observe any visible target within their fields of regard at every time step.

Table 3.1: SOSI Network: Space Electro-Optical Sensors

Spacecraft	Altitude (km)	e	i (°)	Ω (°)	ω (°)	ν (°)	σ_ϑ (°)	σ_φ (°)
HEOSat - 1	20183.627	0.675	153.4	45	0	0	0.00055556	0.00055556
HEOSat - 2	20183.627	0.675	153.4	45	0	180	0.00055556	0.00055556
HEOSat - 3	20183.627	0.675	153.4	225	0	0	0.00055556	0.00055556
HEOSat - 4	20183.627	0.675	153.4	225	0	180	0.00055556	0.00055556
HEOSat - 5	20183.627	0.675	153.4	135	0	90	0.00055556	0.00055556
HEOSat - 6	20183.627	0.675	153.4	135	0	270	0.00055556	0.00055556
HEOSat - 7	20183.627	0.675	153.4	315	0	90	0.00055556	0.00055556
HEOSat - 8	20183.627	0.675	153.4	315	0	270	0.00055556	0.00055556
GEOSat - 1	36121.863	0.0117647	1.5	0	0	0	0.00027778	0.00027778
GEOSat - 2	36121.863	0.0117647	1.5	0	0	180	0.00027778	0.00027778
GEOSat - 3	36121.863	0.0117647	1.5	135	90	0	0.00027778	0.00027778
GEOSat - 4	36121.863	0.0117647	1.5	135	90	180	0.00027778	0.00027778

Table 3.2: SOSI Network: Ground LPAR Sensors

Site	ϕ_{gd} (°N)	λ (°E)	Altitude (km)	σ_ϑ (°)	σ_φ (°)	σ_ρ (km)	$\sigma_{\dot\rho}$ (km/s)
LPAR - East	28.458	-80.535	0.005	0.015	0.015	0.001	0.00001
LPAR - West	33.754	90	0.250	0.015	0.015	0.001	0.00001
LPAR - Midway West	28.21	180	0.250	0.015	0.015	0.001	0.00001
LPAR - Midway East	28.21	270	0.250	0.015	0.015	0.001	0.00001

Table 3.3: SOSI Network: Ground LPAR Specifications

Site	Az Mask (°)	El Mask (°)	d_m (m)	κ_m	P_{tx} (MW)	f_{tx} (MHz)	ω_m (°/s)
LPAR - East	[80, 200]	[1, 89.99999]	50	0.95	35	650	180
LPAR - West	[170, 290]	[1, 89.99999]	50	0.95	35	650	180
LPAR - Midway West	[160, 280]	[1, 89.99999]	50	0.95	35	650	180
LPAR - Midway East	[80, 200]	[1, 89.99999]	50	0.95	35	650	180

Similarly, the ground-based radar sites and sensor specifications are described in Tables 3.4 and 3.5, respectively. For minimum detectable power calculations the radar, in the order they appear in the tables, can detect a target with $\sigma_{vis} = 1$ m^2 at $\rho_0 = 3000$ km, $\rho_0 = 4000$ km, $\rho_0 = 3500$ km, and $\rho_0 = 5000$ km. Slew rates were adjusted based on the aperture diameter to reflect the impact of greater inertia. The sensor capabilities also increase with aperture diameter to reflect a general improvement in resolution.

Table 3.4: SOSI Network: Ground Radar Sensors

Site	ϕ_{gd} (°N)	λ (°E)	Altitude (km)	σ_ϑ (°)	σ_φ (°)	σ_ρ (km)
Radar-VT	37.205	-80.417	0.1	0.03	0.03	0.0005
Radar-Maui	20.708	-156.257	1.8	0.028	0.0275	0.0005
Radar-Paris	48.845	2.302	0.025	0.029	0.028	0.0005
Radar-Denver	39.7486	-105.0075	0.025	0.025	0.025	0.0005

Table 3.5: SOSI Network: Ground Radar Specifications

Site	Az Mask (°)	El Mask (°)	d_m (m)	κ_m	P_{tx} (kW)	f_{tx} (GHz)	ω_m (°/s)
Radar-VT	[0, 359.99999]	[1, 89.99999]	10	0.95	150	1.5	10
Radar-Maui	[0, 359.99999]	[1, 89.99999]	20	0.95	150	1.5	5
Radar-Paris	[0, 359.99999]	[1, 89.99999]	15	0.95	150	1.5	7.5
Radar-Denver	[0, 359.99999]	[1, 89.99999]	30	0.95	150	1.5	2.5

The ground-based EOIR sensor sites are described in Table 3.6. All four EOIR ground sensors have a full azimuthal and elevation fields of regard, like the mechanical radar sites. Additionally, $d_m = 1$ m, $\kappa_m = 0.95$, and $\omega_m = 15$ $^\circ/s$ for all four sensors. Because ground-based telescopes tend to be small compared to mechanically steered radar, their slew rates are significantly faster than those specified for the radar. All four EOIR sensors can detect a basketball with $\sigma_{vis} = 0.0491$ m^2 at $\rho_0 = 32500$ km.

Table 3.6: SOSI Network: Ground EOIR Sensors

Site	ϕ_{gd} (°N)	λ (°E)	Altitude (km)	σ_ϑ (°)	σ_φ (°)
EOIR-ABQ	35.106	-106.629	0.015	0.00013889	0.00013889
EOIR-Oahu	21.568	-158.249	0.015	0.00013889	0.00013889
EOIR-USAFA	39.007	-104.882	0.015	0.00013889	0.00013889
EOIR-Etna	37.752	14.995	1.25	0.00013889	0.00013889

The full Test SOSI Network layout is presented in Figure 3.2.

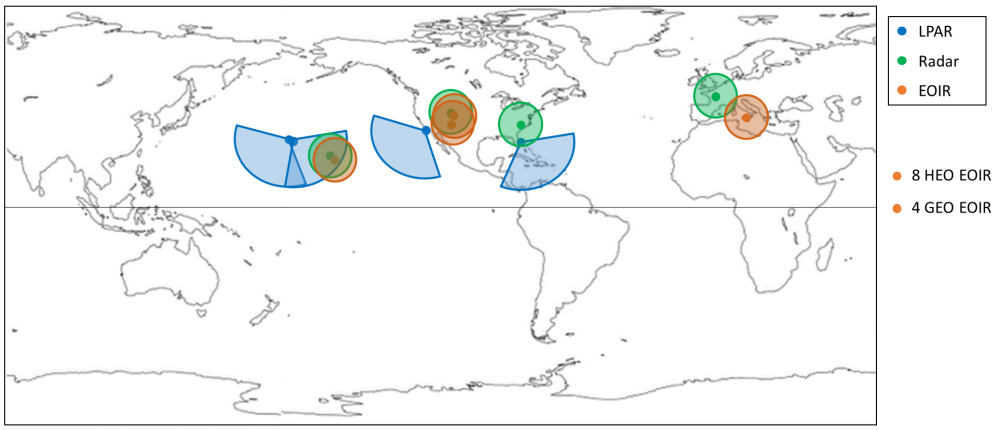

Figure 3.2: Test SOSI Network Map

3.2 Resident Space Objects

3.2.1 Preliminary Test Constellation

For the preliminary test constellation, the target satellites are modeled as a collection of Walker constellations [105], which efficiently distribute satellites to optimize ground coverage. Many large networks of satellites, like Iridium and GPS, are Walker constellations. Table 3.7 describes each constellation. "Phasing" refers to the relative phase angle between spacecraft in neighboring planes. If f is the relative phasing given in Table 3.7, then the change in true anomaly from one satellite to the next spacecraft in the adjacent plane is $\Delta\nu = 360° \frac{f}{N}$. N in this case is the number of satellites within the particular Walker constellation. Figure 3.3 depicts the preliminary test constellation with non-maneuvering target satellite orbits denoted in gray. The spacecraft in the SOSI Network are denoted in blue. The initial true anomaly for the first spacecraft in each constellation is randomly chosen to ensure the collective test constellation is well distributed. In many coding languages the random number generator can be seeded to create a repeatable random sequence. Thus, the test constellation's overall distribution can be repeated from one simulation to another by seeding the random number generator.

Table 3.7: Preliminary Constellation Topology

Constellation	Altitude (km)	i (°)	# of Satellites	# of Planes	Phasing	Cross Section (m^2)
LEO 1	500	63.4	20	5	1	6
LEO 2	1000	98.1	20	5	1	9
LEO 3	1500	40	20	5	1	8
MEO	20200	55	20	5	1	12
GEO	35786	1.5	20	5	1	14

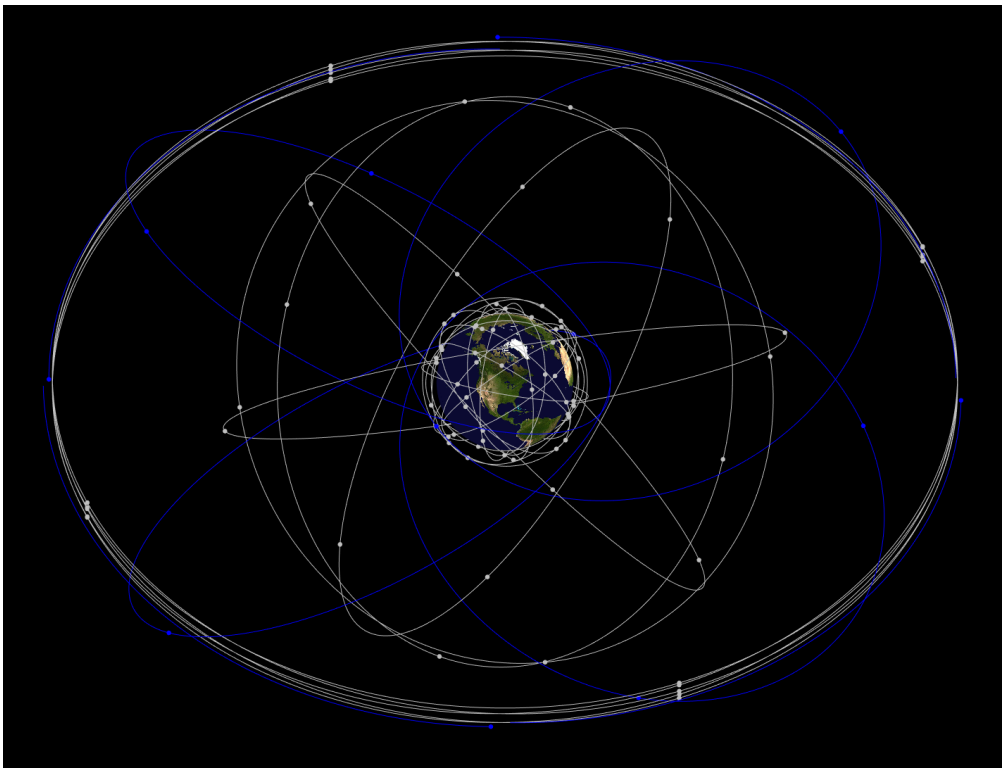

Figure 3.3: Preliminary Test Constellation Map

The preliminary test constellation only consists of non-maneuvering spacecraft. The purpose of this constellation is to provide a means of thoroughly testing decision processes without using adaptive estimation. The preliminary constellation is used to help determine the appropriate weights in the objective functions associated with each decision process. Once the weights are assessed the preliminary constellation is used to verify decision process functionality before the more representative testing is conducted with the full test constellation.

3.2.2 Full Test Constellation

The full test constellation is modeled as a collection of Walker constellations [105], like in [29, 30, 31], but in greater quantity. Table 3.8 describes each constellation. A description of how a Walker constellation is distributed can be found in Section 3.2.1.

Table 3.8: Full Constellation Topology

Constellation	Altitude (km)	i (°)	# of Satellites	# of Planes	Phasing	Cross Section (m^2)
LEO 1	400	63.4	44	11	1	6
LEO 2	500	98.1	30	15	1	9
LEO 3	750	30	24	8	1	4
LEO 4	1000	40	18	6	1	8
LEO 5	1500	60	12	6	1	10
MEO	20200	55	30	10	1	12
GEO 1	35786	3	12	6	1	14
GEO 2	35786	0.5	30	10	1	18

The LEO Walker constellations are placed at a variety of inclinations and constitute approximately 64% of the entire satellite population used in the model. The MEO constellation models a set of spacecraft at GPS altitude and inclination. The GEO constellations consists of spacecraft in roughly geostationary orbits.

The satellites in Table 3.8 are non-maneuvering satellites and represent the set of satellites the tracking algorithm must continue to monitor while also tracking maneuvering targets. Seven maneuverable satellites are added to the constellation and distributed across each orbital regime. Each satellite performs an impulsive tangential burn at a different time in the scenario. Table 3.9 provides the relevant information for these targets. Figure 3.4 shows the full test constellation with non-maneuvering satellites denoted in gray and maneuvering spacecraft in red. The SOSI Network spacecraft are presented in blue.

Unlike in [29, 30, 31], the thrust magnitudes of the maneuvering spacecraft vary to assess how well the integrated command and control strategy detects, characterizes, and tracks through each maneuver in each orbital regime.

Table 3.9: Maneuvering Target Topology

Constellation	Altitude (km)	e	i (°)	Ω (°)	ω (°)	ν (°)	$t_{\Delta V}$ (hr)	ΔV (m/s)	Cross Section (m^2)
LEOMnvr-1	500	0.00002	63.4	45	0	15	6.75	10	6
LEOMnvr-2	1000	0.00002	98.1	45	0	15	16.5	15	6
LEOMnvr-3	1500	0.00002	40	45	0	15	12.5	2.5	6
MEOMnvr-1	20200	0.00002	55	45	0	15	9	12.5	6
MEOMnvr-2	20200	0.00002	55	225	0	15	14.25	5	6
GEOMnvr-1	35786	0.00002	1.5	45	0	0	8.5	15	6
GEOMnvr-2	35786	0.00002	1.5	225	0	0	11.75	5	6

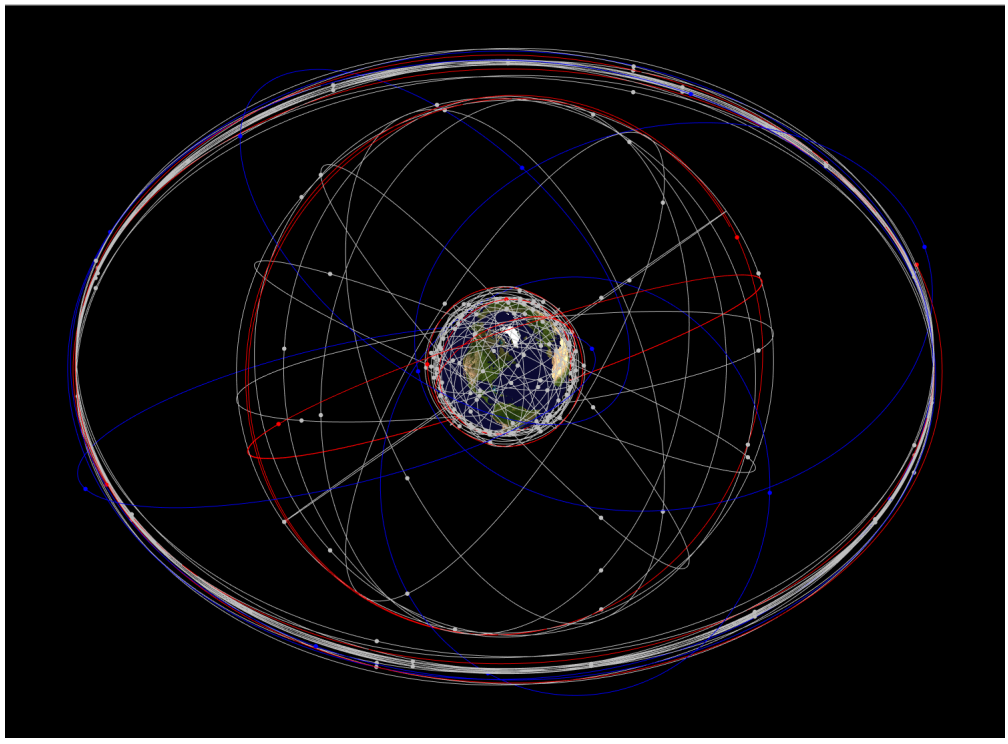

Figure 3.4: Full Test Constellation Map

3.3 Initialization

All scenarios are initialized with the time and physical properties provided in Table 3.10. The process noise covariance used to propagate the true state of the constellation spacecraft

Table 3.10: Temporal & Physical Properties

Property	Value
t_0	0 s
t_f	86400 s
Δt	60 s
$\omega_\oplus$	$7.29212 \cdot 10^{-5}$ rad/s
$r_\oplus$	6378.137 km
$e_\oplus$	0.081819221456
$\mu_\oplus$	398600.5 $\text{km}^3/\text{ s}^2$

is the same as that used in the estimation process. The nominal process noise covariance is given in Equation (3.17).

$$\mathbf{Q} = \begin{bmatrix} \mathbf{0} & \mathbf{0} \\ \mathbf{0} & (4.125 \cdot 10^{-7})^2 \, \mathbf{I} \end{bmatrix} \delta(t - \tau) \tag{3.17}$$

where $\mathbf{0}$ and $\mathbf{I}$ are 3×3 matrices. The non-zero elements of $\mathbf{Q}$ have units of km^2/s^4. These values are based roughly on [44] with some modification after some preliminary trials.

Each UKF within the tasking algorithm is given an initial state $\hat{\mathbf{x}}_0$, based on an initial covariance $\hat{\mathbf{P}}_0$ and the associated target satellite's initial state.

$$\hat{\mathbf{P}}_0 = 0.00025 \begin{bmatrix} ||\mathbf{r}_0||_2 \mathbf{I} & \mathbf{0} \\ \mathbf{0} & ||\mathbf{v}_0||_2 \mathbf{I} \end{bmatrix}$$
$$\hat{\mathbf{x}}_0 = \mathbf{x}_0 + \boldsymbol{w}, \quad \boldsymbol{w} \sim \mathcal{N}(\mathbf{0}, \hat{\mathbf{P}}_0)$$

where $\mathbf{0}$ and $\mathbf{I}$ are 3×3 matrices.

The time interval t_i in the MMAE algorithms in Chapter 4 is 120 seconds.

3.4 Summary

In this chapter the model used to test the adaptive estimation and decision processes was presented. Radar and EOIR sensors are defined by sensor characteristics and target specifications to create realistic and unique detection and tracking thresholds for each system. The globally distributed SOSI network and target constellations used to test the developed tasking strategies were also defined in this chapter.

Chapter 4

Adaptive Estimation Development

4.1 Introduction

In this chapter several adaptive estimation techniques are developed. These algorithms range in complexity from a covariance inflation process to static and dynamic Multiple Model Adaptive Estimation (MMAE). The covariance inflation process is presented as a baseline approach for mitigating the risk of divergence after an unknown maneuver. The MMAE methods developed for this dissertation seek to characterize the unknown maneuver while also mitigating the divergence risk. How efficiently each of these processes inflates the overall covariance estimate directly impacts how sensors are tasked. A delicate balance must be maintained. Overinflating the covariance may force an unnecessarily large number of sensors to observe a single target at a given time step, to the detriment of other target estimates. The sudden influx of observational data, however, could result in a rapid reconvergence on a viable state estimate. The adaptive estimation techniques developed in this dissertation all seek to manipulate the covariance estimate in markedly different ways to efficiently mitigate unknown maneuvers.

4.2 Discrete Process Noise Covariance

Before discussing the adaptive estimation methods developed for this dissertation its important to first describe how the discrete process noise covariance is determined in the continuous-time, discrete observation UKF. As discussed in Section 2.2.6, the continuous-time process noise $\boldsymbol{w}(t)$ introduces additive accelerative disturbances. It is assumed that accelerative disturbances are constant over the discrete time interval, such that

$$\boldsymbol{w}(t) \equiv \boldsymbol{w}_k \tag{4.1}$$

Because observations are only possible at discrete step intervals, defined in Section 2.2.2, its necessary to formulate a value for $\mathbf{Q}_k$ that appropriately incorporates the accrued process noise into the predicted covariance estimate.

To calculate the discrete process noise covariance this dissertation implements a multidimensional piecewise constant white noise acceleration model, as described in [32]. In the UKF, $\boldsymbol{w}(t)$ is assumed to be constant over the interval $\Delta t = t_{k+1} - t_k$. Thus, the discrete position noise and the discrete velocity noise are calculated using Equation (4.2) based the definition of the continuous-time process noise in Equation (2.23).

$$\boldsymbol{w}_{\mathbf{r},k+1} = \frac{1}{2}\Delta t^2 \boldsymbol{\sigma}_{\boldsymbol{w},k}^T \tag{4.2a}$$

$$\boldsymbol{w}_{\mathbf{v},k+1} = \Delta t \boldsymbol{\sigma}_{\boldsymbol{w},k}^T \tag{4.2b}$$

The resulting discrete process noise covariance $\mathbf{Q}_k$ used in the UKF is defined in Equation (4.3).

$$\mathbf{Q}_k = \begin{bmatrix} \frac{1}{4}\Delta t^4 \text{DIAG}\left(\boldsymbol{\sigma}_{\boldsymbol{w},k}^2\right) & \frac{1}{2}\Delta t^3 \text{DIAG}\left(\boldsymbol{\sigma}_{\boldsymbol{w},k}^2\right) \\ \frac{1}{2}\Delta t^3 \text{DIAG}\left(\boldsymbol{\sigma}_{\boldsymbol{w},k}^2\right) & \Delta t^2 \text{DIAG}\left(\boldsymbol{\sigma}_{\boldsymbol{w},k}^2\right) \end{bmatrix} \tag{4.3}$$

The units of $\sigma_{w,k}$ in this discrete process noise covariance model are km/s^2.

In the MMAE methods developed in this dissertation, the thrust $\mathbf{u}_\text{j}\left(t_{\text{mvr,j}}\right)$ is added to the covariance estimate as additional noise covariance. It is not incorporated into the two-body dynamics. When a thrust occurs within a time step the UKF prediction phase, in Algorithm 2.3, must be parsed into subintervals. This piecewise process is depicted in Figure 4.2

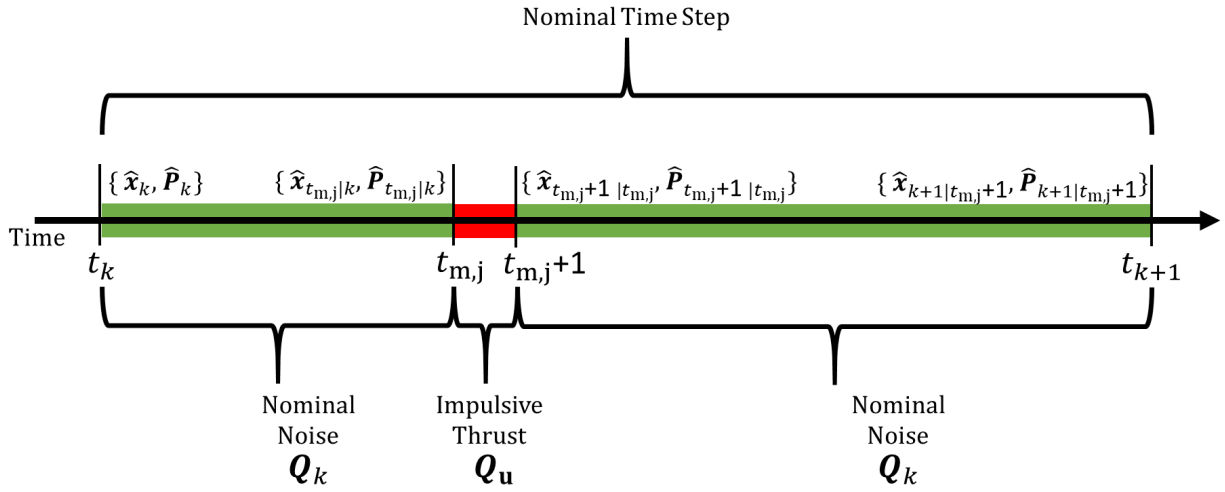

Figure 4.1: Parsed Time Step with Thrust

First, if $t_k \neq t_{t_{\text{mvr,j}}}$, then the predicted estimate up to the maneuver time $\{\hat{\mathbf{x}}_{\text{j},t_{\text{mvr,j}}|k}, \hat{\mathbf{P}}_{\text{j},t_{\text{mvr,j}}|k}\}$

must be calculated using Algorithm 2.3. The predicted estimated over the thrust duration $\{\hat{\mathbf{x}}_{\mathrm{j},t_{\mathrm{mvr,j}}+1|t_{\mathrm{mvr,j}}}, \hat{\mathbf{P}}_{\mathrm{j},t_{\mathrm{mvr,j}}+1|t_{\mathrm{mvr,j}}}\}$ is then calculated. The predicted covariance equation in Algorithm 2.3, Line 6 is modified to incorporate only the thrust, as shown in Equation (4.4).

$$\hat{\mathbf{P}}_{\mathrm{j},t_{\mathrm{mvr,j}}+1|t_{\mathrm{mvr,j}}} = \left[\Delta\hat{\boldsymbol{\mathcal{X}}}\right] \mathbf{W_P} \left[\Delta\hat{\boldsymbol{\mathcal{X}}}\right]^T + \mathbf{Q_u} \tag{4.4}$$

$\mathbf{Q_u}$ is calculated using Equation (4.3), with the thrust $\mathbf{u}_{\mathrm{j}}\left(t_{\mathrm{mvr,j}}\right)$ replacing the variance $\boldsymbol{\sigma}^2_{\boldsymbol{w},k}$, and $\Delta t = 1$. Once the estimate prediction has incorporated the thrust effects, the remainder of nominal time step proceeds as usual to find the predicted estimate at the end of the time step.

$$\{\hat{\mathbf{x}}_{\mathrm{j},k+1|k}, \hat{\mathbf{P}}_{\mathrm{j},k+1|k}\} \leftarrow \{\hat{\mathbf{x}}_{\mathrm{j},k+1|t_{\mathrm{mvr,j}}+1}, \hat{\mathbf{P}}_{\mathrm{j},k+1|t_{\mathrm{mvr,j}}+1}\} \tag{4.5}$$

4.3 Baseline Covariance Inflation Process

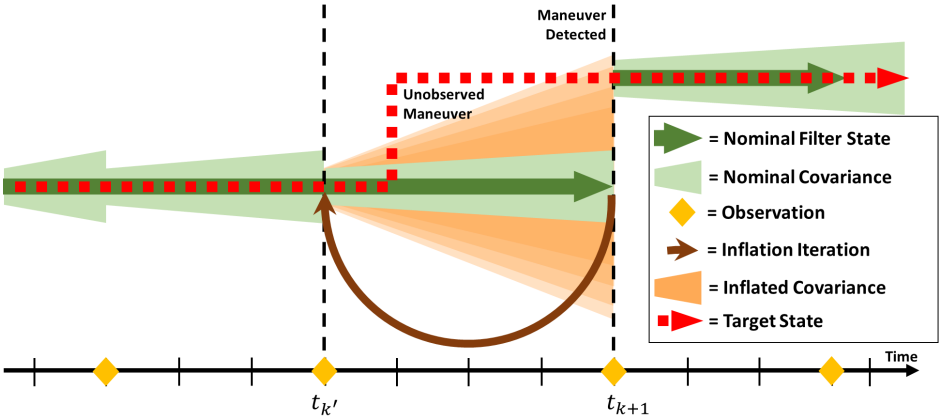

Figure 4.2: Covariance Inflation Process

The baseline Covariance Inflation Filter (CIF) developed in this dissertation uses the maneuver detection metric described in Chapter 2, Section 2.4.5 to scale the process noise covariance in the nominal UKF. If the maneuver detection threshold is surpassed at time t_{k+1}, then the covariance inflation process is initiated. The nominal filter returns to the previous observation at time t'_k and the continuous-time process noise covariance is multiplied by a scalar factor. The state and covariance estimates are propagated to t_{k+1} and updated with the original observation. This process is repeated until the maneuver detection threshold is no longer breached, indicating that the covariance at t_{k+1} is large enough to include the target's newly observed trajectory. This process is shown graphically in Figure 4.2.

The scalar factor by which the continuous-time process noise covariance is multiplied is determined via the bisection or binary search method. The Intermediate Value Theorem, upon which the binary search method is founded, states that for a given continuous function

$f(\cdot)$ defined over an interval $[a, b]$ there exists an input p where $f(p) = 0$, given that $f(a)$ and $f(b)$ have opposite signs.

Algorithm 4.1 Binary Search Function

1: **function** $f(p)$

Require: $\hat{\mathbf{x}}_{n,k'}$, $\hat{\mathbf{P}}_{n,k'}$, $t_{k'}$

2: Reinitialize nominal filter with $\hat{\mathbf{x}}_{n,k'}$ and $\hat{\mathbf{P}}_{n,k'}$ at $t_{k'}$

3: Scale nominal filter's process noise covariance: $\mathbf{Q}(t) = p\mathbf{Q}(t)$

4: Predict state, $\hat{\mathbf{x}}_{n,k+1|k}$, and covariance, $\hat{\mathbf{P}}_{n,k+1|k}$ using Algorithm 2.3

5: Update state, $\hat{\mathbf{x}}_{n,k+1}$, and covariance, $\hat{\mathbf{P}}_{n,k+1}$ using Algorithm 2.4 and Algorithm 2.5

6: Calculate output of binary search function

$$f(p) = \Psi_{m,k+1} - \psi_{(n,m),k+1} \tag{4.6}$$

To minimize the degree of covariance inflation, the proposed method uses the difference between the maneuver detection metric and threshold as the needed continuous function. By the fact that the maneuver detection threshold was surpassed, it is known that the current maneuver detection metric is greater than the threshold.

$$\psi_{(n,m),k+1} > \Psi_{m,k+1}$$

Therefore, $f(a)$ is negative, and $f(b)$ must be positive. To find $f(p)$ one must re-estimate the target state and covariance at t_{k+1} from the previously updated state and covariance estimate at $t_{k'}$, using Algorithm 4.1. By multiplying the nominal process noise covariance by a positive scalar factor, the covariance estimate remains positive definite.

The overall covariance inflation filter is presented in Algorithm 4.2.

The covariance inflation approach developed in this dissertation offers a robust and responsive means of tracking through an unknown maneuver. While the CIF attempts to minimize the amount of additional noise needed to appropriately inflate the covariance estimate, using a scalar multiplier means that the process noise is increased in every dimension equally. Inflation in some dimensions may not be necessary to maintain convergence, and only adds error that must be mitigated by future observations. The MMAE approaches in subsequent sections offer several means of tailoring the added process noise to suit the problem. Nonetheless, covariance inflation methods in general are computationally cost-efficient, making them a widely implemented adaptive estimation technique.

4.4 General Multiple Model Adaptive Estimation

The three MMAE methods developed in this dissertation all build from the same multiple-model framework. Therefore its valuable to describe the mechanics of this framework before

Algorithm 4.2 Covariance Inflation Filter

procedure PREDICTION PHASE($\hat{\mathbf{x}}_{n,k}$, $\hat{\mathbf{P}}_{n,k}$, t_k, t_{k+1})
    Use nominal filter prediction phase (Algorithm 2.3)
procedure FORECAST PHASE($\hat{\boldsymbol{\mathcal{X}}}_{n,i,k+1|k}$, $\hat{\mathbf{P}}_{n,k+1|k}$, t_{k+1})
    Use nominal filter forecast phase (Algorithm 2.4)
procedure UPDATE PHASE($\hat{\mathbf{x}}_{n,k+1|k}$, $\tilde{\mathbf{y}}_{(n,m),k+1}$, $\hat{\mathbf{y}}_{(n,m),k+1|k}$)
    Use nominal filter update phase (Algorithm 2.5)
    if $\psi_{(n,m),k+1} > \Psi_{m,k+1}$ **then**
        Initialize Binary Search Method: $a = 1$ and $b = 1000$
        Store lower bound: $\mathcal{L} = f(a)$
        Check that upper bound is positive: $f(b) \geq 0$
        while $f(b) < 0$ **do**
            $b = b + 10$
        while $\frac{b-a}{2} \geq 1e{-}6$ **do**
            Calculate intermediate point: $p = a + \frac{b-a}{2}$
            if $f(p) = 0$ **then**
                Output p and end algorithm
            else if $\mathcal{L} \cdot f(p) > 0$ **then** Set lower limit and bound: $a = p$ & $\mathcal{L} = f(p)$
            elseSet upper interval limt: $b = p$
        Reset nominal $\mathbf{Q}(t)$ for future time steps

discussing the three developed methods. The multiple-model approach enables the estimation of an unknown parameter, such as an unknown maneuver, by instantiating and filtering over a set of dynamics models where the unknown parameter is varied. For clarity this dissertation defines a model as an independent sequential estimator (the UKF) and a unique dynamical system that are together used to propagate the model's state estimate and covariance. The term "mode" refers to the unique dynamical system in each model.

For example, a satellite conducts an unknown maneuver of an unknown thrust and direction. A MMAE approach happens to be running during the maneuver with bank of models. Each mode in the multiple-model estimator includes a maneuver with unique characteristics as part of its two-body equations of motion. All models continue to run as new observations are collected. Modal probabilities are calculated based on the observations, and used to update a set of modal weights. The modes that most accurately emulate the actual dynamics will have the highest probabilities. The estimates from all models are combined using the modal weights to determine the overall state and covariance estimates. A key assumption is that the actual dynamics are captured within the range of modes, even if no mode exactly matches the actual dynamics. This constraint is a critical characteristic of MMAE, because the filter will fail if the actual dynamics fall outside the range of what can be accounted for in the set of models [106].

Traditionally, MMAE methods are initiated at the beginning of a scenario, and continue until the conclusion. For situations like space surveillance, however, in which a large number of spacecraft must be simultaneously tracked, using a MMAE approach for every target becomes computationally infeasible and unnecessary. This dissertation uses a selective approach that initiates an MMAE method when a maneuver is detected and continues until prescribed convergence criteria have been satisfied.

4.4.1 Multiple Model Adaptive Estimation Initialization

When a maneuver is detected at t_{k+1} in the nominal filter, using the maneuver metric and threshold equations outlined in Section 2.4.5, a multiple-model framework is initialized at the last observation time $t_{k'}$, or an otherwise specified time. The number of models $\mathfrak{N}$ is dependent on the MMAE method used. Each model j includes an impulsive maneuver defined by a time and acceleration, $\mathbf{u}_{\mathrm{j}}\left(t_{\mathrm{mvr,j}}\right)$. The maneuver time and acceleration are determined by the specific MMAE method. For all developed approaches the time interval between models is constant, $\Delta t_{\mathrm{int}} = 120\mathrm{s}$.

Each model $\mathcal{N}$ uses a UKF that is initialized as shown in Equation (4.7).

$$\boldsymbol{\mathcal{N}} = \begin{cases} \left\{\hat{\mathbf{x}}_{\mathrm{j},k'},\ \hat{\mathbf{P}}_{\mathrm{j},k'}\right\} & \text{if } \mathrm{j} = 1 \\ \left\{\hat{\mathbf{x}}_{\mathrm{j},k'},\ \hat{\mathbf{P}}_{\mathrm{j},k'},\ \mathbf{u}_{\mathrm{j}}\left(t_{\mathrm{mvr,j}}\right)\right\} & \text{if } \mathrm{j} > 1 \end{cases} \quad \text{for} \quad \mathrm{j} = [1, \mathfrak{N}] \tag{4.7}$$

The initial modal weights are calculated using Equation (4.8).

$$\mathbf{w}_{k'} = \frac{1}{\mathfrak{N}}\mathbf{1}_{(\mathfrak{N}\times 1)} \tag{4.8}$$

4.4.2 Multiple Model Adaptive Estimation Execution

All $\mathfrak{N}$ models are propagated in time in parallel. In the static multiple model approach the estimates and modal weights from each model never mix. Once initialized, the static multiple model executes Algorithm 4.3 to propagate and update the state and covariance estimates until a convergence metric is reached. The convergence metrics are discussed in each unique MMAE method.

4.5 Intermittent Shotgun Static Multiple Model Process

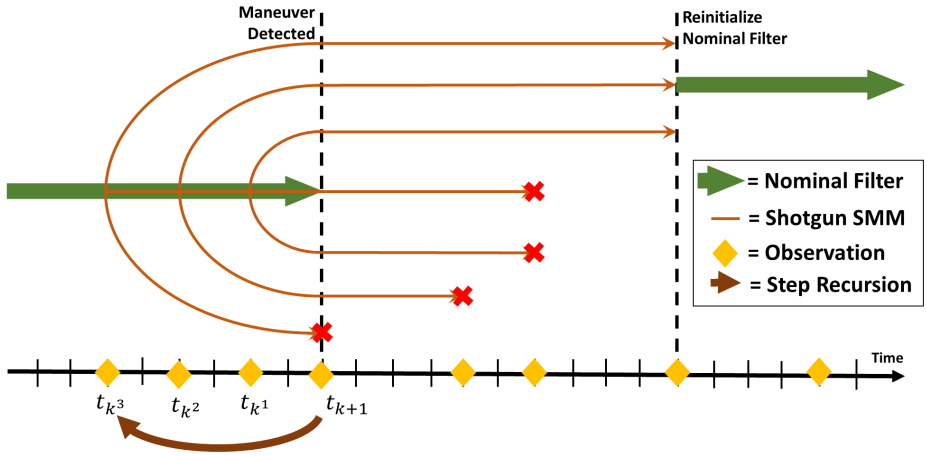

Figure 4.3: Shotgun Static Multiple Model

The first MMAE process developed for this dissertation is the simplest of the proposed methods. Termed the "Shotgun" Static Multiple Model method, this process creates a subset of models at each interval time step Δt_{int}, as depicted in Figure 4.5. Each model within a subset incorporates either a positive or negative tangential thrust of varying magnitude. Originally, these thrusts were directly incorporated into the state estimate, but later revisions to the overall SMM process incorporated the thrust into the process noise covariance. By adding the thrust to $\mathbf{Q}_k$, issues can arise because the thrust signs are dropped resulting in duplicate models at each time step. While this induces unnecessary error, the impact on the algorithms ability to sufficiently converge on a viable orbit estimate were negligible.

Algorithm 4.3 Static Multiple Model Filter

procedure PREDICTION PHASE
  for $\mathrm{j} = 1 \rightarrow \mathfrak{N}$ **do**
    Use nominal filter prediction phase (Algorithm 2.3) for Model j
procedure FORECAST PHASE
  for $\mathrm{j} = 1 \rightarrow \mathfrak{N}$ **do**
    Use nominal filter forecast phase (Algorithm 2.4) for Model j
procedure UPDATE PHASE
  for $\mathrm{j} = 1 \rightarrow \mathfrak{N}$ **do**
    Use nominal filter update phase (Algorithm 2.5) for Model j
    Calculate modal probability, $p(\tilde{\mathbf{y}}_{\mathrm{j},k+1}|\hat{\mathbf{x}}_{\mathrm{j},k+1|k})$, for Model j

$$p(\tilde{\mathbf{y}}_{\mathrm{j},k+1}|\hat{\mathbf{x}}_{\mathrm{j},k+1|k}) = \frac{1}{\sqrt{\det\left(2\pi\hat{\mathbf{S}}_{\mathrm{j},k+1|k}\right)}}\exp\{-\frac{1}{2}\tilde{\boldsymbol{\varepsilon}}^{T}_{(\mathrm{j},m),k+1}\left(\hat{\mathbf{S}}_{\mathrm{j},k+1|k}\right)^{-1}\tilde{\boldsymbol{\varepsilon}}_{(\mathrm{j},m),k+1}\} \tag{4.9}$$

    Calculate the modal weight for $\mathbf{w}_{\mathrm{j},k+1}$, for Model j

$$\mathrm{w}_{\mathrm{j},k+1} = \mathrm{w}_{\mathrm{j},k}\; p(\tilde{\mathbf{y}}_{\mathrm{j},k+1}|\hat{\mathbf{x}}_{\mathrm{j},k+1|k}) \tag{4.10}$$

    Normalize the modal weights

$$\mathbf{w}_{k+1} = \frac{\mathbf{w}_{k+1}}{\sum_{\mathrm{j}=1}^{\mathfrak{N}}\mathrm{w}_{\mathrm{j},k+1}} \tag{4.11}$$

    Compile the overall state estimate

$$\hat{\mathbf{x}}_{n,k+1} = \hat{\mathbf{X}}_{\boldsymbol{\mathcal{N}},k+1}\mathbf{w}_{k+1} \tag{4.12}$$

    where, $\hat{\mathbf{X}}_{\boldsymbol{\mathcal{N}},k+1}$ is a $6 \times \mathfrak{N}$ horizontally concatenated array of the updated state estimates from each model
    Compile the overall covariance estimate

$$\hat{\mathbf{P}}_{n,k+1} = \sum_{\mathrm{j}=1}^{\mathfrak{N}}\mathrm{w}_{\mathrm{j},k+1}\left[\left(\hat{\mathbf{x}}_{\mathrm{j},k+1} - \hat{\mathbf{x}}_{n,k+1}\right)\left(\hat{\mathbf{x}}_{\mathrm{j},k+1} - \hat{\mathbf{x}}_{n,k+1}\right)^{T} + \hat{\mathbf{P}}_{\mathrm{j},k+1}\right] \tag{4.13}$$

    Compile the maneuver detection metric

$$\psi_{(n,m),k+1} = \boldsymbol{\psi}_{(\boldsymbol{\mathcal{N}},m),k+1}\mathbf{w}_{k+1} \tag{4.14}$$

    where, $\boldsymbol{\psi}_{(\boldsymbol{\mathcal{N}},m),k+1}$ is a $1 \times \mathfrak{N}$ array of maneuver detection metrics from all the models.

When a maneuver is detected, the Shotgun SMM goes back to the third to last observation at t_{k^3} and instantiates a number of models over the duration of time from t_{k^3} to t_{k+1}. The number of models is defined by the interval time and the number of desired models at each interval step. In this case the number of models per interval step is six. The total number of models is calculated using Equation (4.15).

$$\mathfrak{N} = 6\lceil \frac{t_{k+1} - t_{k^3}}{\Delta t_{\text{int}}} \rceil + 1 \tag{4.15}$$

The maneuver time $t_{\text{mvr,j}}$ is defined in Equation (4.16).

$$t_{\text{mvr,j}} = t_{k^3} + \lfloor \frac{\mathfrak{j} - 2}{6} \rfloor t_{\text{int}} \qquad \text{for} \quad \mathfrak{j} = [2, \mathfrak{N}] \tag{4.16}$$

The impulsive thrust acceleration $\mathbf{u}_{\mathfrak{j}}(t_{\text{mvr,j}})$ for each model is defined in Equation (4.19). The variables s, $\mathfrak{a}$, and $\mathfrak{b}$ are auxiliary variables used in the following sequence of equations.

$$\mathrm{s} = \begin{cases} \mathfrak{a} & \text{if } \mathfrak{a} \neq 0 \\ 6 & \text{if } \mathfrak{a} = 0 \end{cases} \qquad \text{where } \mathfrak{j} - 1 \equiv \mathfrak{a} \bmod 6 \qquad \text{for} \quad \mathfrak{j} = [2, \mathfrak{N}] \tag{4.17}$$

$$u_{\mathfrak{j}}(t_{\text{mvr,j}}) = \begin{cases} 0.005(\mathfrak{b}+1) & \text{if s} \leq 3 \\ -0.005(\mathfrak{b}+1) & \text{if s} > 3 \end{cases} \quad \text{where } \mathfrak{j} - 1 \equiv \mathfrak{b} \bmod 3 \qquad \text{for} \quad \mathfrak{j} = [2, \mathfrak{N}] \tag{4.18}$$

$$\mathbf{u}_{\mathfrak{j}}^{(\text{NTW})}(t_{\text{mvr,j}}) = \begin{bmatrix} 0 & u_{\mathfrak{j}}(t_{\text{mvr,j}}) & 0 \end{bmatrix} \tag{4.19}$$

Thus at each maneuver time t_{mvr} six impulsive thrust modes are created in which $u_{\mathfrak{j}}(t_{\text{mvr,j}})$ is either $\pm 5\text{m/s}^2$, $\pm 10\text{m/s}^2$, or $\pm 15\text{m/s}^2$. Instantiating a set of models at each maneuver time improves the Shotgun SMM's robustness by increasing the range of possible modes from which the unknown maneuver can be estimated. It's important to note that the thrust calculated in the Shotgun SMM is in the NTW frame and must be mapped to the ECI frame when incorporated into predicted covariance estimate. Additionally, the first model, $\mathfrak{j} = 1$, is uses a non-maneuvering mode to accommodate false maneuver detection.

Once initialized the Shotgun SMM follows the standard SMM process in Algorithm 4.3. After processing an observation, models are removed from the SMM if their modal weights fall below a threshold, per Algorithm 4.4. In this dissertation the pruning threshold is set as $\omega_{\text{prune}} = 1e^{-20}$. Setting the pruning threshold sufficiently low ensures that only the most implausible models are removed. Before the selected POMDP can task sensors for the next time step, the Shotgun SMM must process the existing observation up to the current time step.

After an observation update, the Shotgun SMM may be terminated and the nominal filter reinitialized if one of two convergence criteria are met. Obviously the SMM has converged

Algorithm 4.4 Multiple Model Pruning Process

for $\mathrm{j} = 1 \rightarrow \mathfrak{N}$ **do**
  if $\mathrm{w}_{\mathrm{j},k+1} \leq \omega_{\text{prune}}$ **then**, remove model j and $\mathfrak{N} = \mathfrak{N} - 1$
Renormalize modal weights with Equation (4.11)

to the most appropriate model if there is one model remaining after an estimate update. Secondly, the SMM has converged if the sum of the maneuver detection metrics over the last three observed time steps, including the current observation step, is less than the threshold over the same interval.

$$\text{Convergence Criteria} = \begin{cases} \mathfrak{N} = 1 \\ \sum_{\mathrm{j}=k^2}^{k+1} \psi_j \leq \Psi_{k^2 \rightarrow k+1} \end{cases} \tag{4.20}$$

An important limitation of the proposed Shotgun SMM is that it only models tangential maneuvers and does not consider out of plane maneuvers, such as inclination changes. This limitation is not without a purpose. First, creating multiple thrust modes in all three principal directions would potentially create an enormous number of models over a long duration observation gap. The computational load in such a situation would be impractical. Second, impulsive tangential burns are far more efficient than out-of-plane impulsive maneuvers [107]. All other things being equal, significant plane changes are executed by the launch vehicle's primary or secondary stage. Once in the desired orbital plane, satellites will raise or lower their orbital altitude using tangential thrust to meet mission needs. Lastly, in the absence of orbital perturbations, only tangential maneuvers will create secular drift in a satellite's kinematic state. Estimation errors due to this drift would be exacerbated by long observation gaps when the satellite can drift far from the filter's state estimate. Purely radial and cross-track impulsive maneuvers result in periodic drift where the spacecraft's states oscillates about the position it would have had without a maneuver. The spacecraft has no secular drift, because the orbit's specific energy does not change. Nonetheless, the tangential maneuver limitation is one that can be overcome with a more sophisticated means of thrust modeling, which is the purpose of the following MMAE methods.

4.6 Intermittent, Lambert Targeting Static Multiple Model Process

The next MMAE method, called the "Lambert SMM", uses the same intermittent pruning SMM described in 4.5, but seeks to improve how maneuvers are modeled. Instead of manually selected thrust vectors, the Lambert Targeting SMM uses the Universal Variables Method for solving the Lambert Problem to determine the appropriate thrust magnitude and direction at a selected maneuver time. With this approach far fewer than the Shotgun SMM models

are required; almost a factor of six reduction, in fact. The number of models needed in the Lambert SMM are defined in Equation (4.21).

$$\mathfrak{N} = \lceil \frac{t_k - t_{k^3}}{\Delta t_{\text{int}}} \rceil + 1 \tag{4.21}$$

Like in the Shotgun SMM, the first mode in the Lambert SMM is a stationary one, where the modeled spacecraft does not maneuver.

Similarly, the maneuver time $t_{\text{mvr,j}}$ is modified from the Shotgun SMM, as shown in Equation (4.22). Once again, when a maneuver is detected the Lambert SMM returns to the third to last observation step at t_{k^3} and instantiates a set of models over the time interval $[t_{k^3}, t_{k+1}]$. Preliminary testing showed that going back three observations was sufficient within the developed simulation environment to ensure the maneuver was included in the MMAE time duration.

$$t_{\text{mvr,j}} = t_{k^3} + \lfloor \text{j} - 2 \rfloor \Delta t_{\text{int}} \qquad \text{for} \quad \text{j} = [2, \mathfrak{N}] \tag{4.22}$$

Using the state estimate history, the Lambert SMM determines the state estimate at $t_{\text{mvr,j}}$ prior to the proposed maneuver $\hat{\mathbf{x}}^-_{\text{j},t_{\text{mvr,j}}}$. If the filter's state history does not include a state estimate at $t_{\text{mvr,j}}$, due to the discrete observation nature of the estimation process, the appropriate state estimate is predicted from the closest preceding time step. Thus, two position vectors are known: the observed position after the maneuver $\hat{\mathbf{r}}_{n,k+1}$, which can include significant errors, and the estimated position at the proposed maneuver time $\hat{\mathbf{r}}^-_{\text{j},t_{\text{mvr,j}}}$. Additionally, the time of flight between these position vectors ΔT is also known from Equation (4.23).

$$\Delta T = t_{k+1} - t_{\text{mvr,j}} \tag{4.23}$$

Using the position estimate after the maneuver is detected does inject error, but the versatility of the SMM initialized over a long time period helps mitigate errors in the Lambert targeting. The Lambert Targeter is used as soon as a maneuver is detected to maintain the algorithms responsiveness. It would certainly be worthwhile to wait until additional observations are collected, thus reducing the error in the Lambert Targeter, but the sensor tasking behavior of the overall network would remain unchanged even though a maneuver was detected.

These three parameters are the foundation of the Lambert Problem [33]. Solving the Lambert Problem effectively answers the question, "how does a spacecraft get from point A to point B in the time allotted?" The impulsive thrust needed at $t_{\text{mvr,j}}$ can be calculated using the Universal Variables Method, described in Algorithm 4.6.1, to solve the Lambert Problem. The number of models generated with this approach can be significant. With one assumption, the maneuver information from the Lambert Targeter can be used to eliminated unrealistic models before the Lambert SMM is executed. Because the maneuvers in this dissertation are modeled as one second impulsive burns, the change in velocity from the Lambert Targeter can be viewed as an acceleration. The one environment where a satellite

will experience its most significant accelerations, or g-loads, aside from an orbital collision, is launch. Satellite structures are designed to handle the g-load environment of launch and often little more. Greater g-load capacity often requires additional structural capacity and mass, which incurs increased launch costs. Therefore, models can be initially removed if the impulsive acceleration calculated in the Lambert Targeter is greater than what the satellite might experience at launch. The SpaceX Falcon 9 [108] and ULA Atlas V [109] payload users' guides specify maximum g-loads of 8.5g and 6g, respectively. Rounding up to 10g yields an upper thrust limit of $981 m/s^2$. Thus,

if $||\mathbf{u}_{\mathrm{j}}^{(\mathrm{ECI})}(t_{\mathrm{mvr,j}})||_2 > 981\mathrm{m/s}^2$ **then** remove model j from the filter.

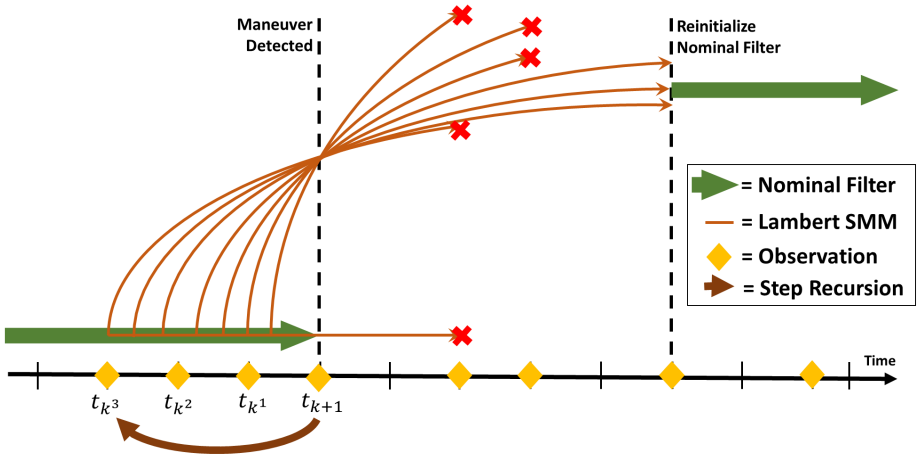

Figure 4.4: Lambert-Targeting Static Multiple Model

As depicted in Figure 4.4, this method results in modes that place the target satellite at the observed position at the observed time. However, while the position vectors for each model at t_{k+1} should be roughly equivalent, their velocity vectors will not be. As evident in Figure (4.4), the differences in velocity produce varying trajectories with only one, or a small subset, emulating the actual orbit. Once the Lambert SMM has processed the previous observations up to the current time step, the pruning method described in Algorithm 4.4 is used to remove models as new observations are collected. The convergence criteria in Equation (4.20) are used to determine when the Lambert SMM has sufficiently converged to a new orbit estimate. Once convergence is reached, the nominal UKF is reinitialized with the updated estimate from the Lambert SMM.

4.6.1 Universal Variable Lambert Targeter

In what is now known as the Lambert Problem, a satellite's orbit must be determined from two position vectors separated by a duration of time. From two position vectors alone there are an infinite number of possible orbits, but only two trajectories exist when the time of

flight is considered. Johann Heinrich Lambert's original solution calculated the minimum energy transfer between the two points [33]. Several variations and improvements on this original method have been developed since then. Carl Friedrich Gauss proposed a method, while determining the orbit of Ceres in the early 1800s, that essentially develops a solution based on the area swept out by the satellite from one position to the next [110]. This method is limited to position vectors with relatively small angular separations, which isn't a likely condition given two observations of a near-earth orbiting spacecraft. One method that overcomes this limitation is the universal variable approach used in this dissertation, which seeks to relate specific mechanical energy, time-of-flight, and the change in eccentric anomaly [33]. First the universal variable, χ, is defined in Equation (4.24).

$$\dot{\chi} = \frac{\sqrt{\mu_{\oplus}}}{||\mathbf{r}^{(\mathrm{ECI})}||_2} \tag{4.24}$$

An auxiliary variable ψ is defined in Equation (4.25).

$$\psi = \frac{\chi^2}{a} \tag{4.25}$$

where a is the orbits semi-major axis. ψ is positive for elliptical orbits, and negative for hyperbolic orbits.

From ψ two universal variable functions, c_2 and c_3, are defined using Algorithm 4.5. The outputs of these functions are calculated iteratively in the universal variable approach to solving the Lambert Problem and are used to determine the velocities associated with each position vector.

Algorithm 4.5 Universal Variable Function

1: **function** $\mathcal{C}(\psi_{\mathrm{n}})$

2: **if** $\psi_{\mathrm{n}} > 1e{-}6$ **then**

$$c_2 = \frac{1 - \cos\left(\sqrt{\psi_{\mathrm{n}}}\right)}{\psi_{\mathrm{n}}} \qquad c_3 = \frac{\sqrt{\psi_{\mathrm{n}}} - \sin\left(\sqrt{\psi_{\mathrm{n}}}\right)}{\sqrt{\psi_{\mathrm{n}}^3}} \tag{4.26}$$

3: **else if** $\psi_{\mathrm{n}} < -1e{-}6$ **then**

$$c_2 = \frac{1 - \cosh\left(\sqrt{-\psi_{\mathrm{n}}}\right)}{\psi_{\mathrm{n}}} \qquad c_3 = \frac{\sinh\left(\sqrt{-\psi_{\mathrm{n}}}\right) - \sqrt{-\psi_{\mathrm{n}}}}{\sqrt{\left(-\psi_{\mathrm{n}}\right)^3}} \tag{4.27}$$

4: **else**

$$c_2 = \frac{1}{2} \qquad c_3 = \frac{1}{6} \tag{4.28}$$

In the Universal Variable Lambert Targeter (Algorithm 4.6.1), the two position vectors are provided in two state estimates: $\hat{\mathbf{x}}_{n,k+1}$ and $\hat{\mathbf{x}}^{-}_{n,t_{\mathrm{mvr}}}$. $\hat{\mathbf{x}}_{n,k+1}$ is the updated state estimate

associated with the observation that detected the maneuver. $\hat{\mathbf{x}}^{-}_{n,t_{\text{mvr}}}$ is the pre-maneuver state estimate at the maneuver time $t_{\text{mvr,j}}$ which is based on the original series of observations. The traditional output of the universal variable Lambert solution would be the satellite's velocity at $t_{\text{mvr,j}}$ after the maneuver ($\hat{\mathbf{v}}^{+}_{n,t_{\text{mvr}}}$). Thus, the impulsive thrust can be calculated by subtracting the post-maneuver velocity vector from the pre-maneuver velocity, as shown in Equation (4.29).

$$\mathbf{u}_{\text{j}}^{(\text{ECI})}\left(t_{\text{mvr,j}}\right) = \hat{\mathbf{v}}^{+}_{n,t_{\text{mvr}}} - \hat{\mathbf{v}}^{-}_{n,t_{\text{mvr}}} \tag{4.29}$$

Overall, the Lambert SMM provides an efficient means of mitigating errors incurred by an unknown maneuver, and can even estimate the maneuver time, direction, and magnitude. It is important to note that each model in the SMM, once established, runs independently of the others until it is either removed or the filter converges. If the actual maneuver is large or the gap in time between observations is long, then a large number of models could carried from one time step to the next. The combined effect introduces a risk that the Lambert SMM could run for an extended period of time before convergence is reached, thus burdening limited computational resources. A dynamic MMAE approach could relieve this issue.

4.7 Intermittent, Lambert Targeting Generalized Pseudo-Bayesian of First Order Process

The Lambert SMM described in Section 4.4 works well in many situations, but its responsiveness could be improved by making the approach dynamic. A Generalized Pseudo-Bayesian of First Order Multiple Model (GPB1) approach, termed the Lambert GPB1, is introduced to dynamically implement the Universal Variable Lambert Targeter approach described in Section 4.6.1. As depicted in Figure 4.5, the combined state and covariance estimates after each observed time step are used to inform how a new set of models are initialized in the next time step. Unlike in the Lambert SMM, models are distributed only over the gap in time since the last observation. Multiple model information is only retained over a single duration of time from one observation to the next. As a result, the Lambert GPB1 can carry fewer models over time, and could potentially accommodate continuous thrust, though that analysis is outside the scope of this dissertation.

As described in [32], the GPB1 approach has the same computational requirements as the SMM. A GPB1 process differs from the IMM method in that the models in the GPB1 are mixed completely after each observation. In an IMM models are partially mixed based on mixing probabilities derived from on prior knowledge. Additionally, preliminary analyses indicated that the IMM is appropriate when modes are always mutually exclusive. For example, as shown in [47], an IMM works well if the thrust in each mode is in a principal direction. Thus, only one mode can be true at any given time. In this dissertation, where the thrust is impulsive, the modes are all equivalent once the maneuvers are complete. At

Algorithm 4.6 Universal Variable Lambert Targeter

procedure UNIVERSAL VARIABLE LAMBERT TARGETER($\hat{\mathbf{x}}_{n,k+1}$, $\hat{\mathbf{x}}^{-}_{n,t_{\text{mvr}}}$, ΔT)

Determine short (+) or long (-) trajectory

$$\varpi = \text{sign}\left[\left(\hat{\mathbf{r}}^{-}_{n,t_{\text{mvr}}} \times \hat{\mathbf{v}}^{-}_{n,t_{\text{mvr}}}\right) \cdot \left(\hat{\mathbf{r}}^{-}_{n,t_{\text{mvr}}} \times \hat{\mathbf{r}}_{n,k+1}\right)\right] \tag{4.30}$$

Calculate the cosine of the difference in True Anomaly from t_{mvr} to t_{k+1}

$$\cos(\Delta\nu) = \frac{\hat{\mathbf{r}}_{n,k+1} \cdot \hat{\mathbf{r}}^{-}_{n,t_{\text{mvr}}}}{||\hat{\mathbf{r}}_{n,k+1}||_2 ||\hat{\mathbf{r}}^{-}_{n,t_{\text{mvr}}}||_2} \tag{4.31}$$

Calculate $A = \varpi\sqrt{1-\cos^2(\Delta\nu)}$

if $A = 0$ **then** Cannot calculate orbit (Singularity)

Initialize Binary Search Method

$$\psi_{\text{low}} = -4\pi^2 \qquad \psi_{\text{high}} = 4\pi^2 \qquad c_2 = \frac{1}{2} \qquad c_3 = \frac{1}{6} \qquad \Delta T_{\text{n}} = 2\Delta T \tag{4.32}$$

while $|\Delta T_{\text{n}} - \Delta T| \geq 1e{-}6$ **do**

Calculate intermediate point

$$\psi_{\text{n}} = \frac{\psi_{\text{low}} + \psi_{\text{high}}}{2} \tag{4.33}$$

Calculate Intermediate Value

$$y_{\text{n}} = ||\hat{\mathbf{r}}^{-}_{n,t_{\text{mvr}}}||_2 + ||\hat{\mathbf{r}}_{n,k+1}||_2 + \frac{A\left(\psi_{\text{n}} c_3 - 1\right)}{\sqrt{c_2}}, \text{ where } [c_2, c_3] = \mathcal{C}(\psi_{\text{n}}) \tag{4.34}$$

if $A > 0$ **then**

while $y_{\text{n}} < 0$ **do**

$\psi_{\text{low}} = \psi_{\text{low}} + 0.001\psi_{\text{high}}$

Recalculate ψ_{n} with Equation (4.33), and y_{n} with Equation (4.34)

Calculate universal variables: $\chi_{\text{n}} = \sqrt{\frac{y_{\text{n}}}{c_2}} \qquad \Delta T_{\text{n}} = \frac{\chi_{\text{n}}^3 c_3 + A\sqrt{y_{\text{n}}}}{\sqrt{\mu_\oplus}}$

if $\Delta T_{\text{n}} \leq \Delta T$ **then** $\psi_{\text{low}} = \psi_{\text{n}}$

else $\psi_{\text{high}} = \psi_{\text{low}}$

Calculate impulsive thrust, $\mathbf{u}_{\text{m}}$

$$\mathbf{u}_{\text{j}}^{(\text{ECI})}\left(t_{\text{mvr,j}}\right) = \frac{1}{A}\sqrt{\frac{\mu_\oplus}{y_{\text{N}}}}\left(\hat{\mathbf{r}}_{k+1} - \left(1 - \frac{y_{\text{n}}}{||\hat{\mathbf{r}}^{-}_{n,t_{\text{mvr}}}||_2}\right)\hat{\mathbf{r}}^{-}_{n,t_{\text{mvr}}}\right) - \hat{\mathbf{v}}^{-}_{n,t_{\text{mvr}}} \tag{4.35}$$

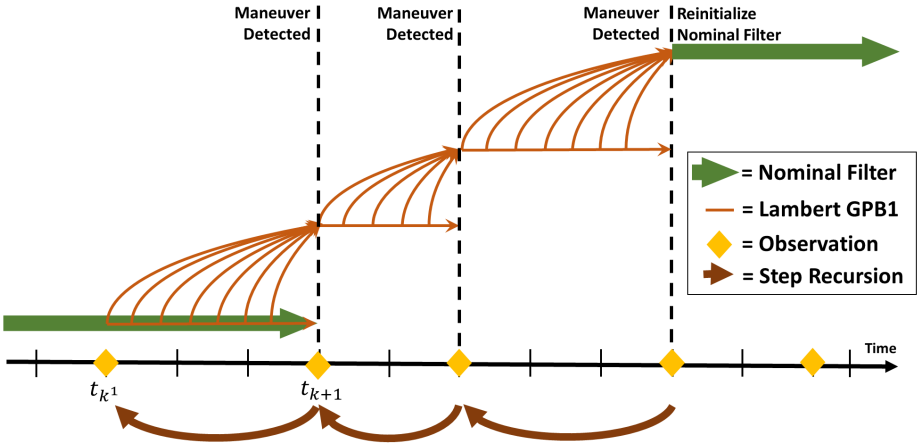

Figure 4.5: Lambert-Targeting GPB1

this point, the modal weights in an IMM begin to distribute evenly across the models. The Lambert GPB1 method can accommodate impulsive or continuous thrust, with no modifications to the algorithm, hence why it was selected for this dissertation.

One limitation of the Lambert GPB1 is that it will only estimate a thrust over the preceding observation gap. If the Lambert GPB1 does not sufficiently converge on an estimate the first time it is called, the maneuver detection threshold will continue to be tripped. Succeeding iterations of the Lambert GPB1 will estimate a maneuver over those future windows, even if only the initially detected maneuver occurred. As a result, the Lambert GPB1 may parse the estimate for a sufficiently large maneuver over multiple time windows.

4.8 Summary

This section presented four adaptive estimation techniques that were developed to detect unknown maneuvers, track through the resulting errors, and, in some cases, estimate the impulsive maneuver's characteristics. A scalar covariance inflation method was implemented using a binary search method to optimize the degree of inflation. A "Shotgun" SMM was introduced that created a set of fixed models to track through tangential maneuvers. An advantage of the "Shotgun" approach is that the models are user defined and not dependent on the accuracy nor number of new observations. This MMAE approach, however, is computationally burdensome as the number of models needed can be large. Instead, the Lambert SMM approach was developed to reduce the number of models by using a Universal Variable Lambert Targeter to determine the appropriate maneuver at a specified maneuver time. The Lambert SMM is also not limited to tangential maneuvers. Lastly, the Lambert SMM can be used to estimate the maneuver time, direction, and magnitude. The principal disadvantage of the Lambert SMM is that once the models are instantiated they remain

fixed until a convergence criterion is achieved. A dynamic variation of the Lambert SMM was introduced, known as the Lambert GPB1, to improve overall MMAE responsiveness. All four adaptive estimation techniques are only executed when a maneuver is detected, and terminated when the filter has reached predefined convergence criteria.

Chapter 5

Decision Process Development

5.1 Introduction

This chapter describes the three decision processes developed for this dissertation. The first method, described in Section 5.3.1, provides a baseline approach that uses only Fisher Information Gain to determine appropriate tasking decisions. Multiple information and system-based metrics are used in the second and third methods, but in distinct ways. The second method, described in Section 5.3.2, is designed so that every sensor makes an observation at each time step as long as a target is visible. The third method, described in Section 5.3.3, tasks sensors only if the information-based reward metrics outweigh the system-based cost metric.

5.2 The Overall Command & Control Strategy

The integrated POMDP and adaptive estimation command and control algorithm is presented in Figure 5.1. Observations are used to assess whether a spacecraft has maneuvered, and if so, the selected adaptive estimation process is initialized. The resulting updated states estimate and covariance are propagated forward to the next time step. The POMDP algorithms described in this chapter use these predicted state and covariance estimates to determine the appropriate sensor tasking for the next time step. The cycle begins again as new observations are collected, based on the sensor tasking.

Decisions are determined based on one of three objective functions, which are described in Section 5.3. At each time step, an objective function yields a matrix, which is then used to determine the decision matrix, defined in Section 5.4. While other POMDP research seeks to optimize the decision making process over a finite time horizon or window, this dissertation implements a suboptimal POMDP approach that bases decisions on the current decision

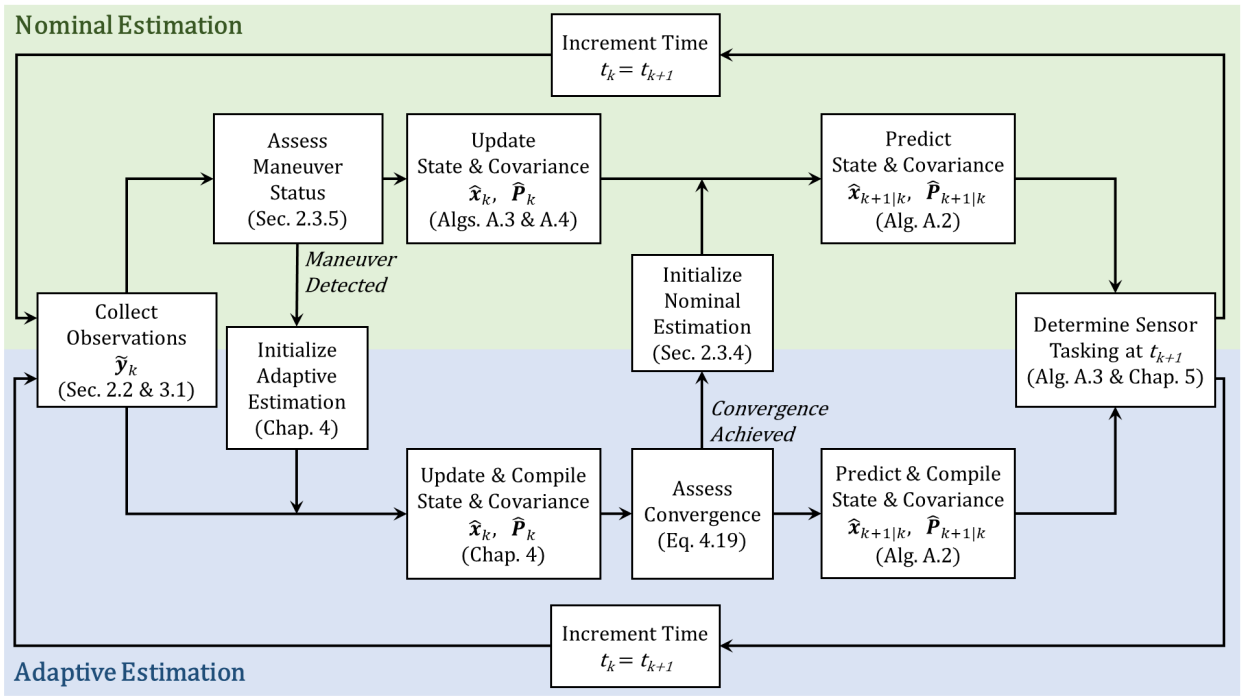

Figure 5.1: General Algorithm Flow Block Diagram

metrics. Using a suboptimal POMDP allows the overall algorithm to immediately respond to unknown maneuvers rather than having to wait until the next time window, or restarting the optimization process. An optimized POMDP assumes the dynamics remain known throughout the time horizon. If an unknown maneuver were to occur within this window, the remaining optimized decisions would no longer be optimal. Suboptimal POMDPs have been seen in similar situations where responsiveness is a key driver, such as ballistic missile tracking [69].

5.3 Objective Function Development

5.3.1 Baseline Single Information Metric, Continuous Tasking

The first suboptimal POMDP developed for this dissertation serves as a baseline approach, based on [87, 72, 69], among others. This method only considers Fisher Information Gain (FIG) when deciding how sensors should be tasked on the next time step t_{k+1}. The baseline process is designed to task a sensor at each time step as long as a target is predicted to be

visible. The resulting objective function, $\boldsymbol{\mathcal{J}}_{k+1}$, is defined in Equation (5.1).

$$\boldsymbol{\mathcal{J}}_{k+1} = \boldsymbol{\mathcal{F}}_{k+1} \tag{5.1}$$

where $\boldsymbol{\mathcal{F}}_{k+1}$ is an $N \times M$ matrix, and termed the FIG metric matrix. Each element of the $\boldsymbol{\mathcal{F}}_{k+1}$ metric matrix, defined in Equation (5.2), corresponds to the FIG metric that would be obtained if sensor m observed sensor n at time t_{k+1}.

$$\mathcal{F}_{(n,m),k+1} = \begin{cases} \hat{\phi}_{(n,m),k+1} & \text{if } \{\mathrm{o}_n, \mathrm{s}_m\} \text{ is observable} \\ 0 & \text{if } \{\mathrm{o}_n, \mathrm{s}_m\} \text{ is unobservable} \end{cases} \quad \forall \quad n = [1, N],\ m = [1, M] \tag{5.2}$$

5.3.2 Multiple Phenomenology, Continuous Tasking

The second suboptimal POMDP developed for this dissertation uses three metrics to assess the rewards associated with a specified observation. All three metrics describe the rewards associated with a particular action. As a result, a sensor will always be tasked if there is at least one target in view. The maximal Lyapunov exponent approximation (MLEA) metric, described in Section 2.5.3, is used to account for the rate of divergence associated with a target's covariance. The MLEA metric is only dependent on the target estimate, and not the sensors. The greater the MLEA metric is for a particular target, the greater the rate of divergence for its associated covariance estimate.

The MLEA metric data for all targets are compiled into a stability metric matrix, $\boldsymbol{\mathcal{L}}_{k+1}$, as defined in Equation (5.3).

$$\boldsymbol{\mathcal{L}}_{k+1} = \mathrm{DIAG}\left(\frac{\hat{\boldsymbol{\lambda}}^{\mathrm{eff}}_{k+1} - \min(\hat{\boldsymbol{\lambda}}^{\mathrm{eff}}_{1\ldots N,k+1})}{\max(\hat{\boldsymbol{\lambda}}^{\mathrm{eff}}_{1\ldots N,k+1}) - \min(\hat{\boldsymbol{\lambda}}^{\mathrm{eff}}_{1\ldots N,k+1})} \right) \boldsymbol{\mathcal{V}}_{k+1} \tag{5.3}$$

$\boldsymbol{\mathcal{L}}_{k+1}$ is an $N \times M$ matrix where each element corresponds to a specific target-sensor pair. $\hat{\boldsymbol{\lambda}}^{\mathrm{eff}}$ is an $N \times 1$ array of MLEA metrics corresponding to each target. A binary visibility matrix $\boldsymbol{\mathcal{V}}_{k+1}$ specifies which target-sensor pairs are observable at t_{k+1}. To facilitate integration with other metrics in the objective function, $\hat{\boldsymbol{\lambda}}^{\mathrm{eff}}$ is normalized over all N MLEA data at each time step.

While the MLEA metric only considers the target estimate relative to a baseline, FIG is used to account for the capabilities of a particular sensor. The sensor's measurement noise covariance and geometry to the specified target impact the Fisher Information Gain that can be obtained with the proposed observation. The version of the FIG metric matrix developed for this objective function is similar to the baseline in Section 5.3.1, but normalized over the range of FIG values for a given sensor, as shown in Equation (5.4).

$$\boldsymbol{\mathcal{F}}_{k+1} = \begin{cases} \frac{\hat{\phi}_{(n,m),k+1}}{\max(\hat{\boldsymbol{\phi}}_{1\ldots N,m,k+1})} & \text{if } \{\mathrm{o}_n, \mathrm{s}_m\} \text{ is observable} \\ 0 & \text{if } \{\mathrm{o}_n, \mathrm{s}_m\} \text{ is unobservable} \end{cases} \quad \forall \quad n = [1, N],\ m = [1, M] \tag{5.4}$$

MLEA and FIG are effective metrics for managing target covariances over time, but they do not consider the physical limitations of the sensors. Therefore, this dissertation incorporates a system-based metric, termed the Degrees of Transport (DOT), to consider the impact on the physical system that a particular observation tasking might have. The DOT metric is the supplementary angle associated with the angle between the sensor's current boresight vector, defined by Equation (3.15), and the observation state vector, defined by Equation (2.25), for a particular target-sensor pair. The angle between these two vectors is represented in the left hand side of the inequality in Equation (3.16). The DOT metric, defined in Equation (5.5), characterizes the angular distance the sensor does *not* have to move to observe a particular target. Therefore, it is maximized when the target is aligned with the boresight vector $\boldsymbol{\varrho}_{m,k}$ and minimized when the target is in the $-\boldsymbol{\varrho}_{m,k}$ direction.

$$\tau_{(n,m),k+1} = \pi - \cos^{-1}\left(\frac{\boldsymbol{\varrho}_{m,k} \cdot \boldsymbol{\rho}_{k+1}^{(SEZ)}}{||\boldsymbol{\rho}_{k+1}^{(SEZ)}||_2}\right) \tag{5.5}$$

An assumption with the DOT metric is that the distance a sensor must slew can be correlated to the workload being placed on the sensor. Lastly, the DOT metric matrix, described by Equation (5.6), is constructed in a similar fashion to the FIG metric matrix. $\boldsymbol{\mathcal{T}}_{k+1}$ is an $N \times M$ matrix where each element corresponds to a specific target-sensor pair, and zero terms are placed where a target-sensor pair is not predicted to be observable at t_{k+1}.

$$\boldsymbol{\mathcal{T}}_{k+1} = \begin{cases} \frac{\tau_{(n,m),k+1}}{\pi} & \text{if } \{\mathrm{o}_n, \mathrm{s}_m\} \text{ is observable} \\ 0 & \text{if } \{\mathrm{o}_n, \mathrm{s}_m\} \text{ is unobservable} \end{cases} \quad \forall \quad n = [1, N],\ m = [1, M] \tag{5.6}$$

The DOT metric matrix is normalized over the maximum possible angle a sensor may travel, which in this case is π.

At each time step, the objective function $\boldsymbol{\mathcal{J}}_{k+1}$ is calculated using Equation (5.7) with elements ranging in value from 0 to 1.

$$\boldsymbol{\mathcal{J}}_{k+1} = \frac{1}{3}(\alpha - \gamma + 1)\,\boldsymbol{\mathcal{L}}_{k+1} + \frac{1}{3}(\beta - \alpha + 1)\,\boldsymbol{\mathcal{F}}_{k+1} + \frac{1}{3}(\gamma - \beta + 1)\,\boldsymbol{\mathcal{T}}_{k+1} \tag{5.7}$$

The scalar coefficients, α, β, and γ, are predetermined and provide weight factors for each metric. α describes the degree to which the MLEA metric is preferred over FIG. β similarly scales the FIG and DOT metrics. γ defines the preference of the DOT metric over MLEA. To define these weights the objective function in Equation (5.7) was modified to isolate the appropriate coefficient, as shown in Equation (5.8).

$$\boldsymbol{\mathcal{J}}_{\alpha,k+1} = \alpha\boldsymbol{\mathcal{L}}_{k+1} + (1-\alpha)\boldsymbol{\mathcal{F}}_{k+1} \tag{5.8a}$$
$$\boldsymbol{\mathcal{J}}_{\beta,k+1} = \beta\boldsymbol{\mathcal{F}}_{k+1} + (1-\beta)\boldsymbol{\mathcal{T}}_{k+1} \tag{5.8b}$$
$$\boldsymbol{\mathcal{J}}_{\gamma,k+1} = (1-\gamma)\boldsymbol{\mathcal{L}}_{k+1} + \gamma\boldsymbol{\mathcal{T}}_{k+1} \tag{5.8c}$$

Each weight was scaled from 0 to 1 in multiple six hour simulations using the Test SOSI Network, described in Section 3.1.1, and the preliminary constellation described in Section 3.2.1. Each iteration was run three times and averaged. The resulting data was compiled into plots of percent root mean squared error versus coefficient value for position and velocity. A target estimate's average RMS error over time is converted to a percentage of the satellite's position and velocity magnitude. The error is presented as a percentage to enable a more qualitative comparison of the estimates across orbital regimes. Outliers were removed using the standard Tukey Fences method [111]. The plots show that the position and velocity errors are generally constant across weight values, thus allowing for a wide range of possible weight factors. The velocity error plots are presented here, while the position error plots are provided in Appendix A.1. As shown in Figure 5.2, any α value is potentially viable, but the error distribution shrinks between 0.55 and 1. The error distribution in Figure 5.2, and similar plots, refers to the distribution of percent RMS error for a particular weight factor value over repeated simulation runs. These error bars convey the variability in the percent RMS error for a particular weight factor value based on the stochastic nature of the simulation. $\alpha = 0.75$ was chosen for this dissertation. This weight favors the MLEA metric three times more than FIG metric, thus emphasizing overall covariance stability over what a specific sensor may provide.

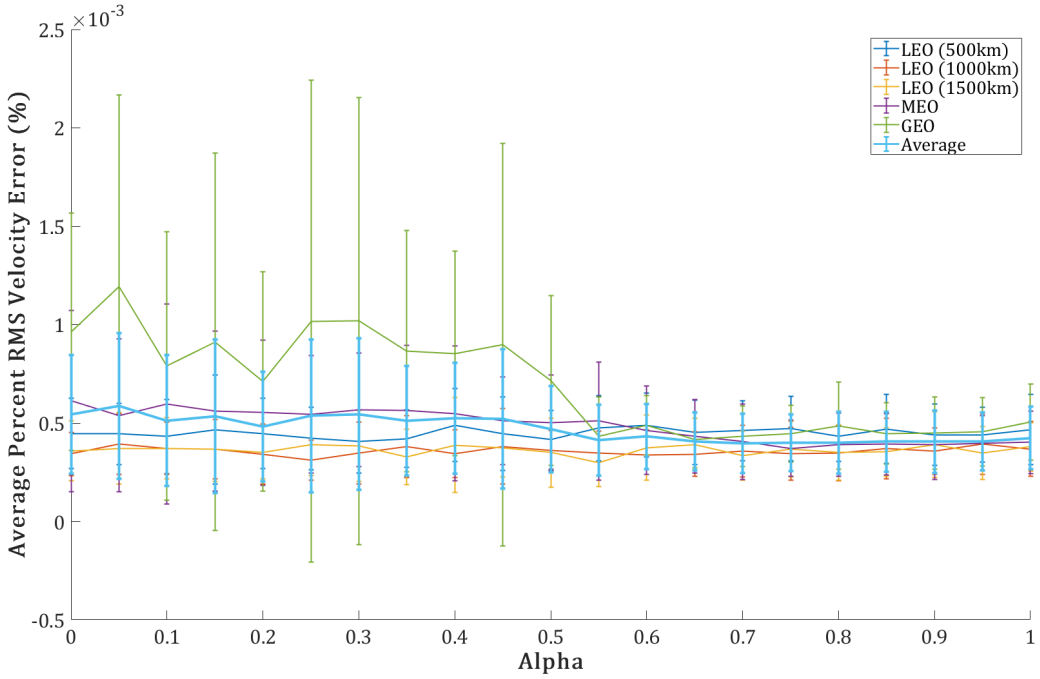

Figure 5.2: Percent RMS Velocity Error Vs. Alpha

β showed a more distinctive trend from volatility to accuracy with increasing values, as depicted in Figure 5.3. This trend isn't surprising as lower values of β place greater significance

on the DOT metric, which is not used to manage covariance like the FIG metric does. The viable range for β is roughly from 0.3 to 1, and $\beta = 0.7$ was selected for this dissertation. This weight places greater importance on FIG than slew angle, but still places significant emphasis on the system-based metric.

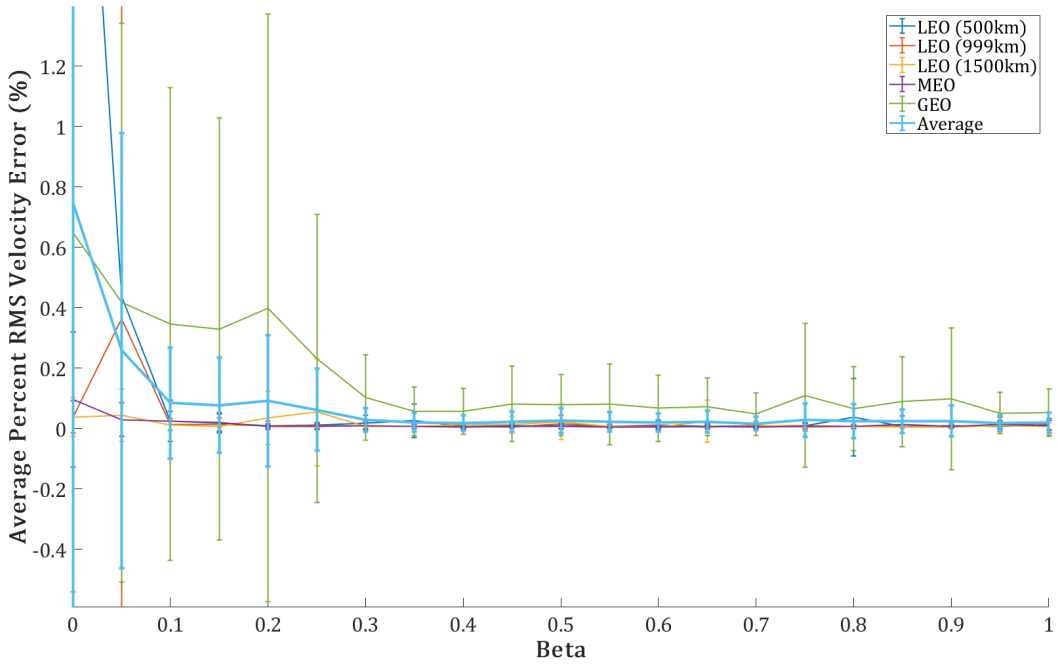

Figure 5.3: Percent RMS Velocity Error Vs. Beta

In a similar, but inverse fashion to β, higher values for the γ coefficient resulted in greater RMS velocity error and variance. The reason is the same. High values of γ emphasize the DOT metric over the covariance-based MLEA metric. Viable values for γ range roughly from 0 to 0.7. For this dissertation, $\gamma = 0.2$ was chosen, which corresponds to the minimum percent RMS velocity error in Figure 5.4. This weight makes the MLEA four time more important than the slew angle, but still forces the tasking strategy to place significant value on the system-based metric. Thus a very large slew angle may dissuade the tasking strategy from selecting that particular observation.

For clarity, the overall objective function for the suboptimal multi-phenomenology, continuous observation POMDP is given in Equation (5.9).

$$\boldsymbol{\mathcal{J}}_{k+1} = \frac{31}{60}\boldsymbol{\mathcal{L}}_{k+1} + \frac{19}{60}\boldsymbol{\mathcal{F}}_{k+1} + \frac{10}{60}\boldsymbol{\mathcal{T}}_{k+1} \tag{5.9}$$

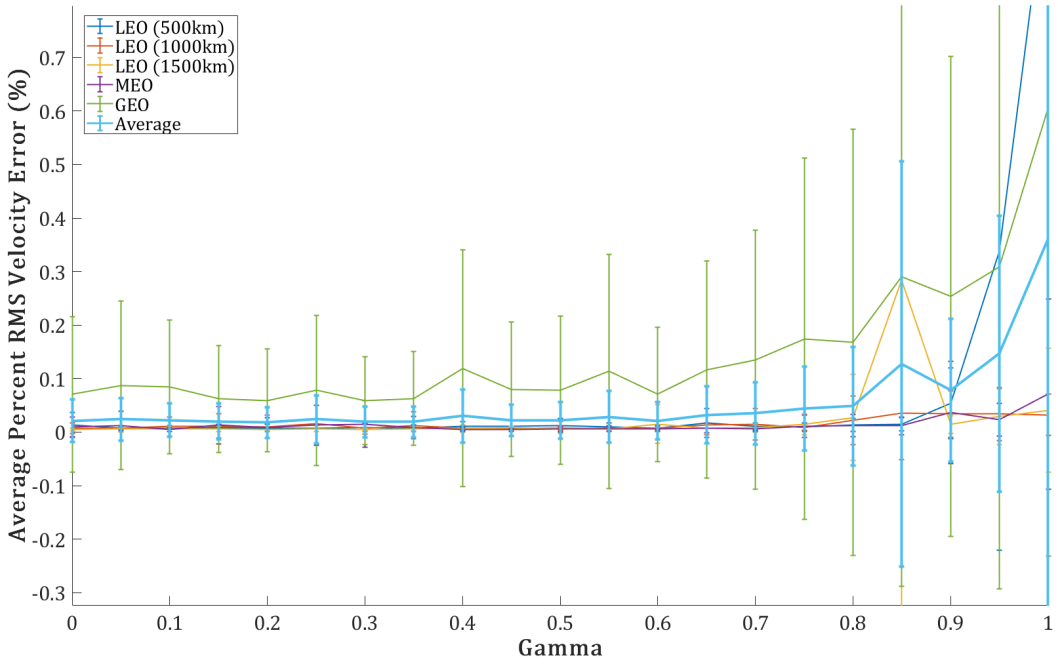

Figure 5.4: Percent RMS Velocity Error Vs. Gamma

5.3.3 Multiple Phenomenology, Cost-Constrained Tasking Process

The third suboptimal POMDP developed for this dissertation also uses three information and system-based metrics to assess potential sensor taskings, but is designed to only task sensors under a limited set of circumstances. This method uses the normalized FIG metric matrix defined in Equation (5.4), except the sign of each element of $\boldsymbol{\mathcal{F}}_{k+1}$, is determined by the corresponding MLEA metric. Thus, the FIG metric matrix for the cost-constrained tasking process is defined by Equation (5.10).

$$\mathcal{F}^{\text{eff}}_{(n,m),k+1} = \begin{cases} \text{SIGN}\left(\hat{\lambda}^{\text{eff}}_{n,k+1}\right) \frac{\hat{\phi}_{(n,m),k+1}}{\max(\hat{\boldsymbol{\phi}}_{1\ldots N,m,k+1})} & \text{if } \{\text{o}_n, \text{s}_m\} \text{ is observable} \\ 0 & \text{if } \{\text{o}_n, \text{s}_m\} \text{ is unobservable} \end{cases} \quad \forall \quad n = [1, N],\ m = [1, M] \tag{5.10}$$

The sign of the MLEA is used to ensure the SOSI network does not observe a given target when its associated MLEA is negative, thus indicating a converging covariance. A negative FIG metric ensures a negative value for the objective function value associated with that particular target-sensor pair. Because an unobservable target-sensor pair is assigned a zero value, the SOSI network will choose to neglect any potential observation associated with teh given target at the next time step. Observations are therefore only considered is the MLEA for a particular target is positive, indicating that the associated covariance estimate is diverging or expanding beyond the user-defined initial value.

For system-based considerations, this dissertation introduces a slew time metric to serve as a cost of sensor transport. The slew time system metric is simply the time a particular sensor requires to turn from its current boresight direction to the target, as shown in Equation (5.11).

$$t_{\omega,(n,m),k+1} = \frac{\cos^{-1}\left(\frac{\boldsymbol{\varrho}_{m,k}\cdot\boldsymbol{\rho}_{k+1}^{(SEZ)}}{||\boldsymbol{\rho}_{k+1}^{(SEZ)}||_2}\right)}{\omega_m} \tag{5.11}$$

where ω_m is the sensor slew rate defined in Section 3.1.1.

The slew time metric will yield a very small cost for the electronically Large Phased Array Radar, and a sizable value for slower moving mechanical radar and space-based EOIR sensors. Thus, the costs in this objective function are much more sensor-dependent than the DOT reward metric used in Section 5.3.2. The slew time matrix, defined in Equation (5.12), used in the objective function is normalized over the scenario time step. Like the DOT metric, it is assumed that the time a sensor takes to slew to a target is indicative of the workload and strain being placed on the sensor.

$$\boldsymbol{\mathcal{S}}_{k+1} = \begin{cases} \frac{t_{\omega,(n,m),k+1}}{\Delta t} & \text{if } \{\mathrm{o}_n, \mathrm{s}_m\} \text{ is observable} \\ 0 & \text{if } \{\mathrm{o}_n, \mathrm{s}_m\} \text{ is unobservable} \end{cases} \quad \forall \quad n = [1, N],\ m = [1, M] \tag{5.12}$$

The overall objective function is defined in Equation (5.13).

$$\boldsymbol{\mathcal{J}}_{k+1} = \delta\boldsymbol{\mathcal{F}}_{k+1}^{\text{eff}} + (1-\delta)\boldsymbol{\mathcal{S}}_{k+1} \tag{5.13}$$

Using this objective function, a sensor m will only be tasked to track target n if the normalized Fisher Information Gain is greater than the normalized slew time, and the predicted covariance is greater than the threshold specified in the MLEA metric. These constraints significantly reduce the times during which a sensor will be tasked to collect an observation, making the entire SOSI network more efficient, and each observation more influential.

The scalar coefficient δ, in Equation (5.13), was assessed with the same methodology used in Section 5.3.2. Like with the continuous tasking weight factors, low values for δ resulted in higher percent RMS error by favoring the slew time metric over the covariance-dependent FIG metric. Viable δ values ranged from 0.1 to 1, as shown in Figure 5.5. $\delta = 0.5$ was chosen for this dissertation, giving equal weighting to the FIG metric and the slew time metric. The percent RMS position error versus δ plot is provided in Appendix A.2.

5.4 Decision Matrix

The Decision Matrix, $\boldsymbol{\mathcal{U}}_{k+1}$, is a binary matrix populated with elements $\mathcal{U}_{(n,m),k+1}$ that are either 0, indicating an ignored target-sensor pair, or 1, indicating a tasked pair. Each sensor

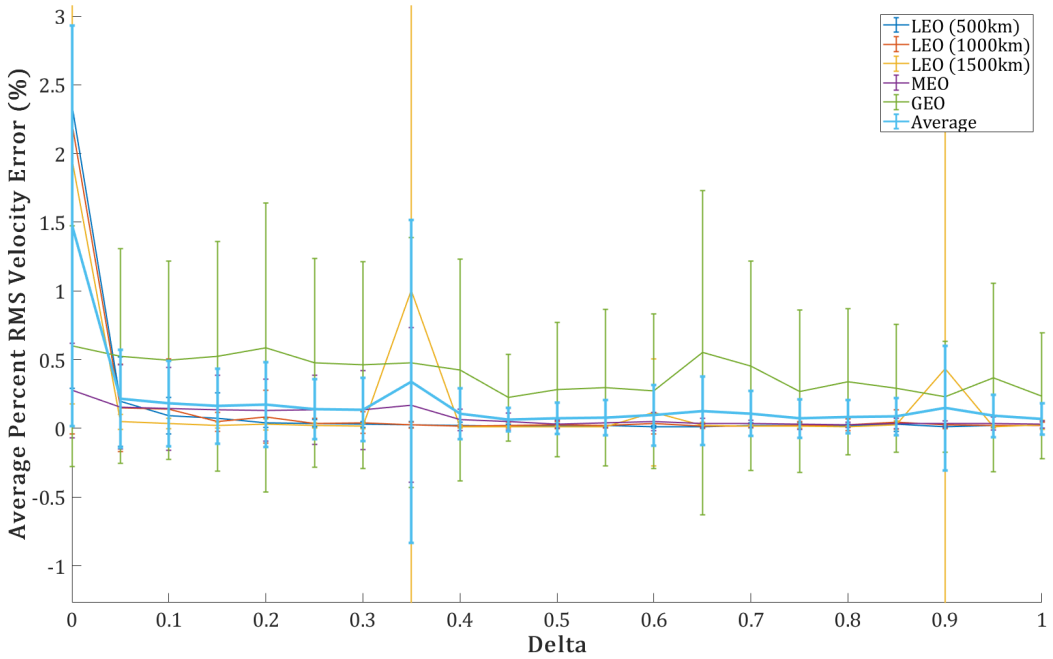

Figure 5.5: Percent RMS Velocity Error Vs. Delta

m can only observe one target at a time, but a single target may be observed by multiple sensors. The elements of the $N \times M$ Decision Matrix are constrained using Equation (5.14).

$$\sum_{n=1}^{N} \mathcal{U}_{(n,m),k+1} \leq 1, \quad \mathcal{U}_{(n,m),k+1} \in \{0,1\} \quad \forall \quad n = [1,N],\ m = [1,M] \tag{5.14}$$

Because $\mathcal{U}_{(n,m),k+1}$ can only be 0 or 1, and each element is independent of the others, each element is found via Equation (5.15).

$$\mathcal{U}_{(n,m),k+1} = \begin{cases} 1 & \text{if } \mathcal{J}_{(n,m),k+1} = \max(\boldsymbol{\mathcal{J}}_{1\ldots N,m,k+1}) \\ 0 & \text{if } \mathcal{J}_{(n,m),k+1} < \max(\boldsymbol{\mathcal{J}}_{1\ldots N,m,k+1}) \end{cases} \tag{5.15}$$

5.5 Summary

This chapter described the three suboptimal POMDPs that were developed for this dissertation. The first serves as a baseline approach, based on previous research, and only uses the FIG metric to determine sensor tasking. The second method uses FIG, MLEA, and a system-based Degrees of Transport metric to manage sensors, assuming that observations will always be made as long as a target is visible. The third approach provides a cost-constrained alternative that significantly limits the frequency at which a sensor will make observations, thus reducing the overall workload on the SOSI network. In Chapter 6, these

three decision-making processes will be integrated with an adaptive estimation method from Chapter 4, to assess how well each command and control strategy manages a globally distributed SOSI network to track a large population of non-maneuvering and maneuvering spacecraft.

Chapter 6

Process Comparisons & Implications

6.1 Introduction

This chapter presents the results of various analyses that were used to assess the effectiveness and efficiency of each POMDP, adaptive estimation method, and several integrated strategies. First, decision process performance against only non-maneuvering targets was assessed to establish a baseline for how well each decision-making strategy performs without adaptive estimation. Next, the adaptive estimation techniques were analyzed with each POMDP to characterize how well each method reacquired viable orbit estimates for seven maneuvering satellites. Lastly, four integrated command and control strategies are assessed by specifically analyzing how they track the seven maneuvering in the Full Scale Test Scenario described in Section 3.2.

6.2 Decision Process Analysis

The decision process analyses in this section assess how well each POMDP described in Chapter 5 track 200 non-maneuvering targets. The tracked satellites comprise the constellations described in Table 3.8. With so many more targets than sensors, the developed POMDPs cannot collect observations on every spacecraft all the time. The three decision methods are compared using three metrics:

1. The root mean squared error of each target averaged over the duration of the scenario
2. The cumulative Fisher information gain per slewed angle with respect to time over the duration of the scenario
3. The cumulative Fisher information gain per observation with respect to time over the duration of the scenario

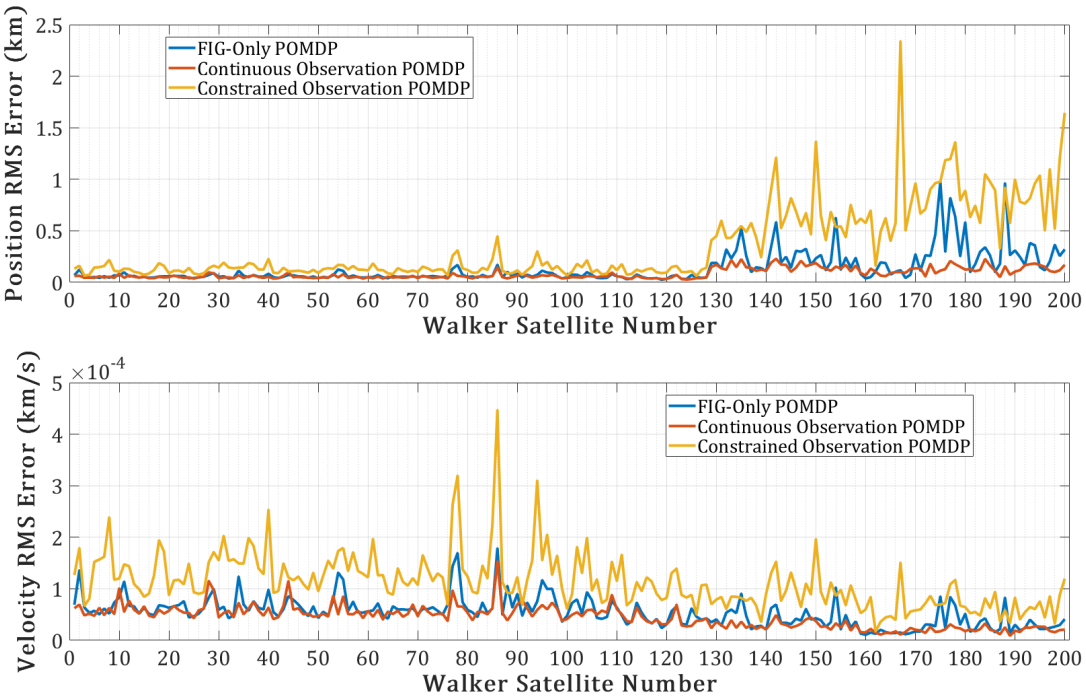

Figure 6.1: Average RMS Error Comparison

Figure 6.1 depicts the average root mean squared position and velocity error per target. The performance of all three decision methods are overlaid for direct comparison. The estimates for the LEO spacecraft, which consist of Walker1 to Walker128, were visibly more accurate than the MEO (Walker129 to Walker158) and GEO (Walker 160 to Walker 200) estimates. This trend is evident for all three POMDPs. The minimum position error for the FIG-Only and Continuous Observation POMDPs were roughly 19m. The minimum position RMS error for the Constrained Observation decision process was almost 42m. All three position error minimums belong to LEO estimates. The MEO and GEO target estimates not only consistently carried higher RMS position error, but the variability in error across targets was also significantly higher. The trend is particularly evident with the Constrained Observation POMDP that significantly reduced the number of collected observations over time. These variations in statistical error are likely due to lower sensor revisit rates compared to LEO targets, as well as the synchronous nature of the orbits at higher altitude. The MEO targets are in a twelve hour, semi-synchronous orbit, and the GEO targets complete an orbit every sidereal day. These trajectories substantially limit the number of terrestrial sensors that can ever observe a particular target. For example, the geostationary Walker190 may perpetually remain over a powerful LPAR, and is therefore always able to be observed when the POMDP determines an observation is warranted. Walker191, however, some significant degrees of longitude away from Walker190, may only be occasionally visible to an orbiting EOIR sensor, thus increasing its average RMS estimate error.

Overall, the FIG-Only and Continuous Observation POMDPs consistently resulted in lower RMS position error than the Constrained Observation POMDP, because of their significantly greater observation frequency. This trend is more evident in the second plot of Figure 6.1, which shows the RMS velocity error. Interestingly, the RMS velocity error for all three decision processes decreases slightly with increasing altitude. This trend is partly the result of the decreasing process noise with altitude, and also because errors in velocity propagate slower in MEO and GEO than in LEO where spacecraft orbital velocities are significantly faster. Thus, accurate velocity estimates for higher altitude satellites will be more tenable over time.

The RMS position and velocity error provides a quantifiable effectiveness metric for each POMDP, but it is only one facet of the overall assessment. First, Figure 6.2 presents the averaged percent RMS error per target for each POMDP. A target estimate's average RMS

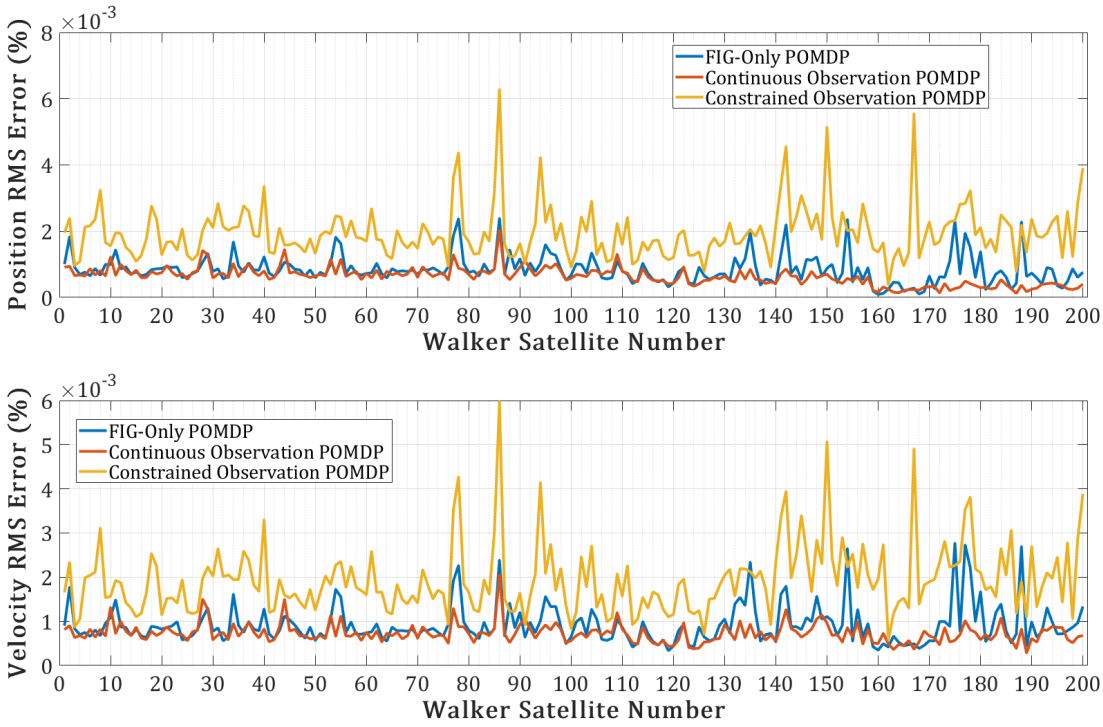

Figure 6.2: Average Percent RMS Error Comparison

error over time is converted to a percentage of the satellite's position and velocity magnitude. The error is presented as a percentage to enable a more qualitative comparison of the estimates across orbital regimes. More sensors with more advanced capabilities can observe LEO satellites than GEO, so a 1km error in LEO would indicate a more significant estimation issue than the same error at GEO. Viewing the RMS error as a percentage provides an acceptable indicator of similar levels of uncertainty across orbital altitudes. A 1% position error in LEO is arguably similar in significance to a 1% position error in GEO.

Figure 6.2 shows the similar error growth and variability with increasing altitude to that seen in Figure 6.1, but the differences between LEO and GEO are much less striking. This observation indicates that the RMS errors are more proportional to the orbit altitude than can be inferred from looking at the scalar position and velocity errors alone.

Assessing true error gives an indication of how effective each POMDP was in the scenario, but it does not give any information on how efficient each tasking strategy was over time. To do that, the cumulative information gain metric over time was measured against two system-based performance metrics. Figure 6.3 presents the cumulative Fisher Information Gain metric per slewed degree over time, with all three POMDPs overlaid for direct comparison. The values for the vertical axis are defined by Equation 6.1, where $\mathfrak{f}_k$ is the value at time step k.

$$\mathfrak{f}_k = \sum_{1}^{k} \frac{\sum_1^n \sum_1^m \phi_{(n,m),k} \mathcal{U}_{(n,m),k}}{\sum_1^n \sum_1^m \cos^{-1}\left(\frac{\boldsymbol{\varrho}_{m,k} \cdot \boldsymbol{\rho}_{k-1}^{(\mathrm{SEZ})}}{||\boldsymbol{\rho}_{k-1}^{(\mathrm{SEZ})}||_2}\right) \mathcal{U}_{(n,m),k}} \tag{6.1}$$

This analysis assesses how much information was collected for every degree the sensors had to turn to make the tasked observation. One would expect a POMDP that includes system-

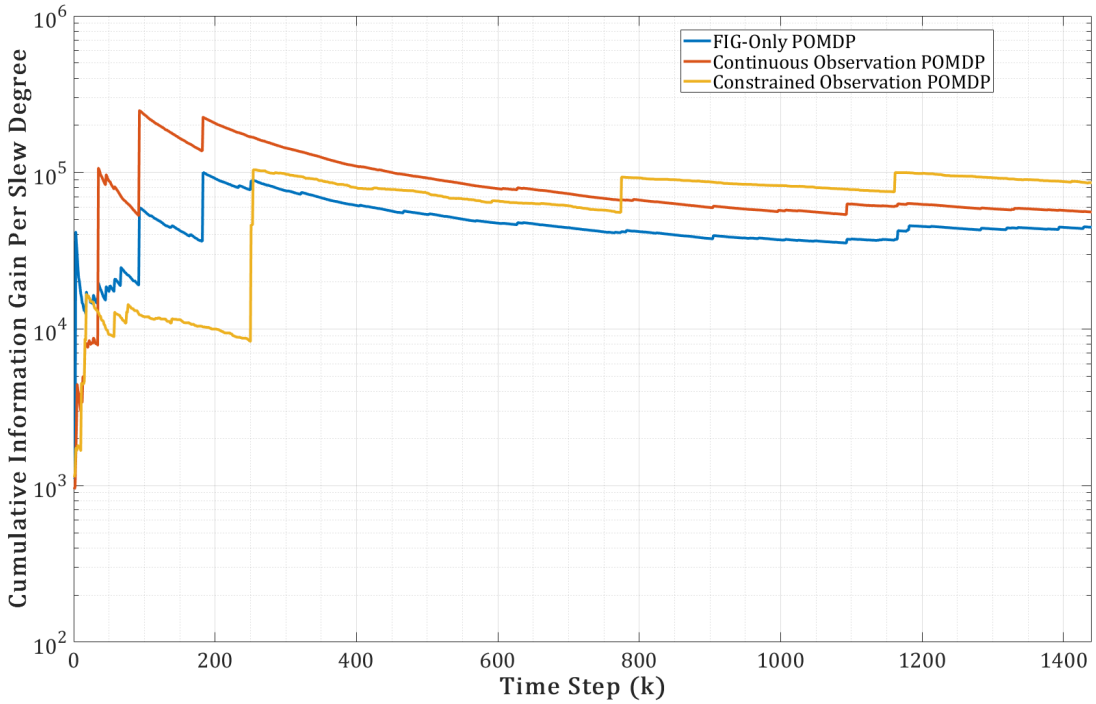

Figure 6.3: Cumulative Information Gain Metric Per Slewed Degree Vs. Time

based tasking metrics, like Degrees of Transport or slew time, to perform better in this assessment than a POMDP that only considers information. Indeed, that hypothesis is observed in Figure 6.3, particularly once the metric reaches a steady state during the latter

half of the scenario. The Continuous Observation POMDP gave the system-based DOT metric an overall weighting of $\gamma = \frac{1}{6}$, and the Constrained Observation POMDP gave the FIG and slew time metrics equal weighting. The baseline FIG-Only POMDP did not consider system-based metrics. At first the Continuous Observation POMDP showed markedly more information per degree than the other two processes. In fact, the Constrained Observation POMDP was a full order of magnitude less than the Continuous case for some time. As time progressed, however, the Constrained Observation POMDP became consistently more efficient than the other two methods. The initial performance that favored the two information-heavy POMDPs was likely the result of initial estimate covariances being high due to the scenario initialization. Once all the targets were observed and covariance estimates reached a steady state, the Constrained Observation POMDP became the most efficient method, based on the information gain per slewed degree metric.

Thus far, assessing the RMS error and the information gain metric per slewed angle for each decision process has yielded two distinct impressions of which method performs better. The RMS error, in Figures 6.1 and 6.2, shows that the Constrained Observation POMDP provides less accuracy than the FIG-Only and Continuous Observation processes, which performed roughly equivalently. On the other hand, the information gain per slewed degree analysis, in Figure 6.3, indicates that the Constrained Observation decision process is the most efficient, followed by the Continuous Observation method, and lastly the FIG-Only POMDP. The final analysis in this section is the cumulative information gain metric per observation over time, as shown in Figure 6.4. The cumulative information gain metric per observation is calculated using Equation 6.2

$$\mathfrak{f}_k = \sum_{1}^{k} \frac{\sum_1^n \sum_1^m \phi_{(n,m),k} \mathcal{U}_{(n,m),k}}{\sum_1^n \sum_1^m \mathcal{U}_{(n,m),k}} \tag{6.2}$$

This assessment gives insight into how much information is collected, on average, with each observation. It does not consider the workload placed on the sensor like the previous metric did. Additionally, this assessment metric normalizes the three POMDPs over their observation frequencies. Even though the FIG-Only and Continuous Observation processes collected observations every time step, they would perform poorly in this assessment if the information gained with each observation was low. One might expect the decision process that places the highest priorty on FIG would perform well against this metric. Considering the FIG-Only decision process only considers information gain, one would hypothesize that it would collect the most information with each observation over time, thus producing the highest cumulative information per observation measure. In fact, the Continuous Observation POMDP performed consistently better than the two other methods, indicating that the inclusion of the MLEA metric had a significant impact. Identifying the potential observation based solely on the highest FIG was not sufficient to guarantee the most information per observation over time.

In summary, all three decision-making strategies were able to maintain viable orbit estimates

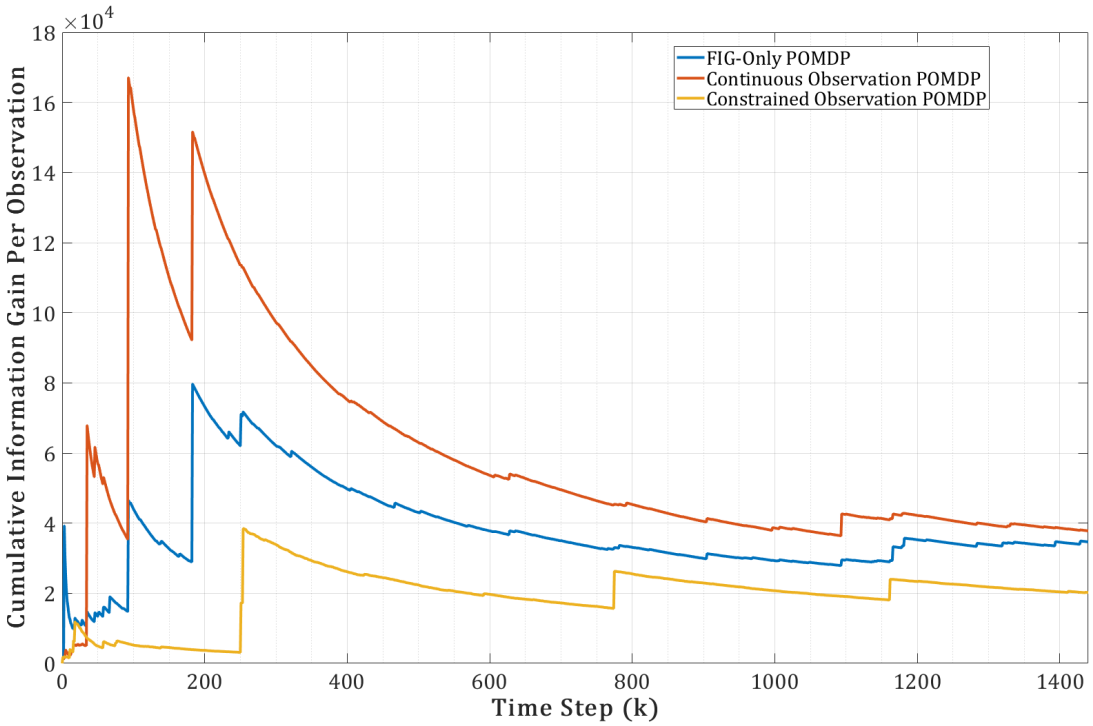

Figure 6.4: Cumulative Information Gain Metric Per Observation Vs. Time

for all 200 non-maneuvering targets across all three orbital regimes for the entire scenario. The FIG-Only and Continuous Observation POMDPs yielded comparable average RMS error, but the Continuous Observation method collected significantly more information per observation that the FIG-Only approach. The Constrained Observation POMDP provided less accurate orbit estimates, but was more efficient, with respect to workload, than the other two processes.

6.3 Adaptive Estimation Analysis

The next set of analyses sought to characterize adaptive estimation performance in all three decision processes against seven maneuvering targets. The maneuvering satellites used in these simulations are defined in Table 3.9. The purpose of this investigation is to isolate the capabilities of each adaptive estimation process for comparison purposes. Only the seven maneuvering satellites are used in these simulations. With a few exceptions, sensors are therefore able to observe all seven spacecraft as long as they are visible. This analysis enables a direct assessment of the adaptive estimation process separate of the sparse observation limitation associated with tracking a large number of targets. In addition to the nominal case, where no adaptive estimation technique is used, five estimation processes are integrated

with each POMDP. In the context of each decision process, plots of the average RMS error for each estimation process are overlaid for comparison. Apart from the estimation processes, the scenario for each POMDP simulation is identical. Therefore, the differences in RMS error are the result of the adaptive estimation technique's ability to converge on a viable orbit estimate after an unknown maneuver occurs.

6.3.1 FIG-Only POMDP

First, the adaptive estimation methods are assessed within the FIG-Only POMDP. The resulting average RMS error plot for all seven maneuvering satellites is presented in Figure 6.5. One observation is that the nominal estimation process (no adaptive capability), in blue, incurred significantly more error than the adaptive estimation processes for all of the maneuvering satellites except MEOMnvr-1 and GEOMnvr-1.

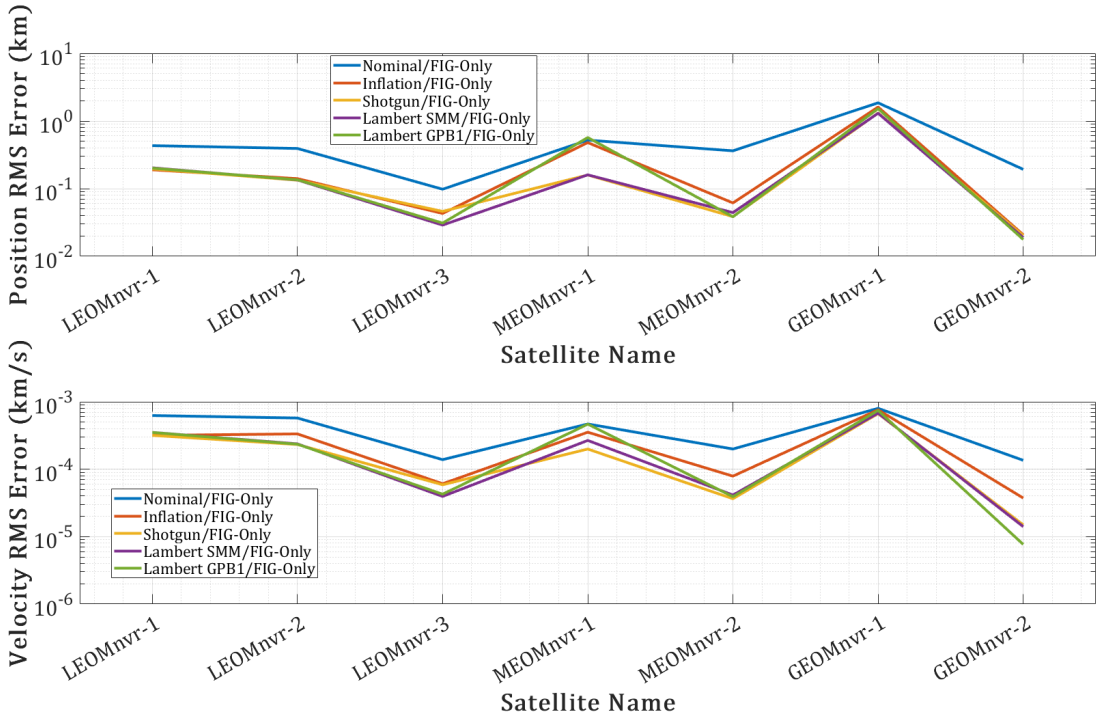

Figure 6.5: FIG-Only: Average RMS Error Comparison

The reasons for why the nominal and adaptive estimation techniques had similar RMS errors for MEOMnvr-1 and GEOMnvr-1 are not evident in Figure 6.5, but the orbit estimate plots in Appendix Section B.1 can give some insight. Figures 6.6 and 6.7 are given here as examples. Black circles denote observations made using the nominal UKF. Red diamonds denote observations made using the presented MMAE approach. Based on those plots, the average RMS error in Figure 6.5 is likely due to the significant observation gap after both

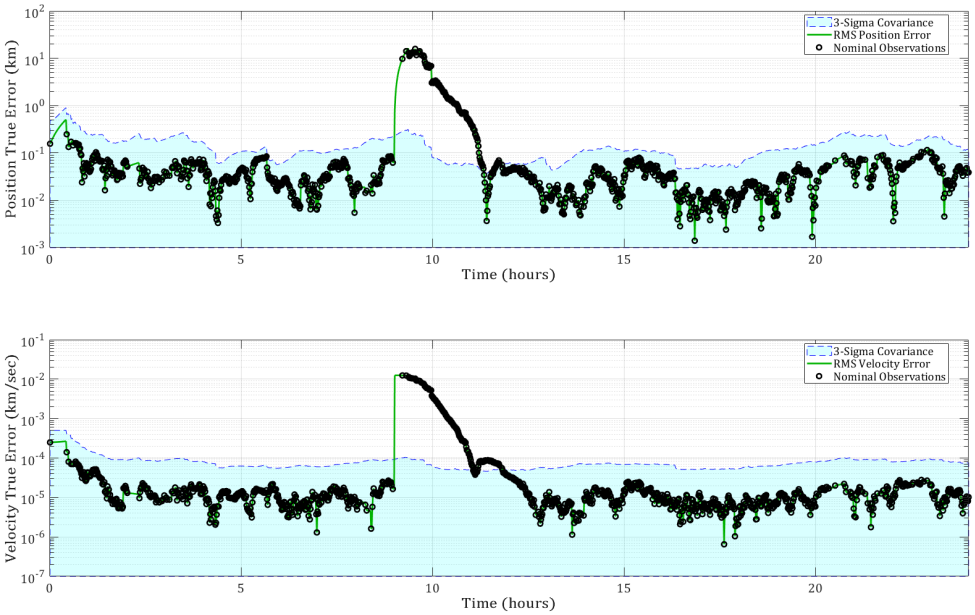

Figure 6.6: A.E. Test: Nominal/FIG-Only MEOMnvr-1 Track

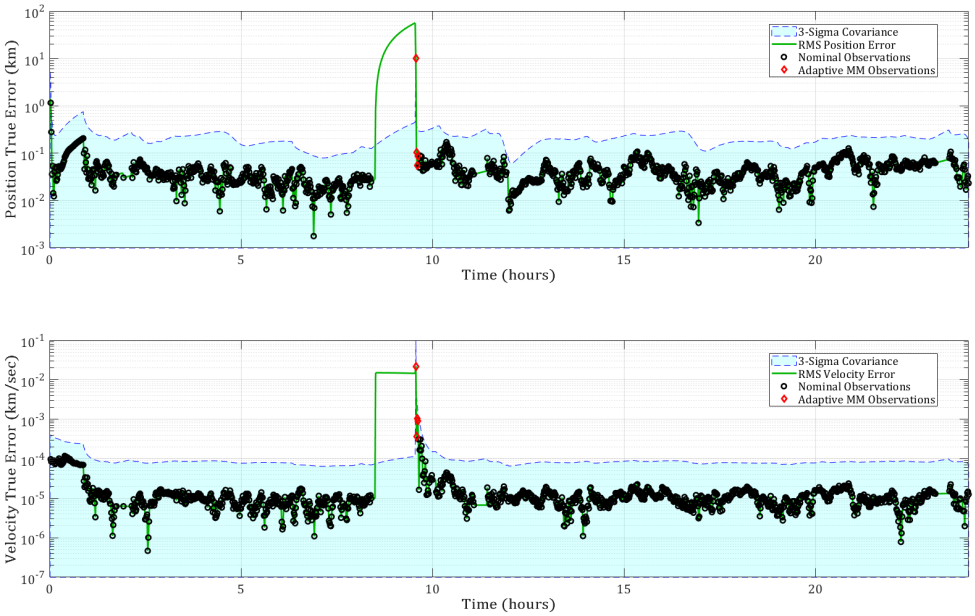

Figure 6.7: A.E. Test: Lambert SMM/FIG-Only GEOMnvr-1 Track

targets maneuver. Observation gaps occurred when a particular target satellite is out of view of all sensors that could potentially observe it. The observational constraints defined in Section 3.1.1 dictate when a target is unobservable for a particular sensor. GEOMnvr-1 has an observation gap because it is eclipsed for 1-2 hours, and therefore not visible to EOIR sensors. Some maneuvers were scheduled to take advantage of known observation gaps to allow the satellite to drift from the estimate for some time before an observation was possible. The substantial error is allowed to propagate for some time before the pertinent estimation algorithm reacts accordingly, thus raising the average RMS error over the whole scenario. It should be noted that the adaptive estimation techniques, particularly the SMM approaches, were considerably more responsive and effective than the nominal estimation method for all of the maneuvering satellites. Additionally, the maneuver magnitudes for MEOMnvr-1 and GEOMnvr-1 were greater than they were for MEOMnvr-2 and GEOMnvr-2, as indicated in Table 3.9. This difference would not only increase the overall average RMS error, but also impose a greater challenge for the adaptive estimation techniques to overcome.

In Figure 6.5 it's also evident that the adaptive estimation algorithms all had RMS error performance within an order of magnitude, especially for the LEO satellites. From a position error sense, the adaptive estimation algorithms performed similarly against the GEO spacecraft as well. Velocity error performance varied over a wider range for the adaptive estimation techniques as the target altitude increased.

It should also be noted that the Lambert GPB1 algorithm was only triggered for one time step in most situations. As shown in Figures B.30 and B.31, the Lambert GPB1 algorithm only executed for multiple time steps when tracking the two MEO maneuvering satellites. When only operating for one time step, the Lambert GPB1 is effectively just an SMM over a single time step. That said, the GPB1 demonstrates its responsiveness as an overall algorithm if it was only needed once to reacquire a viable orbit estimate.

6.3.2 Continuous Observation POMDP

For the Continuous Observation POMDP scenario, the distinction between adaptive and nominal estimation performance is more significant than in the FIG-Only case. Figure 6.8 shows how all four adaptive estimation techniques resulted in a lower RMS error than the nominal estimator for all seven targets. As expected from Section 6.2, the overall average

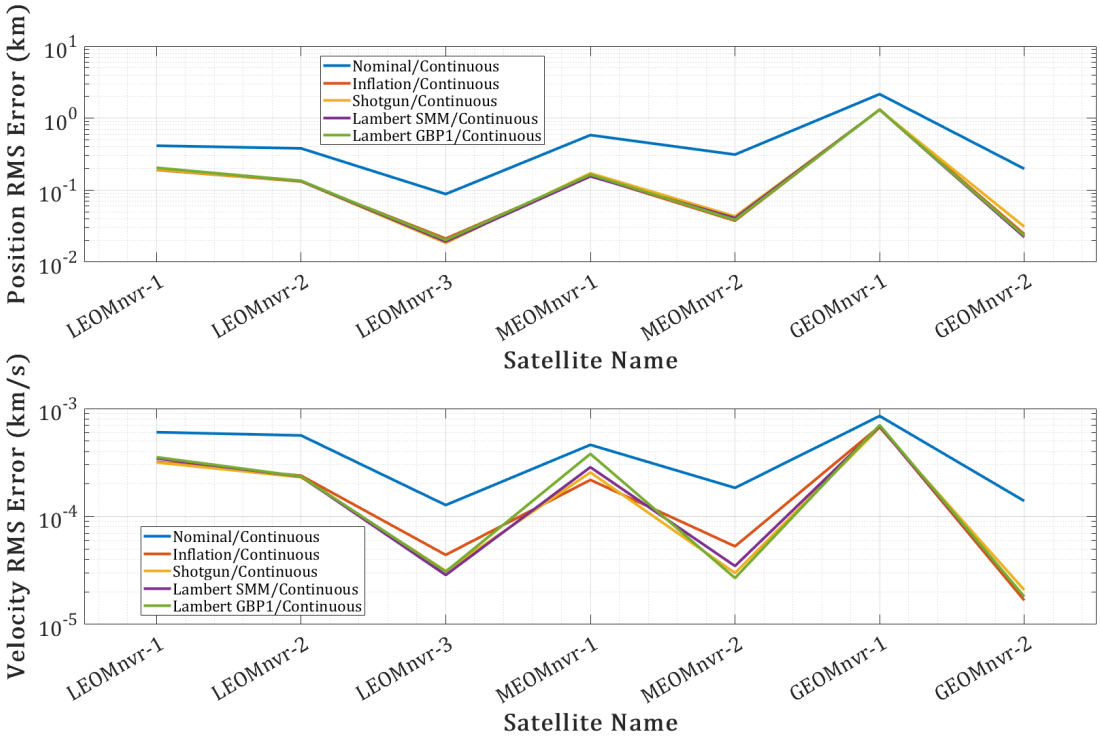

Figure 6.8: Continuous Observation: Average RMS Error Comparison

RMS errors in the Continuous Observation scenario were comparable to the errors incurred in the FIG-Only case. The performance difference between the adaptive estimation algorithms themselves was markedly smaller in the Continuous Observation POMDP than the FIG-Only approach. Adaptive estimation performance against the LEO spacecraft was similar between the Continuous Observation and FIG-Only POMDPs. Of particular note, the Shotgun SMM was implemented twice for the MEOMnvr-1 case in the Continuous Observation scenario, as shown in Figure 6.9, but not the FIG-Only case. Again, black circles denote observations made when the nominal UKF is being used, while red diamonds indicate the observations made when the Shotgun SMM is used. Additionally, the Lambert GPB1 was executed for several time steps for all four MEO and GEO satellites (Figures B.64, B.65, B.66, and 6.10). The rest of the orbit estimate plots for the Continuous Observation POMDP scenario are provided in Appendix Section B.2.

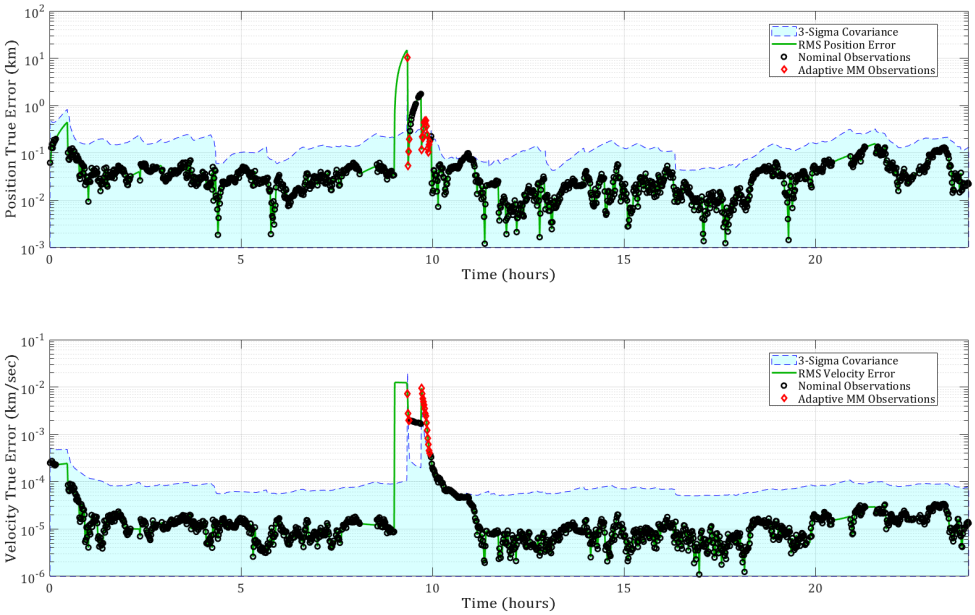

Figure 6.9: A.E. Test: Shotgun SMM/Continuous MEOMnvr-1 Track

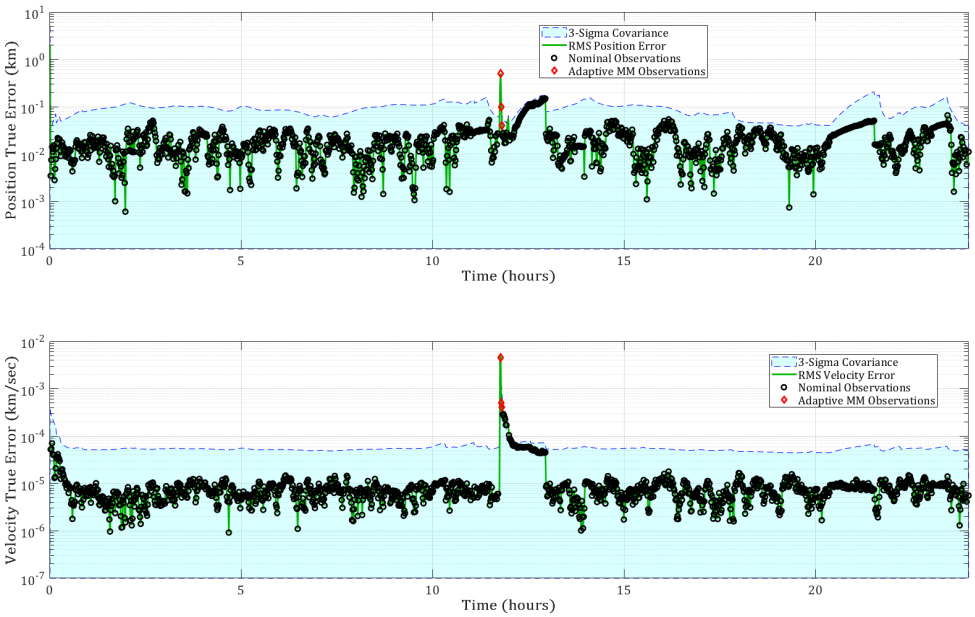

Figure 6.10: A.E. Test: Lambert GPB1/Continuous GEOMnvr-2 Track

6.3.3 Constrained Observation POMDP

Lastly, the nominal and adaptive estimation techniques were integrated with the Constrained Observation POMDP and tested against the seven maneuvering spacecraft. The resulting average RMS position and velocity error plots are provided in Figure 6.11. The increased

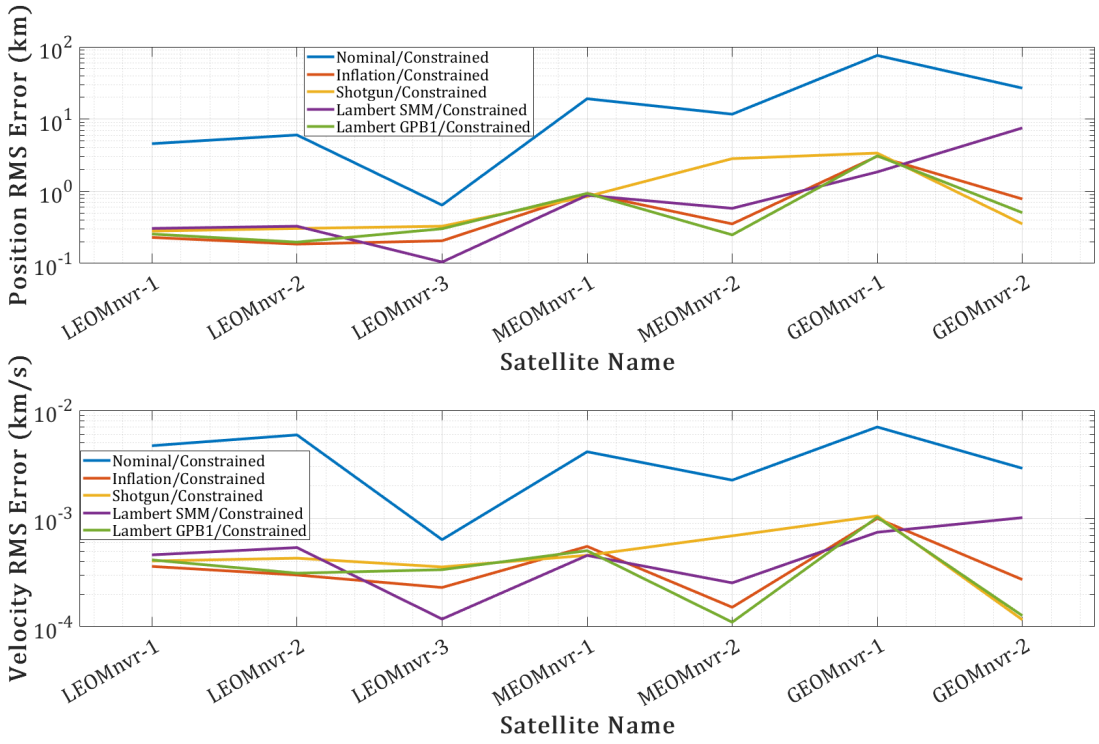

Figure 6.11: Constrained Observation: Average RMS Error Comparison

variability in RMS error that was evident in Section 6.2 has a noticeable impact on the overall effectiveness of the adaptive estimation methods. The nominal estimation approach results in the largest average RMS error for all seven satellites, and in all three POMDP scenarios. Figure 6.12 shows the impact of the Constrained Observation POMDP on the nominal filter's ability to reacquire the MEOMnvr-1 spacecraft after its maneuver. The remaining nominal estimation orbit tracks are provided in Appendix Section B.3.

The adaptive estimation techniques in the Constrained Observation scenario almost always resulted in an order of magnitude better average RMS error than the nominal case. Unlike the other two POMDPs, with which the adaptive estimation techniques performed comparably, the Constrained Observation decision process resulted in greater variability among the adaptive methods. In Figure 6.11, the Shotgun SMM routinely performed worse than the other adaptive estimation techniques, with the exception of GEOMnvr-2. In that case, the Lambert SMM showed unusual difficulty reconverging on a viable orbit estimate compared to the other approaches. The increased error in the Lambert SMM is due to the

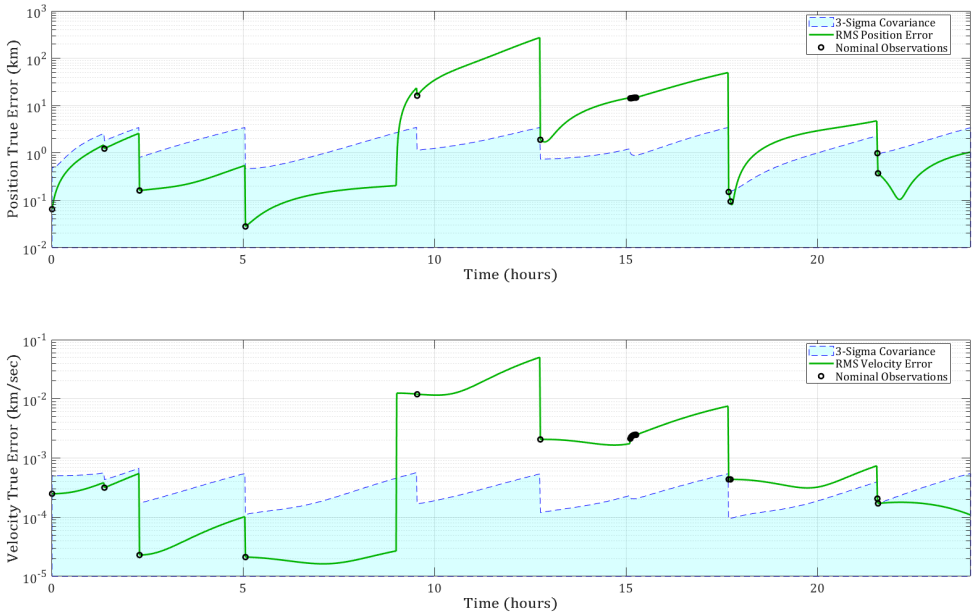

Figure 6.12: A.E. Test: Nominal/Constrained MEOMnvr-1 Track

dramatically small number of observations collected on GEOMnvr-2 after the maneuver, as shown in Figure 6.13. Other adaptive estimation methods, like the covariance inflation approach presented in Figure 6.14, resulted in many more observations of GEOMnvr-2 after the observation.

All other orbit estimate plots for the Constrained Observation scenario are provided in Appendix Section B.3.

Overall, the analysis presented in this section indicates that the adaptive estimation methods developed in this dissertation do produce measurable improvements in responsiveness when tracking maneuvering spacecraft. Additionally, their performance is comparable when integrated with any of the three proposed POMDPs, though the Constrained Observation decision process resulted in greater RMS error in general. Any distinguishing characteristic between the adaptive estimation techniques is therefore predominantly due to the particular algorithm's situational versatility and computational efficiency.

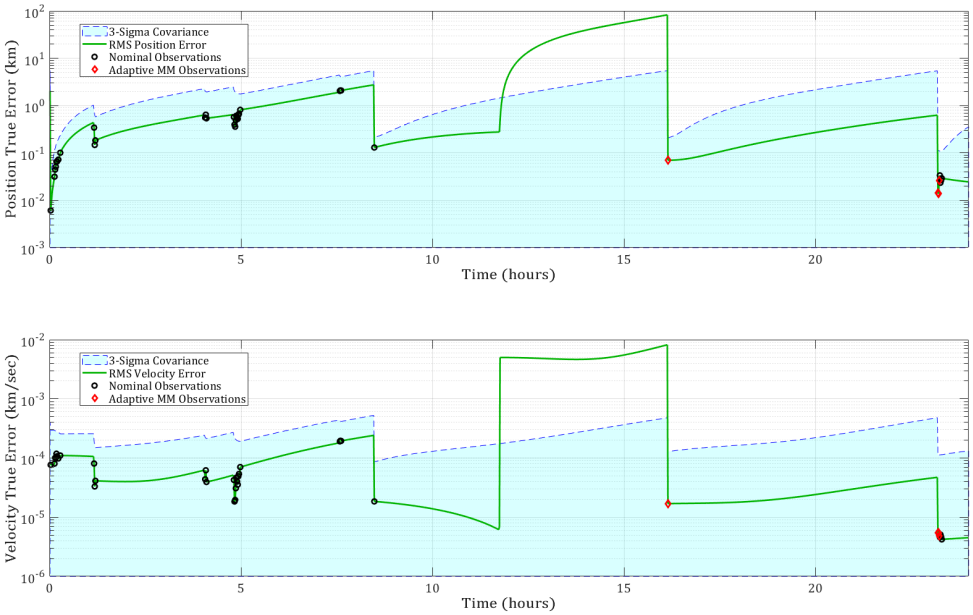

Figure 6.13: A.E. Test: Lambert SMM/Constrained GEOMnvr-2 Track

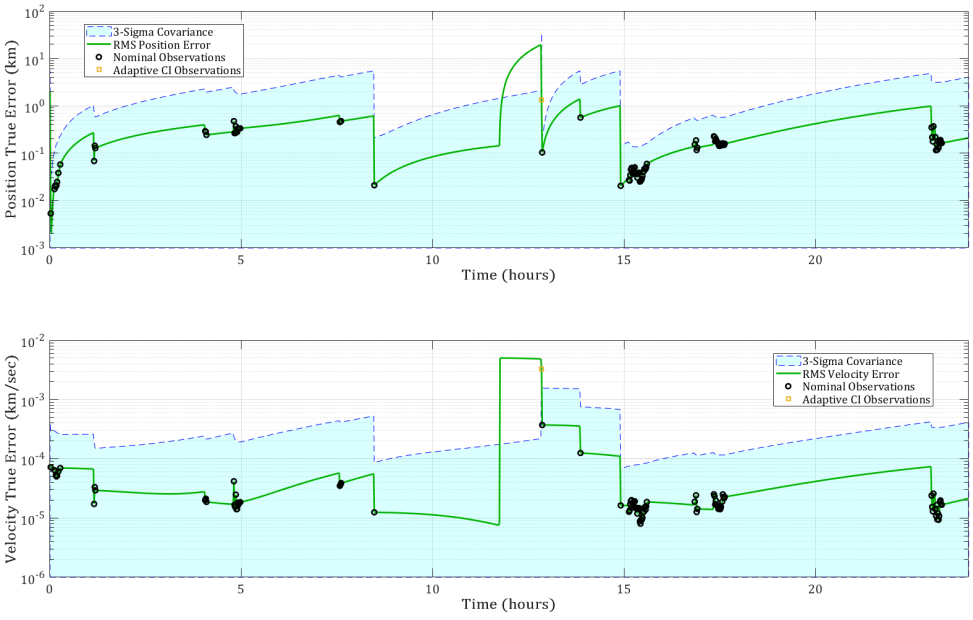

Figure 6.14: A.E. Test: Inflation/Constrained GEOMnvr-2 Track

6.4 Full Scale Assessment

Based on the analyses in Sections 6.2 and 6.3, four command and control strategies were developed that integrate a particular adaptive estimation technique and a decision process. The first is a baseline strategy that combines the developed covariance inflation algorithm with the FIG-Only POMDP. The second method, derived from the previous work in [29] and [30], integrates the Shotgun SMM and the Continuous Observation POMDP. The third and fourth approaches combine the Constrained Observation decision process with the Lambert SMM and Lambert GPB1 algorithms, respectively. Using the test SOSI network specified in Section 3.1.1, all four command and control strategies are tested against the full scale constellation defined in Section 3.2. One unique analytical opportunity this test presents is the ability to observe how the adaptive estimation strategy impacts the overall command and control strategy's sensor tasking behavior after a maneuver is detected. The previous analyses either had no maneuvering targets, or too few targets, thus prohibiting the kind of assessment the full scale test generates. The results of these investigations are presented in the following sections, and in Appendix C.

A preliminary assessment of average RMS error for each command and control strategy against each of the eight non-maneuvering constellations in Table 3.8 is presented in Figure 6.15. This overall analysis indicates that the Continuous Observation POMDP employ-

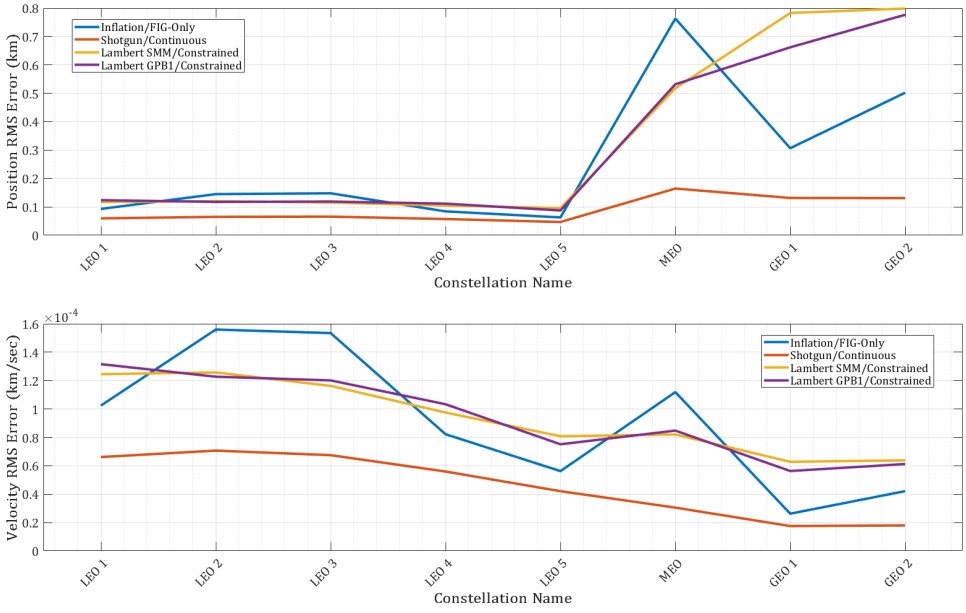

Figure 6.15: Overall Average RMS Error Per Constellation

ing the Shotgun SMM resulted in the lowest average RMS error for all eight constellations, suggesting that it most effectively tracked through the errors incurred after the unknown

maneuvers. The covariance inflation and FIG-Only POMDP fluctuated in effectiveness, with the highest position errors encountered with the MEO constellation. The two Constrained Observation POMDPs resulted in reasonably constant average position error across the LEO regime, but experienced significant position error growth with increasing altitude in the MEO and GEO regimes. All four tasking strategies experienced generally decreasing average velocity RMS error with increasing altitude.

6.4.1 Nominal Estimation POMDPs

For comparison purposes, the three POMDPs were integrated with nominal UKFs that had no adaptive estimation capability. The orbit estimate and observation plots for these scenarios are provided in Appendix Sections C.1, C.2, and C.3, but several are provided here for discussion. Overall, these plots demonstrate how a tasking strategy manages sensors significantly impacts the estimation process's ability to converge on a viable orbit estimate.

For example, in the LEO regime, a high observation rate like the one found with the FIG-Only POMDP allows the filter to eventually converge on an orbit estimate, even after a significant observation gap. The nominal FIG-Only POMDP's orbit estimate for LEOMnvr-2 is presented in Figure 6.16. Convergence is evident towards the end of the plot when the error has finally descended below the three sigma covariance line. Nominal sensor tasking in

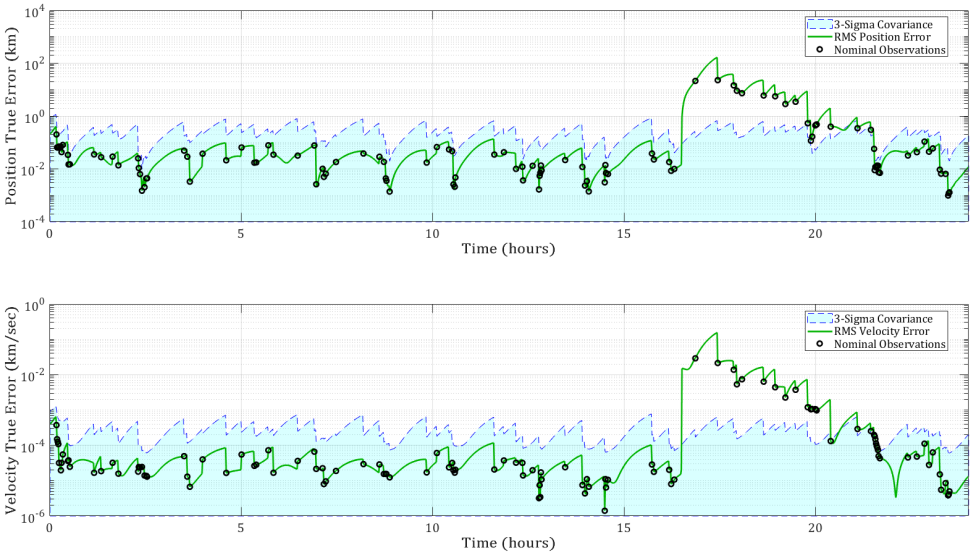

Figure 6.16: Nominal/FIG-Only LEOMnvr-2 Track

the LEO regime is also aided by multiple terrestrial radar and their 3D observations (Section 2.3.1). This is evident in the nominal FIG-Only observation plot for LEOMnvr-2, given

in Figure 6.17, where the ground-based radar are shown contributing multiple observations over time (indicated in blue).

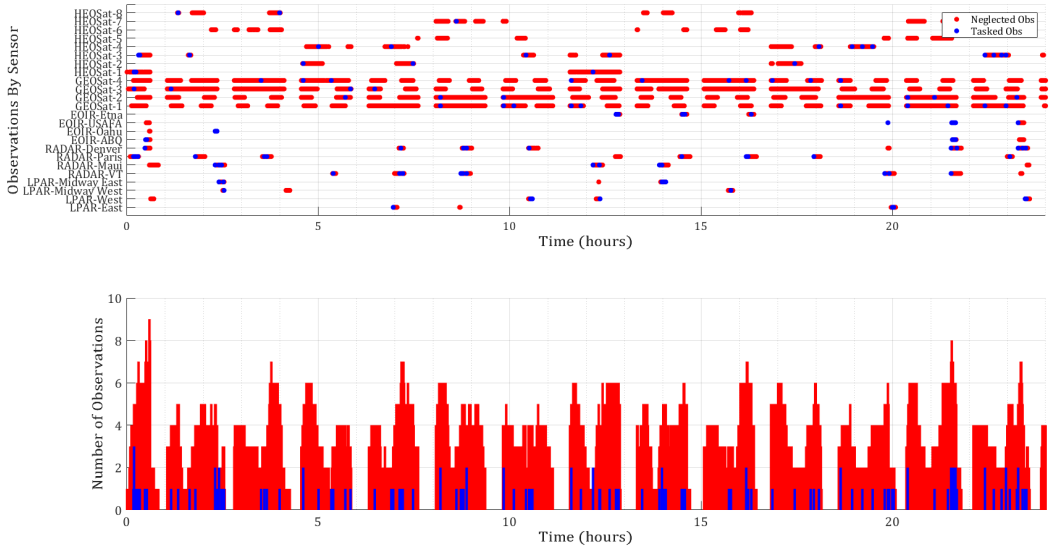

Figure 6.17: Nominal/FIG-Only LEOMnvr-2 Observations

An increased observation rate is particularly advantageous in the MEO regime, as evident in the nominal Continuous Observation POMDP's orbit estimate for MEOMnvr-1 in Figure 6.18. In this plot the filter takes approximately seven hours to converge on a viable orbit estimate after the maneuver, despite a long and nearly continuous sequence of observations from multiple sensors. Figure 6.19 shows that the majority of observations come from ground and space-based EOIR, though the LPAR senosors contribute a significant subset. The challenge with MEO is its extreme distance from most sensors. Indeed, some of the largest drops in error can be attributed to space-based sensors in HEO that were traversing the MEO regime when the observation was made.

Limiting the number of observations, as is the case with the nominal Constrained Observation POMDP, makes converging on a viable orbit estimate after a maneuver extremely difficult without adaptive estimation, particularly in GEO. Figure 6.20 shows GEOMnvr-1 conducting an unknown maneuver at 8.5 hours, and the nominal Constrained Observation POMDP never converging to a viable estimate within the scenario timespan. After the maneuver, only three observations are made before the scenario terminates. Without some form of adaptive estimation, the nominal Constrained Observation decision process has no way to rapidly increase the covariance to force the filter to accept new observations more heavily over the old estimate.

Additionally, as shown in Figure 6.21, the observations of GEOMnvr-2 after the maneuver

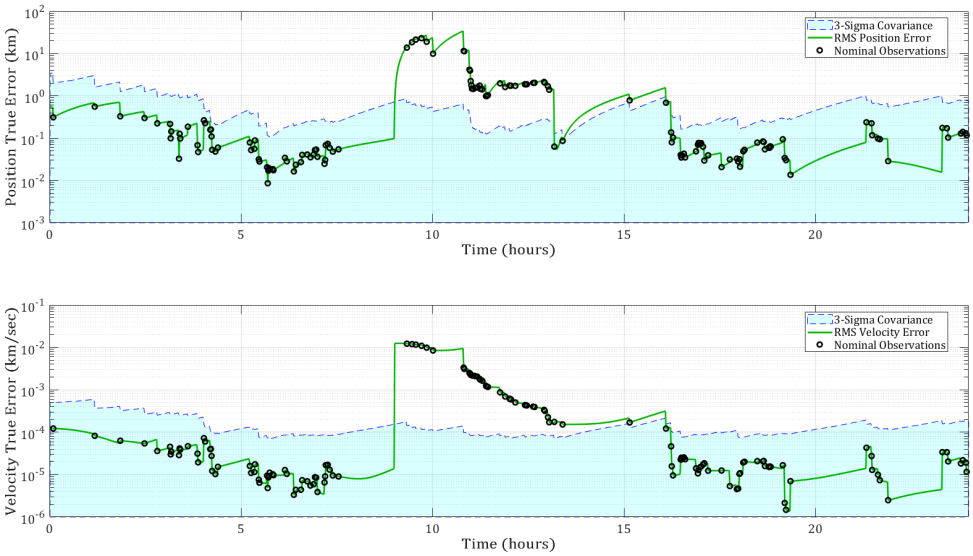

Figure 6.18: Nominal/Continuous MEOMnvr-1 Track

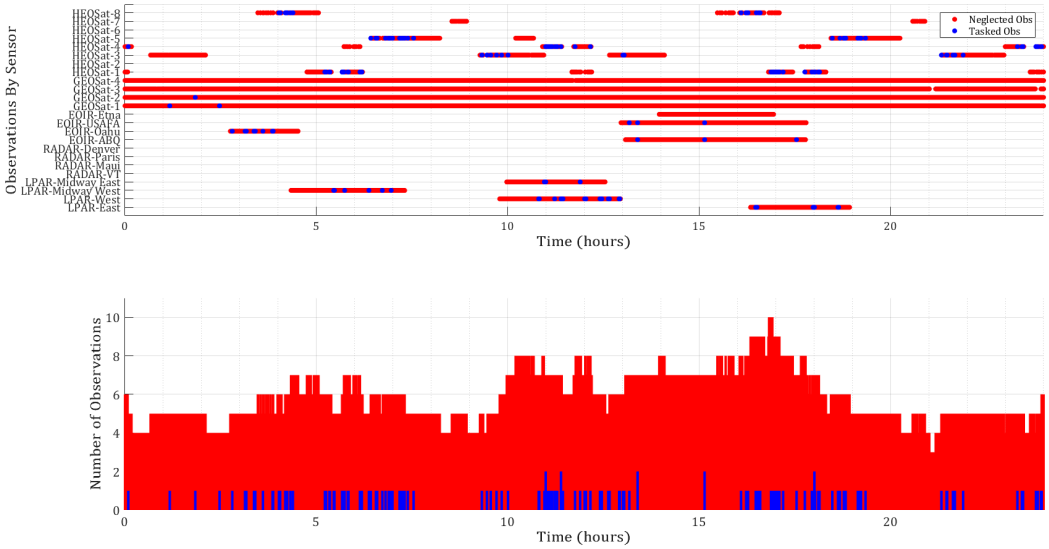

Figure 6.19: Nominal/Continuous MEOMnvr-1 Observations

are all from HEO-based EOIR sensors, which provide the least amount of information gain. Overall, without adaptive estimation to detect a maneuver and inflate the covariance accordingly, the Constrained Observation POMDP will not task additional sensors to observe the maneuvered spacecraft, or weigh new observations more heavily than the previous estimate.

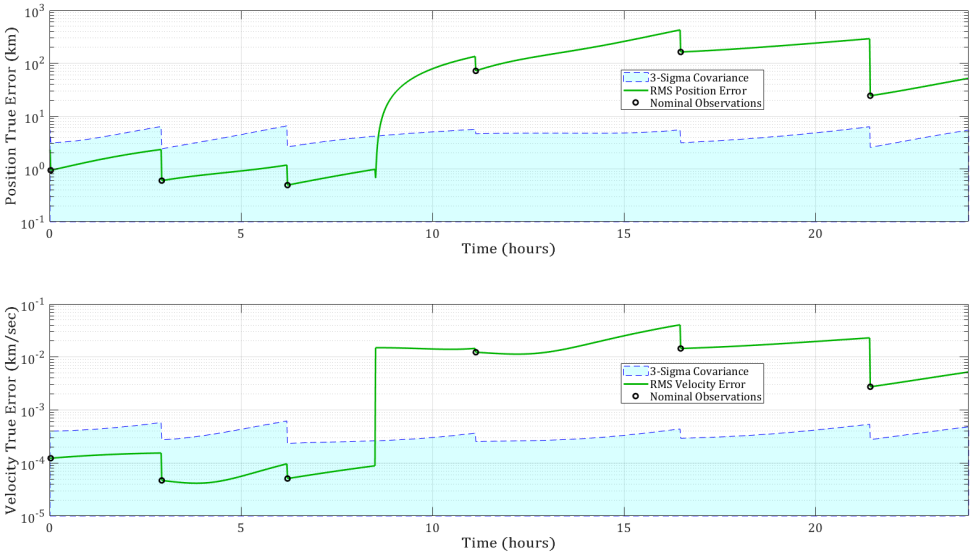

Figure 6.20: Nominal/Constrained GEOMnvr-1 Track

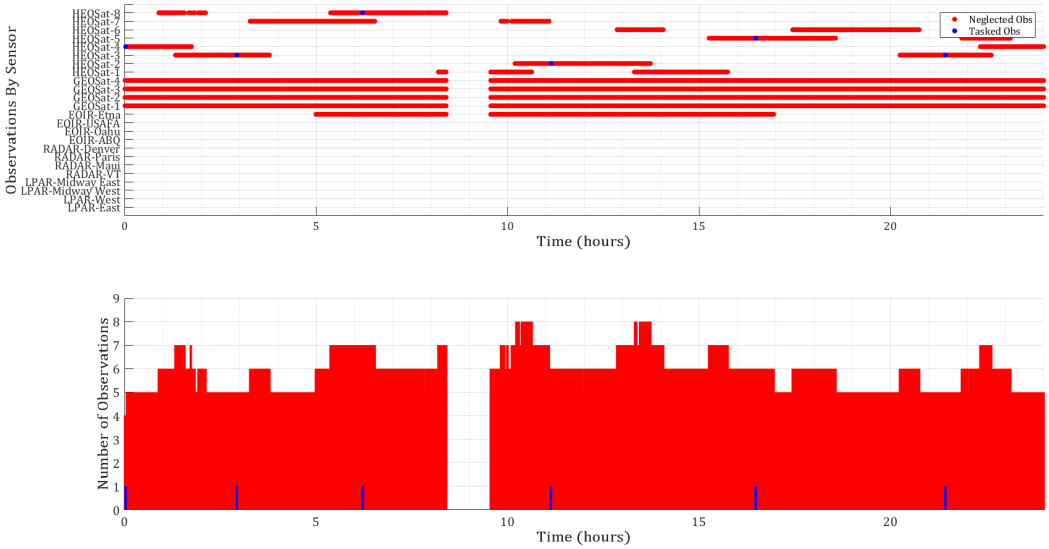

Figure 6.21: Nominal/Constrained GEOMnvr-1 Observations

It should be noted that the assertions made in this section are contingent upon the critical assumption that observations are always correlated to the correct target. After a maneuver, and with only a few widely dispersed observations, it may be difficult to correlate observations to an intended target. The ability to back-project the most likely maneuver is therefore a

key technical contribution that can substantially improve the correlation process.

6.4.2 Covariance Inflation & FIG-Only POMDP

For the baseline Covariance Inflation and FIG-Only tasking strategy, the average RMS errors for the individual non-maneuvering spacecraft are presented in Figure 6.22. The smallest

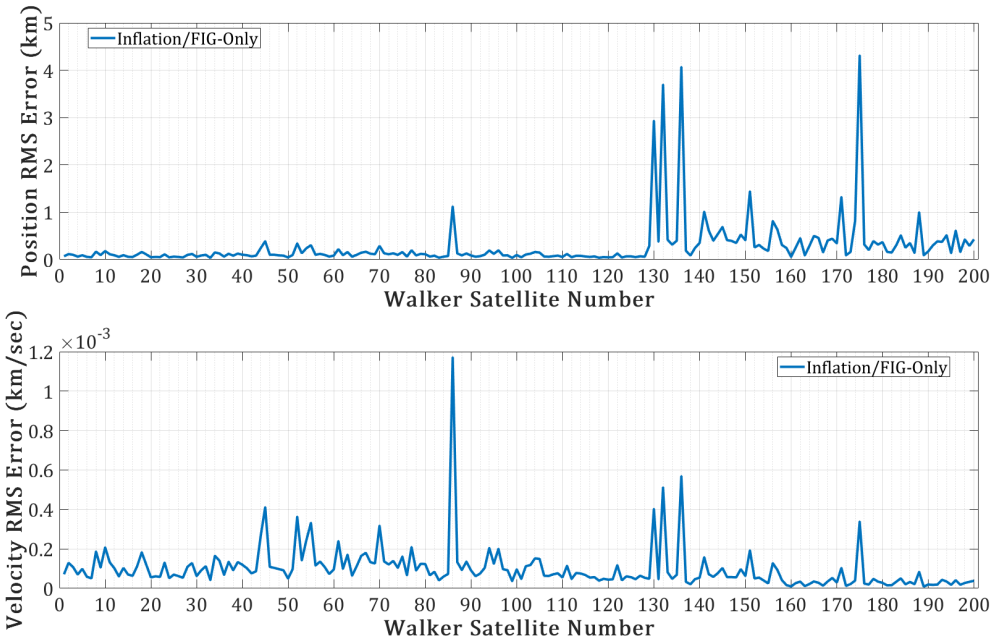

Figure 6.22: Inflation/FIG-Only: Average RMS Error Per Target

average RMS position error, at roughly 37m, belongs to Walker30 in LEO. The smallest average RMS velocity error, at $8.7e{-}6$km/s, is correlated with Walker189 in GEO. Several non-maneuvering satellites exhibit significantly higher average error, which is likely due to the particular set of visible sensors over the course of the scenario, as described in Section 6.2.

For the maneuvering spacecraft, most of the orbit estimate and observation plots are provided in Section C.4, but a few are provided here for discussion. Returning to LEOMnvr-2 in Figure 6.23, it's evident that the Covariance Inflation algorithm detects the maneuver with the first observation after the event. The yellow squares in Figure 6.23 represent the collected observations when the Covariance Inflation algorithm was operating. The covariance is then appropriately inflated as indicated by the rise in the three sigma covariance line to account for the observation. Compared to the orbit estimate plot in Figure 6.16, observations are dispersed more in the Covariance Inflation and FIG-Only POMDP after the maneuver and the error is reduced to within nominal levels after approximately three to four hours.

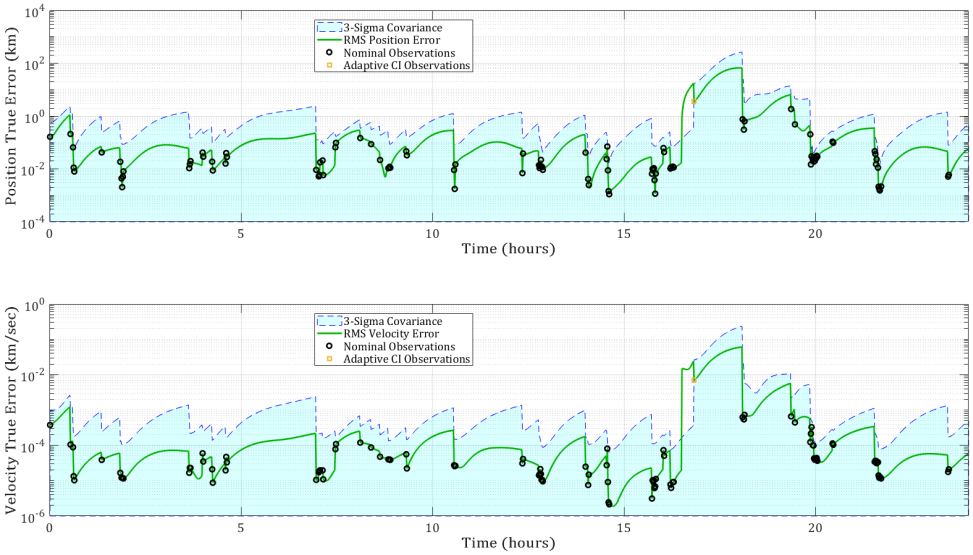

Figure 6.23: Inflation/FIG-Only LEOMnvr-2 Track

Figure 6.24 depicts the observations of LEOMnvr-2 that were taken (blue) or neglected (red), using the Covariance Inflation and FIG-Only tasking strategy. Even though the covariance

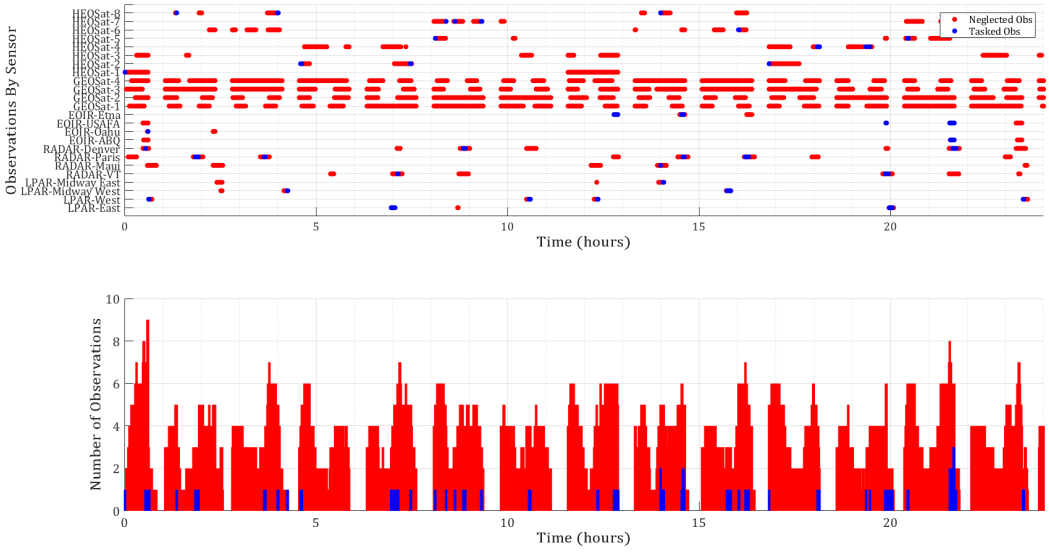

Figure 6.24: Inflation/FIG-Only LEOMnvr-2 Observations

was inflated substantially, the FIG-Only POMDP did not task additional sensors, compared

to the nominal approach.

The impact of the covariance inflation in the MEOMnvr-1 case is much more substantial, as shown in Figure 6.25. The maneuver is once again detected with the first nominally

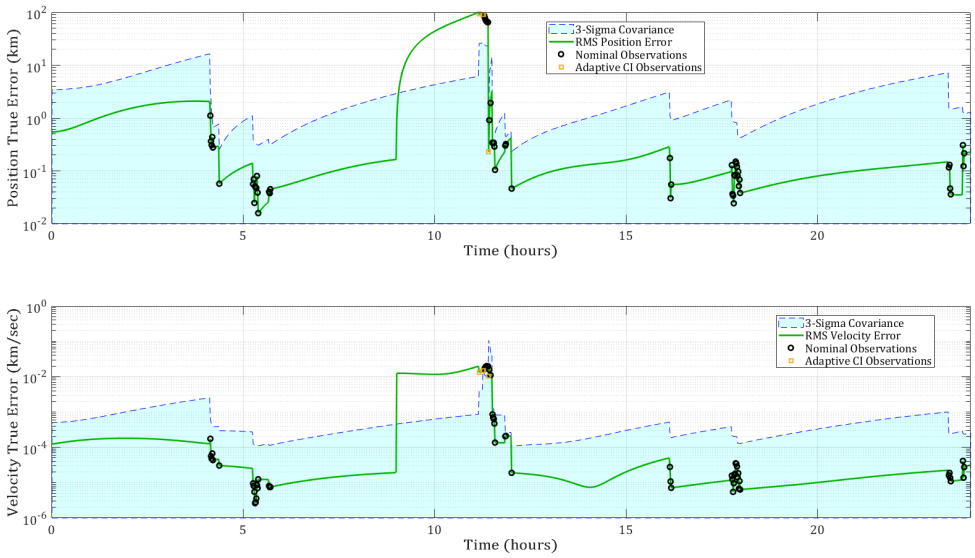

Figure 6.25: Inflation/FIG-Only MEOMnvr-1 Track

scheduled observation after the maneuver and the covariance is inflated accordingly. The resulting drop in error is almost immediate. Where as the nominal case in Figure C.5 required roughly seven hours after the maneuver detection to sufficiently converge, the Covariance Inflation case closed on a new accurate orbit estimate within an hour.

In Figure 6.26, the covariance inflation did not result in any discernible diversion of sensor resources to MEOMnvr-1. The tasking strategy continues to task one or two sensors, which is consistent with the tasking behavior observed before the maneuver. This would suggest that the Covariance Inflation and FIG-Only tasking strategy efficiently managed the covariance so that additional sensors were not required. Those sensors were therefore available to observe other spacecraft in the nominal catalog maintenance mission.

Lastly, the Covariance Inflation and FIG-Only strategy was assessed against GEOMnvr-1. Like the previous examples, this approach was able to detect the GEOMnvr-1 maneuver with the first observation and sufficiently inflate the covariance accommodate the increased error, as depicted in Figure 6.27. Interestingly, the inflation did not necessarily help reduce the error any faster than the nominal case did (Figure C.9). It took roughly five hours for both tasking strategies to effectively reduce the error below the nominal three sigma covariance line.

Like the previous examples, the observation plot in Figure 6.28 indicates that the covariance

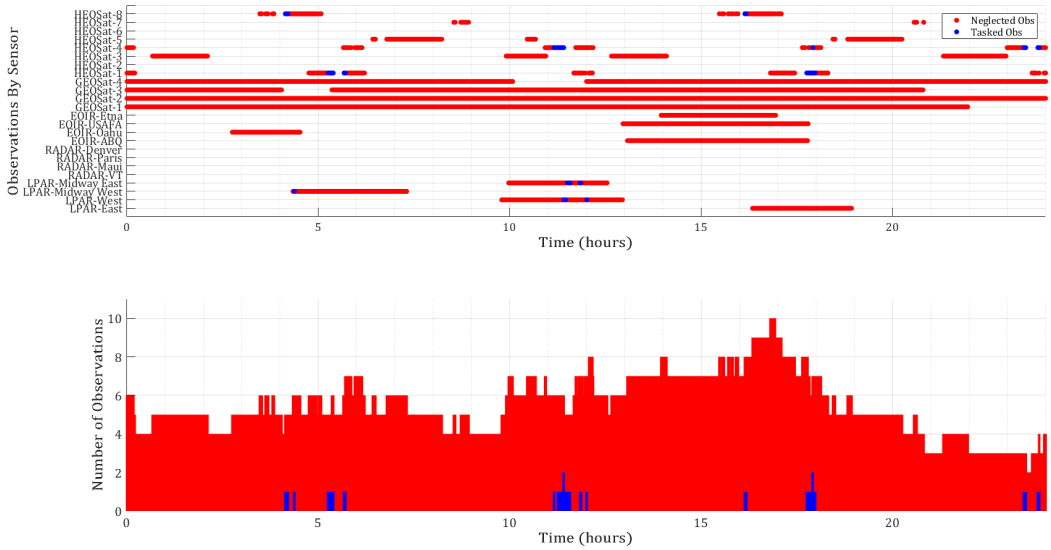

Figure 6.26: Inflation/FIG-Only MEOMnvr-1 Observations

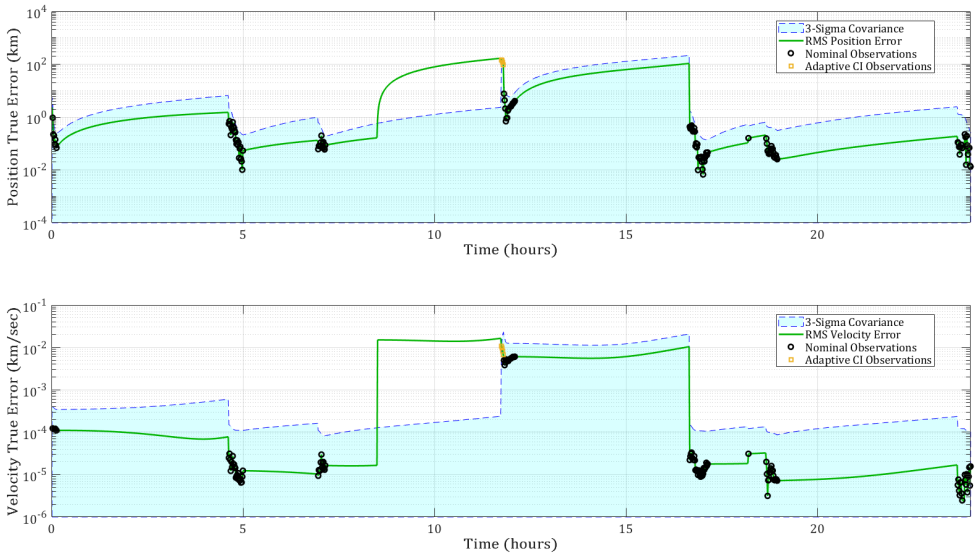

Figure 6.27: Inflation/FIG-Only GEOMnvr-1 Track

inflation was not substantial enough to divert additional sensors after the maneuver. The sensors that were tasked were all HEO sensors with EOIR sensors, which would help explain why the observations after the maneuver did not rapidly reduce the error. The HEOsensors only provide angles-only information from a potentially substantial range, thus significant

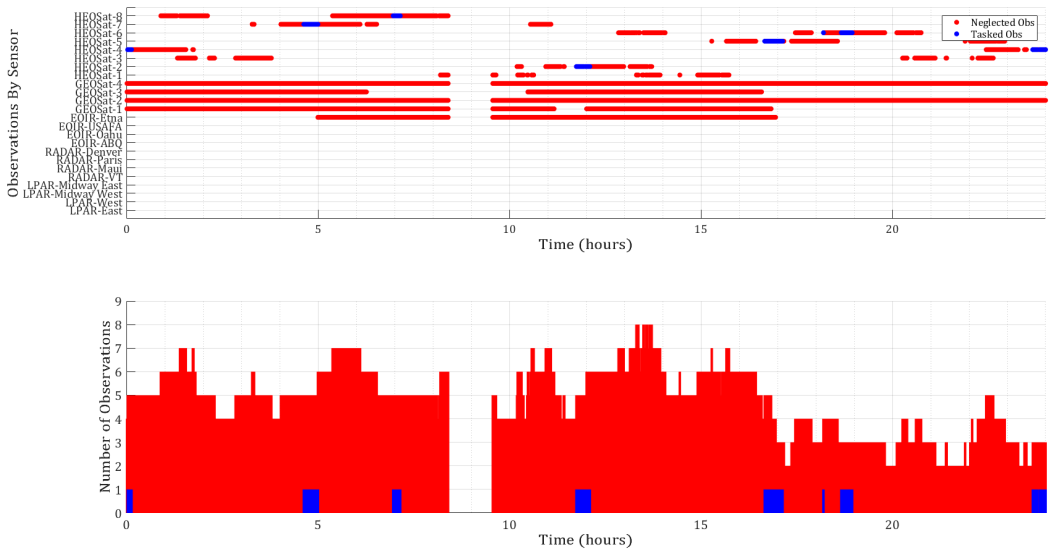

Figure 6.28: Inflation/FIG-Only GEOMnvr-1 Observations

limiting the amount of information collected.

Overall, the Covariance Inflation and FIG-Only POMDP tasking strategy was effective at detecting and tracking through unknown maneuvers. The scalar inflation was not substantial enough to divert additional sensors from other potential targets, yet it was significant enough to improve the filter's ability to rapidly converge on a viable orbit estimate after the maneuver.

6.4.3 Shotgun SMM & Continuous Observation POMDP

For the Shotgun SMM and Continuous Observation POMDP tasking strategy, the average RMS error for the 200 non-maneuvering spacecraft is depicted in Figure 6.29. With this

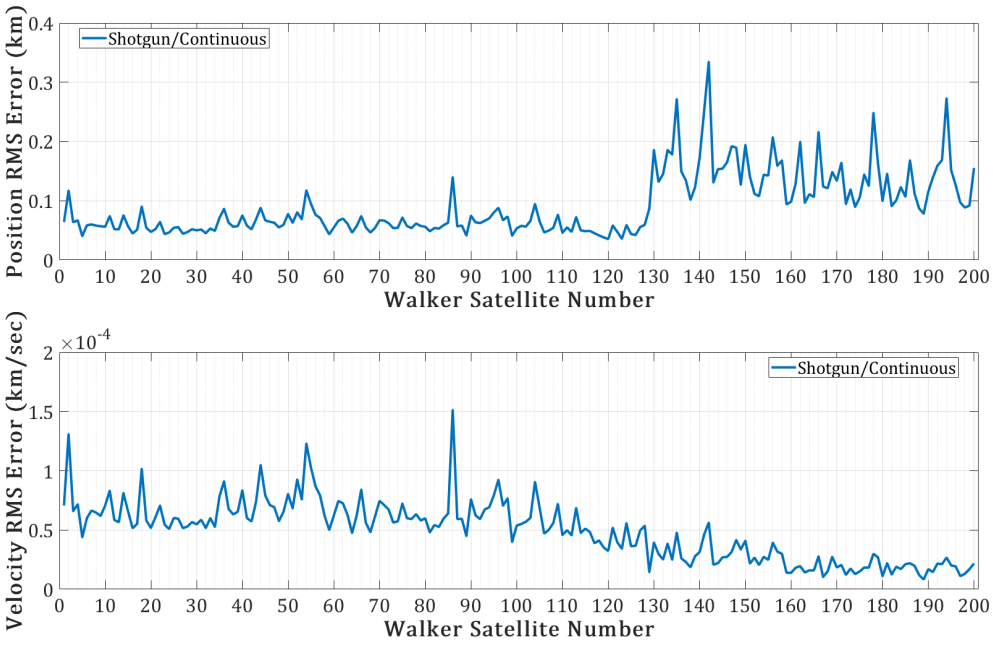

Figure 6.29: Shotgun SMM/Continuous: Percent RMS Error Per Target

approach, the higher altitude satellites incur a higher error than their LEO counterparts, but the estimates are still very accurate. There is also less variability in the RMS error from one target to the next compared to the baseline approach in Figure 6.22. In this scenario the smallest average RMS position error belongs to Walker120 in the 1,500km LEO constellation. The smallest average RMS velocity error is correlated with Walker189 in GEO.

Once again, LEOMnvr-2, MEOMnvr-1, and GEOMnvr-1 are described here, while the remaining maneuvering satellite information is provided in Appendix Section C.5. In the LEOMnvr-2 case, the Shotgun SMM detected the maneuver with the first observation and created a executed the Static Multiple Model described in Section 4.5. As depicted in Figure 6.30, the SMM is executed for four observations and rapidly converges on a viable orbit estimate within an hour.

Though the resulting covariance inflation is not apparent in the plot, it did have a significant impact on how the Continuous Observation POMDP tasked sensors. In Figure 6.30 a series of nearly continuous observations is visible after the Shotgun SMM is terminated. The observation plot in Figure 6.31 shows that after the initial observation that detected the maneuver, all visible sensors were tasked to observe LEOMnvr-2 for one or two time steps.

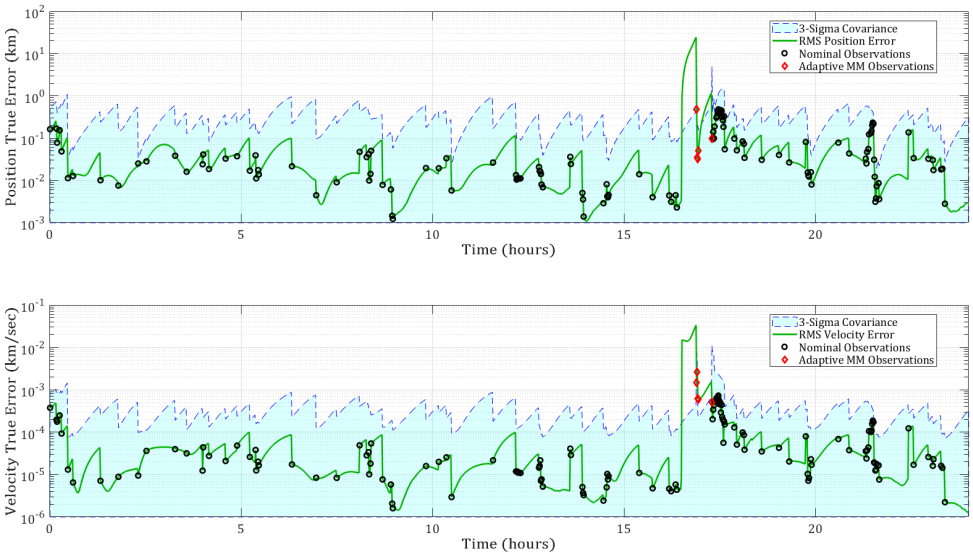

Figure 6.30: Shotgun SMM/Continuous LEOMnvr-2 Track

Red in Figure 6.31 denotes neglected observations, whereas blue denotes tasks observations. After the maneuver, the number of blue observations is equal to the number of red observations, indicating that all possible observations are collected for one or two time steps. Several

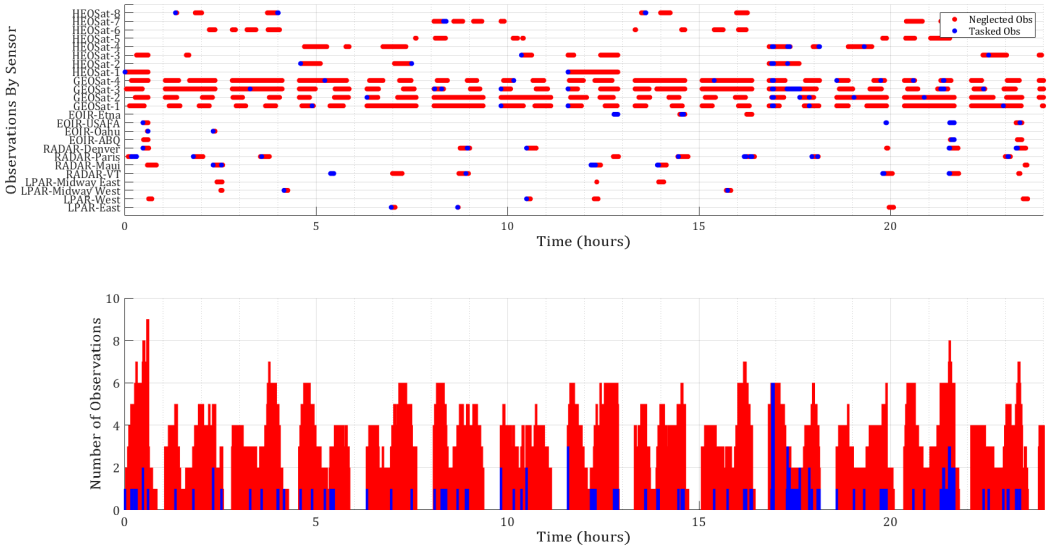

Figure 6.31: Shotgun SMM/Continuous LEOMnvr-2 Observations

instances of simultaneous observations were required in subsequent time steps. This sensor herding behavior is not evident in the previous Covariance Inflation and FIG-Only strategy. While it might not be optimal, the speed at which the filter associated with LEOMnvr-2 is able to converge on a new orbit estimate is substantial.

A similar situation is observed with MEOMnvr-1. In Figure 6.32, the orbit estimate plot shows that the maneuver was once again detected with the first observation, and that the Shotgun SMM was implemented for a total of four sequential time steps. The filter converges on a viable orbit estimate within a few observations. Like in the LEOMnvr-2 case, the

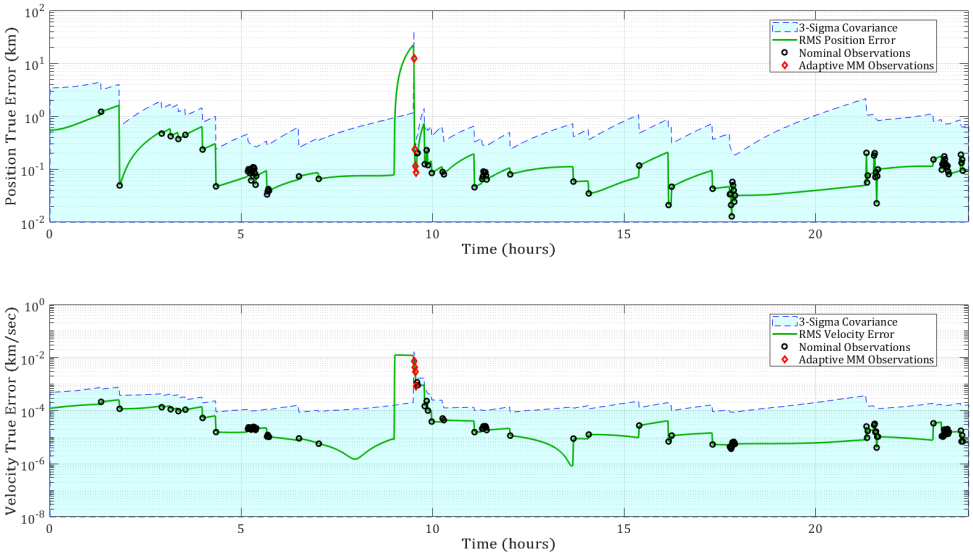

Figure 6.32: Shotgun SMM/Continuous MEOMnvr-1 Track

Shotgun SMM forces the Continuous Observation POMDP to task all of the visible sensors for a time step or two, resulting in a substantial influx of new information. After this initial sensor herding, however, no additional simultaneous observations are tasked for the remained of the scenario.

In the GEOMnvr-1 case, the Shotgun SMM and Continuous Observation approach are able to detect the maneuver and rapidly converge on a new orbit estimate, despite the extended observation gap after the maneuver occurred. As depicted in Figure 6.34, the Shotgun SMM is used during four observations before it is terminated, after which a long series of successive observations are collected using the nominal filter .

Figure 6.35 shows that once again all visible sensors are tasked for a time step or two after the initial observation. The blue (number of tasked observations) line in the lower panel of Figure 6.35 completely overlays the red (number of neglected observations), thus indicating that all possible observations are collected during those time steps. The large influx of new

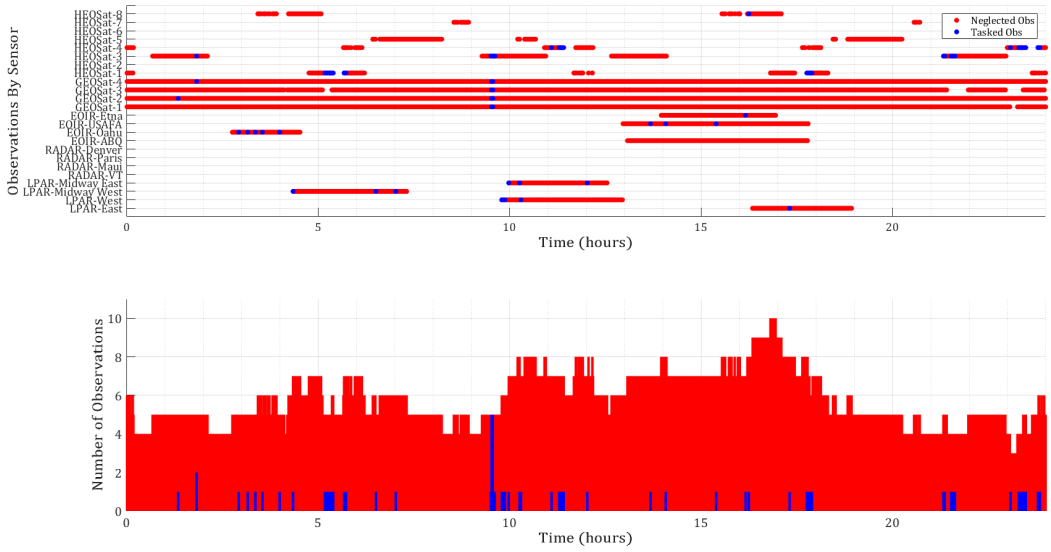

Figure 6.33: Shotgun SMM/Continuous MEOMnvr-1 Observations

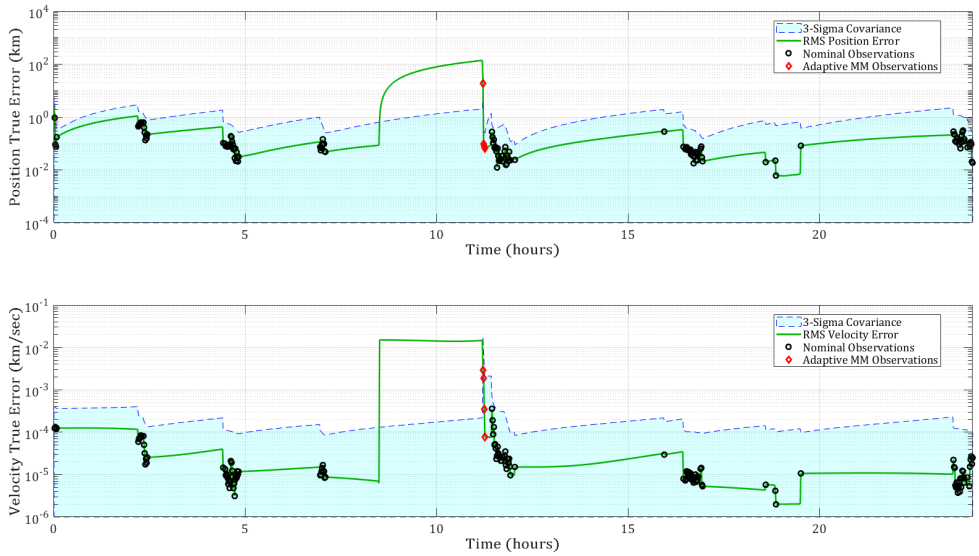

Figure 6.34: Shotgun SMM/Continuous GEOMnvr-1 Track

information aids in the rapid convergence to a viable estimate. The subsequent long series of observations is conducted by a single HEO sensor. These additional observations help reduce the error to pre-maneuver magnitudes.

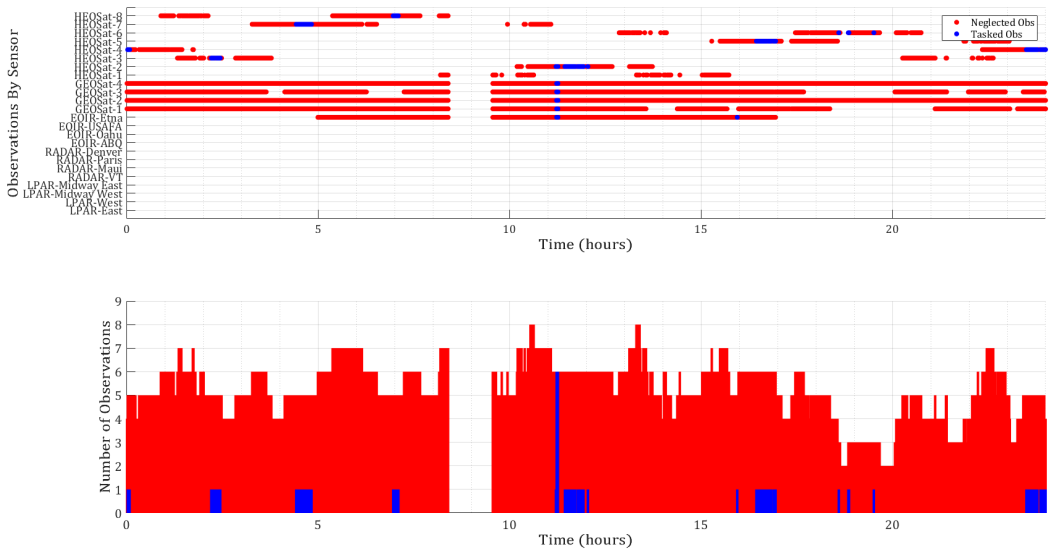

Figure 6.35: Shotgun SMM/Continuous GEOMnvr-1 Observations

Overall, the Shotgun SMM and Continuous Observation POMDP tasking strategy was very effective at rapidly reacquiring a viable orbit estimate after an unknown maneuver. In additional to the benefits incurred with the SMM approach, this strategy was so responsive because a large number of sensors were tasked to observe the targets immediately following maneuver detection. This sensor herding behavior, however, was short lived in all cases.

6.4.4 Lambert SMM & Constrained Observation POMDP

For the Lambert SMM and Constrained Observation POMDP tasking strategy the average RMS error for the 200 non-maneuvering spacecraft is presented in Figure 6.36. The error

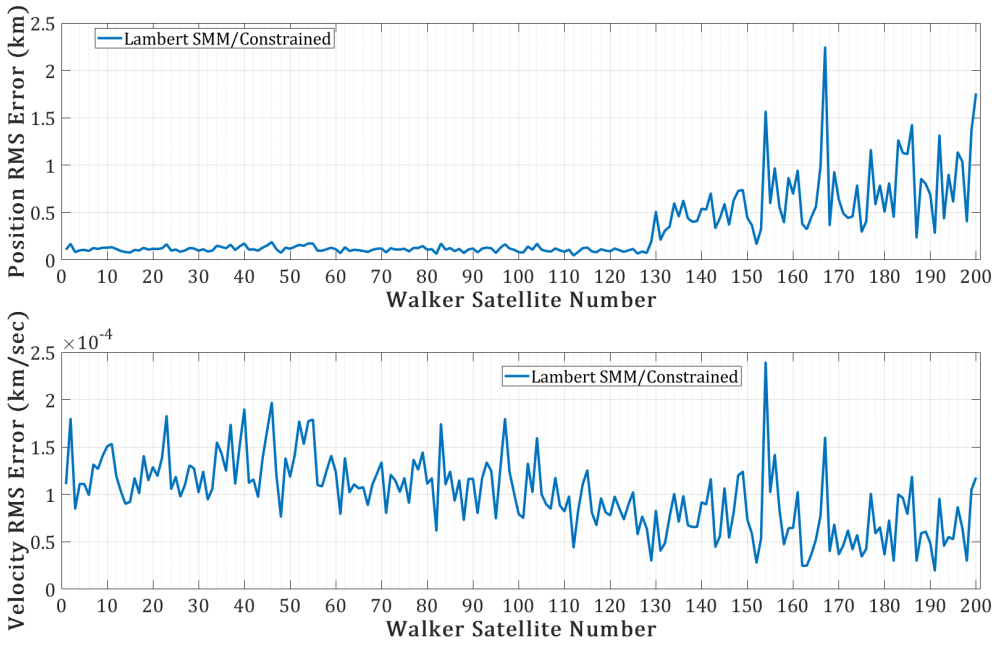

Figure 6.36: Lambert SMM/Constrained: Average RMS Error Per Target

associated with LEO target estimates for this tasking strategy is comparable to that seen in the previous command and control algorithms. For the MEO and GEO regimes, many of the target estimates have considerably higher position error, though the RMS velocity errors are similarly reduced. The smallest position RMS error of almost 48m belongs to Walker112, and the smallest RMS velocity error of almost $2e{-}5$km/s belongs to Walker191.

The Lambert SMM and Constrained Observation POMDP tasking strategy is the first of the four presented sensor management algorithms that significantly reduces the number of observations that are tasked over the course of the scenario. As demonstrated in Section 6.4.1, limiting the number of observations significantly and detrimentally impacts the nominal tasking strategy's ability to track through an unknown maneuver. Therefore, the inclusion of effective and efficient adaptive estimation can significantly improve a Constrained Observation POMDP's ability to manage multiple sensors in a dynamic environment. The first example is the LEOMnvr-2 spacecraft, which performs a maneuver at $t = 16.5$ hours. The orbit estimate plot in Figure 6.37 shows that the Lambert SMM is used during nine observations before the nominal UKF is reinitialized. The Lambert SMM continues to run even after the estimate falls back below the three sigma covariance line, because the Lambert SMM is

forced to execute for at least three observations. The nominal UKF was likely reinitialized when the error first fell below the three sigma line. As evidenced by the rapid regrowth in error above the three sigma covariance line, another Lambert SMM was likely initialized at the next observation and executed for another four observations due the minimum of three observation constraint placed on the adaptive estimation process. The nominal Constrained Observation algorithm in Figure C.27 failed to converge on a viable orbit estimate before the end of the scenario for LEOMnvr-2. The Lambert SMM required roughly five hours to reacquire an appropriate estimate.

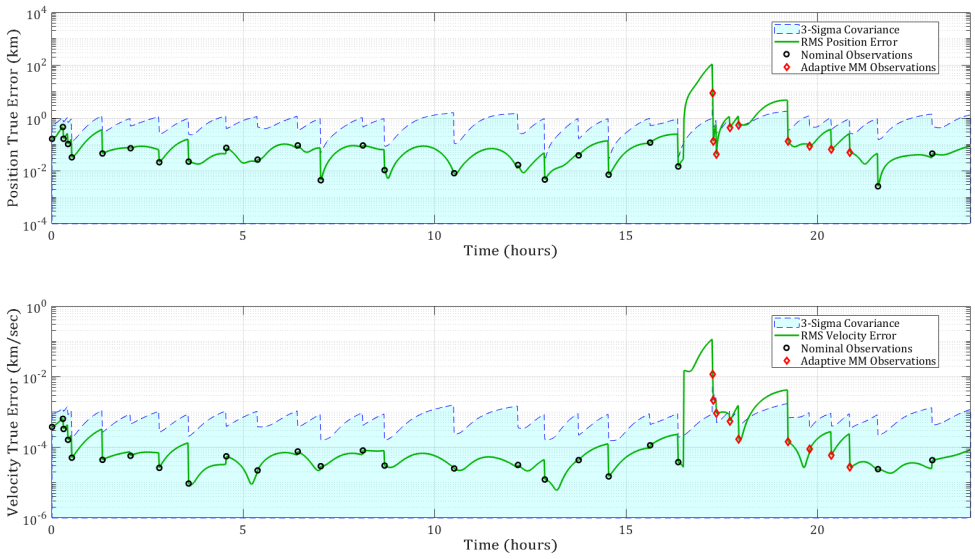

Figure 6.37: Lambert SMM/Constrained LEOMnvr-2 Track

Figure 6.38 depicts the small fraction of total observations that were tasked compared to the total number of available observations. Like in the Shotgun SMM case, the Lambert SMM forced the Constrained Observation POMDP to task all of the available sensors for several time steps after the maneuver was detected. This behavior was only required for two or three observations, and only one or two sensors participated in future Lambert SMM observations.

In the MEOMnvr-1 case, sensor herding is witnessed more often than in previous examples, though the number of observed time steps remains small due to the Constrained Observation POMDP. The maneuver is detected shortly after execution and the Lambert SMM is executed for five time steps spread over approximately eleven hours. The SMM fails to reach a convergence criterion before the end of the scenario, but the position and velocity errors by $t = 17$ hours are of similar magnitude to those before the maneuver.

Figure 6.40 shows that significant sensor herding behavior was present in three of the five time

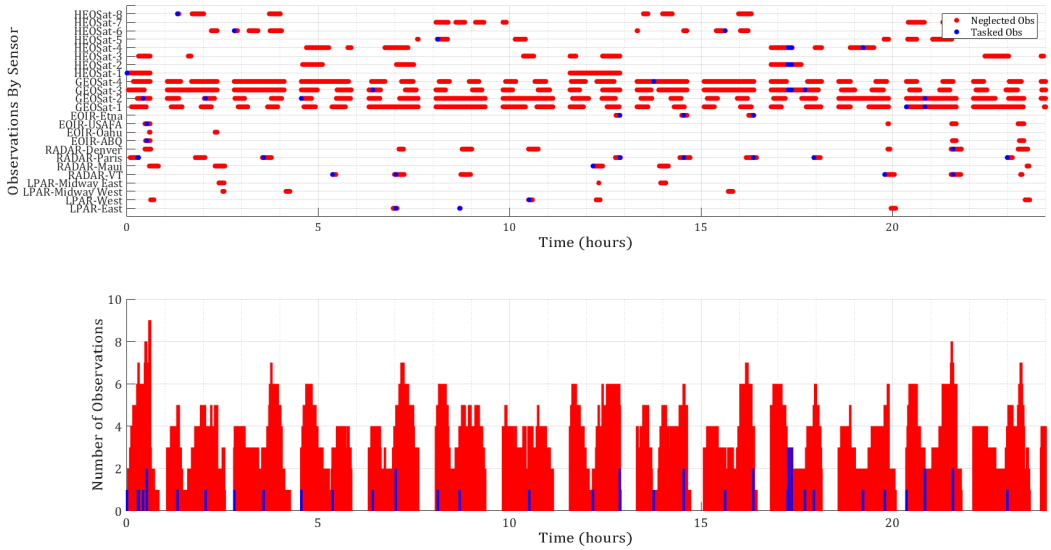

Figure 6.38: Lambert SMM/Constrained LEOMnvr-2 Observations

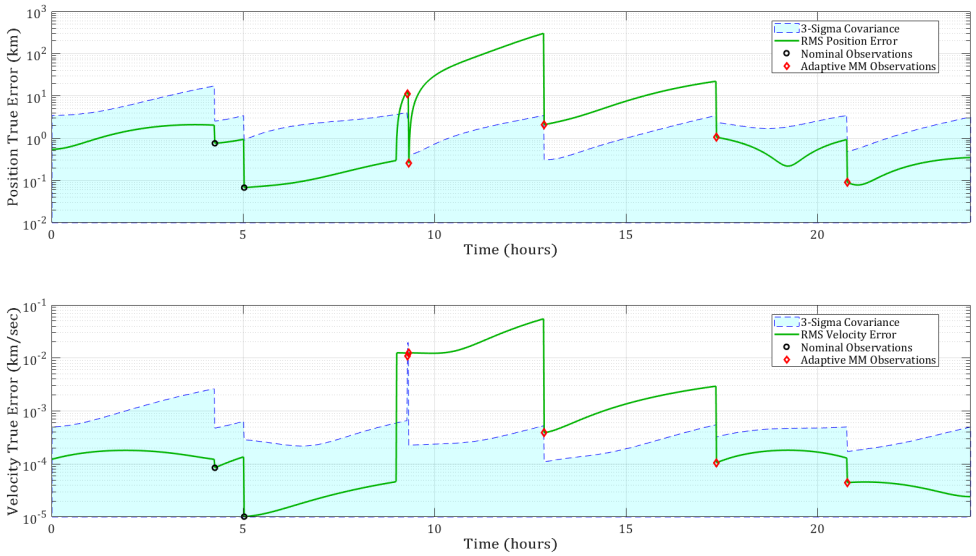

Figure 6.39: Lambert SMM/Constrained MEOMnvr-1 Track

steps where the Lambert SMM was used. The Constrained Observation POMDP repeatedly tasks simultaneous observations during these time steps to reduce the uncertainty. Once the estimate reaches a prescribed convergence criterion, the nominal filter is reinitialized. It should also be noted that the majority of the sensors participating in the simultaneous obser-

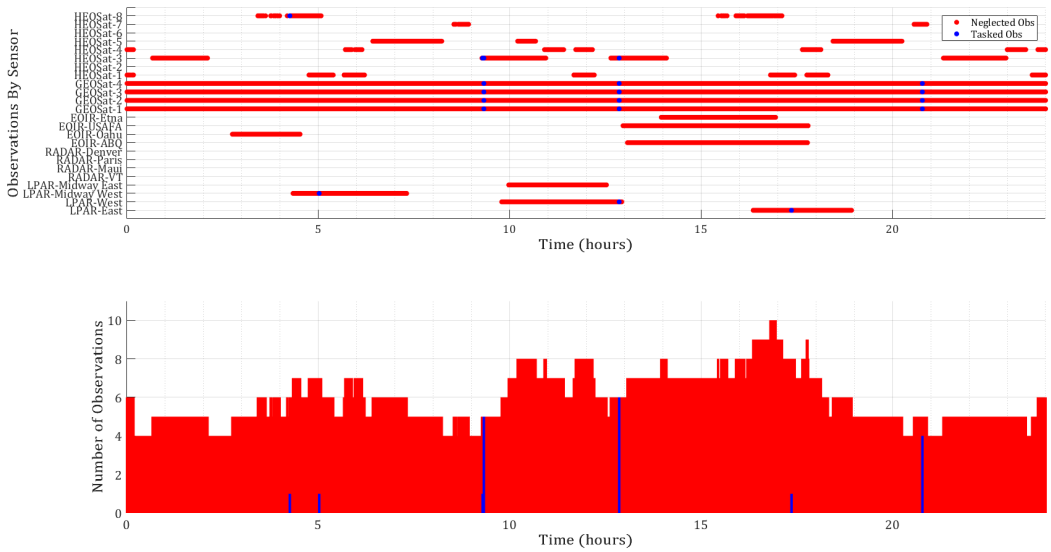

Figure 6.40: Lambert SMM/Constrained MEOMnvr-1 Observations

vations are the space-based EOIR sensors that provide only a limited amount of information with each observation.

The Lambert SMM and Constrained Observation tasking strategy was more effective at tracking through the unknown GEOMnvr-1 maneuver, though significant sensor herding was also present in this case for several observation time steps. Figure 6.41 shows how the Lambert SMM was required for four time steps before the convergence criteria were reached. The initial reduction in error is rapid, with RMS position and velocity error reducing to pre-maneuver magnitudes, or lower, within an hour.

Figure 6.42 depicts the multiple simultaneous observations following the maneuver detection. Once again, the combination of the Lambert SMM and the Constrained Observation POMDP resulted in significant sensor herding during the time steps when adaptive estimation was being applied.

Overall, the Lambert SMM and Constrained Observation POMDP is a responsive and efficient tasking strategy, but it did suffer from significant sensor herding while the SMM was being implemented. This behavior is likely a signficant contributor to the increased average RMS error depicted at higher altitudes in Figure 6.15. If more sensors were being tasked to observed maneuvering spacecraft, then fewer sensors were available to keep track of the larger non-maneuvering satellite population.

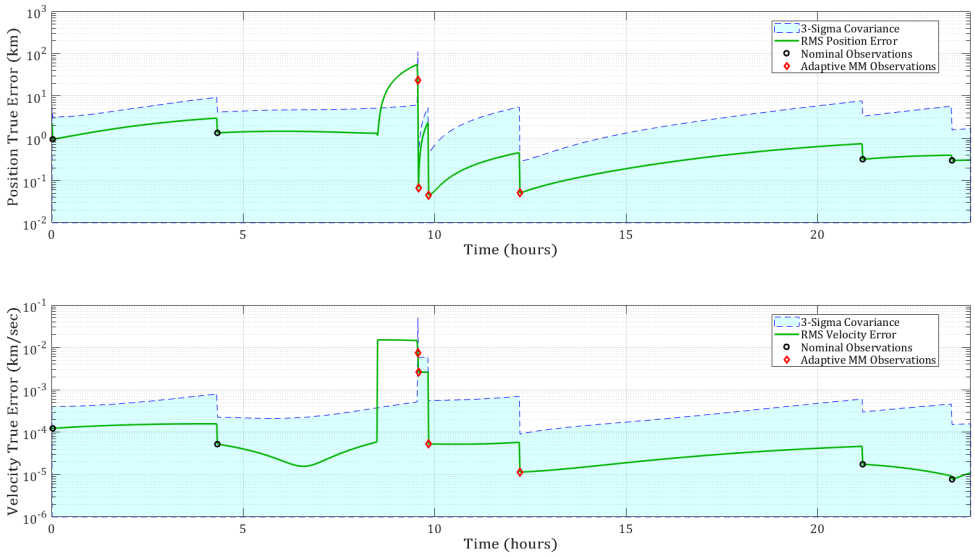

Figure 6.41: Lambert SMM/Constrained GEOMnvr-1 Track

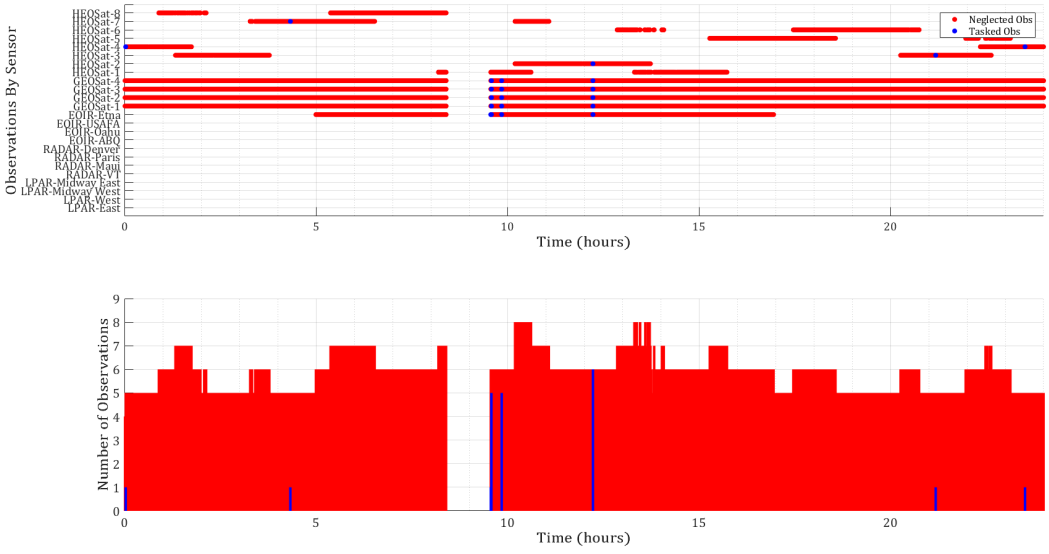

Figure 6.42: Lambert SMM/Constrained GEOMnvr-1 Observations

6.4.5 Lambert GPB1 Constrained Observation POMDP

For the Lambert GPB1 and Constrained Observation POMDP tasking strategy the average RMS error for the 200 non-maneuvering spacecraft is presented in Figure 6.43. The average

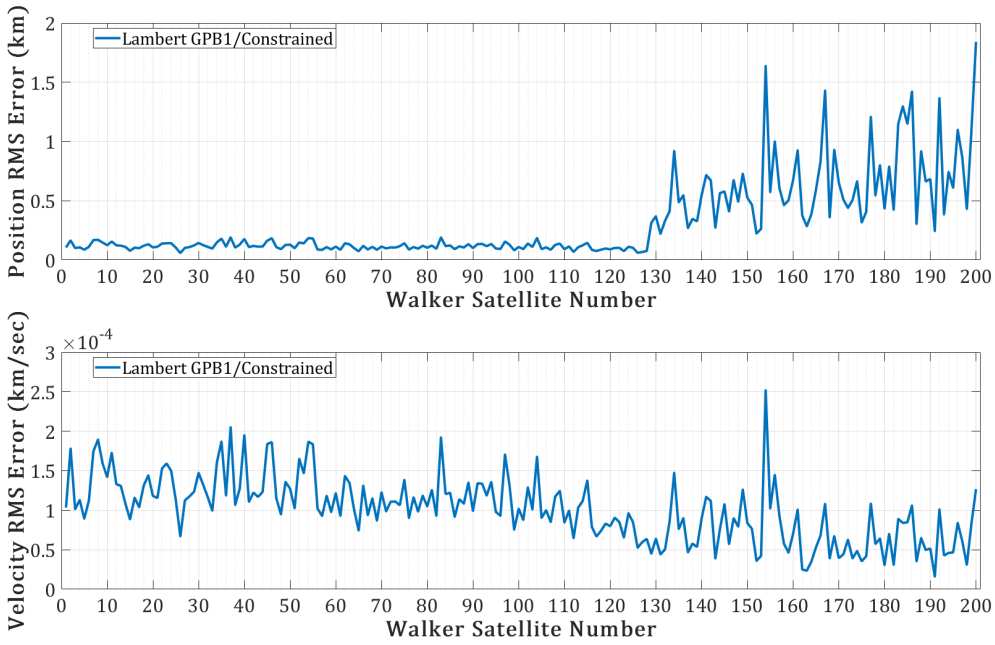

Figure 6.43: Lambert GPB1/Constrained: Average RMS Error Per Target

RMS error for the non-maneuvering spacecraft incurred with this tasking strategy is similar to the those presented for the previous approaches. While the error is notably larger for the higher altitude MEO and GEO satellites, the orbit estimates are still very accurate. Once more the smallest average RMS position error of 59m is associated with a satellite in the 1,500km LEO constellation, Walker126 in this case. The smallest average RMS velocity error of $1.58e{-}6$km/s is associated with Walker191, in GEO.

As discussed in Section 6.3, the Lambert GPB1 is rarely executed for more than one time step, even with the Constrained Observation POMDP. In the full scale test, the combination of the Lambert GPB1 and the Constrained Observation POMDP resulted in an interesting interaction between adaptive and nominal estimation, as shown in Figure 6.44. In the LEOMnvr-2 case, the Lambert GPB1 process was used only once for the first observation after the satellite maneuver. The resulting covariance inflation caused more frequent observations of LEOMnvr-2 using the nominal filter. Once the covariance was reduced to pre-maneuver levels, the Constrained Observation POMDP returned to a more normal observation frequency.

Additionally, sensor herding was far less prevalent with the Lambert GPB1 and the Con-

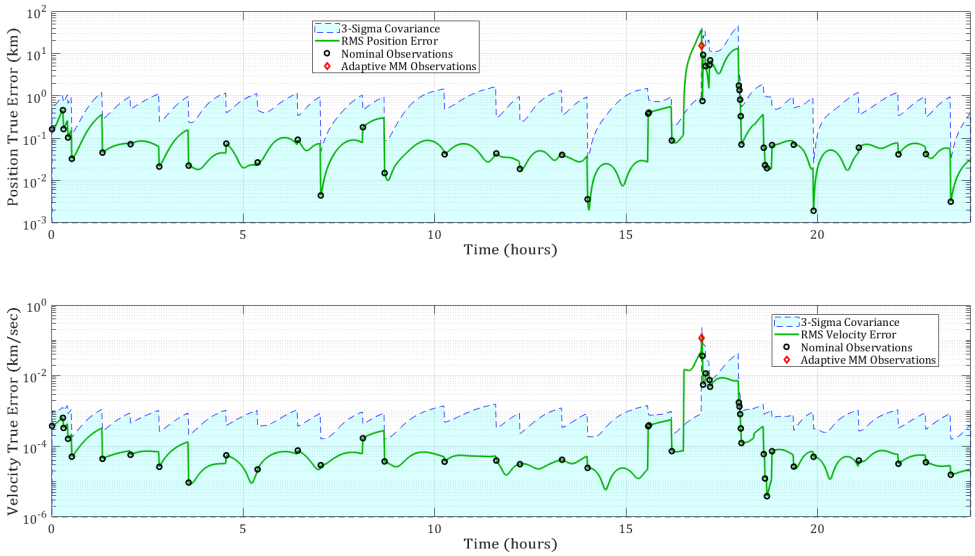

Figure 6.44: Lambert GPB1/Constrained LEOMnvr-2 Track

strained Observation tasking strategy, as is evident in Figure 6.45. Simultaneous observations

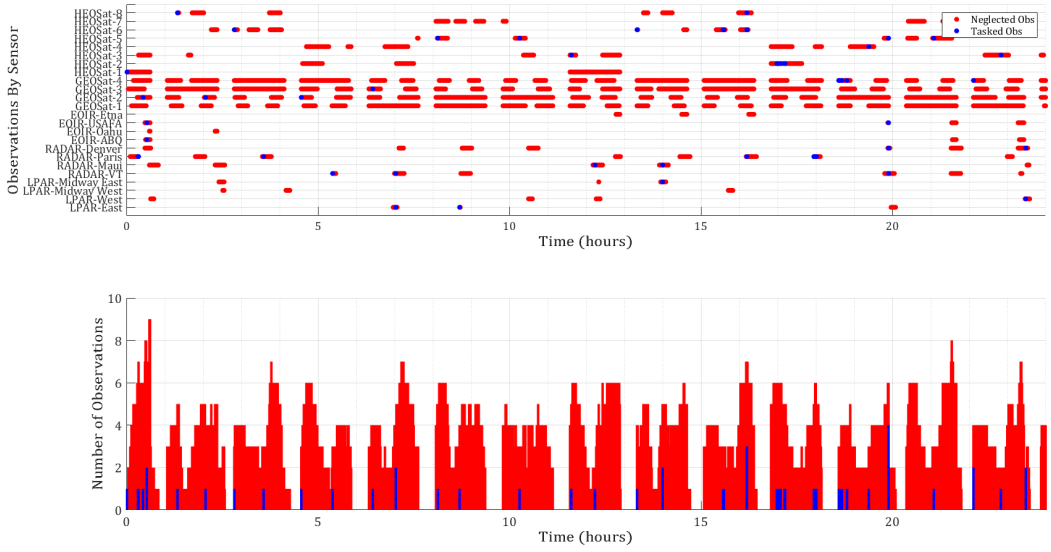

Figure 6.45: Lambert GPB1/Constrained LEOMnvr-2 Observations

after the maneuver are indeed present, but only a subset of the available sensors are tasked during these times. In the LEOMnvr-2 case, several series of sequential observations are

made with a single sensor. The overall strategy is still considerably responsive, converging to a viable orbit estimate within two hours. The key distinction is that the Lambert SMM and the Constrained Observation POMDP use a combination of adaptive and nominal estimation to accomplish the task, which is not generally evident in the other approaches.

In the MEOMnvr-1 case, the Lambert GPB1 algorithm was called three time, though not consecutively. Depicted in Figure 6.46, the GPB1 method is implemented for one time step as soon as the maneuver is detected. A series of consecutive observations are made with the

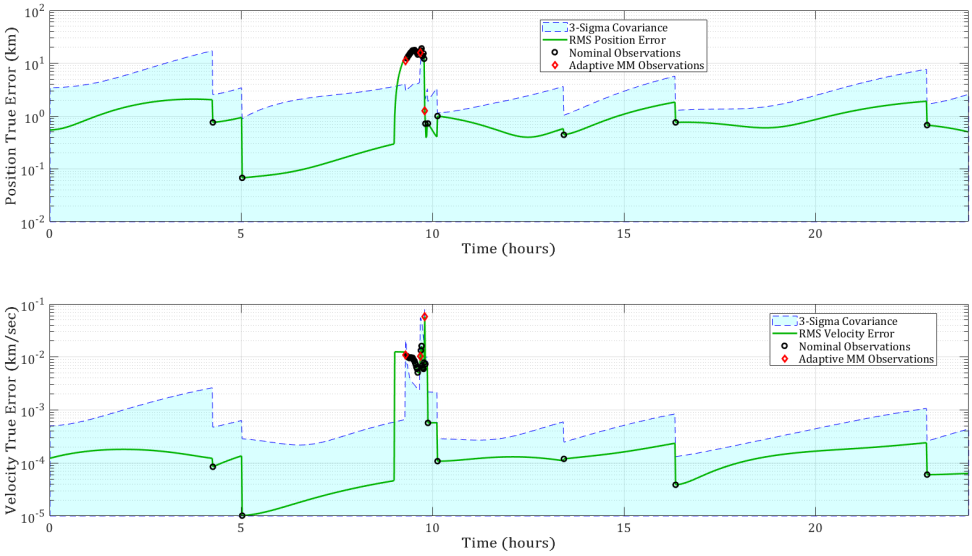

Figure 6.46: Lambert GPB1/Constrained MEOMnvr-1 Track

nominal filter, however, before the Lambert GPB1 algorithm is called again. Finally, a third and separate call to the adaptive estimation is made to reduce the error and covariance to pre-maneuver magnitudes.

Once again, the tasking strategy only uses a long series of single sensor observation, and several two sensor observations, to converge on a viable estimate, rather than the significant sensor herding approach used in the previous SMM methods. As shown in Figure 6.47, the majority of the observations are provided by a HEO spacecraft, followed by several simultaneous observations by the highly capable LPAR sensors. It is particularly noticeable in the MEOMnvr-1 case how few the number of tasked observations are compared to number of neglected observations.

The GEOMnvr-1 example provides perhaps the best instance of the unique interaction between the estimation and POMDP algorithms in the Lambert GPB1 and Constrained Observation tasking strategy. In Figure 6.48, the maneuver is detected once more with the first observation after the maneuver, and the Lambert GPB1 is executed for a single time

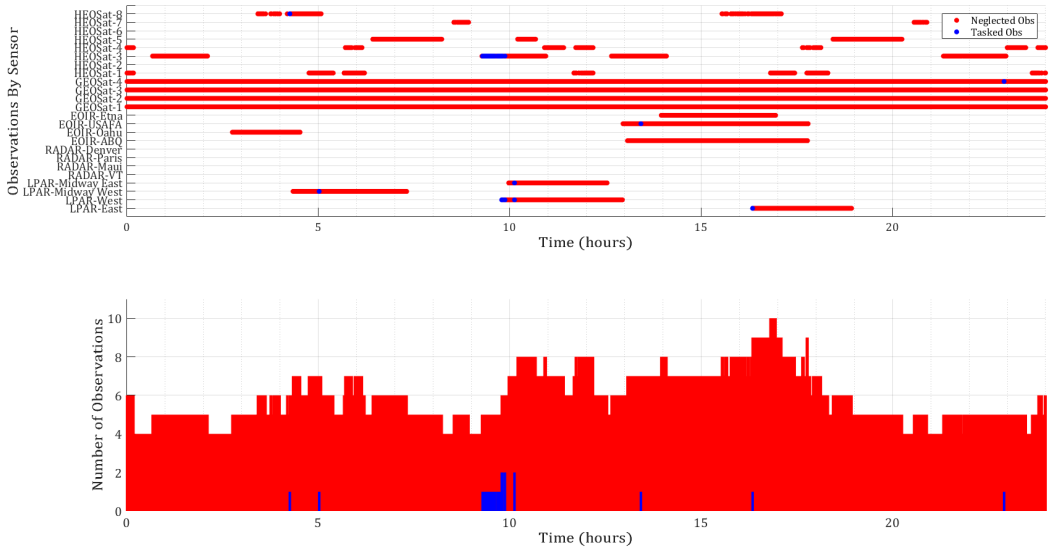

Figure 6.47: Lambert GPB1/Constrained MEOMnvr-1 Observations

step. What follows is a particularly long series of consecutive observations from one of the

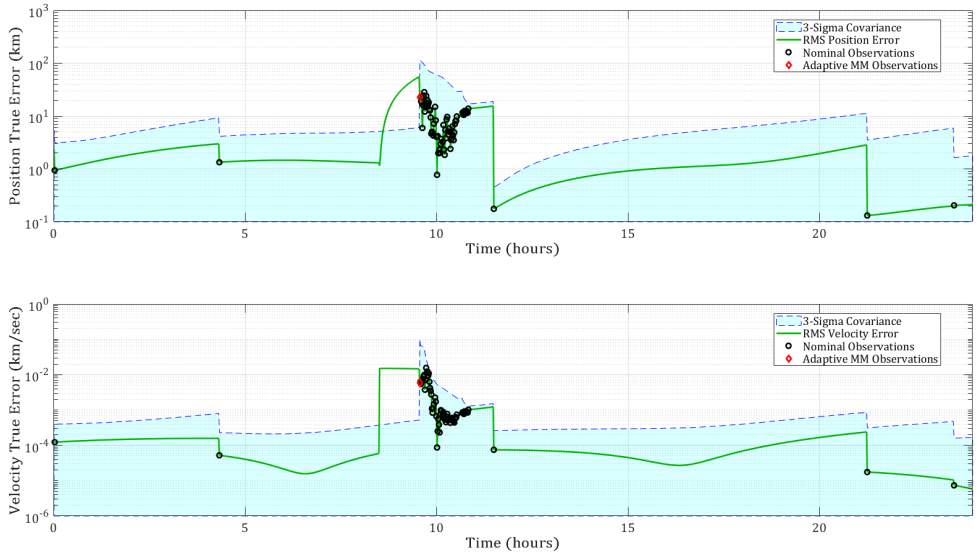

Figure 6.48: Lambert GPB1/Constrained GEOMnvr-1 Track

terrestrial EOIR sensors using only the nominal filter. As depicted in Figure 6.49, at no time are simultaneous observations made, even though the potential certainly exists. In

the previous approaches multiple sensors were indeed tasked to track GEOMnvr-1 after the maneuver was detected. The Lambert GPB1 and Constrained observation tasking strategy, however, consistently limits the number of tasked observations at any given time step to a single sensor, but tasks more observations over time immediately following a maneuver. After approximately two hours, the Constrained Observation POMDP returns to a normal

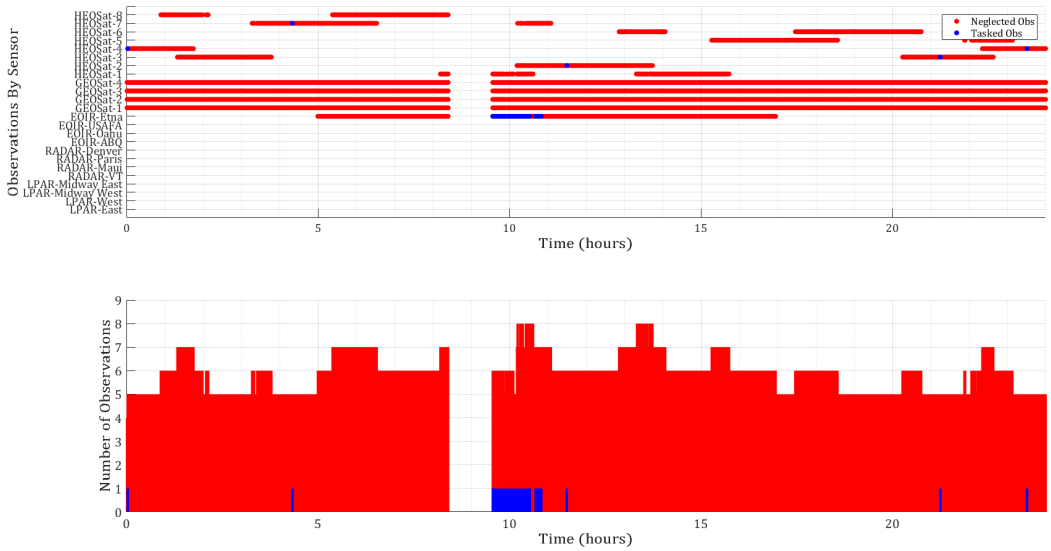

Figure 6.49: Lambert GPB1/Constrained GEOMnvr-1 Observations

observation frequency with a new orbit estimate for GEOMnvr-2.

6.5 Summary

This chapter stepped through a series of analyses to thoroughly assess each aspect of the tasking strategies developed for this dissertation. First the POMDPs were independently assessed to determine which approach performed better. Each method had its advantages and disadvantages. The FIG-Only approach maintained a low average RMS error, but it was neither the most efficient nor the most effective. The Continuous Observation POMDP maintained a similarly low average RMS error, and collect more information per observation than the baseline FIG-Only method. The Continuous Observation approach, however, was not as efficient as the Constrained Observation POMDP, which sacrificed a small amount of accuracy for decreased strain on the physical systems themselves.

Next, the adaptive estimation techniques were assessed with each POMDP against only maneuvering targets. This analysis helped characterize how well each adaptive estimation performed overall. The results of that investigation show that all four adaptive estimation strategies developed in this dissertation are more responsive and effective at tracking through unknown maneuvers than the nominal static filter. Of the four adaptive estimation approaches, the Covariance Inflation and Lambert GPB1 performed consistently well for all three decision processes. The Shotgun and Lambert SMM methods showed degraded performance in some respects when used with the Constrained Observation POMDP, but the effects were comparatively small. Comparing like estimation techniques across POMDPs also shows that the time to reacquire a new orbit estimate for a particular maneuvering target is the result of the interaction between the estimation and the tasking strategy. Convergence times vary significantly for a particular target depending on the combination of adaptive estimation and decision processing.

Lastly, a full scale test was performed against four integrated tasking strategies: Covariance Inflation and the FIG-Only POMDP, Shotgun SMM and the Continuous Observation POMDP, Lambert SMM and the Constrained Observation POMDP, and finally the Lambert GPB1 and the Constrained Observation POMDP. All four methods presented unique characteristics, and all four performed successfully. Perhaps the most successful of the four proposed tasking strategies was the Lambert GPB1 and the Constrained Observation POMDP, which successfully managed 207 non-maneuvering and maneuvering spacecraft with minimal sensor herding behavior and relatively few observations.

Chapter 7

Conclusions

7.1 Summary of Research Motivation & Objectives

Autonomous command and control of a globally distributed Space Object Surveillance & Identification network is a necessary and incredibly complex area of research. Much of what enables modern civilization, from communications and GPS to remote sensing, routes through the space environment, making it a critically important domain. To ensure the future utilization of indispensable space assets, the near-Earth orbital environment must be monitored continuously to maintain actionable Space Situational Awareness. To date, SSA is achieved through highly procedural and slow human-in-the-loop surveillance networks. These processes are currently strained and may soon become inadequate as increasing access to space and advances in satellite propulsion make the space domain more populous and dynamic. The need for autonomous command and control and adaptive estimation to make globally distributed and diversely populated SOSI networks more responsive has been identified by several agencies in recent years.

This dissertation addressed how a large and diverse network of terrestrial and space-based sensors could be autonomously tasked to maintain SSA of a much larger population of non-maneuvering spacecraft, while simultaneously detecting unknown maneuvers and rapidly reacquiring viable orbit estimates for multiple maneuvering satellites. The suboptimal Partially Observed Markov Decision Process was identified as a viable means of autonomously and responsively commanding a sensor network. Multiple Model Adaptive Estimation was identified as a potential approach for tracking through unknown maneuvers without human intervention in the command and control process. Three research objectives were defined to structure the research:

1. Develop a set of decision processes that enable responsive and efficient SOSI network command and control

2. Develop a set of adaptive estimation algorithms to track maneuvering spacecraft
3. Within the defined scenario, assess how effectively decision processes and adaptive estimation algorithms interact to track a large RSO population

Ultimately, how efficiently the integrated tasking strategy controls a global SOSI network determines the degree to which SSA of the entire space domain is maintained.

7.2 Summary of Contributions

This dissertation's primary contribution is the development and assessment of responsive SOSI network command and control algorithms using suboptimal POMDPs and MMAE to track a large number of non-maneuvering and maneuvering satellites with a diverse set of sensors. By achieving the research objectives delineated in Section 5.3, and restated in the previous section, the specific novel contributions of this dissertation are as follows:

1. The development and assessment of a real-time, continuous observation suboptimal POMDP algorithm that uses Fisher Information Gain, maximal Lyapunov exponent approximation, and Degrees of Transport reward metrics to task radar and EOIR sensors
2. The development and assessment of a real-time, cost-constrained suboptimal POMDP algorithms that uses Fisher Information Gain, maximal Lyapunov exponent approximation, and slew time cost to task radar and EOIR sensors
3. The development of a real-time, baseline suboptimal POMDP using only Fisher Information Gain to task radar and EOIR sensors
4. The development and assessment of a "Shotgun" Static Multiple Model algorithm to detect and track through unknown tangential maneuvers
5. The development and assessment of a Lambert Targeter Static Multiple Model algorithm to detect and track through unknown maneuvers in any direction
6. The development and assessment of a Lambert Targeter Generalized Pseudo-Bayesian of First Order Multiple Model algorithm to detect and track through unknown maneuvers in any direction
7. The development of a baseline Covariance Inflation algorithm that optimizes a scalar inflation value using a binary search method to detect and track through unknown maneuvers in any direction

8. The integration of the aforementioned suboptimal POMDPs and adaptive estimation algorithms, and assessment of the combined algorithms in a globally-distributed, diversely populated SOSI network that is tasked to track a large number of maneuvering and non-maneuvering spacecraft

Assessment in this context refers to the comparison of POMDPs, adaptive estimation techniques, and overall tasking strategies against the baseline developed for this dissertation.

Chapter 3 presented the model that was used to test the developed tasking strategies. A centralized SOSI network was devised consisting of LPAR, terrestrial radar and EOIR, and space-based EOIR sensors. Two constellations of target spacecraft were then defined. The first constellation consisted of 100 non-maneuvering satellites distributed across all three principal orbital regimes. This set of satellites was used for preliminary decision process design and testing. The second constellation consisted of 200 non-maneuvering satellites and seven maneuvering spacecraft distributed across all orbital regimes. The larger set of non-maneuvering spacecraft was used to test the developed POMDPs independently of the adaptive estimation techniques. The subset of maneuvering satellites was used to test the adaptive estimation methods independently of the decision processes. The full test constellation was ultimately used to test integrated tasking strategies.

Chapter 4 presented the four adaptive estimation techniques that were developed for this dissertation. A baseline covariance inflation technique was developed using a binary search method to optimize the scalar inflation factor, based on the normalized innovations squared metric and threshold. An intermittent pruning "Shotgun" Static Multiple Model was developed that was executed a set of user-defined models only when a maneuver was detected and removed unlikely models as new observations were collected. A more versatile SMM was then introduced that used the universal variable method for solving the Lambert Problem to determine an appropriate set of models. This algorithm was also only initialized when a maneuver was detected and removed unlikely models as observations were collected. To improve responsiveness, a Generalized Pseudo-Bayesian of First Order Multiple Model version of the Lambert SMM was devised that used the combined state estimate and covariance updates after an observation to inform the next set of models, should the Lambert GPB1 be called again. To conserve computational resources, the adaptive estimation approaches were only initialized when a maneuver was detected and executed only as long as necessary until a viable orbit estimate was attained.

Chapter 5 three suboptimal POMDPs were developed and presented. The first served as a baseline approach based on previous research, and only considered the Fisher Information Gain a potential observation would garner when determining the appropriate set of tasks at a time step. The second method developed for this dissertation, termed the Continuous Observation POMDP, used the maximal Lyapunov exponent approximation, Fisher Information Gain, and Degrees of Transport metrics to determine sensor tasks. Based on preliminary analyses that determine the appropriate weight coefficients for each metric, the Continuous Observation decision process normalizes and takes the weighted sum of three metrics

to determine the reward value for each target-sensor pair. The third method developed for this dissertation, called the Constrained Observation POMDP, limited the number of tasked observations based on a reward and cost objective function. In the Constrained Observation method, observations are only tasked if the normalized FIG metric is greater than the normalized slew time, and if the MLEA metric indicates a diverging target covariance.

Chapter 6, the decision processes and adaptive estimation techniques were assessed independently. The three POMDPs each had advantages and disadvantages. The FIG-Only and Continuous Observation decision processes had lower average root mean squared error than the Constrained Observation approach. The Continuous Observation POMDP was actually more effective at maximizing FIG per observation over time than the FIG-Only decision process. While the Constrained Observation POMDP was less effective in reducing RMS error, it still maintained viable orbit estimates for all targets, and did so more efficiently than the other two decision processes. The adaptive estimation algorithms were first tested against the set of seven maneuvering targets. In general, all four methods had comparable performance, but the two Lambert Targeting Multiple Model Adaptive Estimation approaches were the most responsive. Finally, four integrated tasking strategies were developed to assess how each adaptive estimation technique would perform when integrated with a suboptimal POMDP to track 207 non-maneuvering and maneuvering satellites using the full 24-sensor test SOSI network. The baseline Covariance Inflation and FIG-Only strategy successfully maintained SSA of the whole constellation, but was slower than the MMAE-based strategies at converging to a new orbit estimate after an unknown maneuver. The Shotgun SMM and Continuous Observation, and the Lambert SMM and Constrained Observation tasking strategies rapidly reacquired viable orbit estimates after a maneuver, but often required multiple simultaneous observation from a large number of sensors. The Lambert GPB1 and Constrained Observation tasking strategy provided perhaps the best compromise between the efficient sensor management seen in the Covariance Inflation and FIG-Only approach, and the rapid estimate convergence garnered by the two SMM approaches. The Lambert GPB1 and Constrained Observation strategy provided a relatively rapid response to an unknown maneuver while also efficiently managing the sensor network, compared to the other developed approaches, to maintain SSA of the entire constellation.

Previous research has focused on either the optimal scheduling of similar sensors to track a large population of non-maneuvering Resident Space Objects [87, 44, 91], or the adaptive estimation of one or a few maneuvering satellites without consideration of the larger SSA mission [46, 43]. The former does not require adaptive estimation and is well suited for routine SSA operations that can be scheduled over a 24 hour period, as is currently the case for real-world networks [9]. The latter does not give due consideration to the challenges that arise a SOSI network is over-tasked and may not be able to provide continuous observations of a maneuvering spacecraft. The research presented in this dissertation investigated the intersection of these two research paths to characterize how adaptive estimation could be paired with responsive POMDPs to track a large number of RSOs. The satellite population size was large enough that the SOSI network could not observe all objects all the time. The

developed tasking strategies were required to appropriately manage the SOSI networks to maintain viable orbit estimates for all targets, even when unknown maneuvers were detected. This dissertation proposed several methods for tasking sensors, but ultimately showed that a POMDP with multiple information and system-based decision metrics, coupled with a Lambert Targeting dynamic multiple model approach was the most responsive and efficient method for maintaining overall SSA while tracking through unknown maneuvers.

7.3 Recommendations for Future Work

The possibilities for future work are numerous and multi-faceted. Future work falls into the categories outlined in Section 1.2.4: estimation, data association, sensor registration, data fusion, and decision processing. As discussed in Section 2.4, to confidently detect and characterize unknown maneuvers the estimation process must accurately account for the nonlinear dynamics that are inherent in orbital mechanics. The UKF used in this dissertation was an effective and computationally efficient method, but there are many other approaches, which are computationally more intensive. Implementing a particle filter or some form of Gaussian mixture model, like the Adaptive Entropy-based Gaussian-Mixture Information synthesis (AEGIS) filter described in [44], into the framework developed in this dissertation would be a valuable pursuit. Investigating linear sequential estimation algorithms, or even batch least squares methods, would also be of value. The reason is that current SOSI networks implement Batch Least Squares methods to derive a satellite orbit from a history of observations. Similarly, comparing suboptimal and adaptive POMDPs to the optimized POMDPs that are currently used in real-world networks would be a valuable assessment of the advantages and disadvantages of responsive tasking strategies. The question thus becomes, working within the current real-world command and control framework, how might adaptive estimation be implemented? The current trends in research are pushing towards more sophisticated estimation algorithms that simply cannot be implemented on current systems because the assumed infrastructure does not exist. Many of the assumptions delineated in Section 1.2.4, that are often used in estimation and decision making research for SSA must be overcome for a proposed algorithm to be directly transferable to real-world systems.

From an adaptive estimation standpoint, more complex methods can be developed and tested against more advanced maneuver models, such as continuous maneuvers or multiple impulsive maneuvers. For example, an Interacting Multiple Model could be developed for continuous thrusting satellites that initializes models based on the optimal trajectories to rendezvous with a set of high value satellites. The assumption in this scenario is that the maneuvering satellite is trying to approach another known spacecraft, and is doing so in a generally predictable manner.

As such, future work should focus on removing the aforementioned assumptions and building out the algorithms to accommodate the new complexities. If it is no longer assumed that targets and observations are correctly correlated, then methods for data association must

be used. There are many solutions ranging from simple nearest-neighbor algorithms to probabilistic multiple hypothesis testing. The degree to which data association is integrated into the estimation process, as opposed to a stand alone method, should also be addressed. As the complexity of the overall estimation algorithm grows the computational burden grows, which should always be an important consideration when designing a sensor management strategy to track hundreds or thousands of objects. From a modeling standpoint, how should observations be simulated to allow for multiple objects within a single observation. DeMars [112] and others have investigated data association techniques, and there are many opportunities to build off of their published works. In the same vain, more sophisticated sensor models could be developed to simulate direct imagery or photometric data. Such information could help inform data association and estimation algorithms by refining the set of possible solutions. For example, photometric data of a satellite's thruster plume might indicate the type of propulsion system a spacecraft hosts, which would refine the acceptable range of possible thrust magnitudes in an adaptive estimation algorithm.

The assumption that sensor states are known with absolute certainty can be removed, particularly for space-based sensors. The challenge in this case is how to mitigate the errors and uncertainty that are injected into the target estimate from the sensor. As previously discussed, the sensor state can be estimated when the target state is estimated, but this would significantly increase the computational load. Sensor states could be estimated independently if onboard GPS capabilities are assumed.

Data fusion in this dissertation was conducted at a measurement level because the centralized sequential estimation process is well suited for this approach. If a partially decentralized or fully decentralized SOSI network topology is considered, data fusion becomes more complex. In a partially decentralized network each sensor node could independently update its own target estimate and then a central processing node would fuse the estimate using a technique like covariance intersection. Research into fully decentralized SOSI network data fusion could investigate more sophisticated means of fusion that more resemble social learning and voting than analytical processes.

Perhaps the most significant and impactful future work will be the integration of the suboptimal POMDP and machine learning. Optimizing the decision process over a time window, as is common practice today, will limit how responsive an autonomous network can be. Various machine learning techniques, like reinforcement learning [113], could be used to allow a tasking strategy to "plan ahead" based on past experience. This behavior could increase a tasking strategy's effectiveness over time without sacrificing responsiveness. Indeed, much of the command and control research community is investigating how machine learning could be implemented, and there are many potential options for inclusion in autonomous SOSI network command and control.

Appendix A

POMDP Coefficient Analyses

A.1 Continuous Observation POMDP

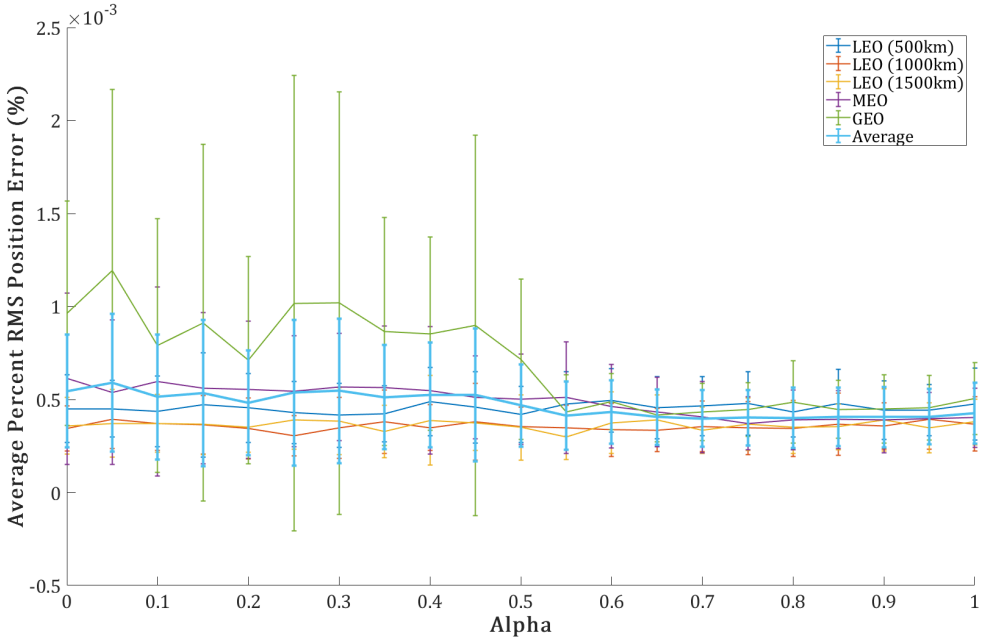

Figure A.1: Percent RMS Position Error Vs. Alpha

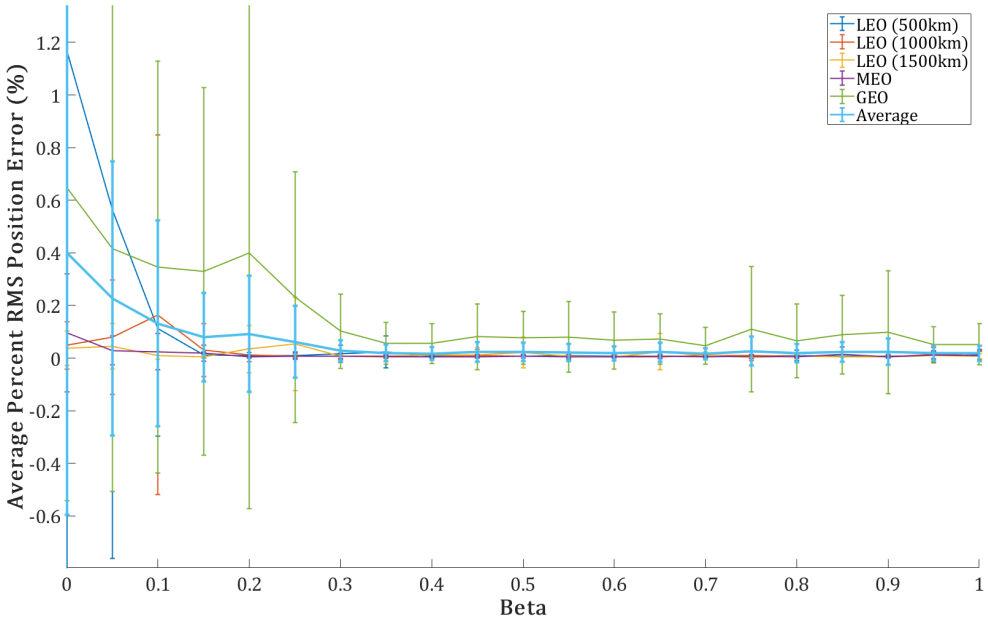

Figure A.2: Percent RMS Position Error Vs. Beta

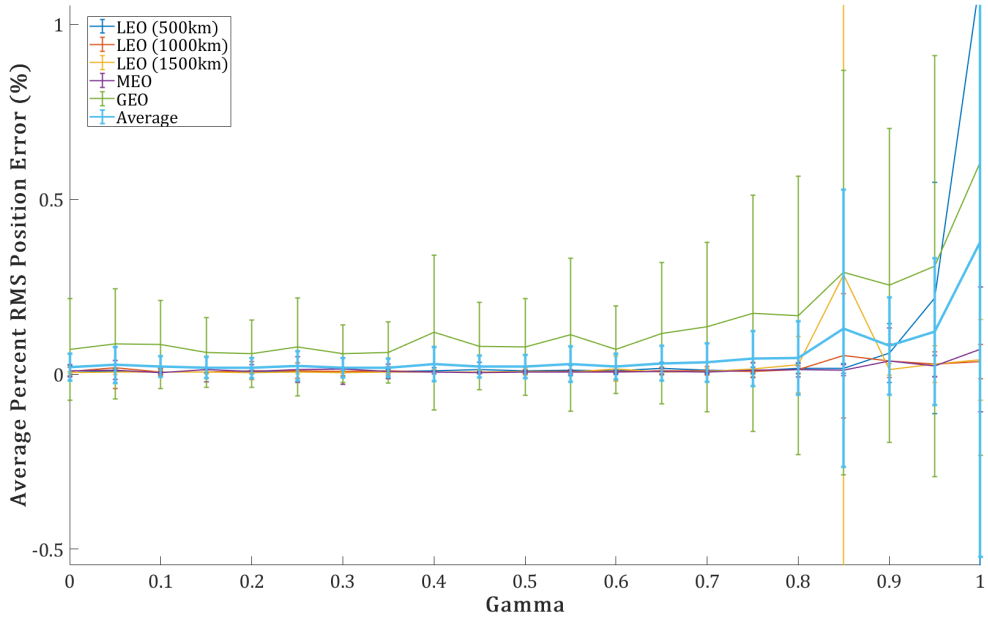

Figure A.3: Percent RMS Position Error Vs. Gamma

A.2 Cost-Constrained POMDP

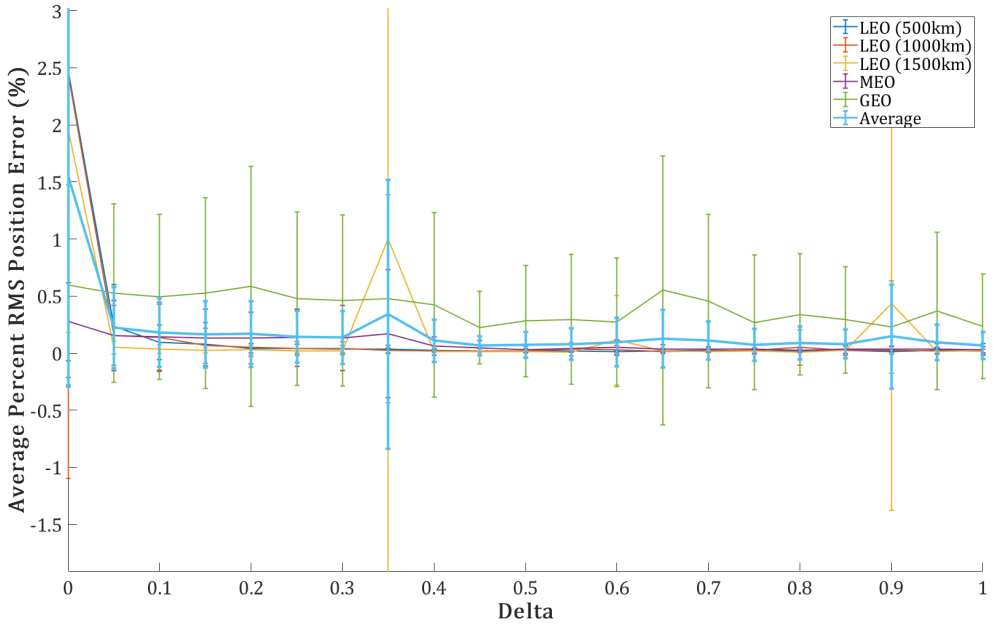

Figure A.4: Percent RMS Position Error Vs. Delta

Appendix B

Adaptive Estimation Test Analysis

B.1 FIG-Only POMDP

B.1.1 No Adaptive Estimation

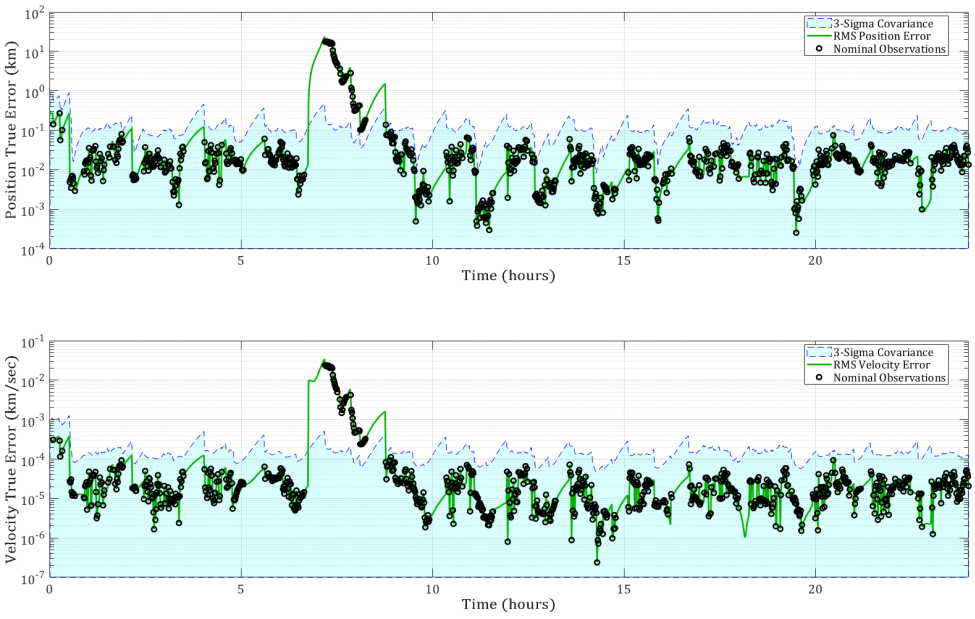

Figure B.1: A.E. Test: Nominal/FIG-Only LEOMnvr-1 Track

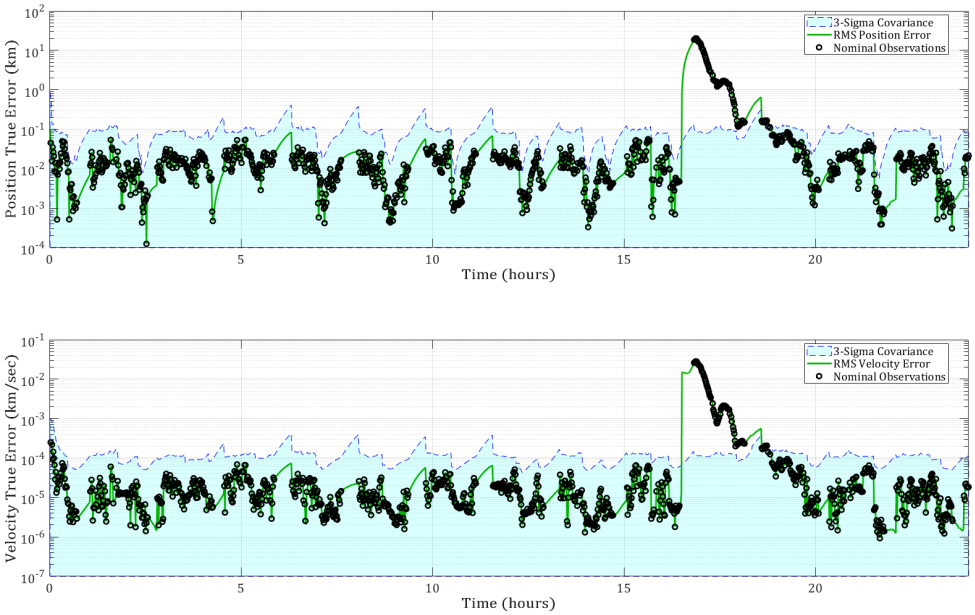

Figure B.2: A.E. Test: Nominal/FIG-Only LEOMnvr-2 Track

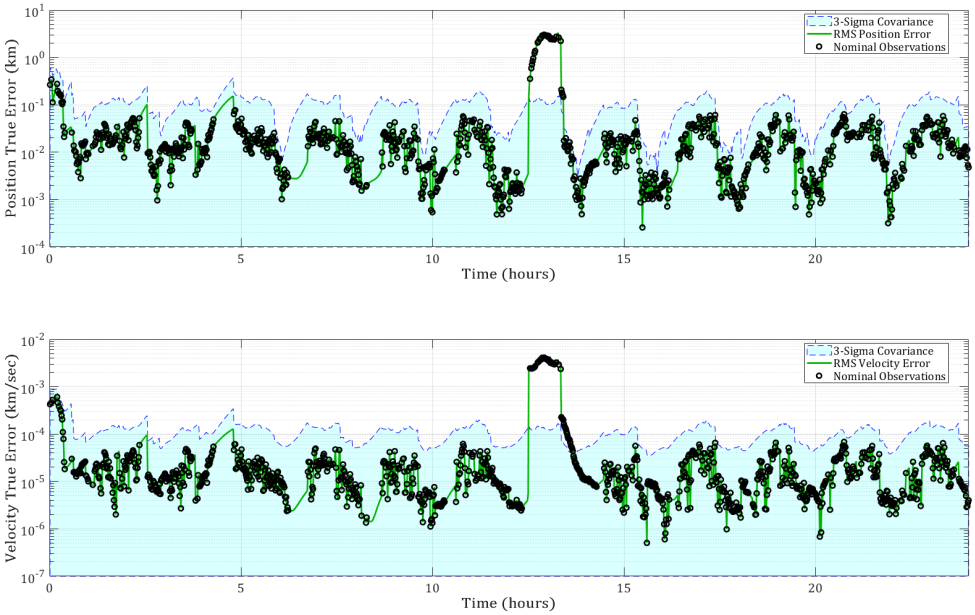

Figure B.3: A.E. Test: Nominal/FIG-Only LEOMnvr-3 Track

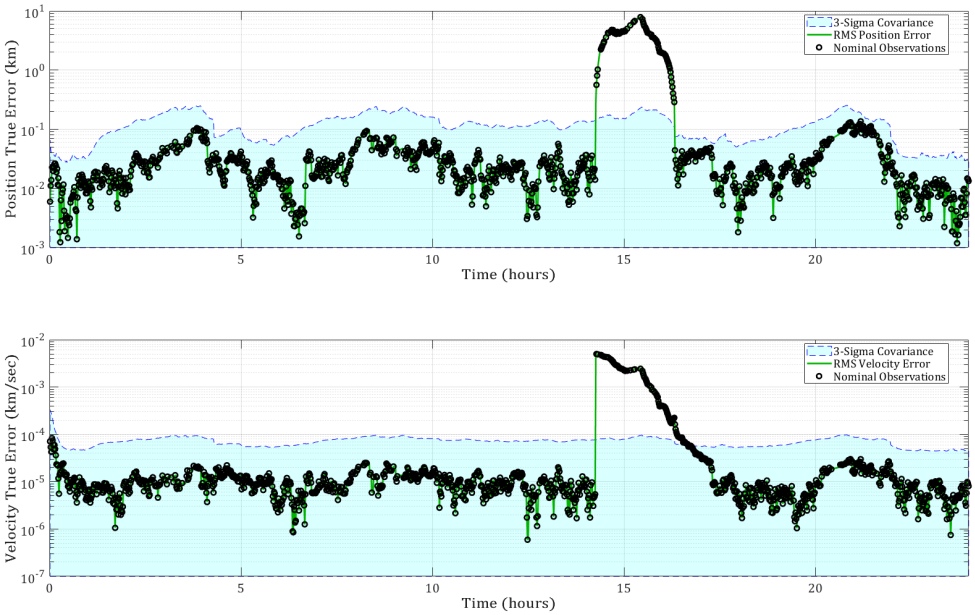

Figure B.4: A.E. Test: Nominal/FIG-Only MEOMnvr-2 Track

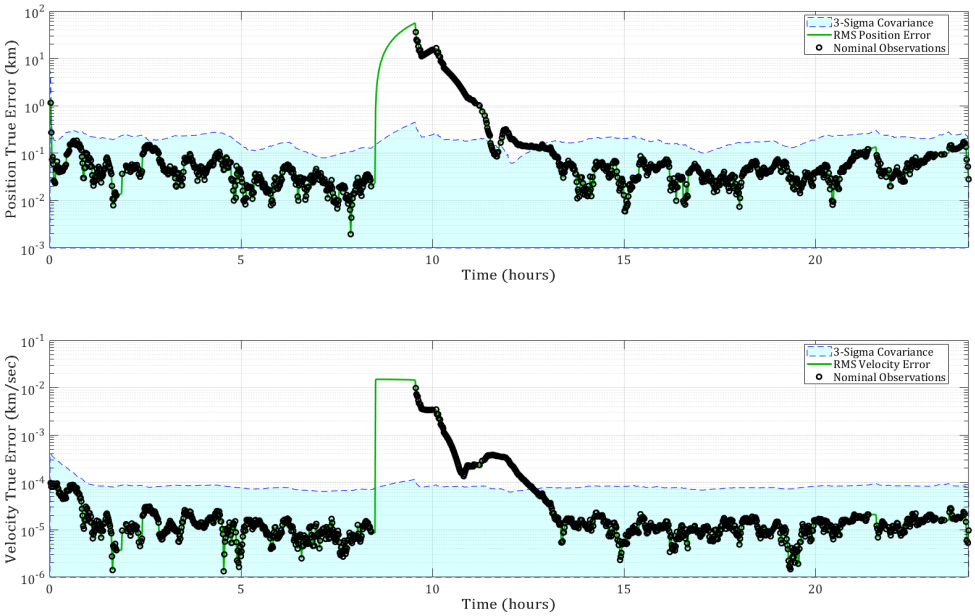

Figure B.5: A.E. Test: Nominal/FIG-Only GEOMnvr-1 Track

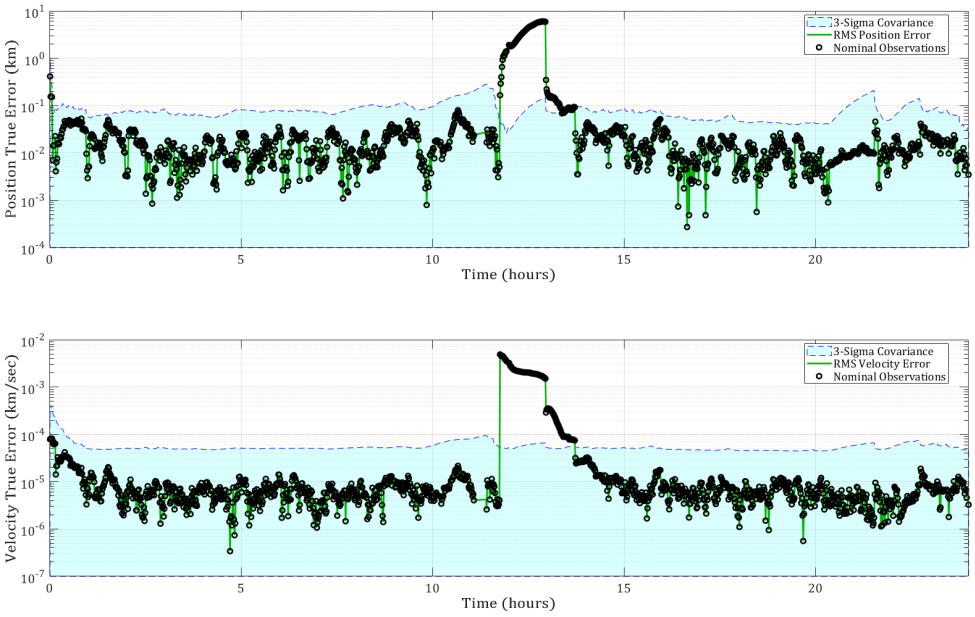

Figure B.6: A.E. Test: Nominal/FIG-Only GEOMnvr-2 Track

B.1.2 Covariance Inflation

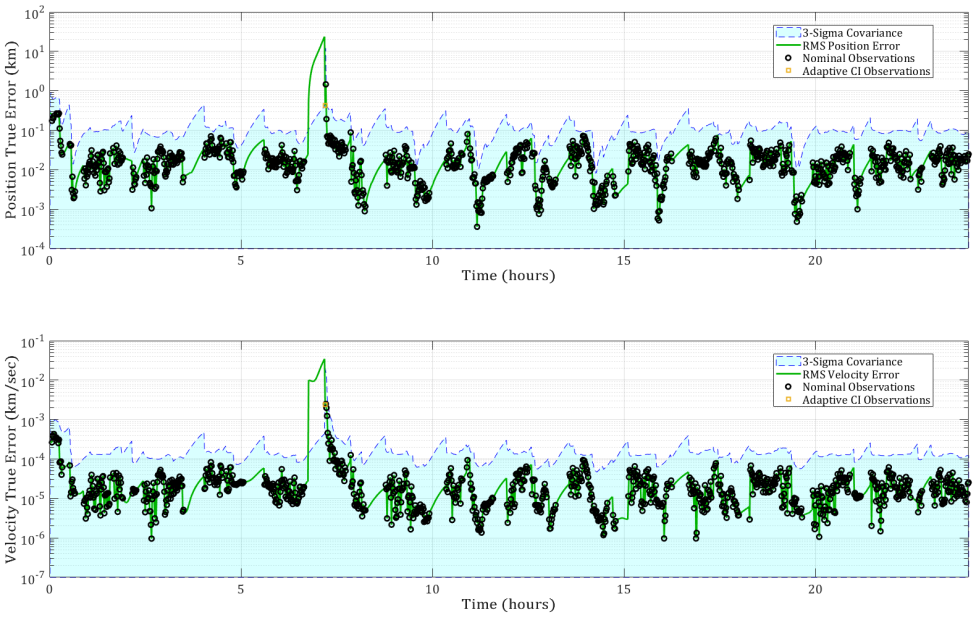

Figure B.7: A.E. Test: Inflation/FIG-Only LEOMnvr-1 Track

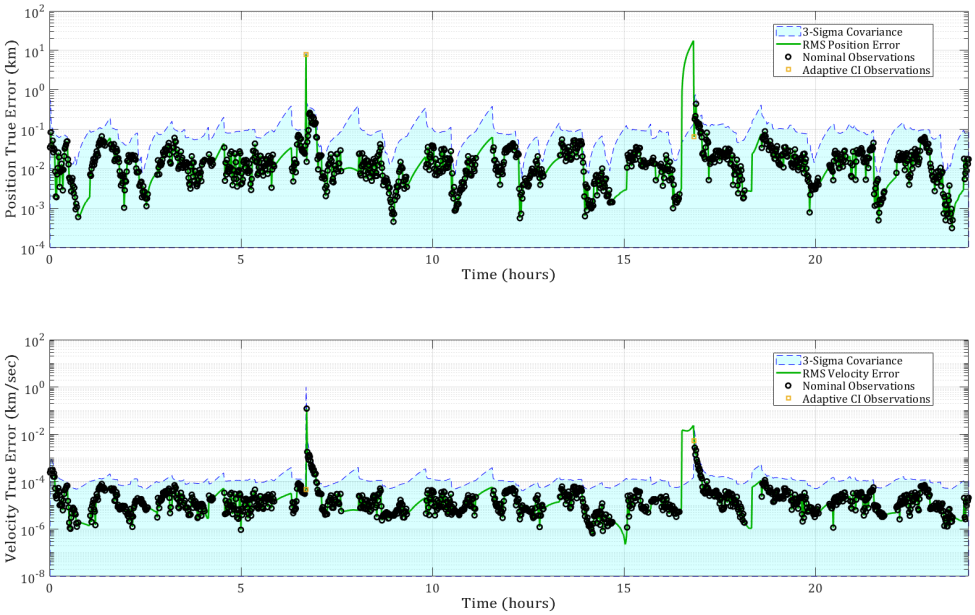

Figure B.8: A.E. Test: Inflation/FIG-Only LEOMnvr-2 Track

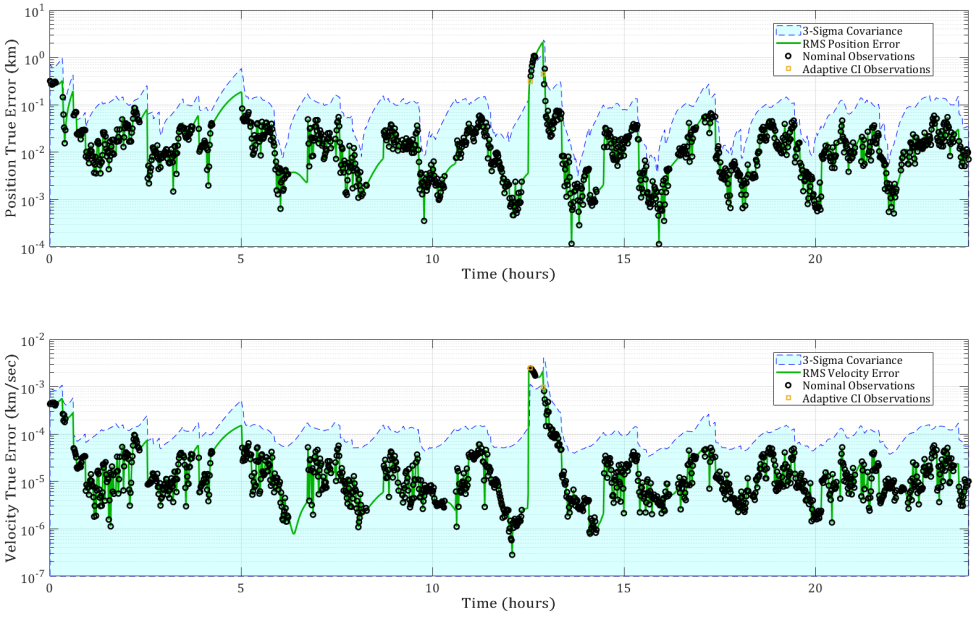

Figure B.9: A.E. Test: Inflation/FIG-Only LEOMnvr-3 Track

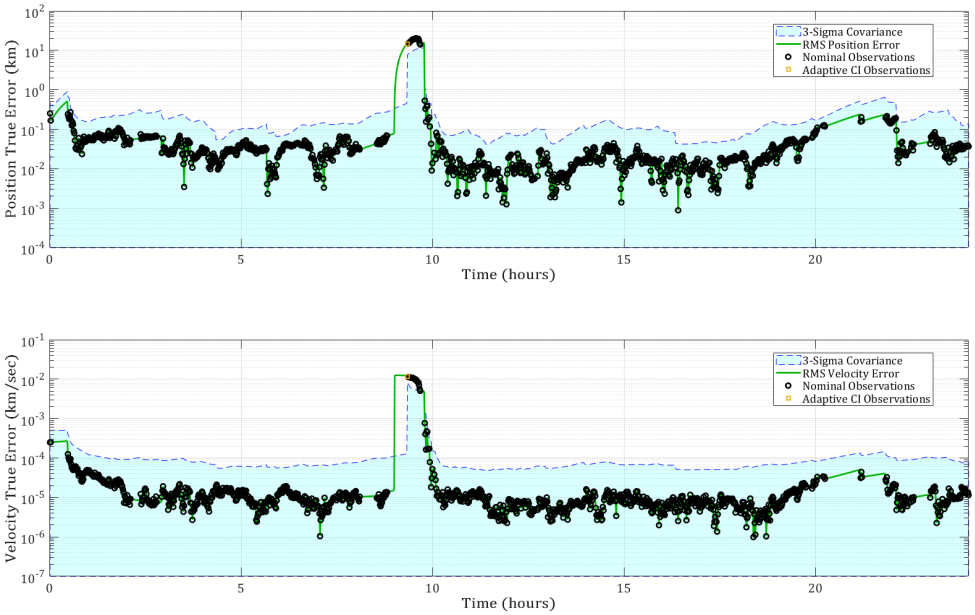

Figure B.10: A.E. Test: Inflation/FIG-Only MEOMnvr-1 Track

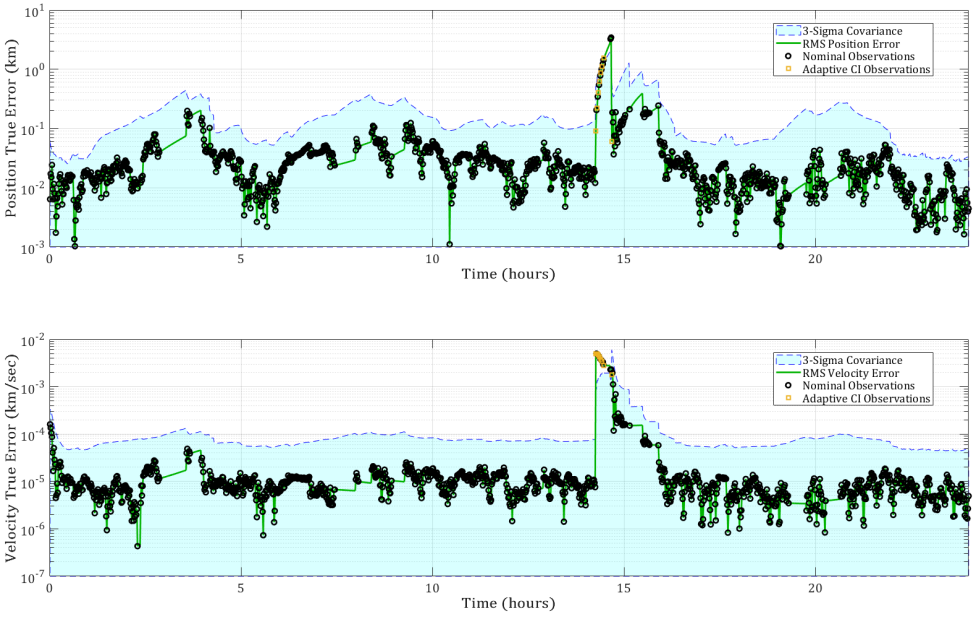

Figure B.11: A.E. Test: Inflation/FIG-Only MEOMnvr-2 Track

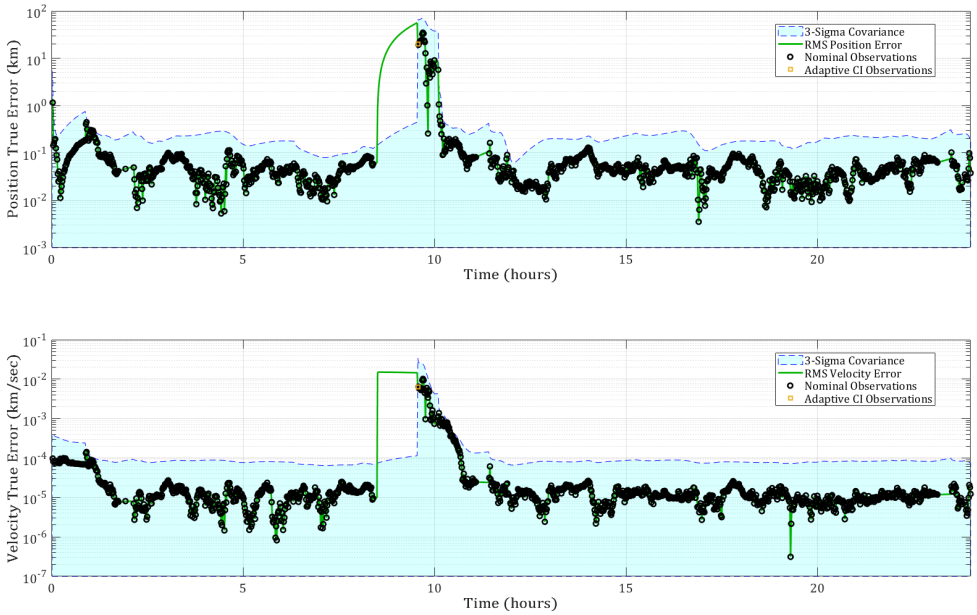

Figure B.12: A.E. Test: Inflation/FIG-Only GEOMnvr-1 Track

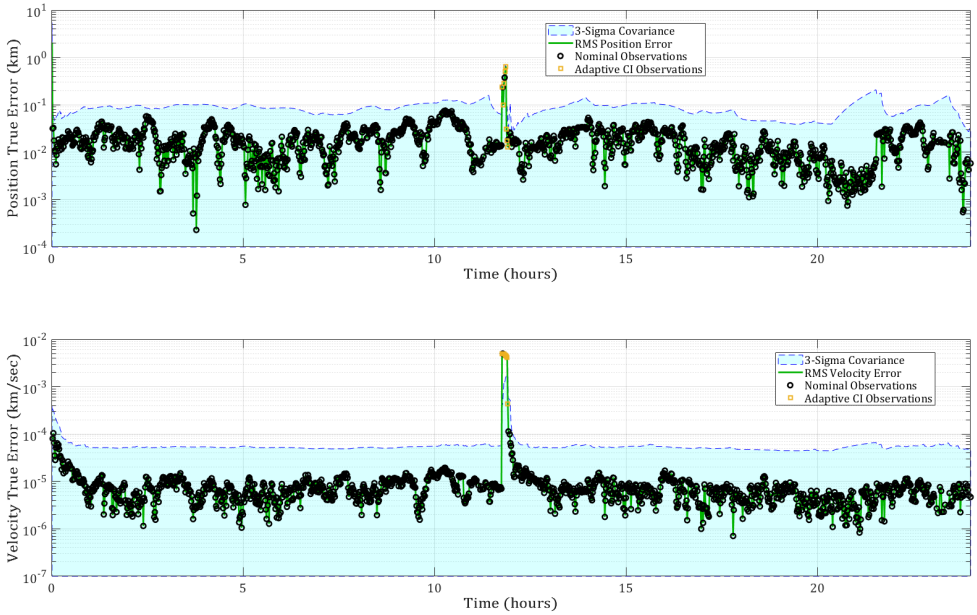

Figure B.13: A.E. Test: Inflation/FIG-Only GEOMnvr-2 Track

B.1.3 Shotgun SMM

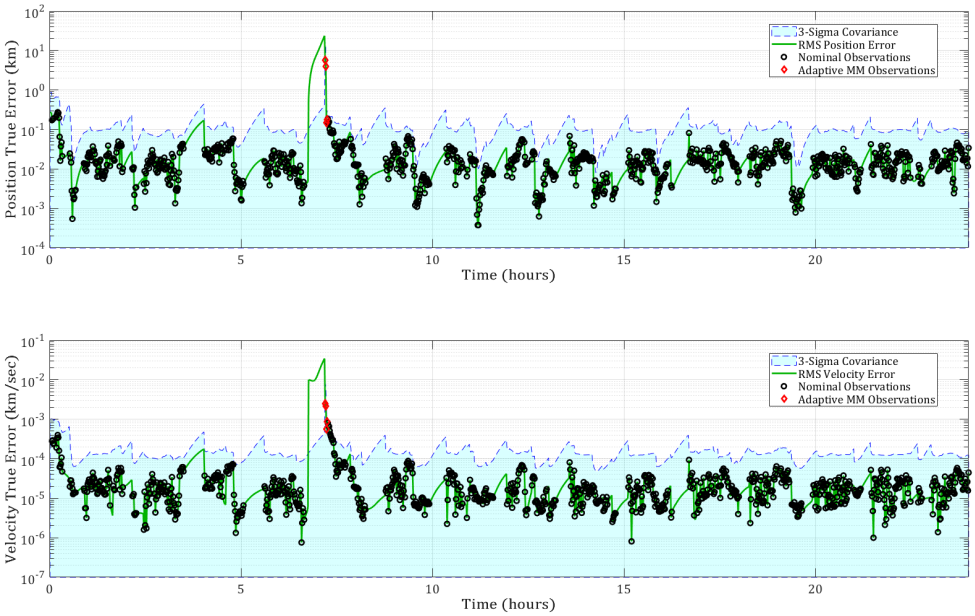

Figure B.14: A.E. Test: Shotgun SMM/FIG-Only LEOMnvr-1 Track

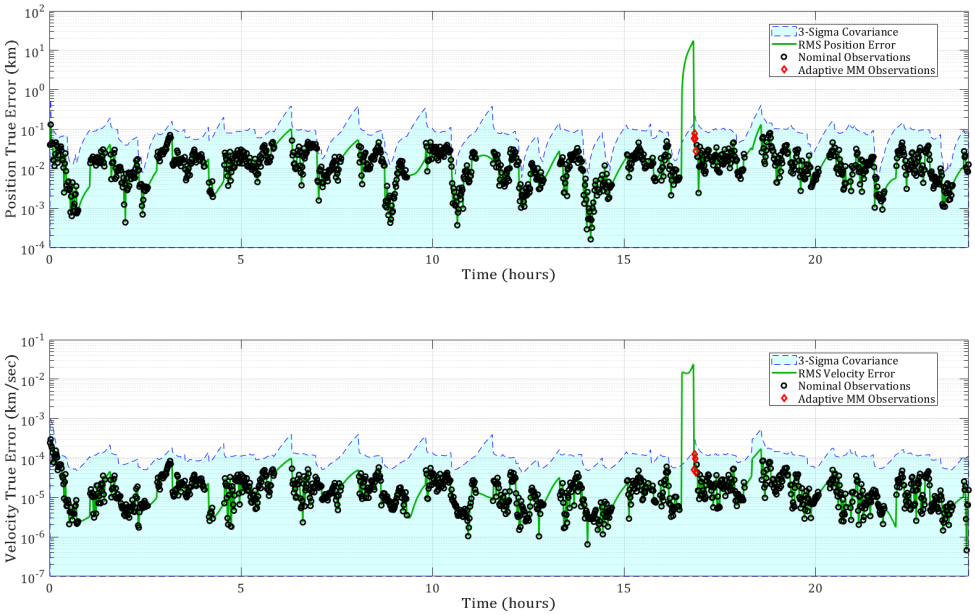

Figure B.15: A.E. Test: Shotgun SMM/FIG-Only LEOMnvr-2 Track

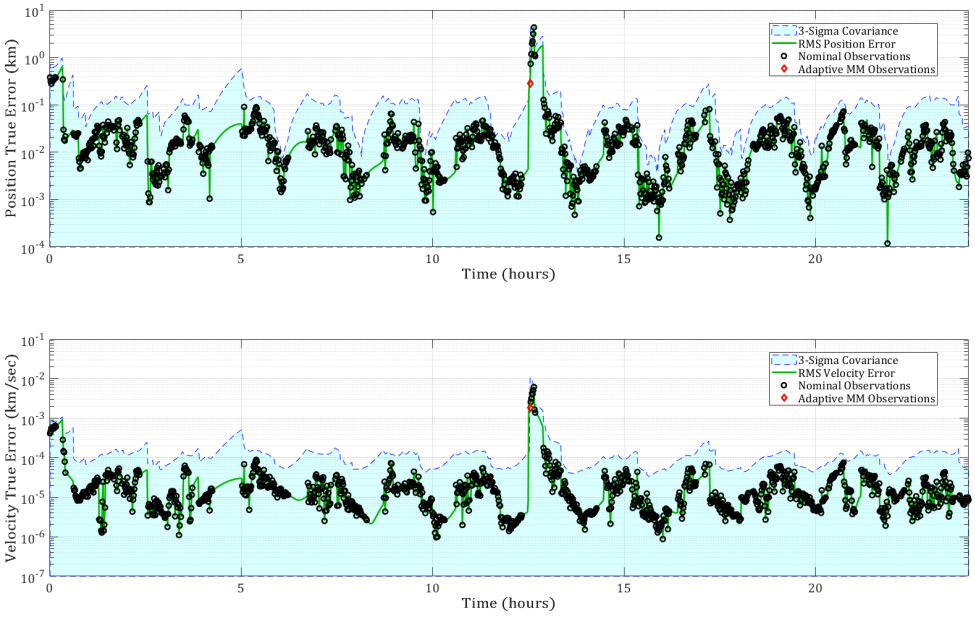

Figure B.16: A.E. Test: Shotgun SMM/FIG-Only LEOMnvr-3 Track

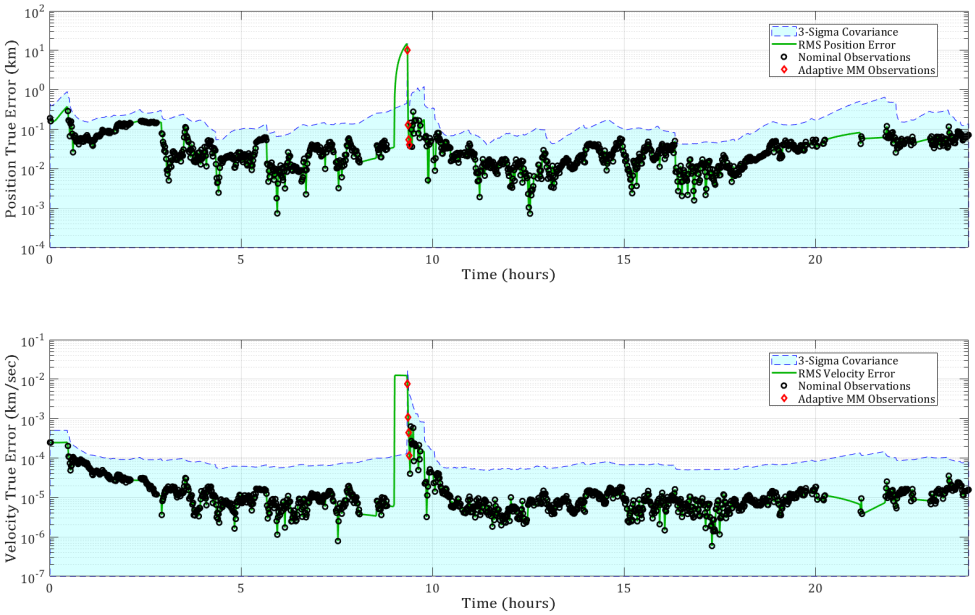

Figure B.17: A.E. Test: Shotgun SMM/FIG-Only MEOMnvr-1 Track

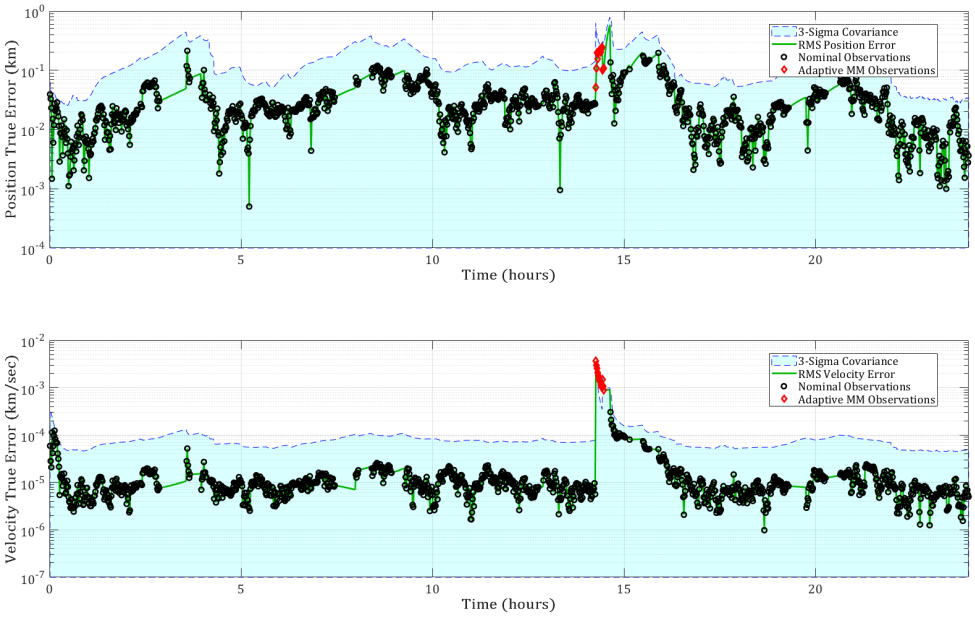

Figure B.18: A.E. Test: Shotgun SMM/FIG-Only MEOMnvr-2 Track

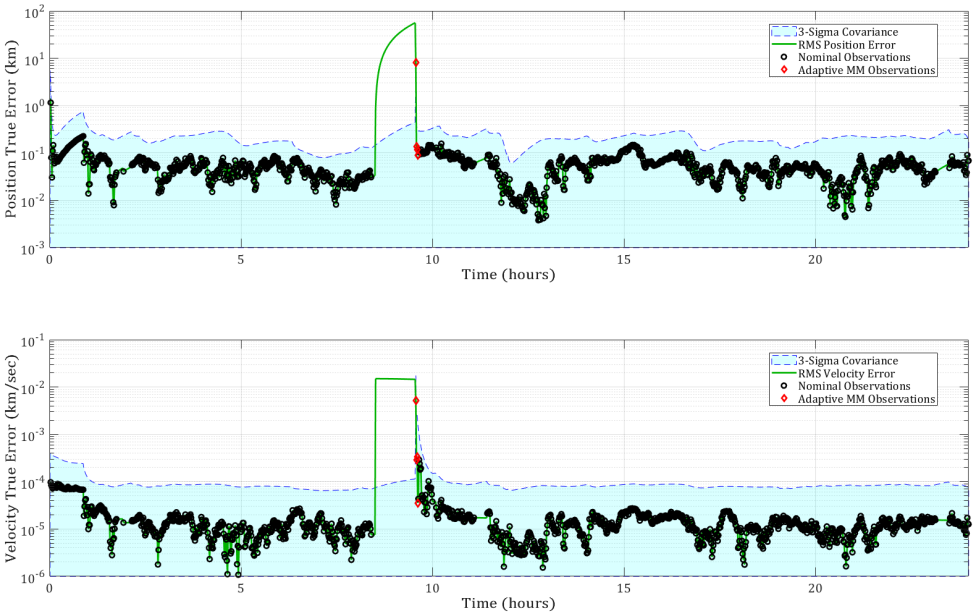

Figure B.19: A.E. Test: Shotgun SMM/FIG-Only GEOMnvr-1 Track

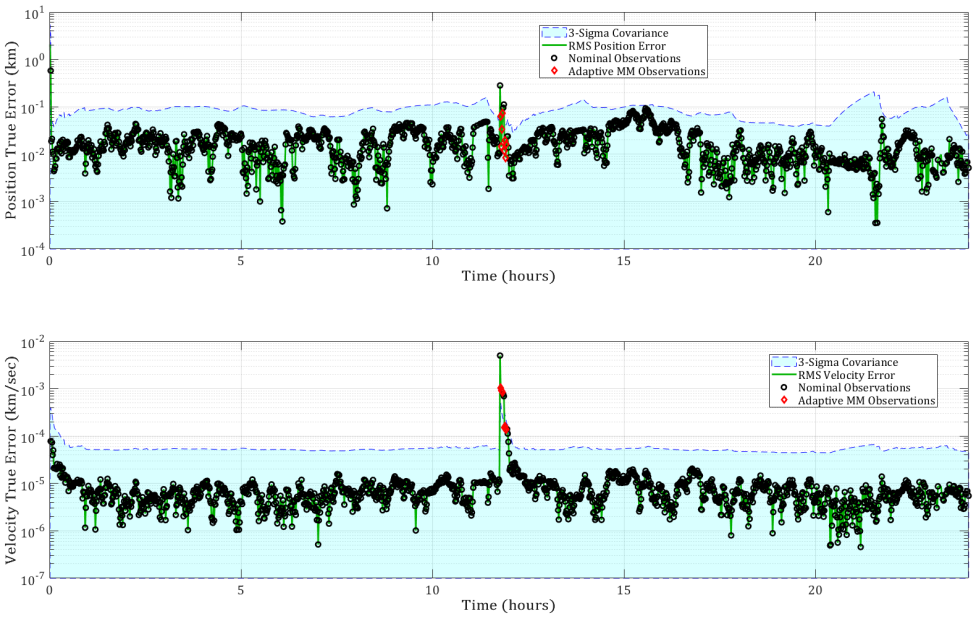

Figure B.20: A.E. Test: Shotgun SMM/FIG-Only GEOMnvr-2 Track

B.1.4 Lambert SMM

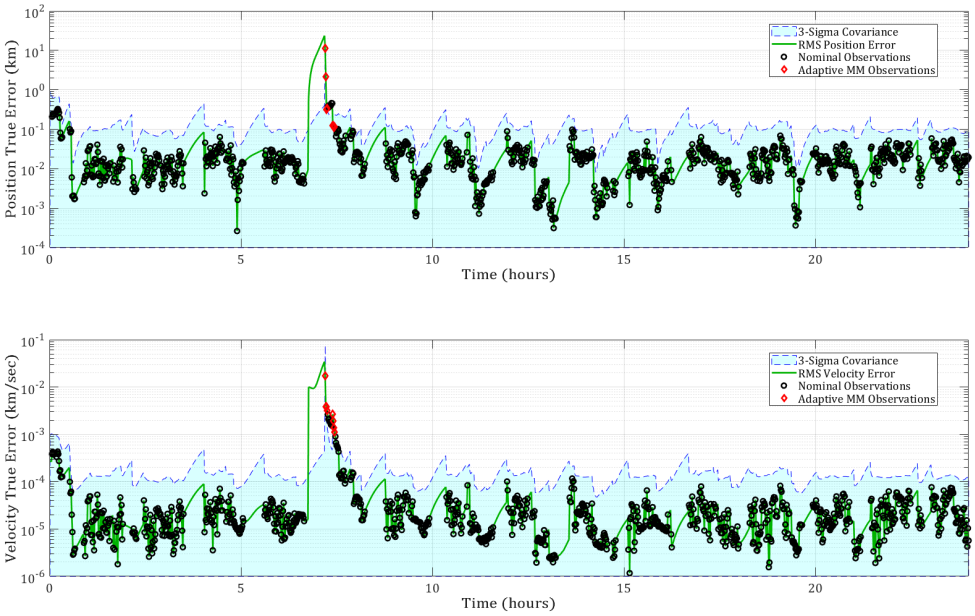

Figure B.21: A.E. Test: Lambert SMM/FIG-Only LEOMnvr-1 Track

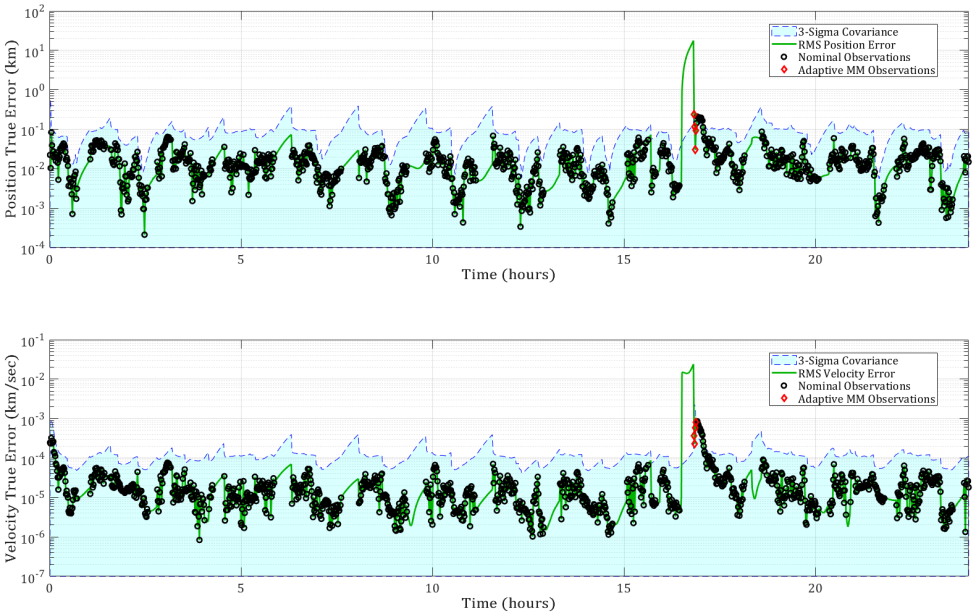

Figure B.22: A.E. Test: Lambert SMM/FIG-Only LEOMnvr-2 Track

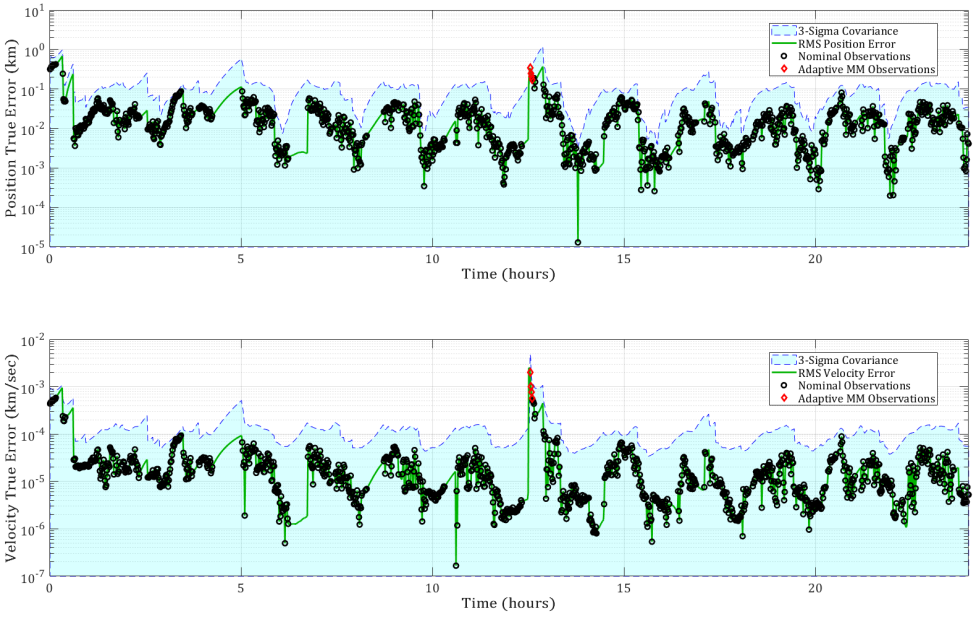

Figure B.23: A.E. Test: Lambert SMM/FIG-Only LEOMnvr-3 Track

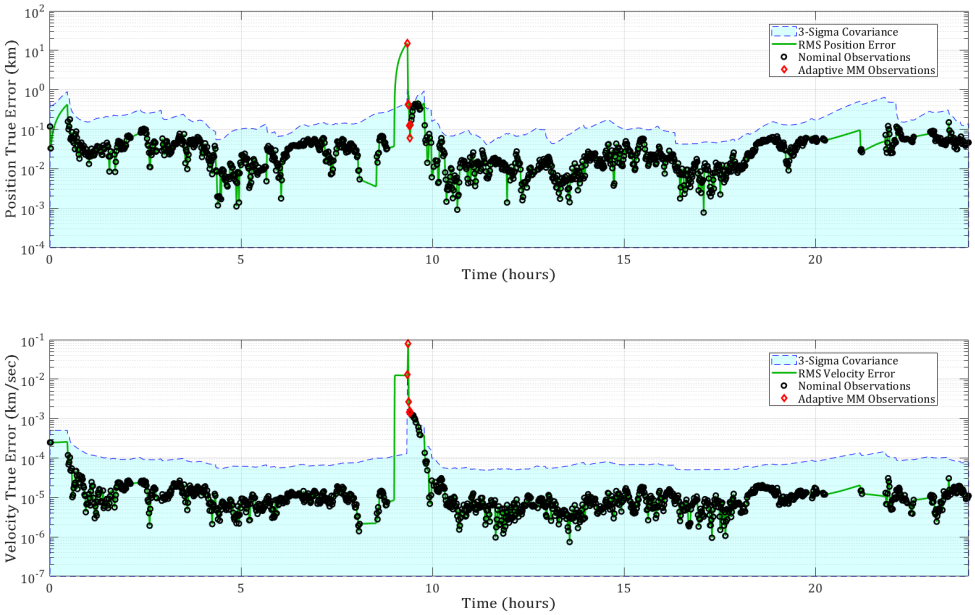

Figure B.24: A.E. Test: Lambert SMM/FIG-Only MEOMnvr-1 Track

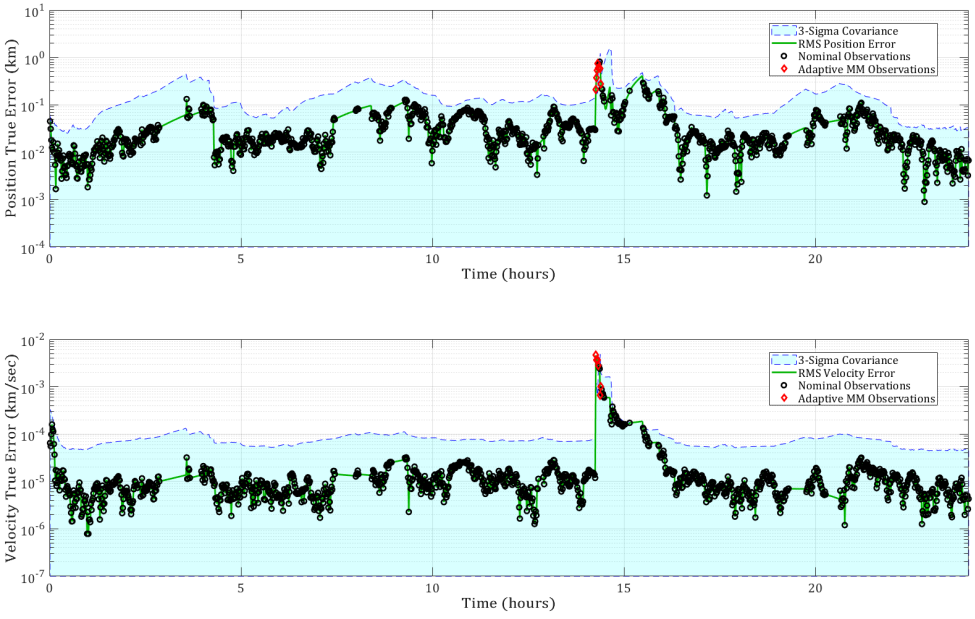

Figure B.25: A.E. Test: Lambert SMM/FIG-Only MEOMnvr-2 Track

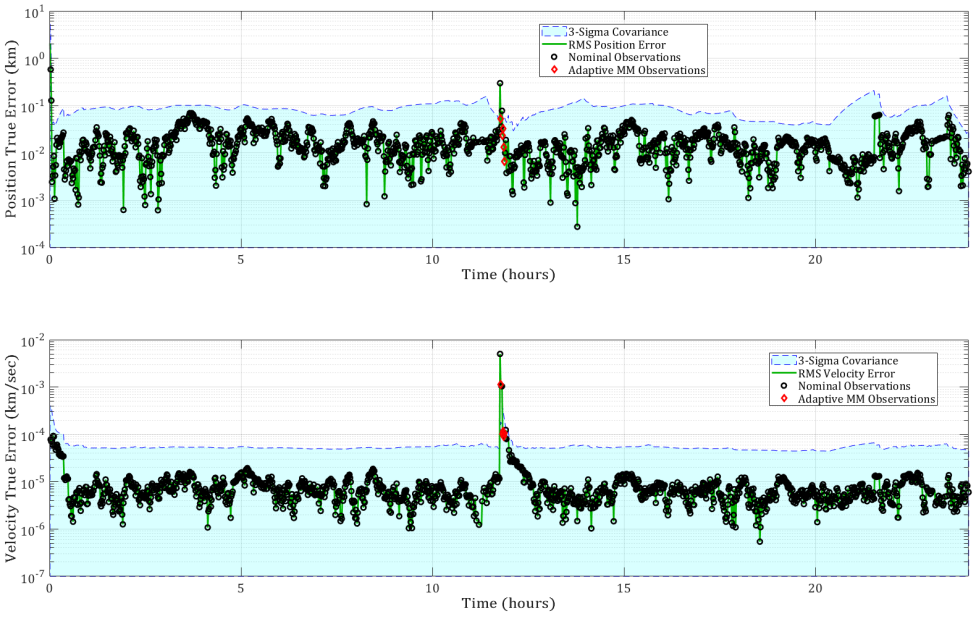

Figure B.26: A.E. Test: Lambert SMM/FIG-Only GEOMnvr-2 Track

B.1.5 Lambert GPB1

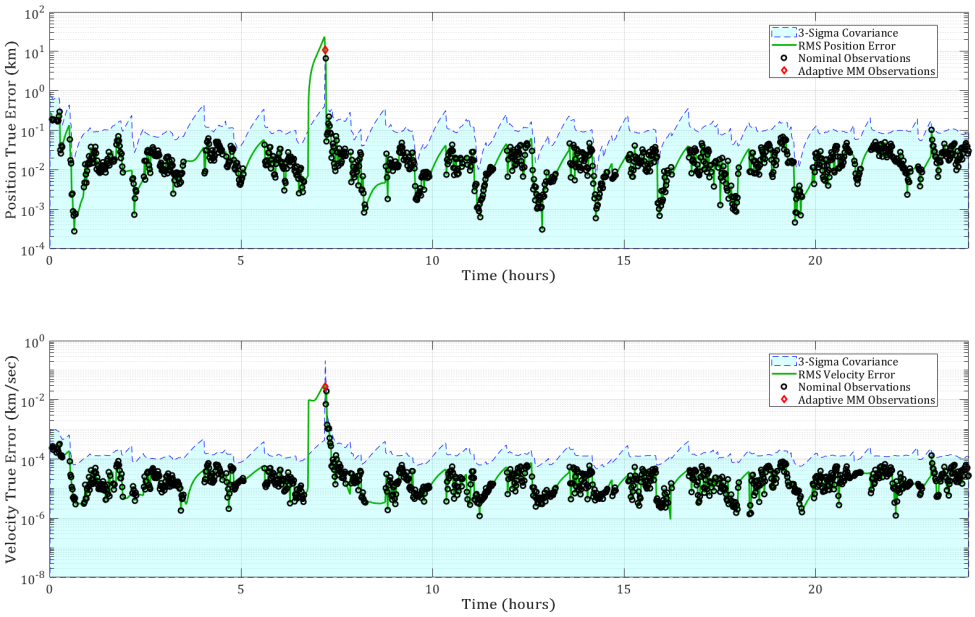

Figure B.27: A.E. Test: Lambert GPB1/FIG-Only LEOMnvr-1 Track

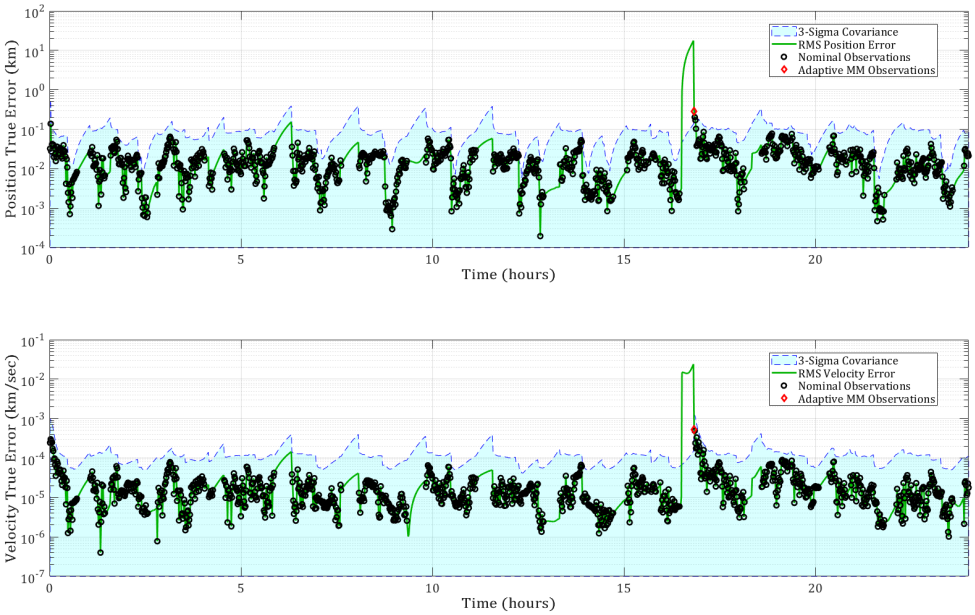

Figure B.28: A.E. Test: Lambert GPB1/FIG-Only LEOMnvr-2 Track

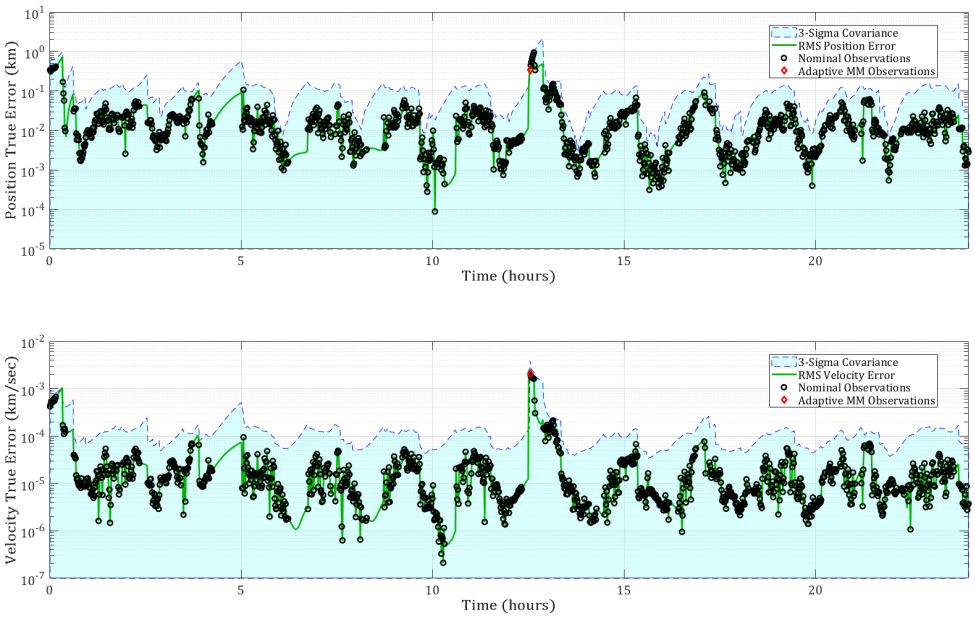

Figure B.29: A.E. Test: Lambert GPB1/FIG-Only LEOMnvr-3 Track

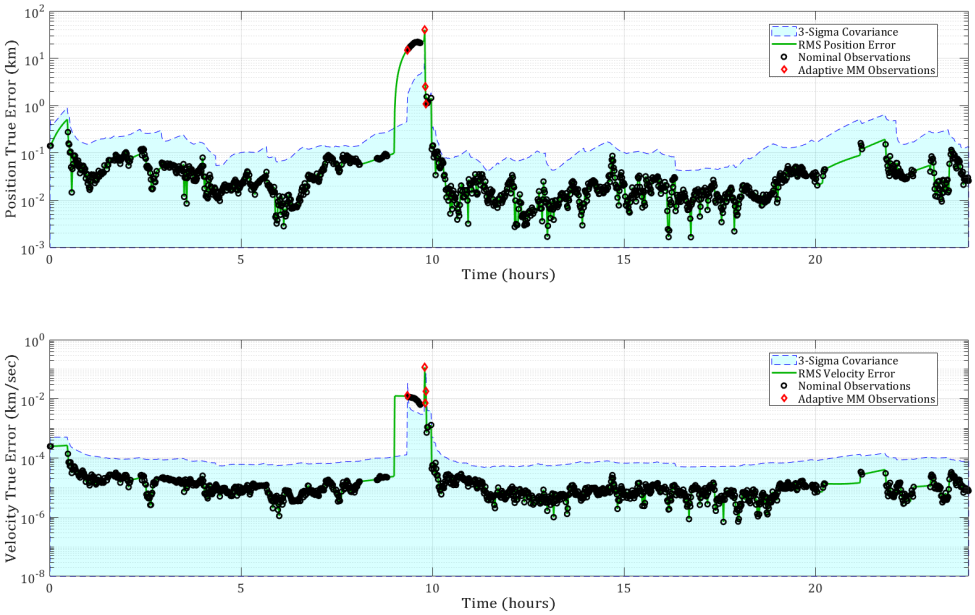

Figure B.30: A.E. Test: Lambert GPB1/FIG-Only MEOMnvr-1 Track

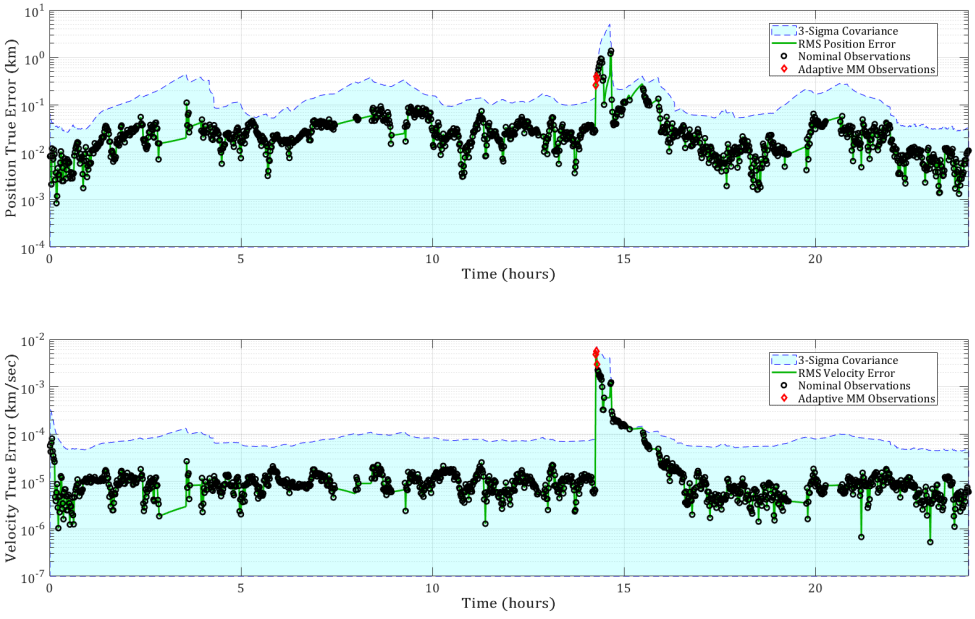

Figure B.31: A.E. Test: Lambert GPB1/FIG-Only MEOMnvr-2 Track

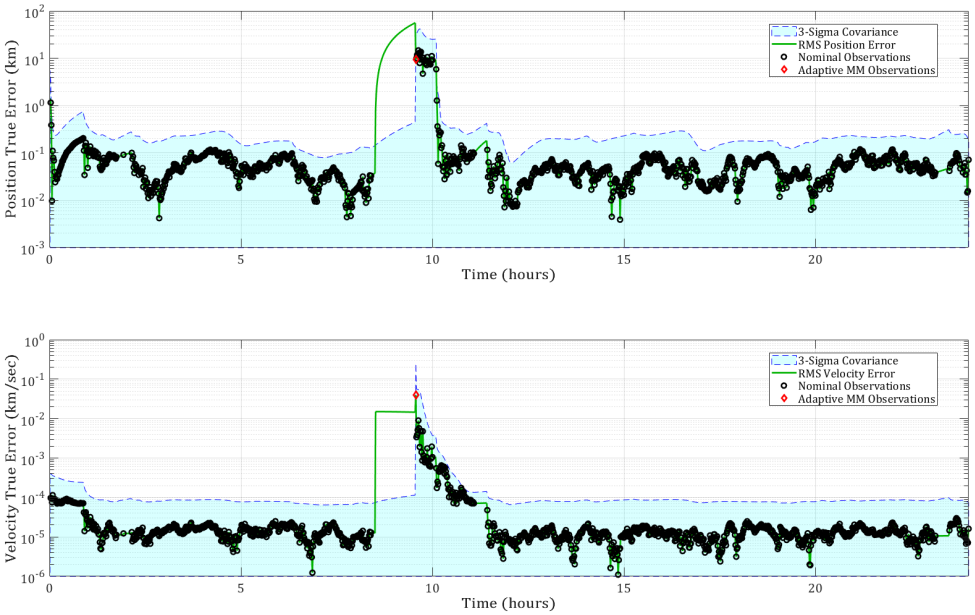

Figure B.32: A.E. Test: Lambert GPB1/FIG-Only GEOMnvr-1 Track

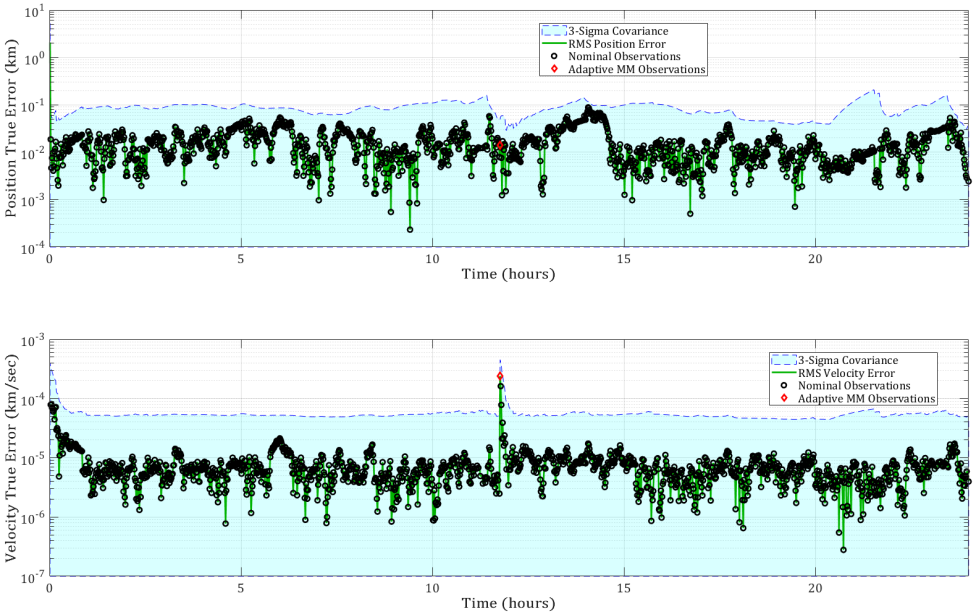

Figure B.33: A.E. Test: Lambert GPB1/FIG-Only GEOMnvr-2 Track

B.2 Continuous Observation POMDP

B.2.1 No Adaptive Estimation

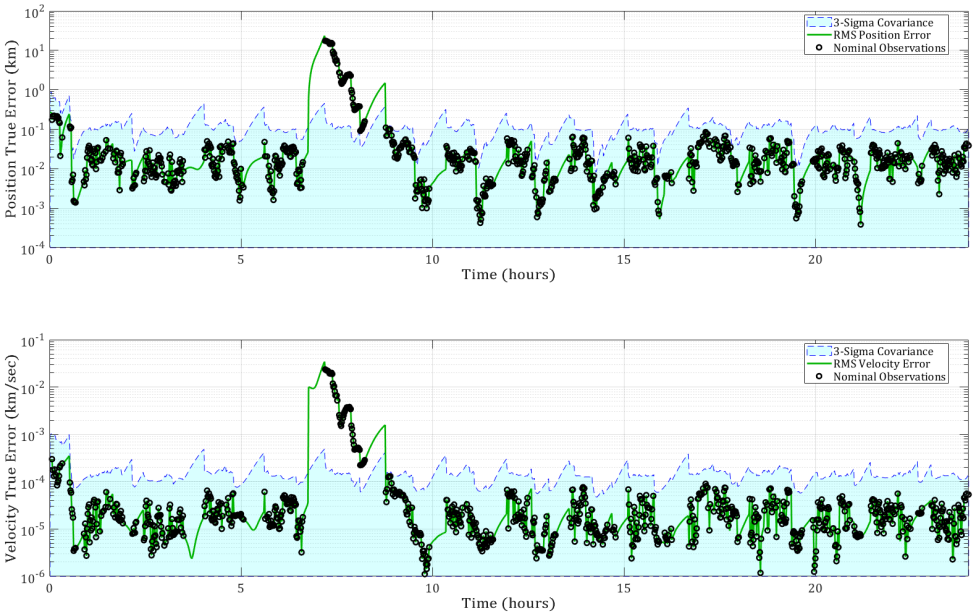

Figure B.34: A.E. Test: Nominal/Continuous LEOMnvr-1 Track

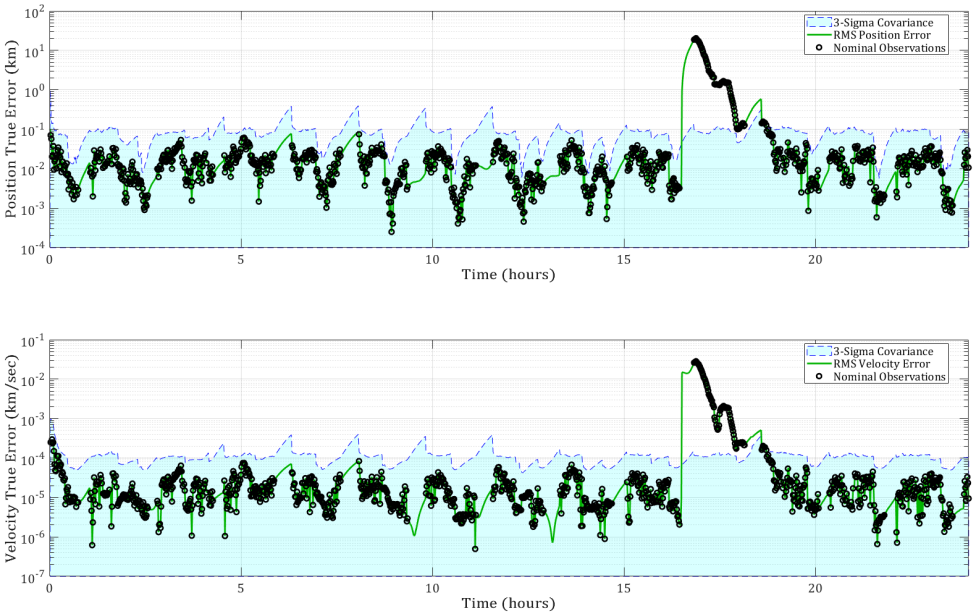

Figure B.35: A.E. Test: Nominal/Continuous LEOMnvr-2 Track

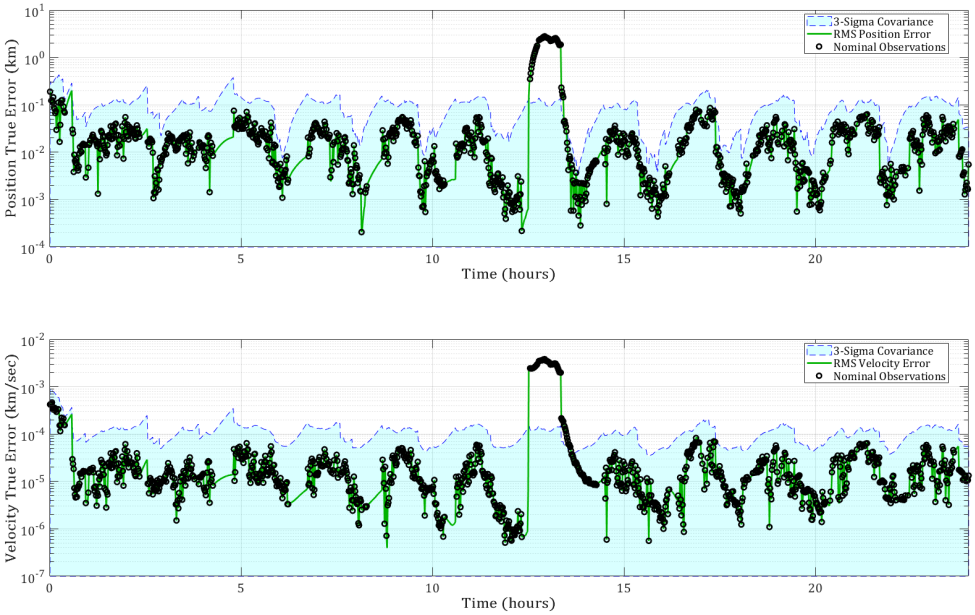

Figure B.36: A.E. Test: Nominal/Continuous LEOMnvr-3 Track

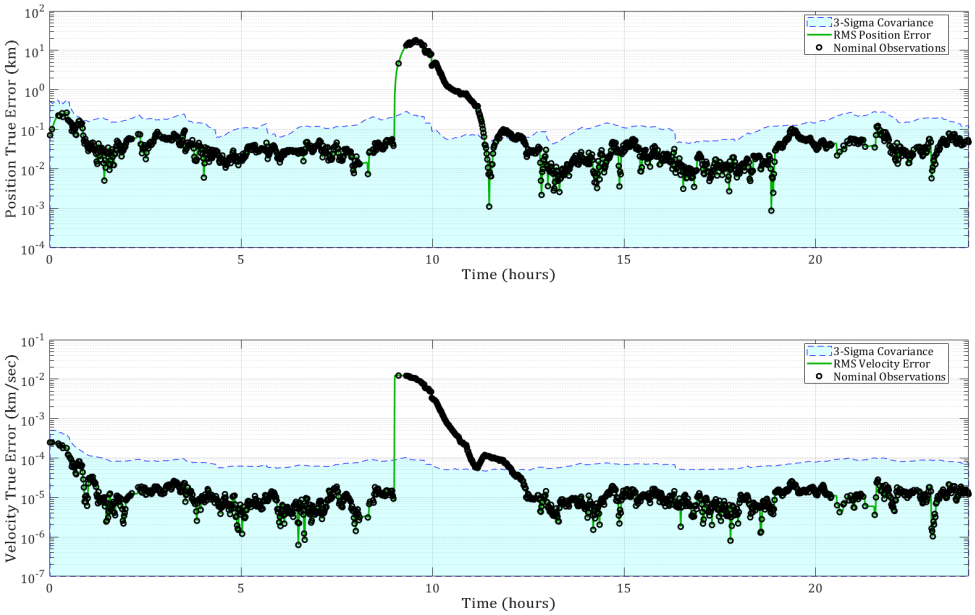

Figure B.37: A.E. Test: Nominal/Continuous MEOMnvr-1 Track

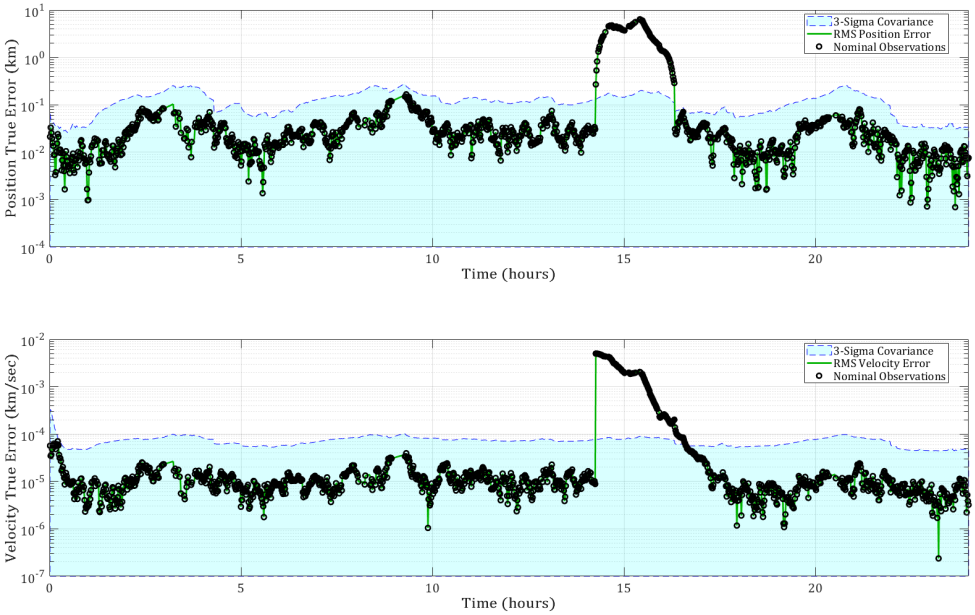

Figure B.38: A.E. Test: Nominal/Continuous MEOMnvr-2 Track

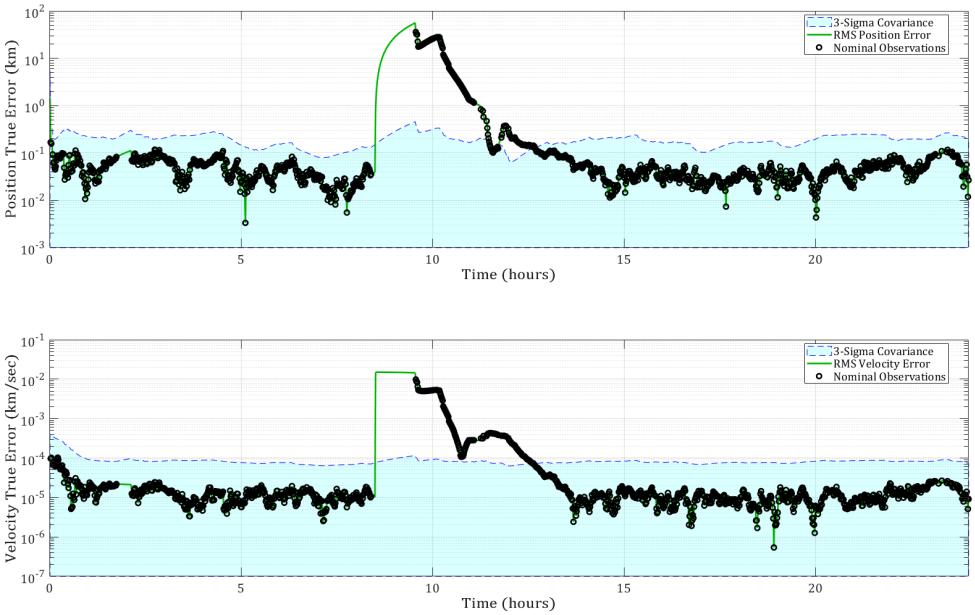

Figure B.39: A.E. Test: Nominal/Continuous GEOMnvr-1 Track

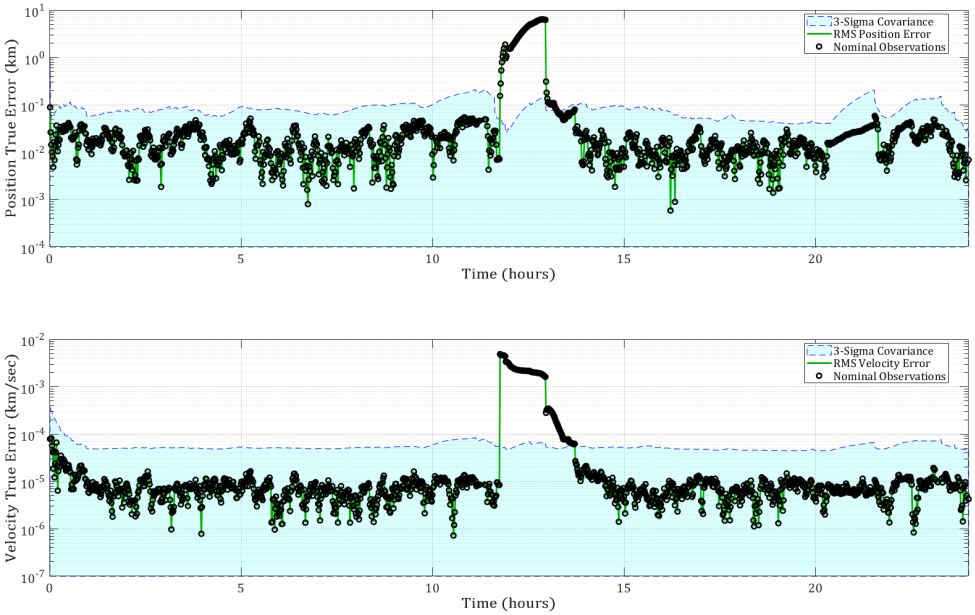

Figure B.40: A.E. Test: Nominal/Continuous GEOMnvr-2 Track

B.2.2 Covariance Inflation

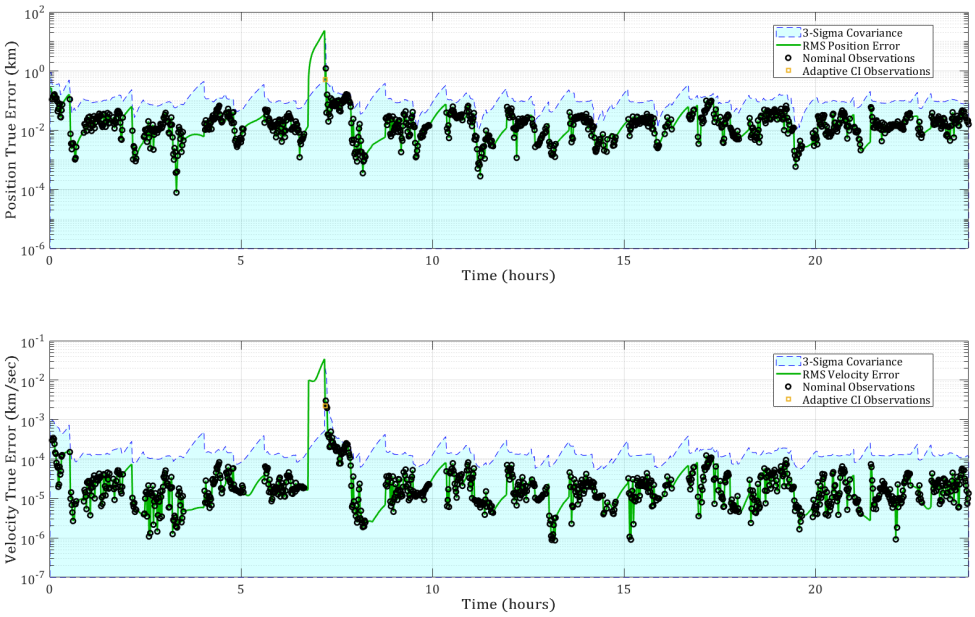

Figure B.41: A.E. Test: Inflation/Continuous LEOMnvr-1 Track

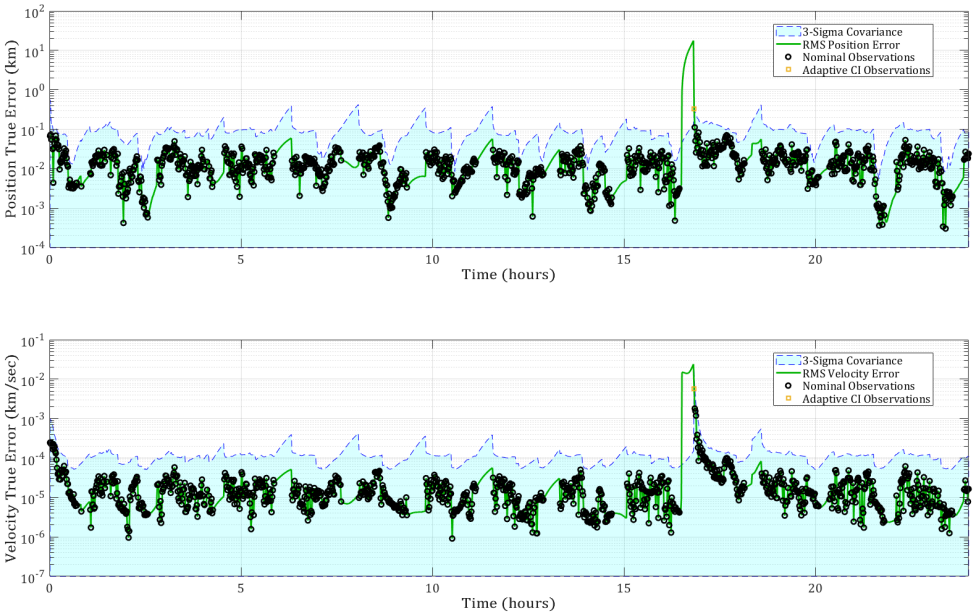

Figure B.42: A.E. Test: Inflation/Continuous LEOMnvr-2 Track

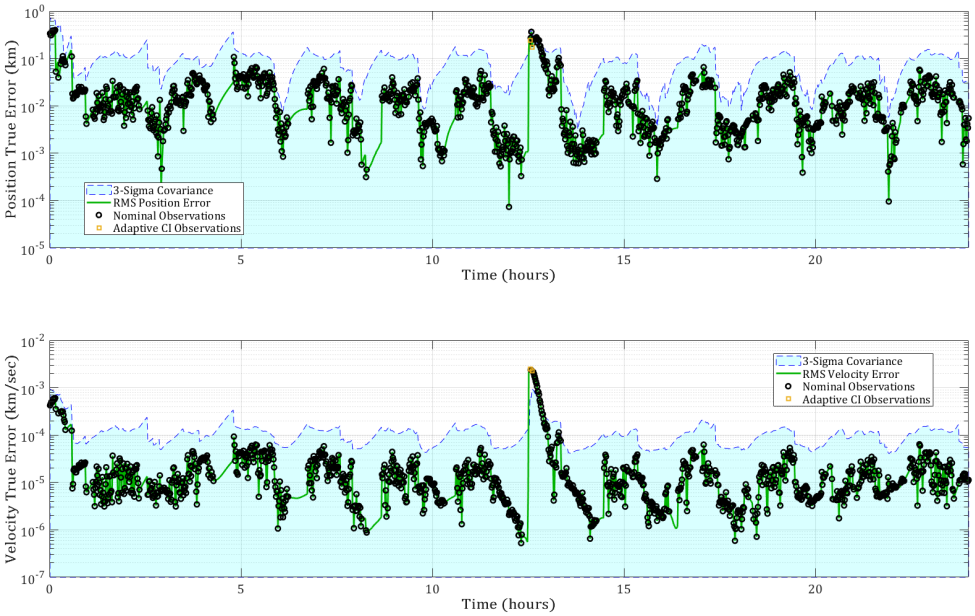

Figure B.43: A.E. Test: Inflation/Continuous LEOMnvr-3 Track

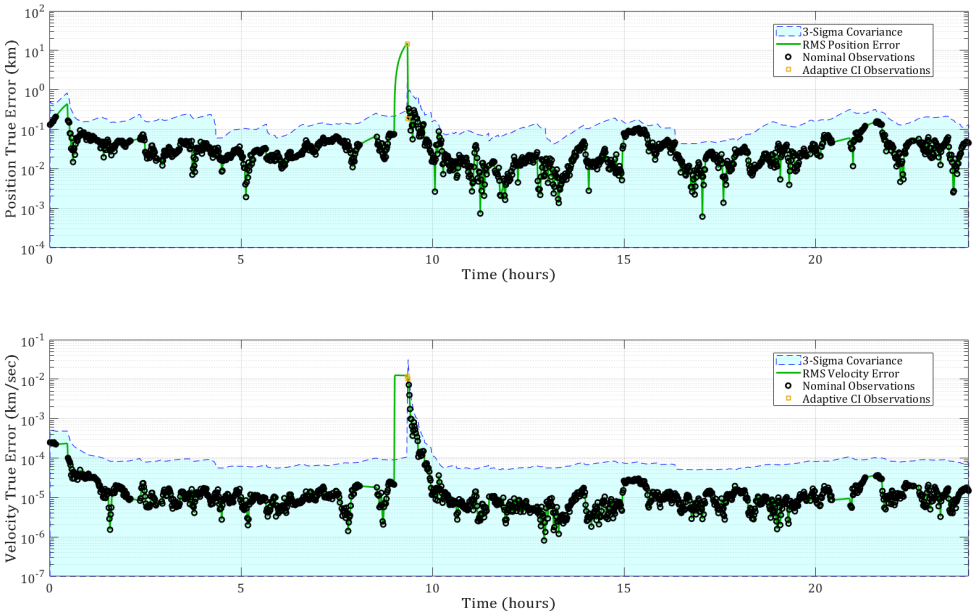

Figure B.44: A.E. Test: Inflation/Continuous MEOMnvr-1 Track

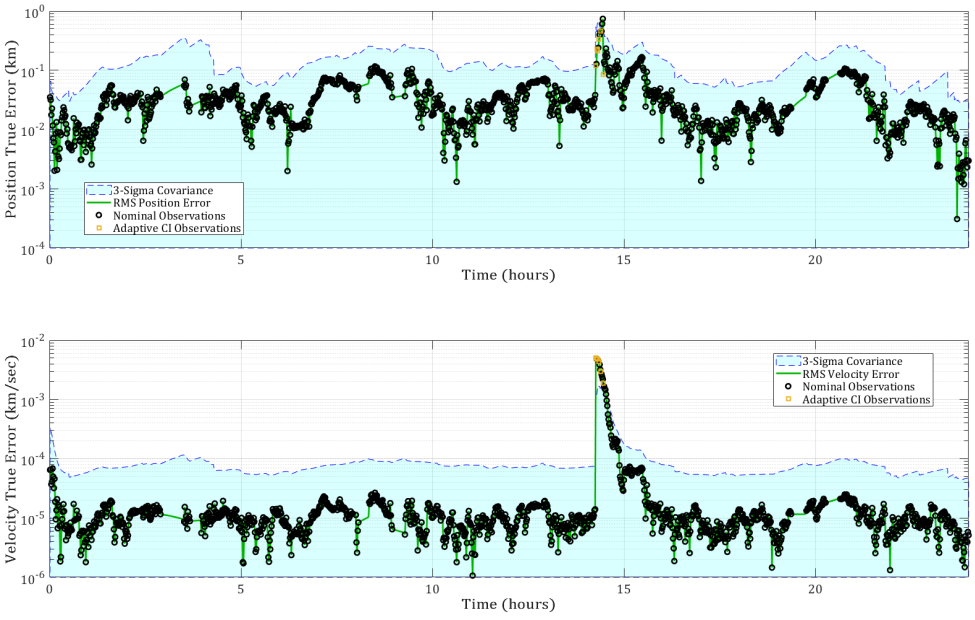

Figure B.45: A.E. Test: Inflation/Continuous MEOMnvr-2 Track

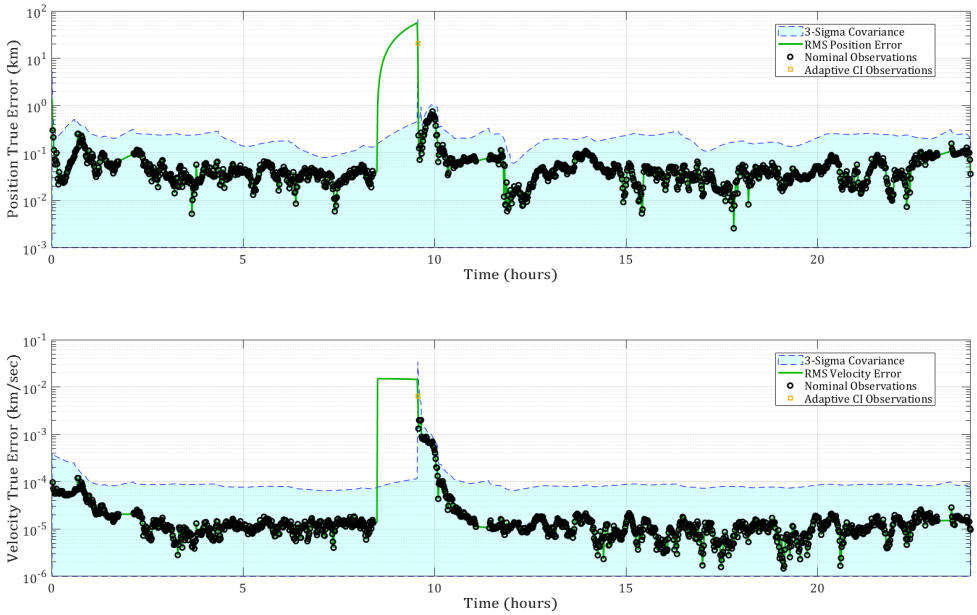

Figure B.46: A.E. Test: Inflation/Continuous GEOMnvr-1 Track

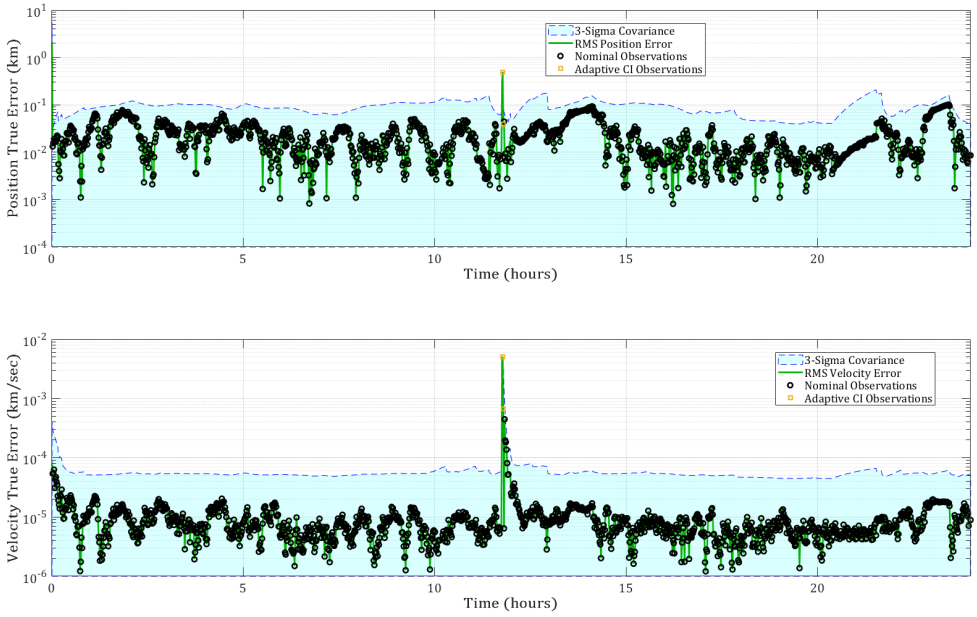

Figure B.47: A.E. Test: Inflation/Continuous GEOMnvr-2 Track

B.2.3 Shotgun SMM

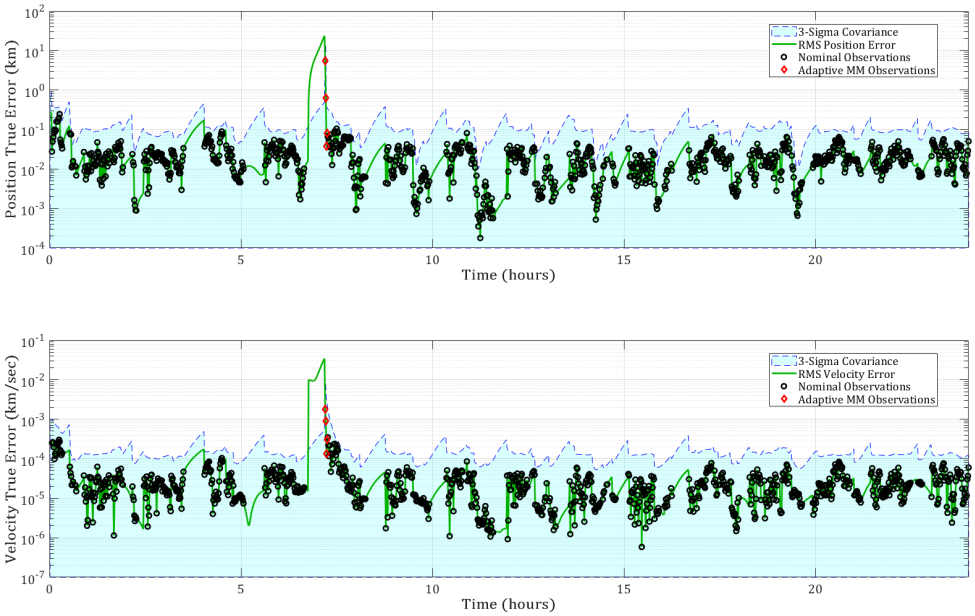

Figure B.48: A.E. Test: Shotgun SMM/Continuous LEOMnvr-1 Track

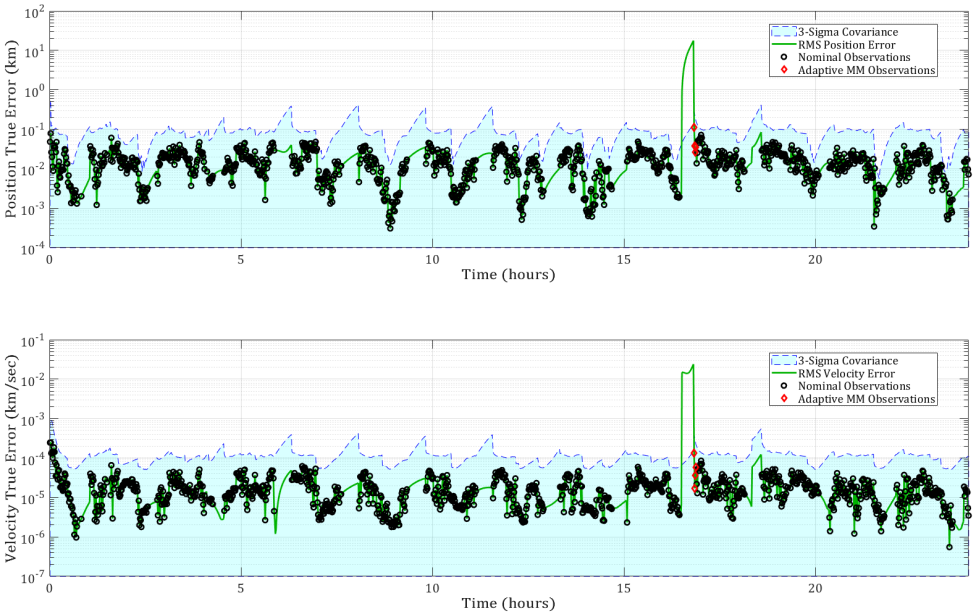

Figure B.49: A.E. Test: Shotgun SMM/Continuous LEOMnvr-2 Track

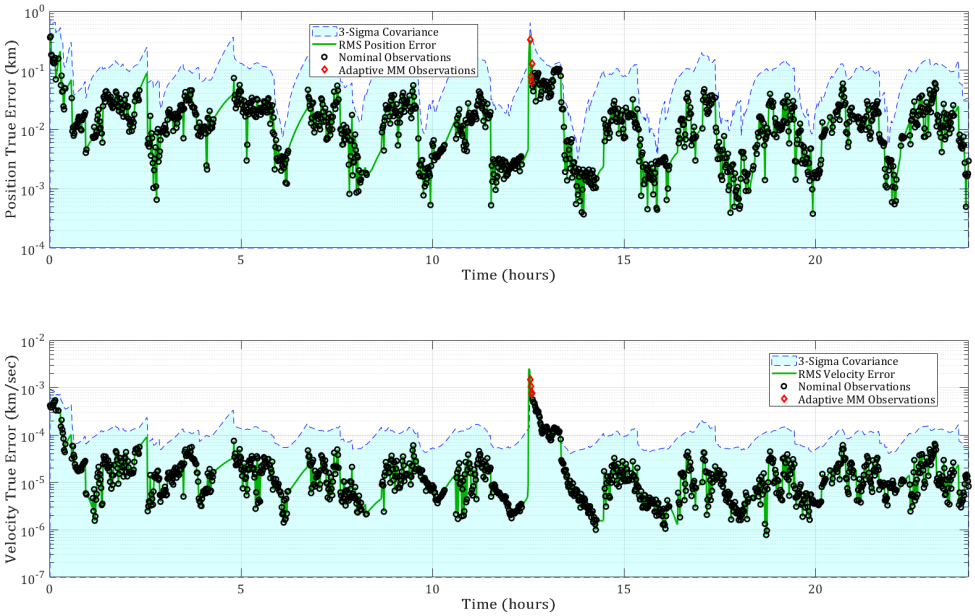

Figure B.50: A.E. Test: Shotgun SMM/Continuous LEOMnvr-3 Track

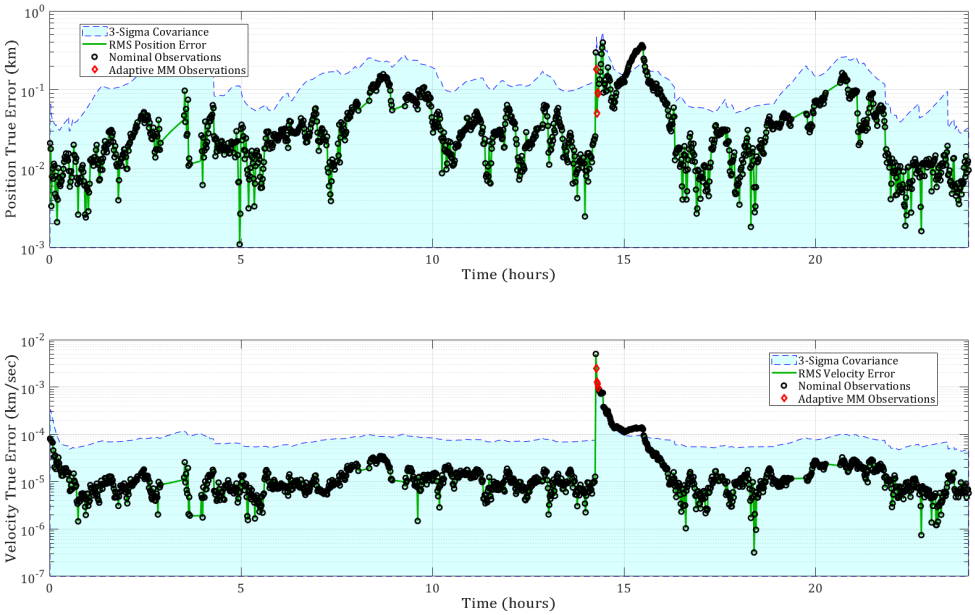

Figure B.51: A.E. Test: Shotgun SMM/Continuous MEOMnvr-2 Track

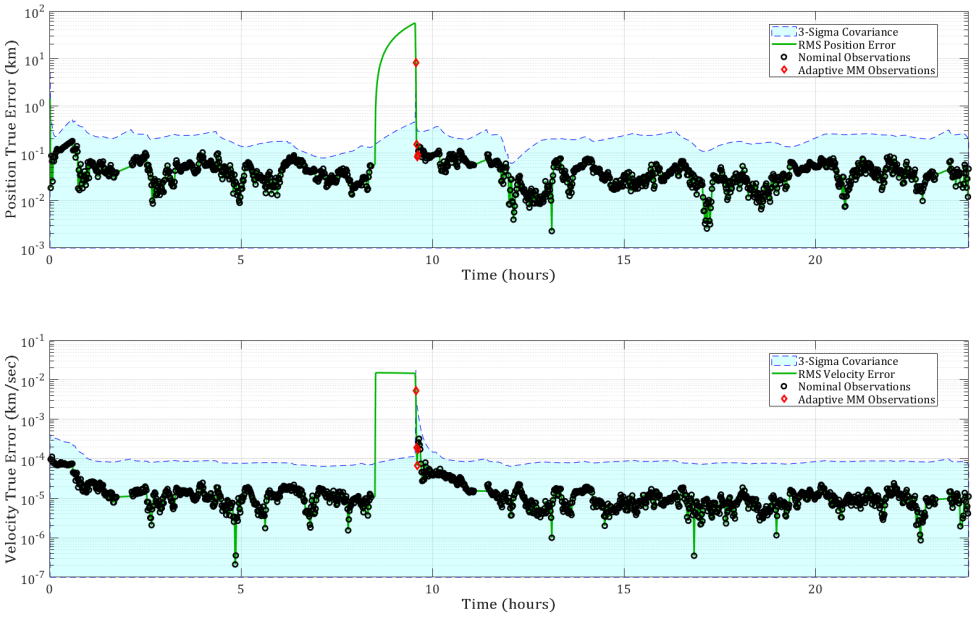

Figure B.52: A.E. Test: Shotgun SMM/Continuous GEOMnvr-1 Track

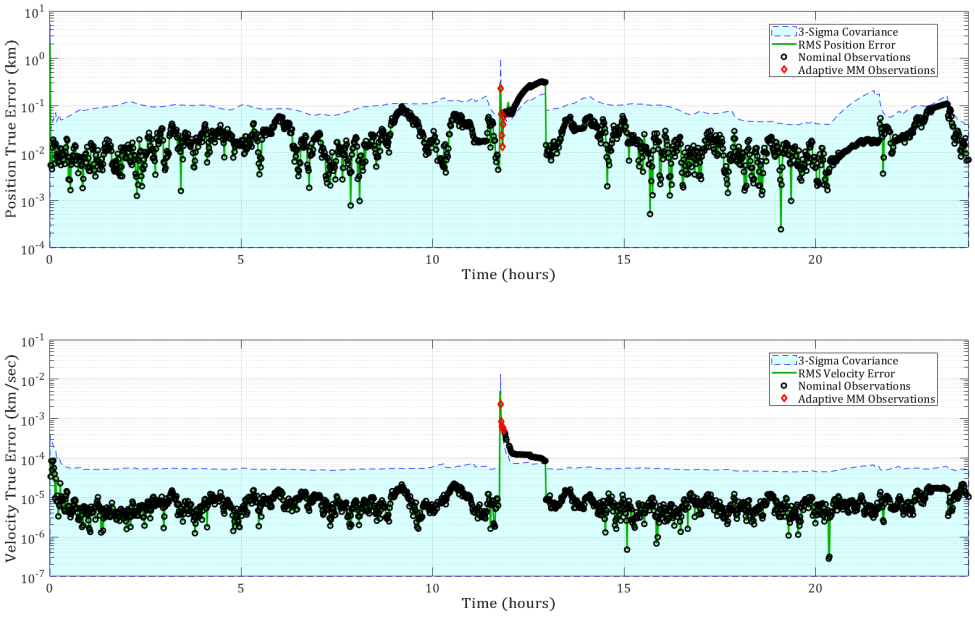

Figure B.53: A.E. Test: Shotgun SMM/Continuous GEOMnvr-2 Track

B.2.4 Lambert SMM

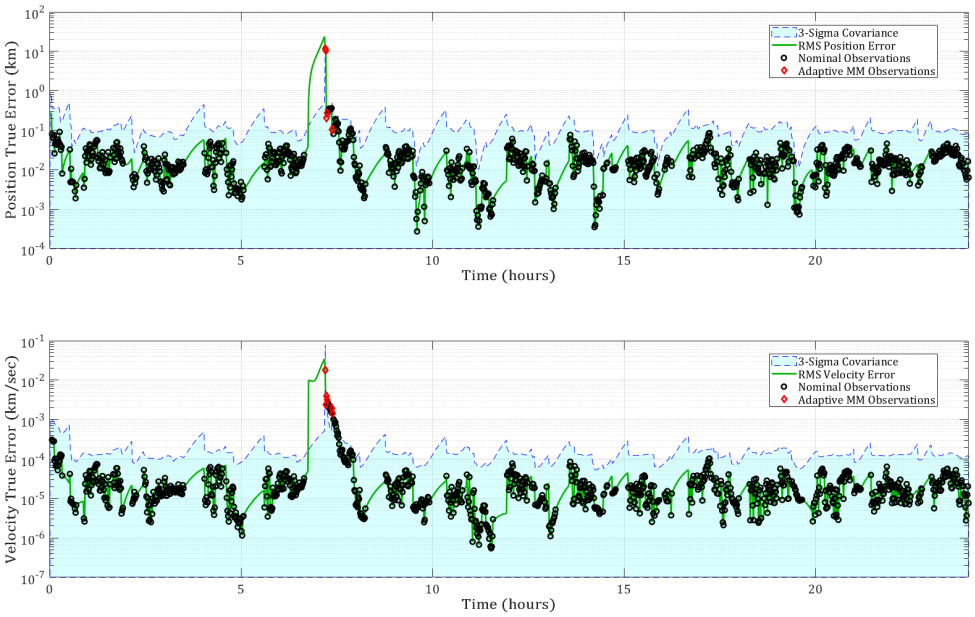

Figure B.54: A.E. Test: Lambert SMM/Continuous LEOMnvr-1 Track

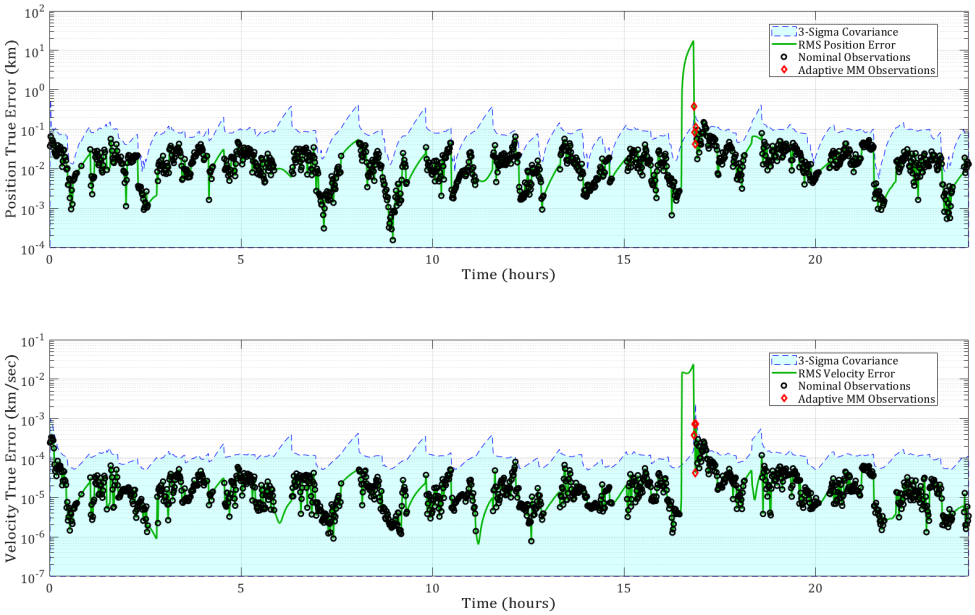

Figure B.55: A.E. Test: Lambert SMM/Continuous LEOMnvr-2 Track

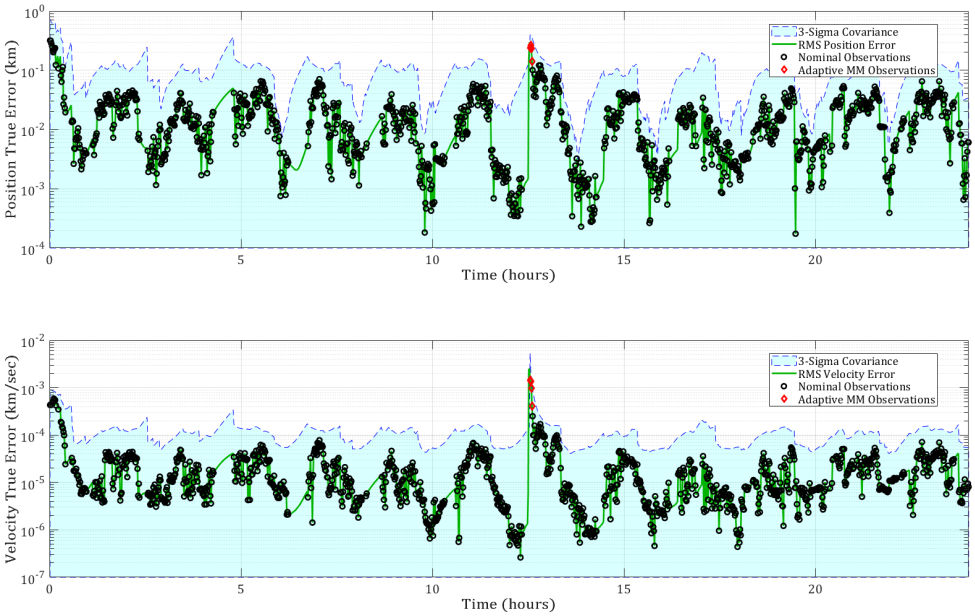

Figure B.56: A.E. Test: Lambert SMM/Continuous LEOMnvr-3 Track

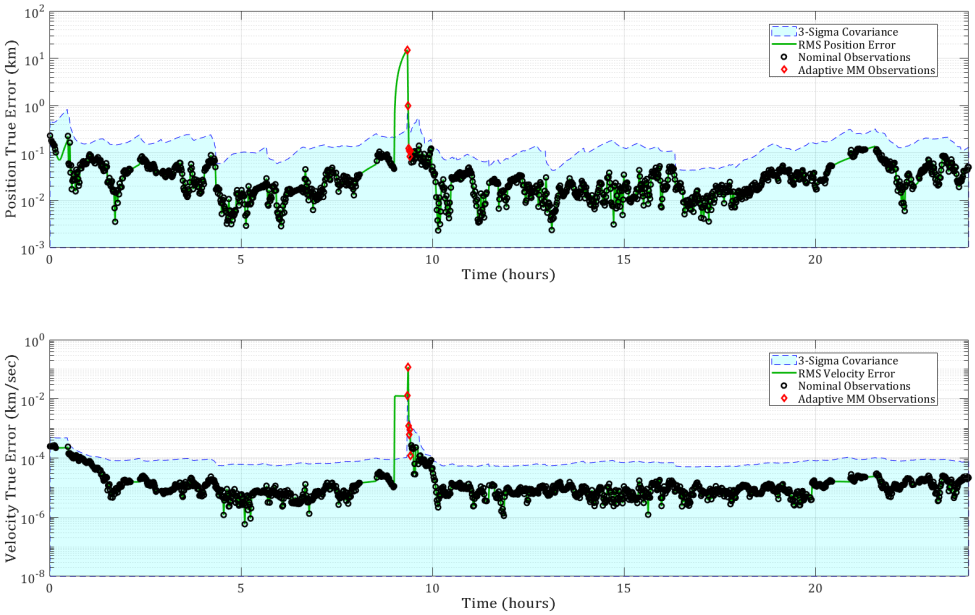

Figure B.57: A.E. Test: Lambert SMM/Continuous MEOMnvr-1 Track

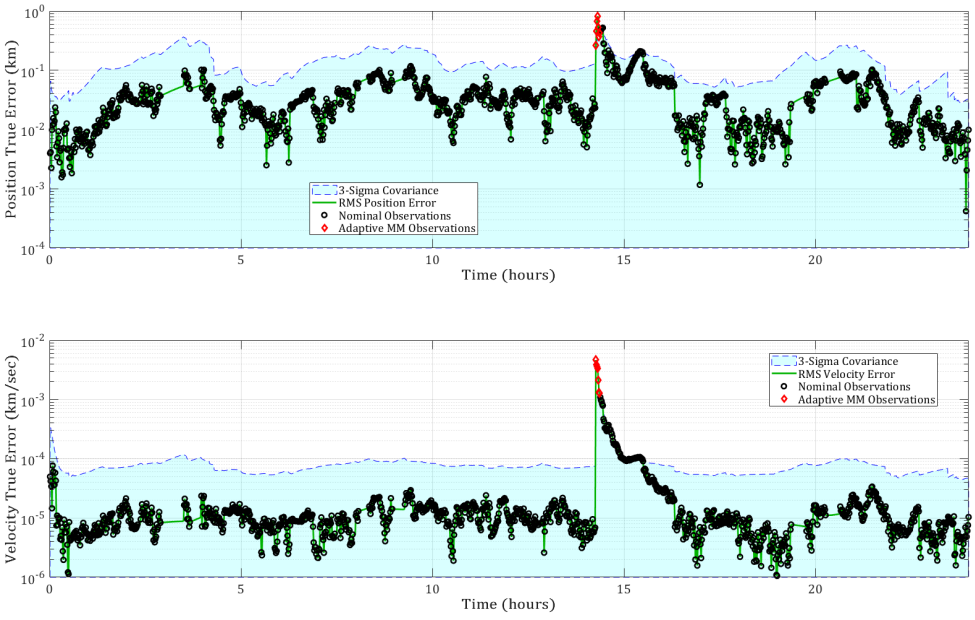

Figure B.58: A.E. Test: Lambert SMM/Continuous MEOMnvr-2 Track

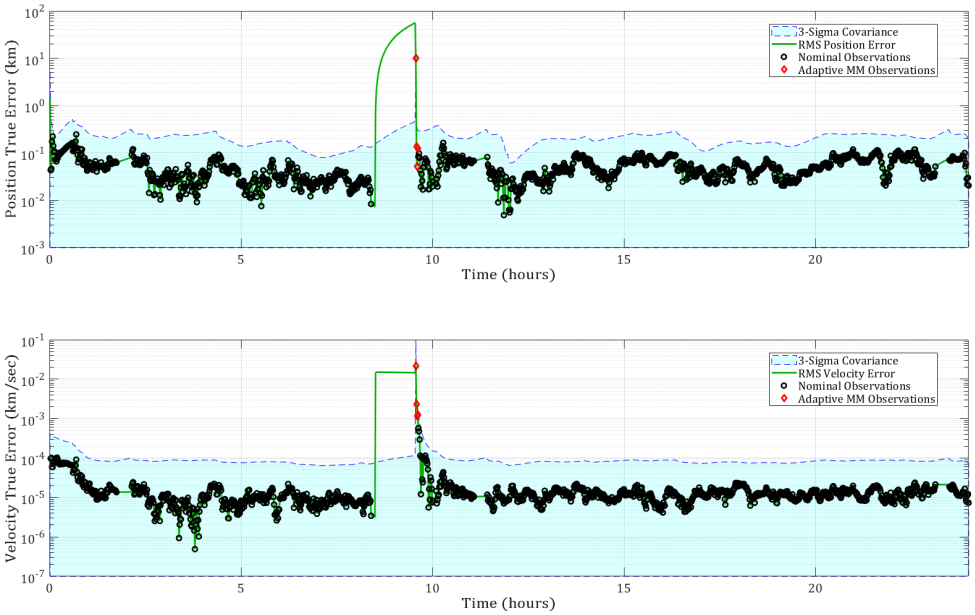

Figure B.59: A.E. Test: Lambert SMM/Continuous GEOMnvr-1 Track

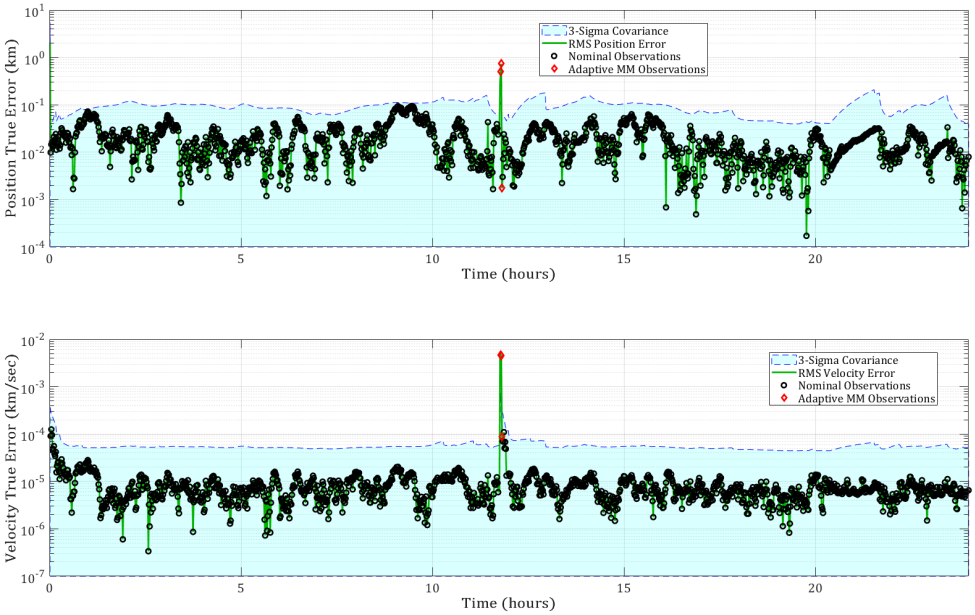

Figure B.60: A.E. Test: Lambert SMM/Continuous GEOMnvr-2 Track

B.2.5 Lambert GPB1

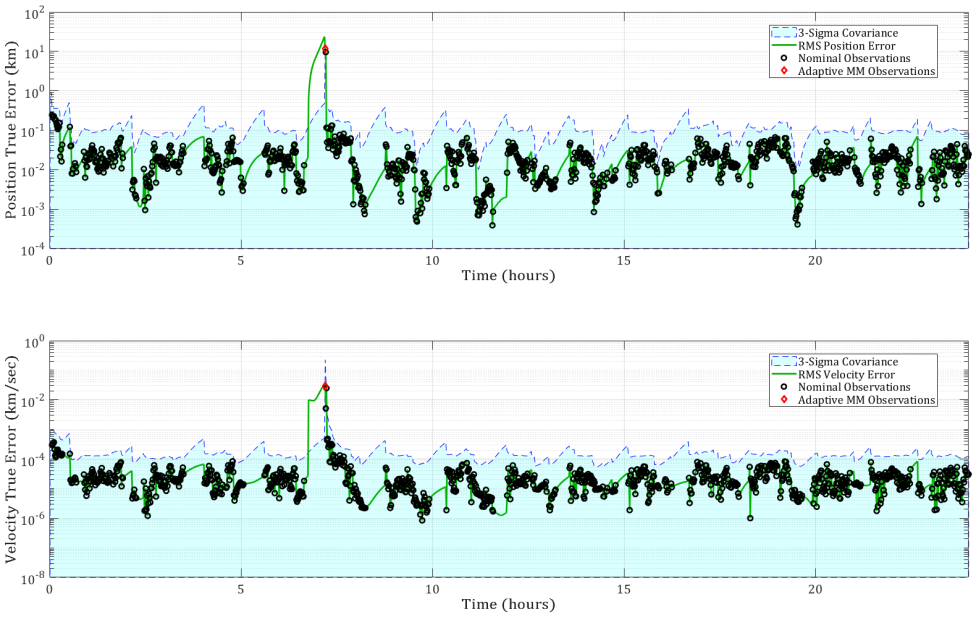

Figure B.61: A.E. Test: Lambert GPB1/Continuous LEOMnvr-1 Track

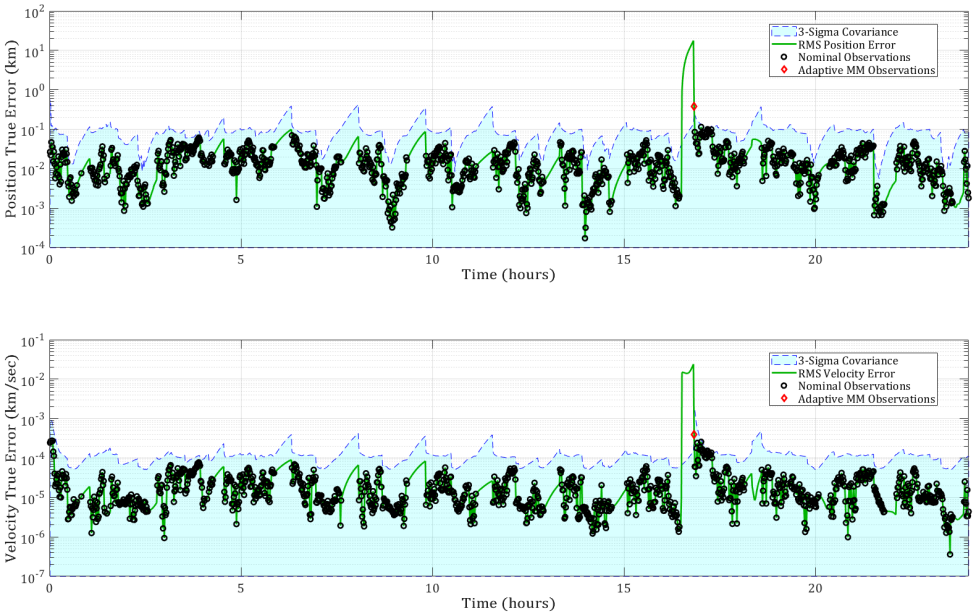

Figure B.62: A.E. Test: Lambert GPB1/Continuous LEOMnvr-2 Track

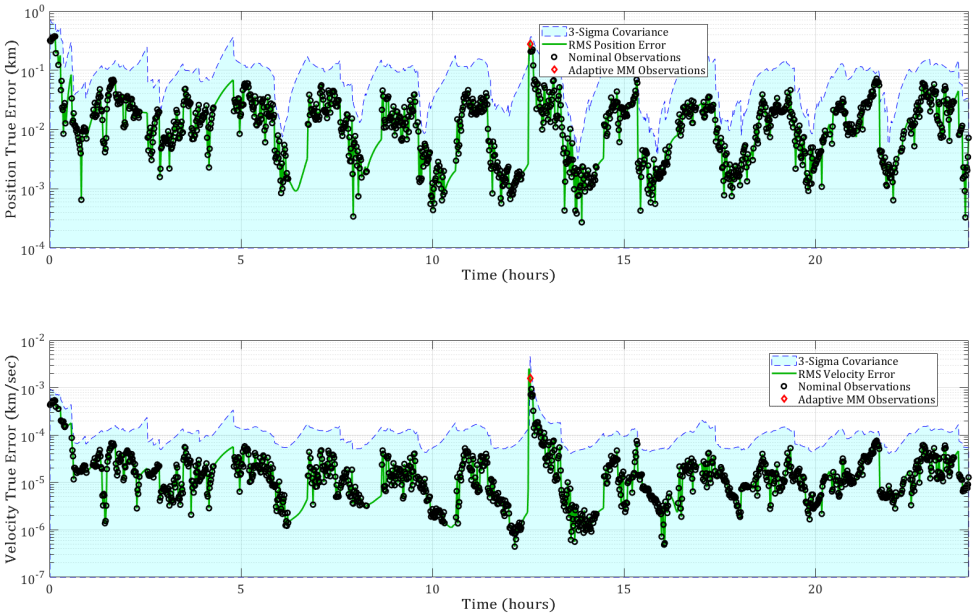

Figure B.63: A.E. Test: Lambert GPB1/Continuous LEOMnvr-3 Track

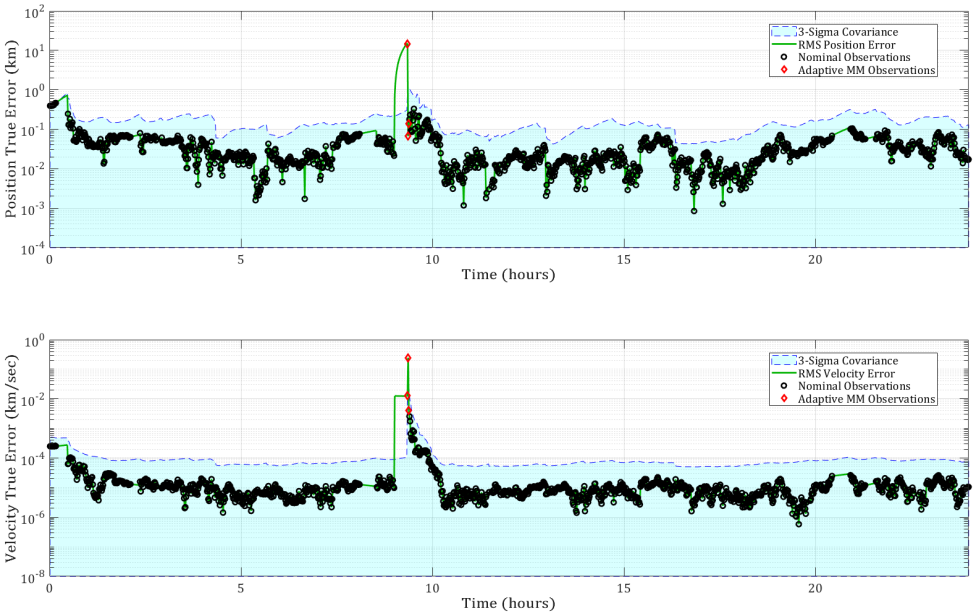

Figure B.64: A.E. Test: Lambert GPB1/Continuous MEOMnvr-1 Track

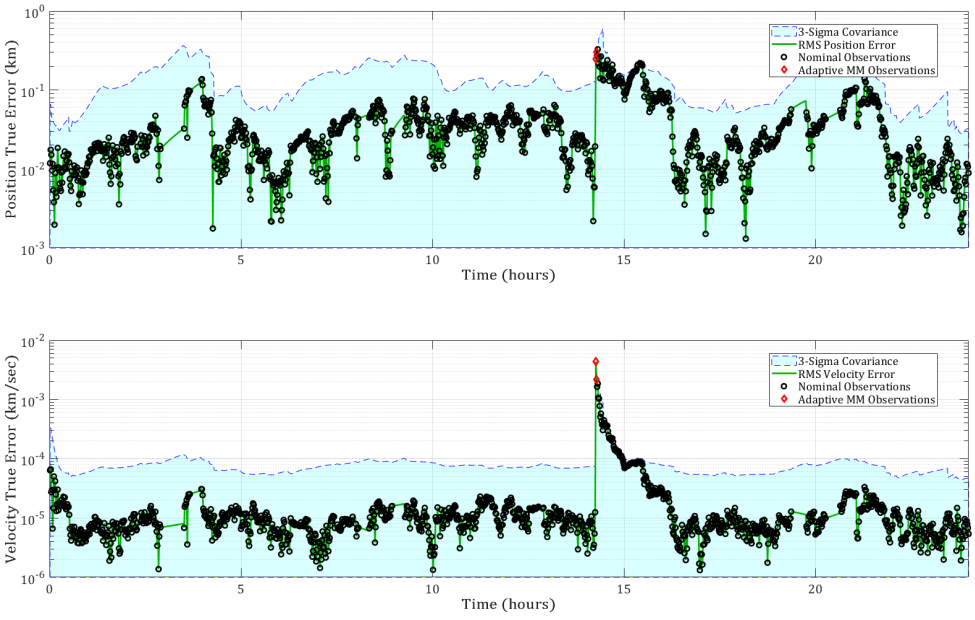

Figure B.65: A.E. Test: Lambert GPB1/Continuous MEOMnvr-2 Track

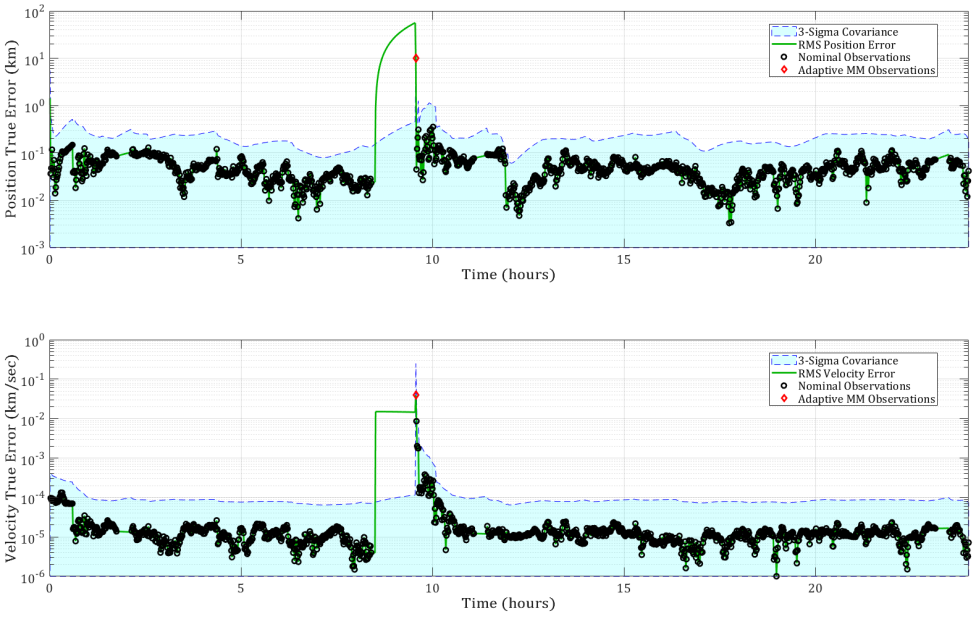

Figure B.66: A.E. Test: Lambert GPB1/Continuous GEOMnvr-1 Track

B.3 Constrained Observation POMDP

B.3.1 No Adaptive Estimation

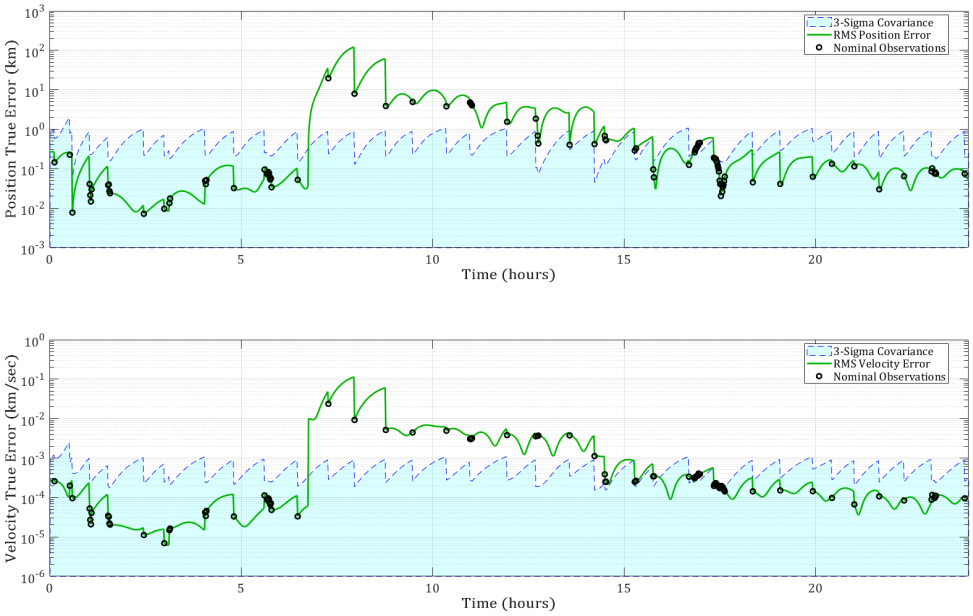

Figure B.67: A.E. Test: Nominal/Constrained LEOMnvr-1 Track

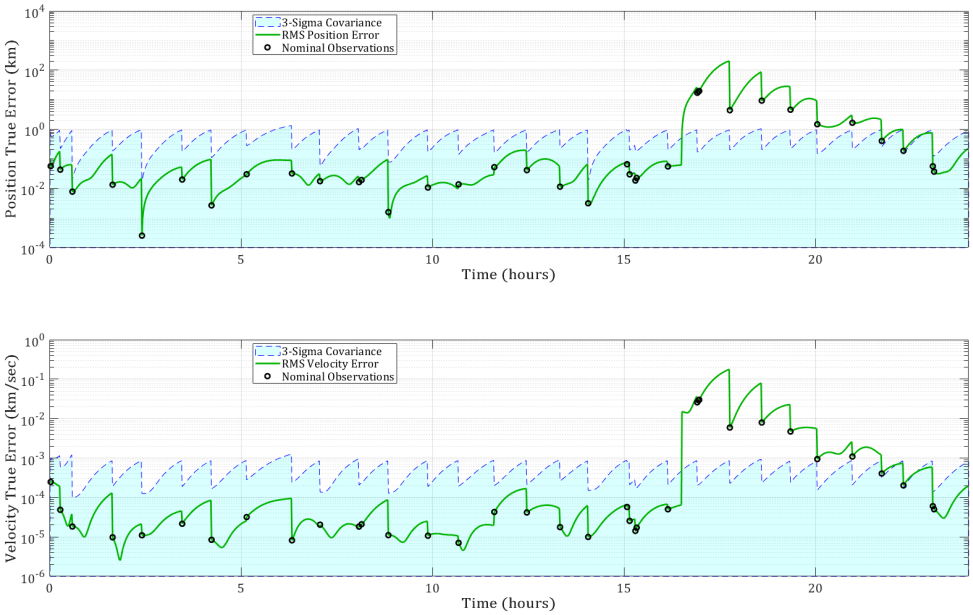

Figure B.68: A.E. Test: Nominal/Constrained LEOMnvr-2 Track

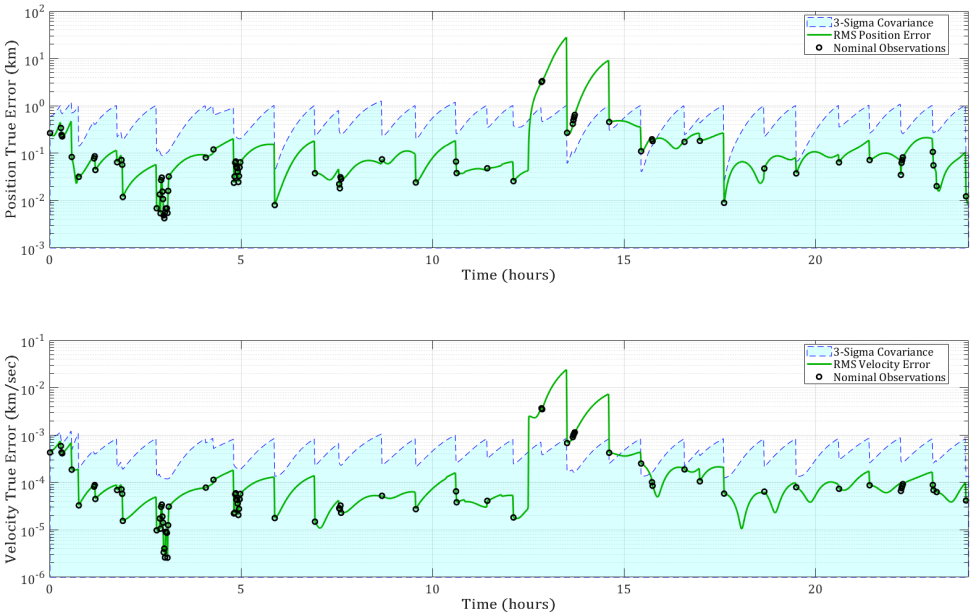

Figure B.69: A.E. Test: Nominal/Constrained LEOMnvr-3 Track

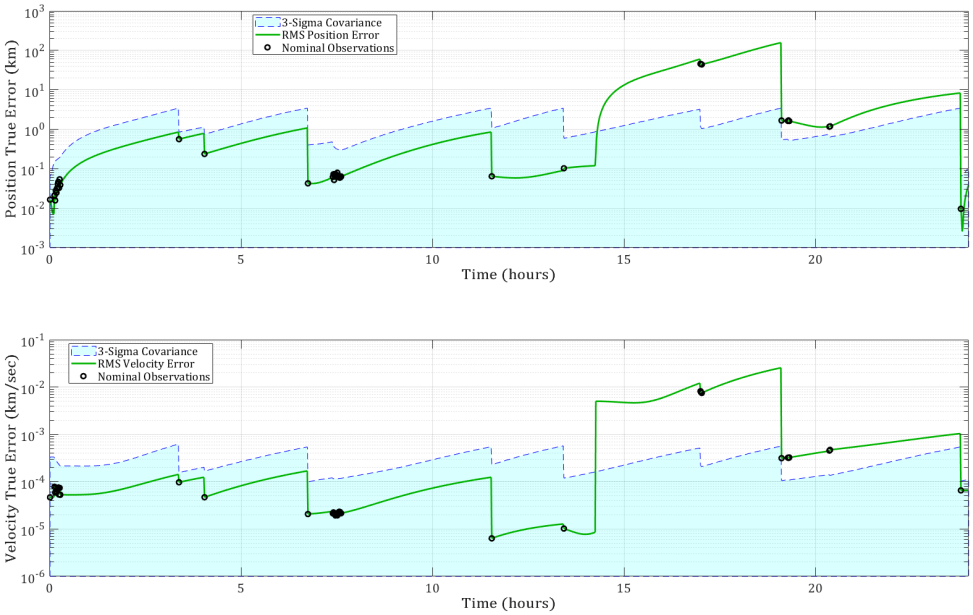

Figure B.70: A.E. Test: Nominal/Constrained MEOMnvr-2 Track

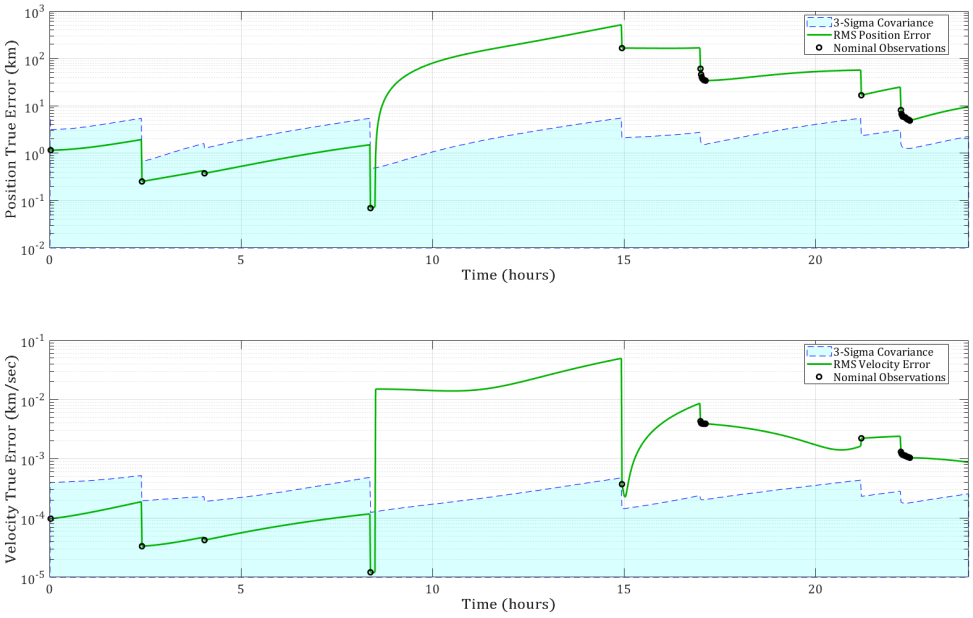

Figure B.71: A.E. Test: Nominal/Constrained GEOMnvr-1 Track

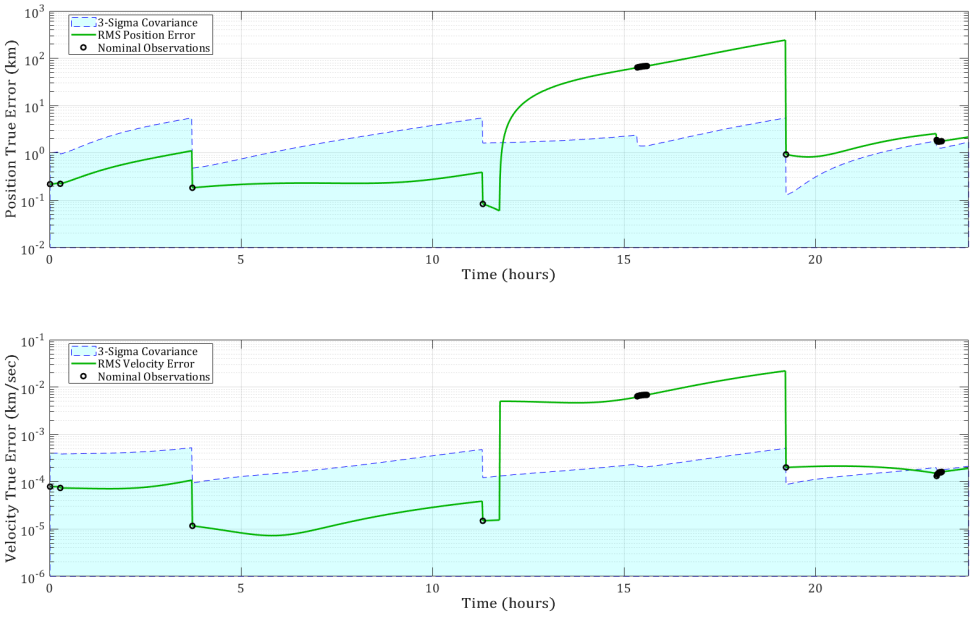

Figure B.72: A.E. Test: Nominal/Constrained GEOMnvr-2 Track

B.3.2 Covariance Inflation

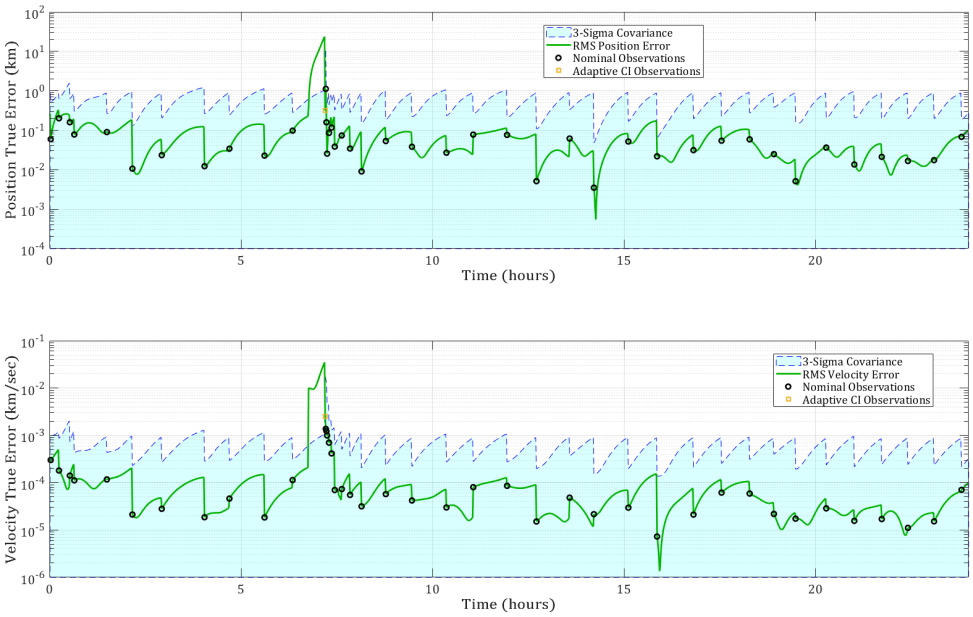

Figure B.73: A.E. Test: Inflation/Constrained LEOMnvr-1 Track

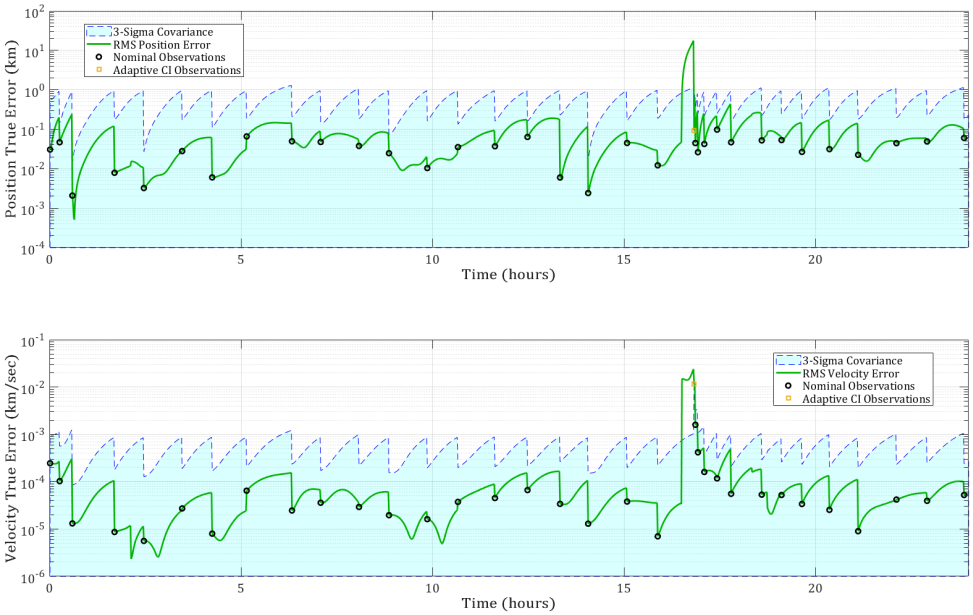

Figure B.74: A.E. Test: Inflation/Constrained LEOMnvr-2 Track

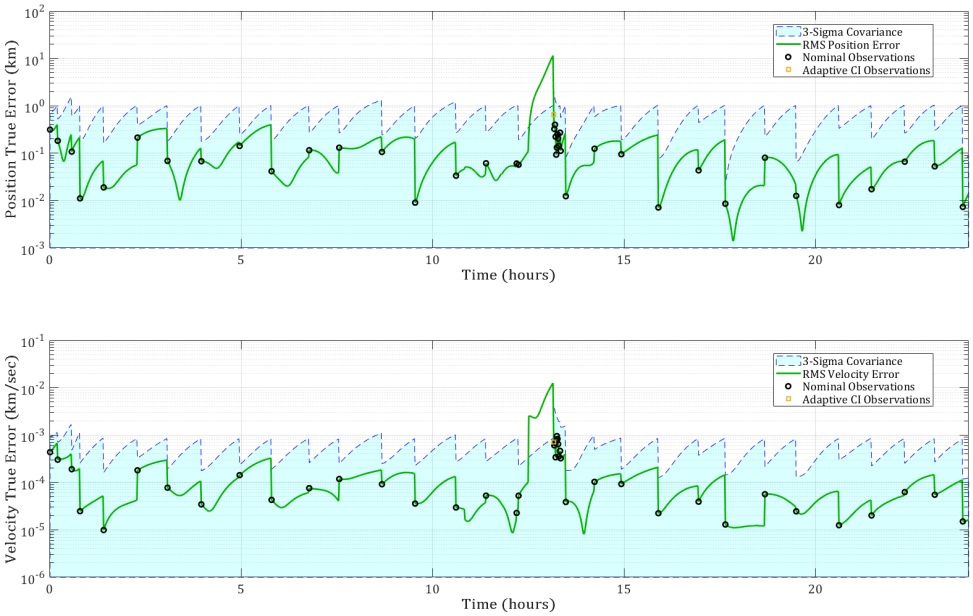

Figure B.75: A.E. Test: Inflation/Constrained LEOMnvr-3 Track

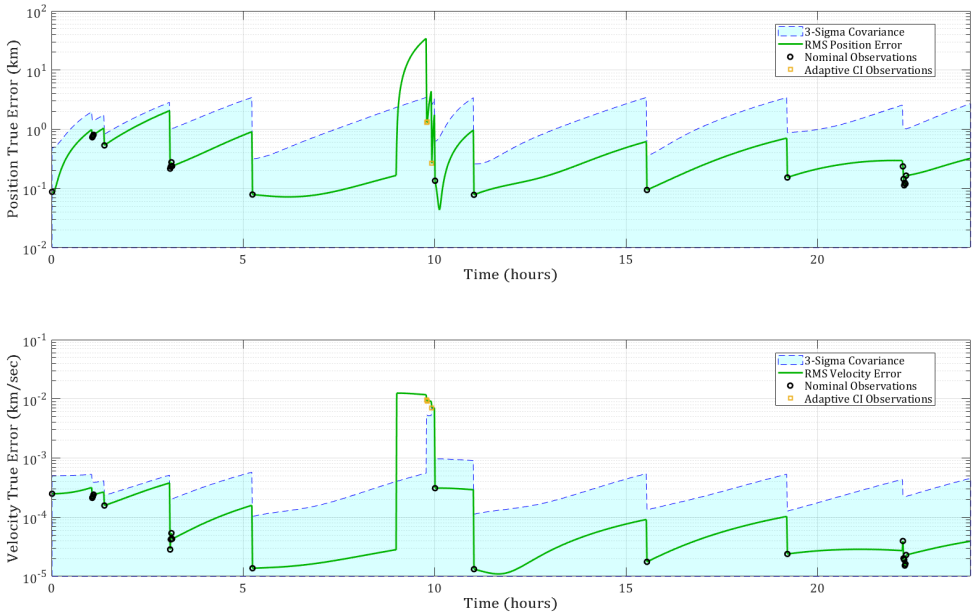

Figure B.76: A.E. Test: Inflation/Constrained MEOMnvr-1 Track

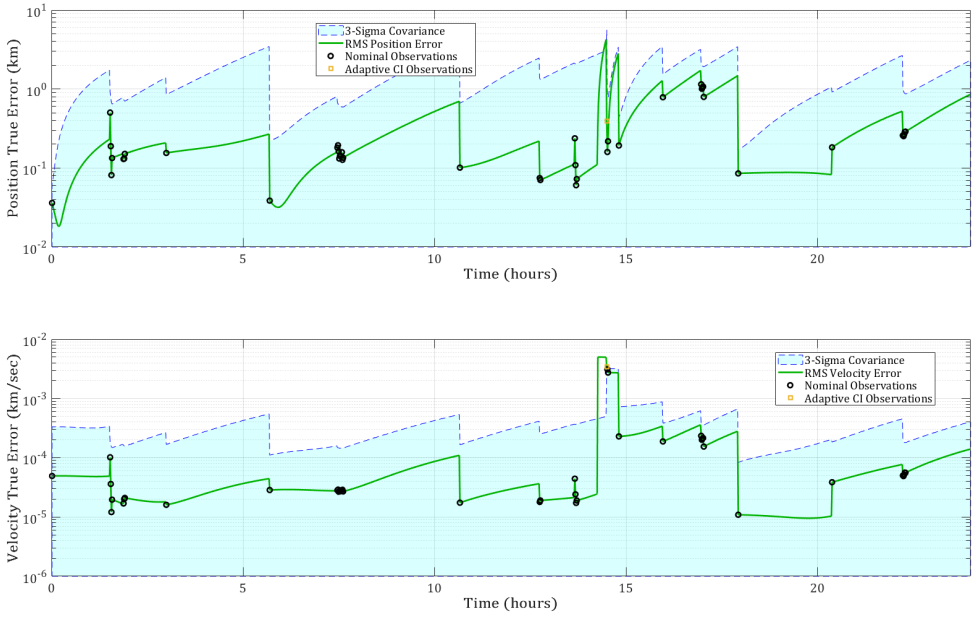

Figure B.77: A.E. Test: Inflation/Constrained MEOMnvr-2 Track

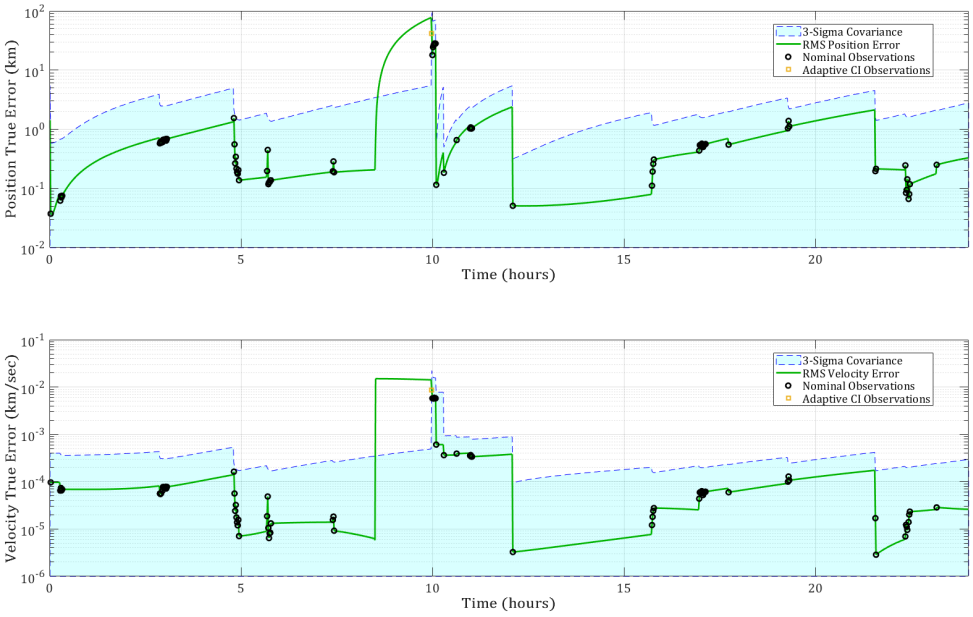

Figure B.78: A.E. Test: Inflation/Constrained GEOMnvr-1 Track

B.3.3 Shotgun SMM

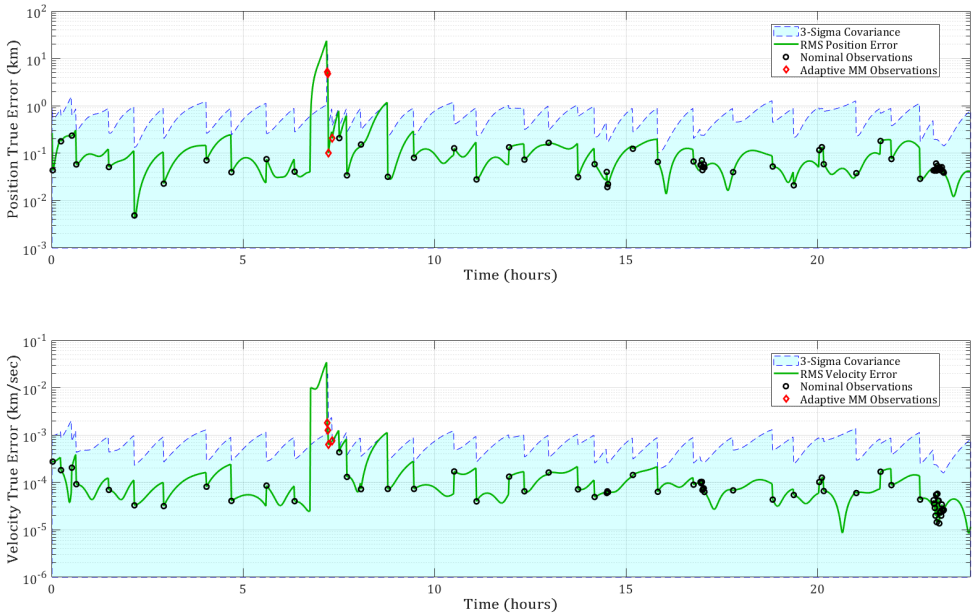

Figure B.79: A.E. Test: Shotgun SMM/Constrained LEOMnvr-1 Track

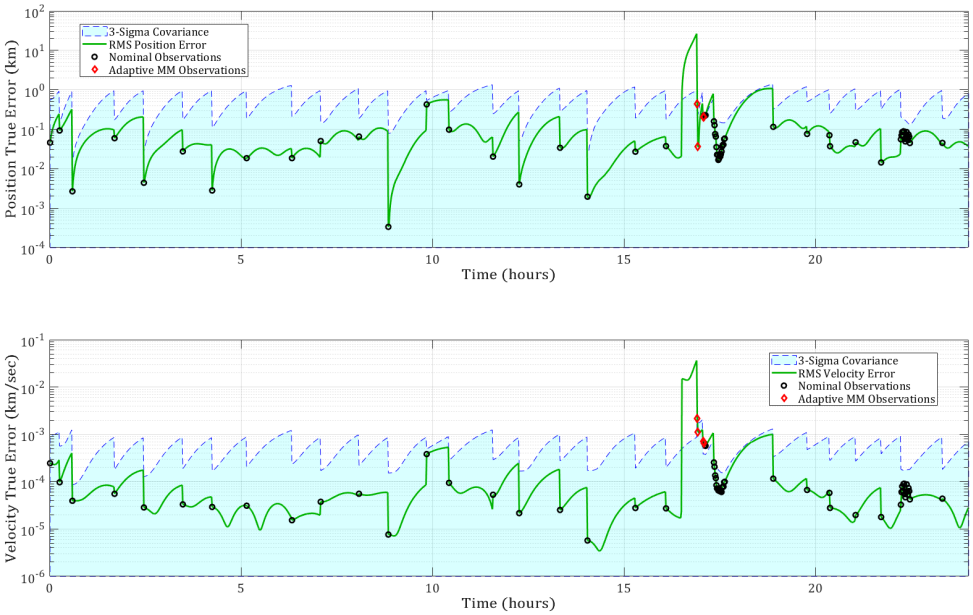

Figure B.80: A.E. Test: Shotgun SMM/Constrained LEOMnvr-2 Track

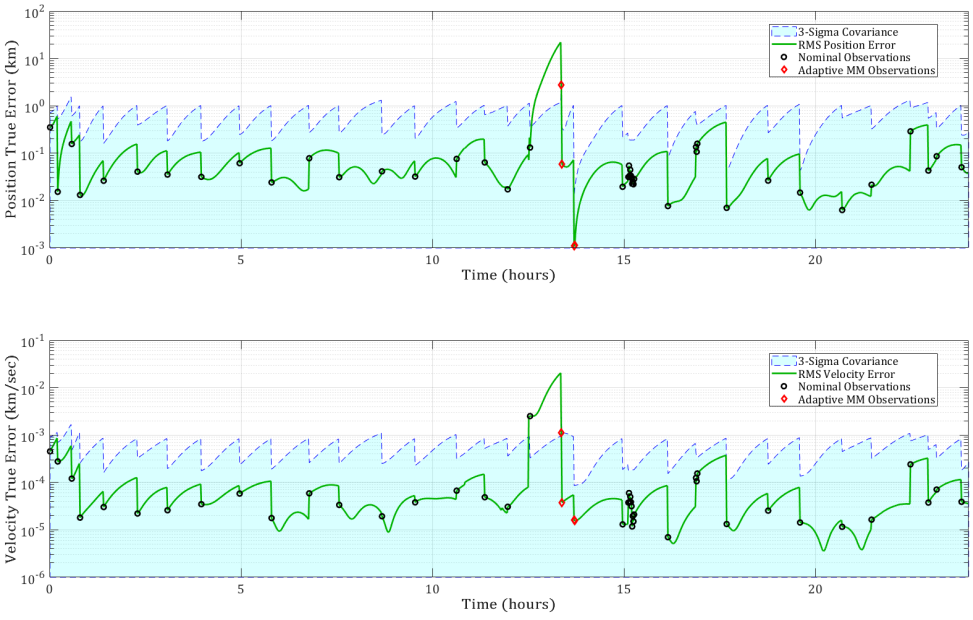

Figure B.81: A.E. Test: Shotgun SMM/Constrained LEOMnvr-3 Track

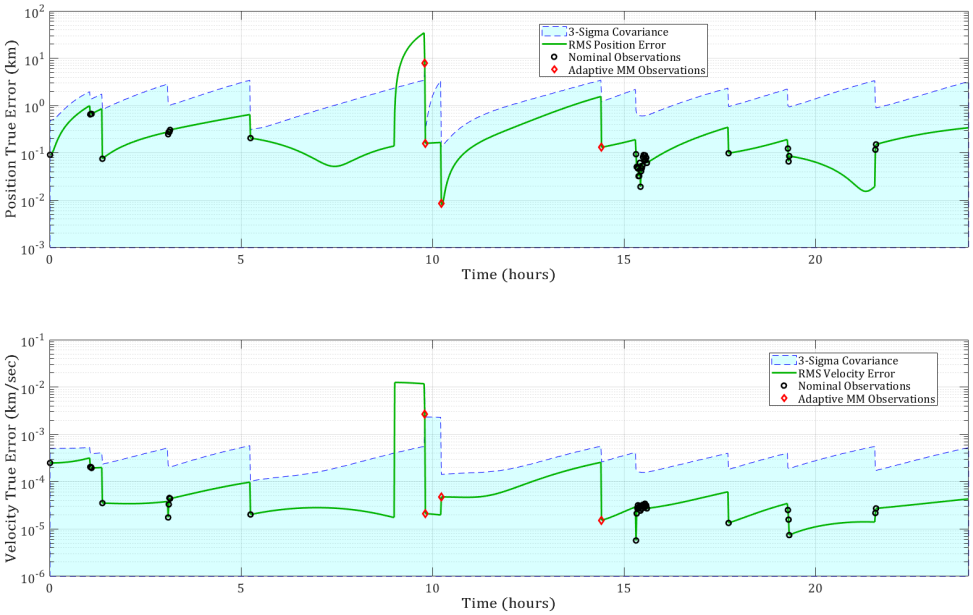

Figure B.82: A.E. Test: Shotgun SMM/Constrained MEOMnvr-1 Track

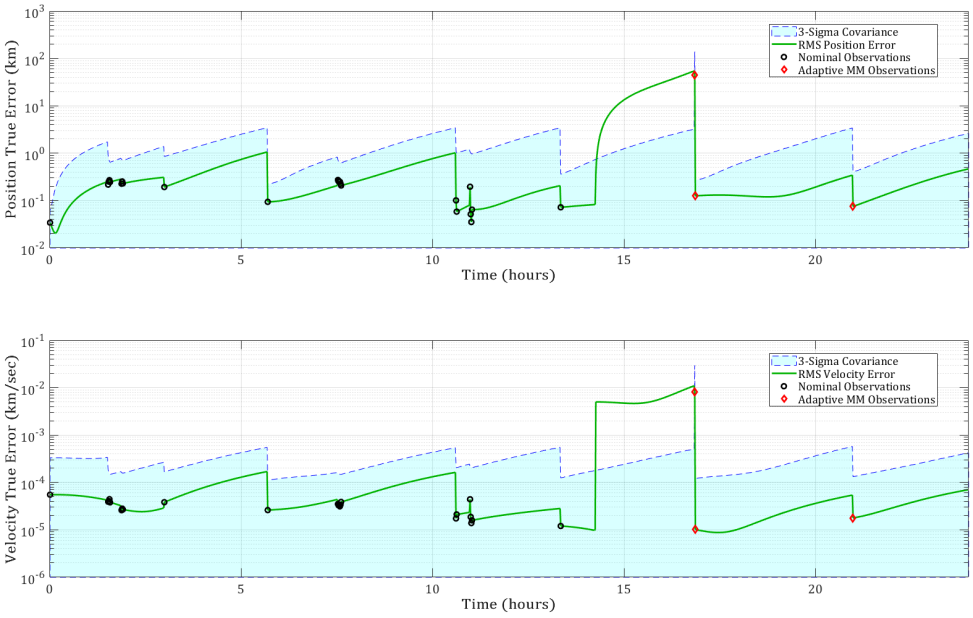

Figure B.83: A.E. Test: Shotgun SMM/Constrained MEOMnvr-2 Track

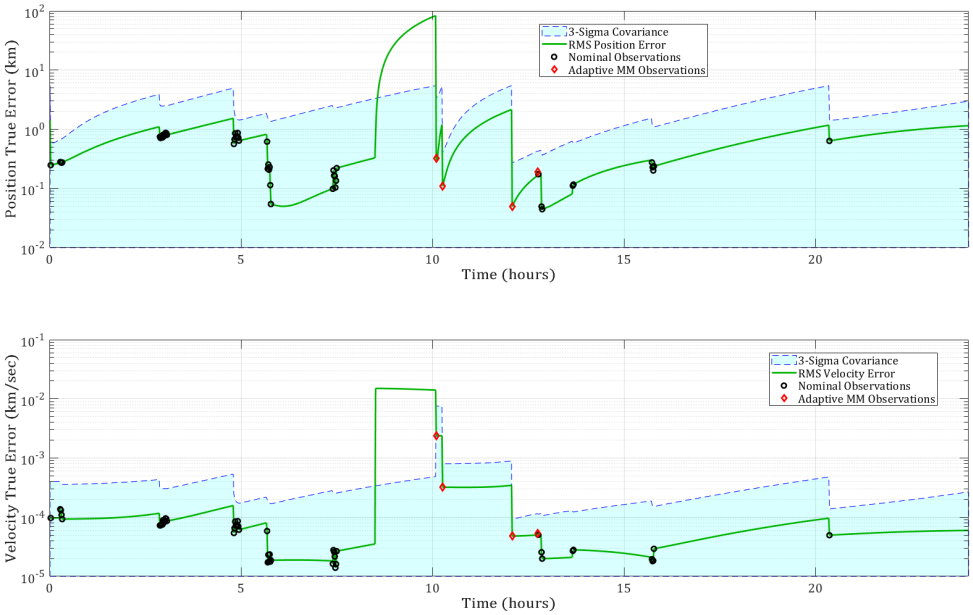

Figure B.84: A.E. Test: Shotgun SMM/Constrained GEOMnvr-1 Track

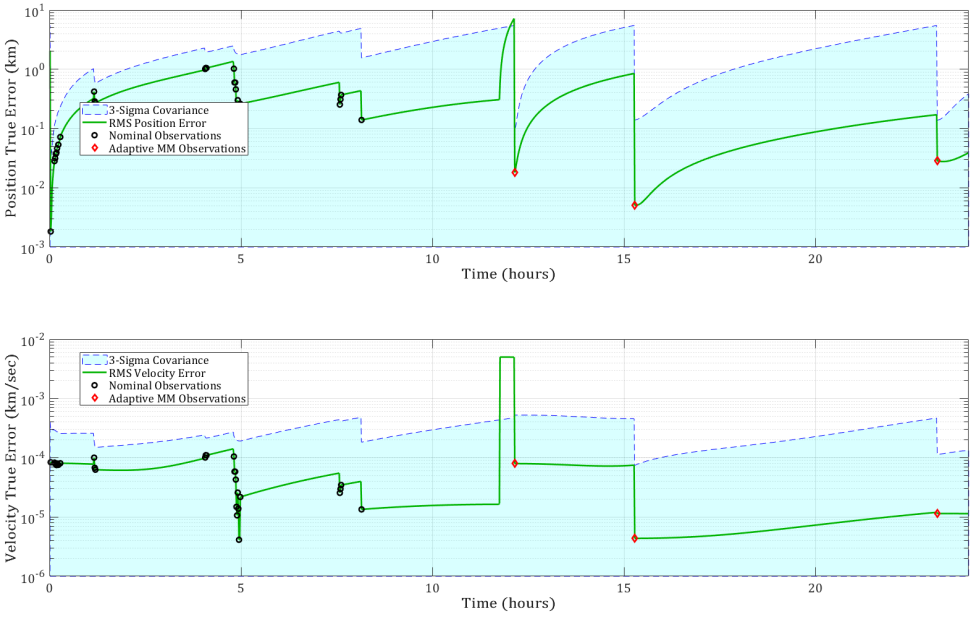

Figure B.85: A.E. Test: Shotgun SMM/Constrained GEOMnvr-2 Track

B.3.4 Lambert SMM

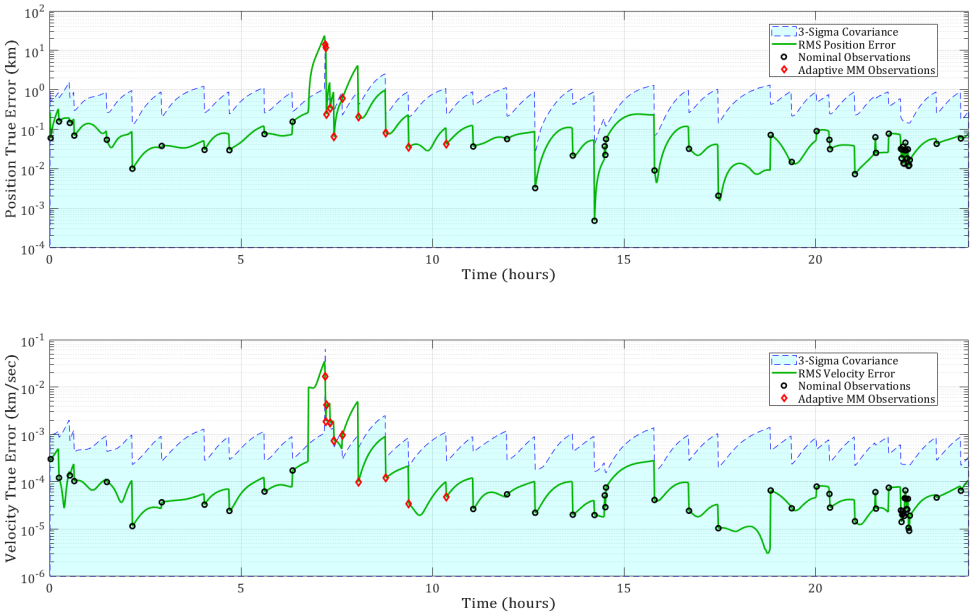

Figure B.86: A.E. Test: Lambert SMM/Constrained LEOMnvr-1 Track

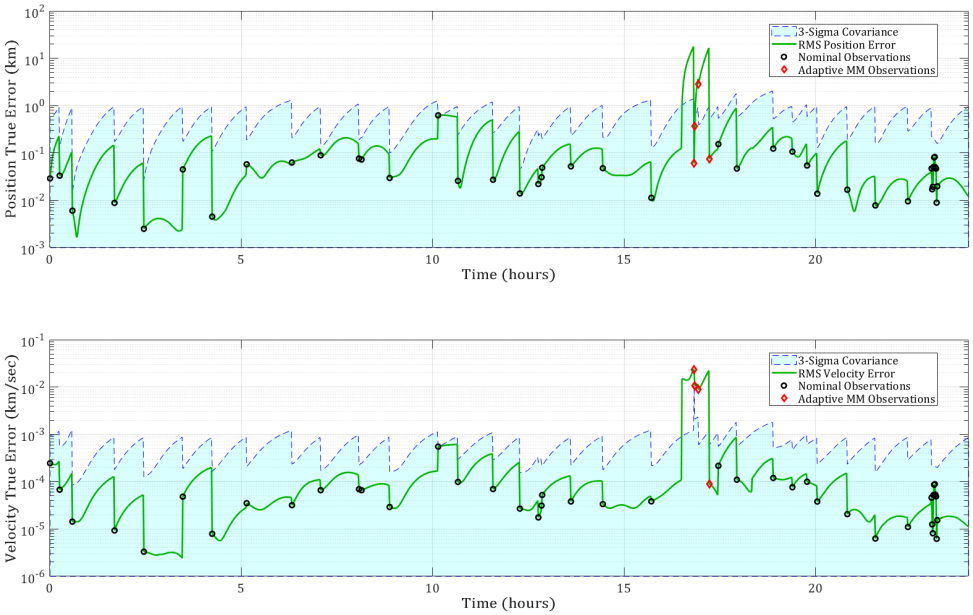

Figure B.87: A.E. Test: Lambert SMM/Constrained LEOMnvr-2 Track

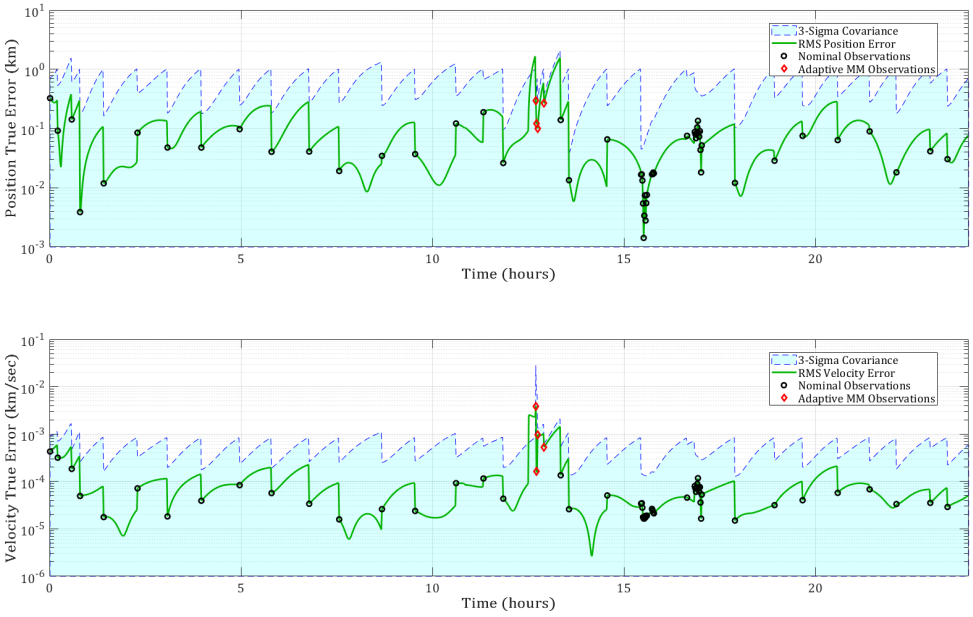

Figure B.88: A.E. Test: Lambert SMM/Constrained LEOMnvr-3 Track

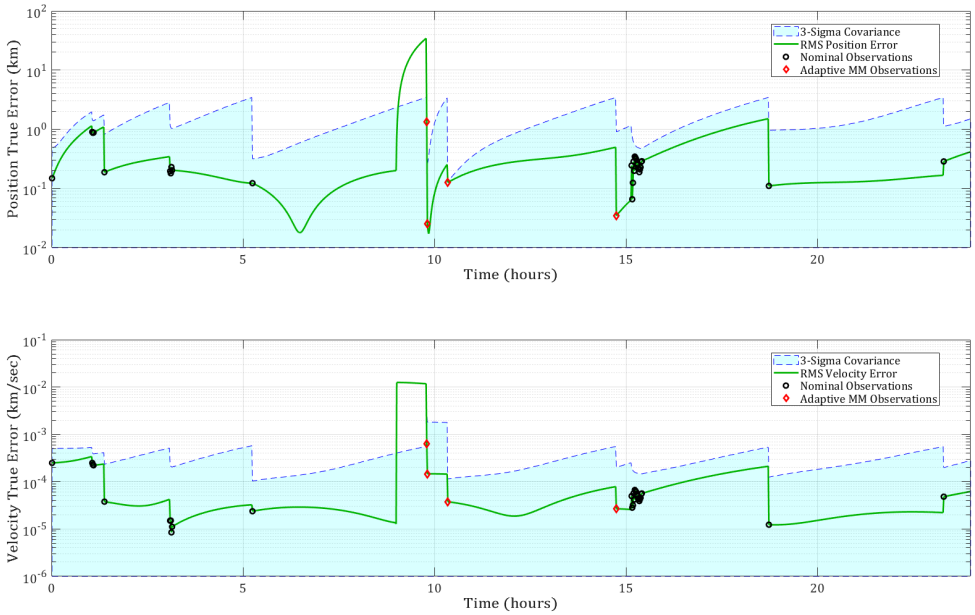

Figure B.89: A.E. Test: Lambert SMM/Constrained MEOMnvr-1 Track

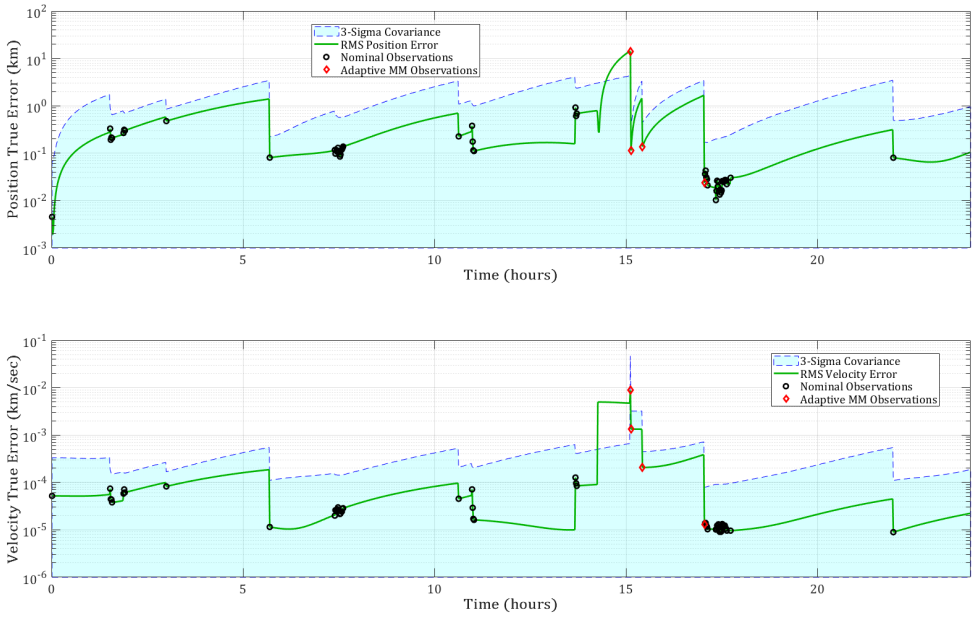

Figure B.90: A.E. Test: Lambert SMM/Constrained MEOMnvr-2 Track

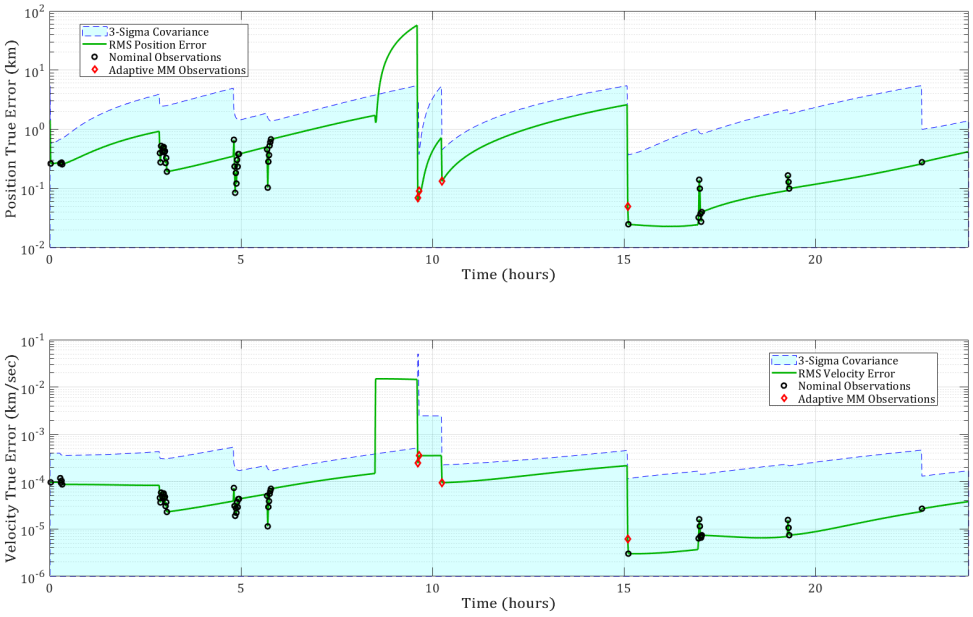

Figure B.91: A.E. Test: Lambert SMM/Constrained GEOMnvr-1 Track

B.3.5 Lambert GPB1

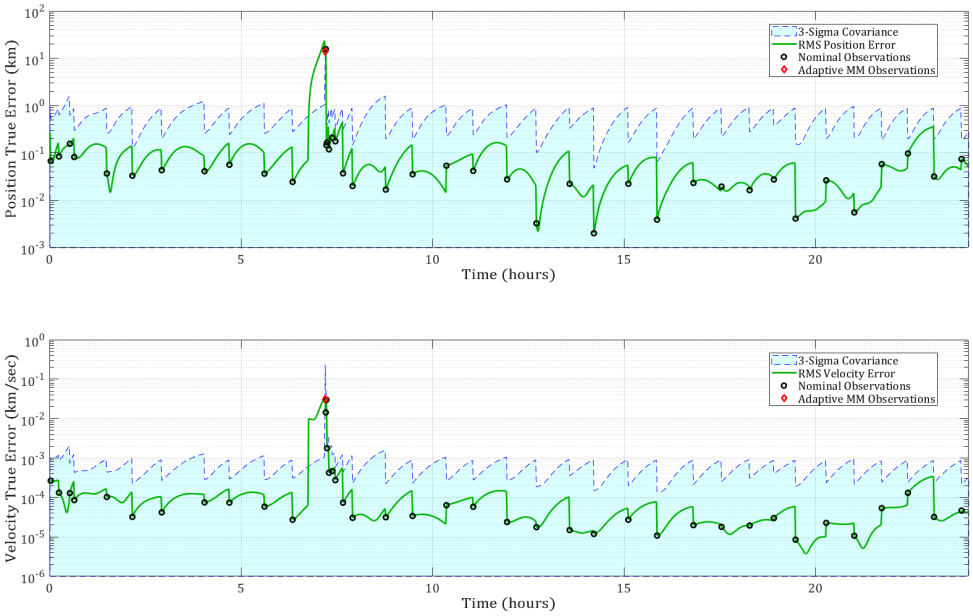

Figure B.92: A.E. Test: Lambert GPB1/Constrained LEOMnvr-1 Track

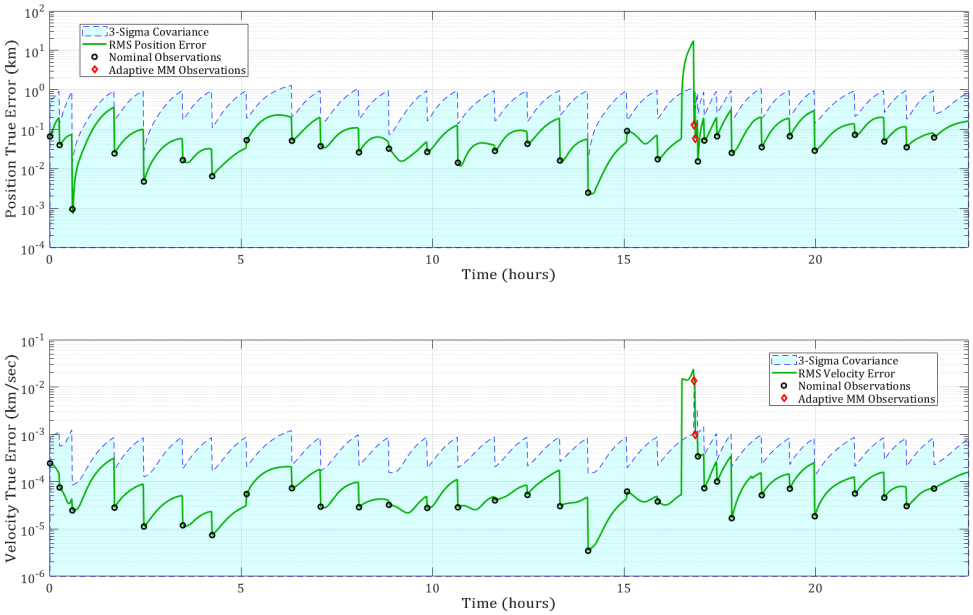

Figure B.93: A.E. Test: Lambert GPB1/Constrained LEOMnvr-2 Track

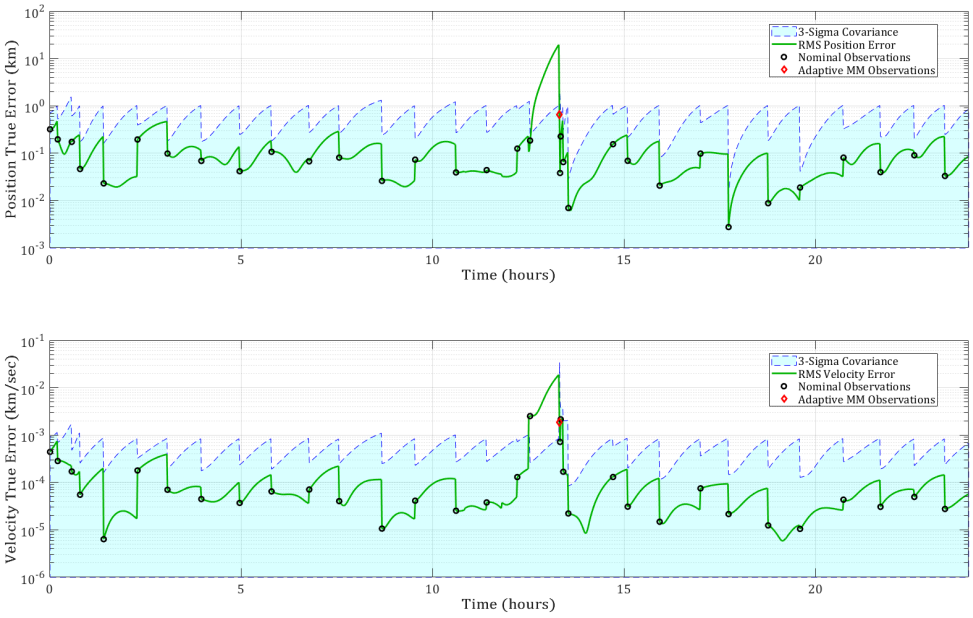

Figure B.94: A.E. Test: Lambert GPB1/Constrained LEOMnvr-3 Track

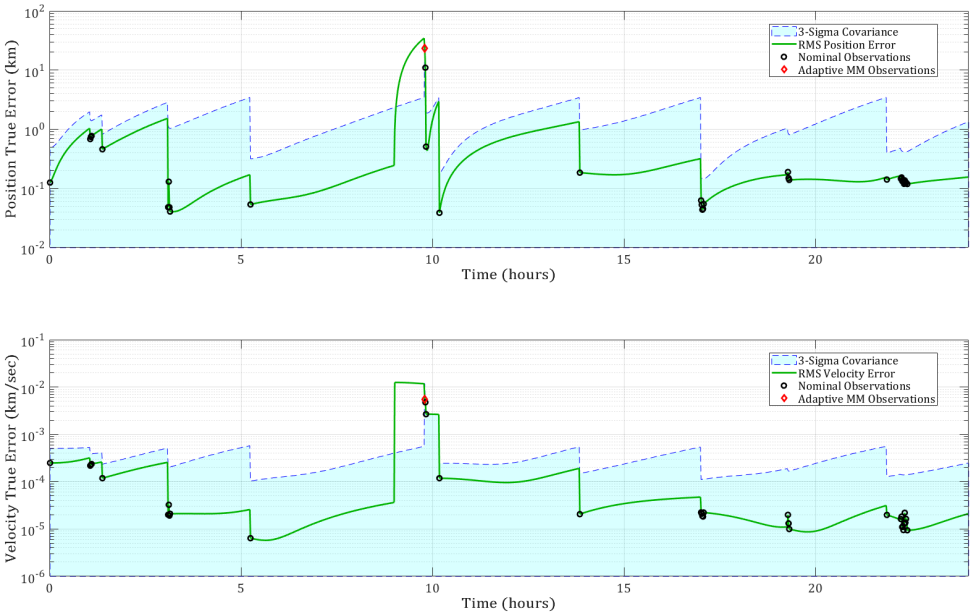

Figure B.95: A.E. Test: Lambert GPB1/Constrained MEOMnvr-1 Track

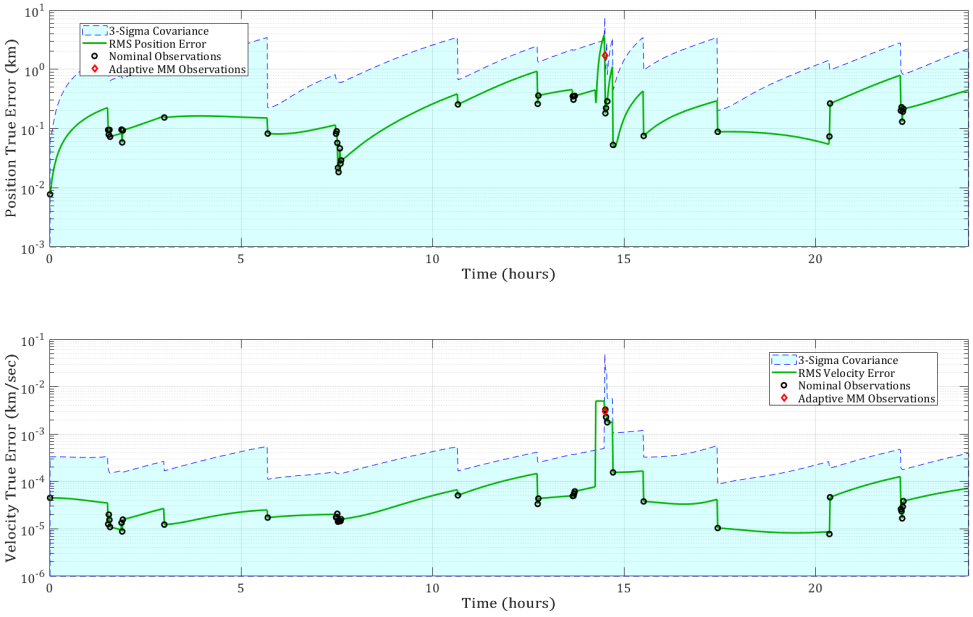

Figure B.96: A.E. Test: Lambert GPB1/Constrained MEOMnvr-2 Track

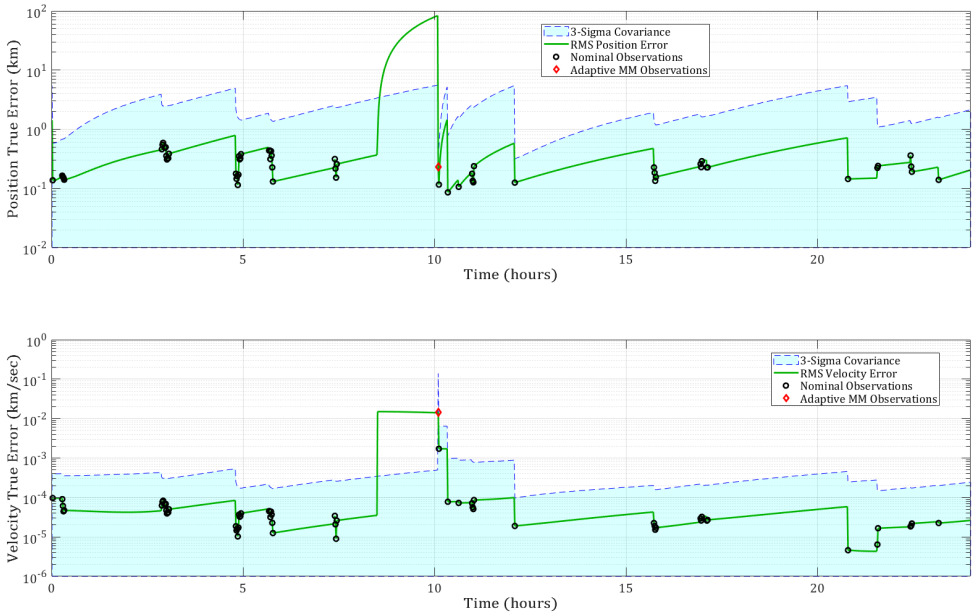

Figure B.97: A.E. Test: Lambert GPB1/Constrained GEOMnvr-1 Track

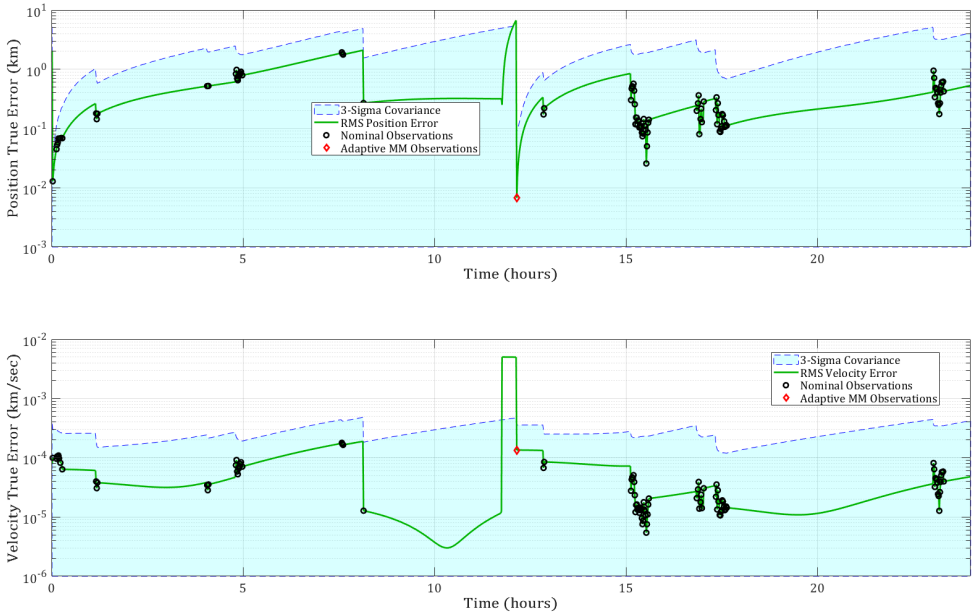

Figure B.98: A.E. Test: Lambert GPB1/Constrained GEOMnvr-2 Track

Appendix C

Full Scale Test Analysis

C.1 No Adaptive Estimation & FIG-Only POMDP

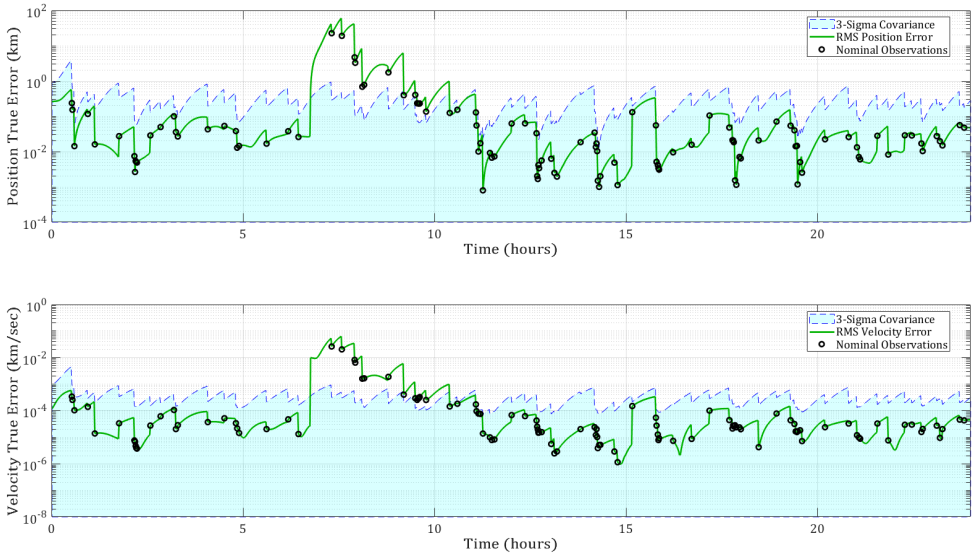

Figure C.1: Nominal/FIG-Only LEOMnvr-1 Track

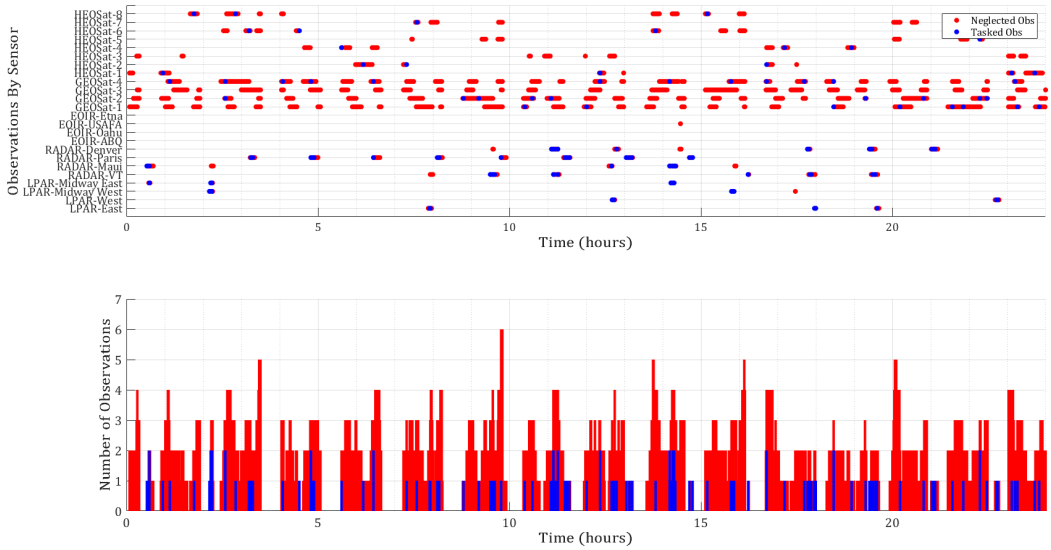

Figure C.2: Nominal/FIG-Only LEOMnvr-1 Observations

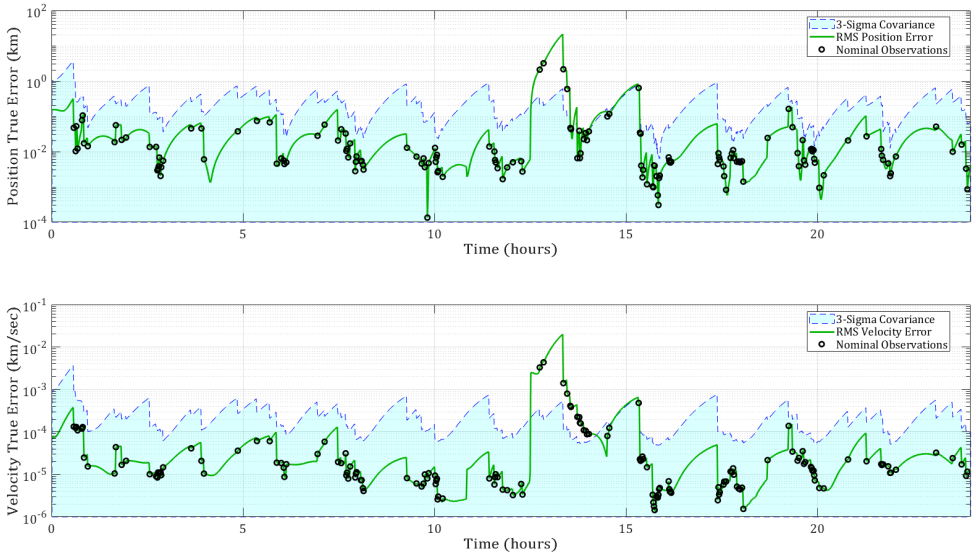

Figure C.3: Nominal/FIG-Only LEOMnvr-3 Track

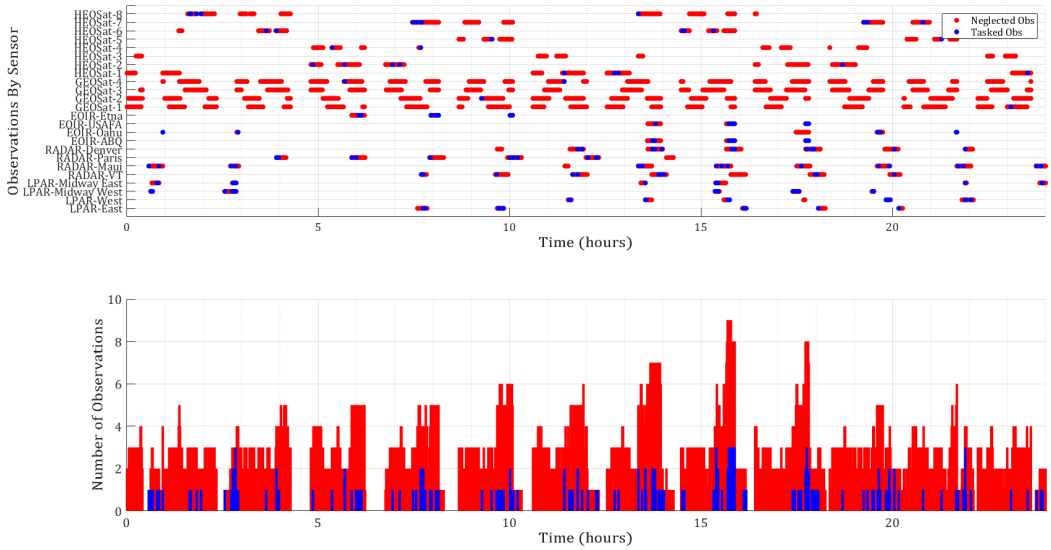

Figure C.4: Nominal/FIG-Only LEOMnvr-3 Observations

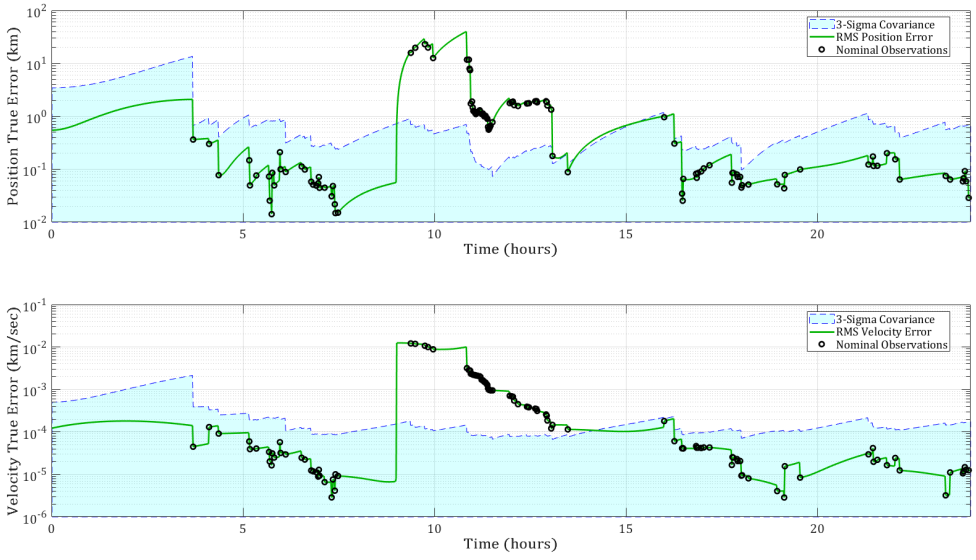

Figure C.5: Nominal/FIG-Only MEOMnvr-1 Track

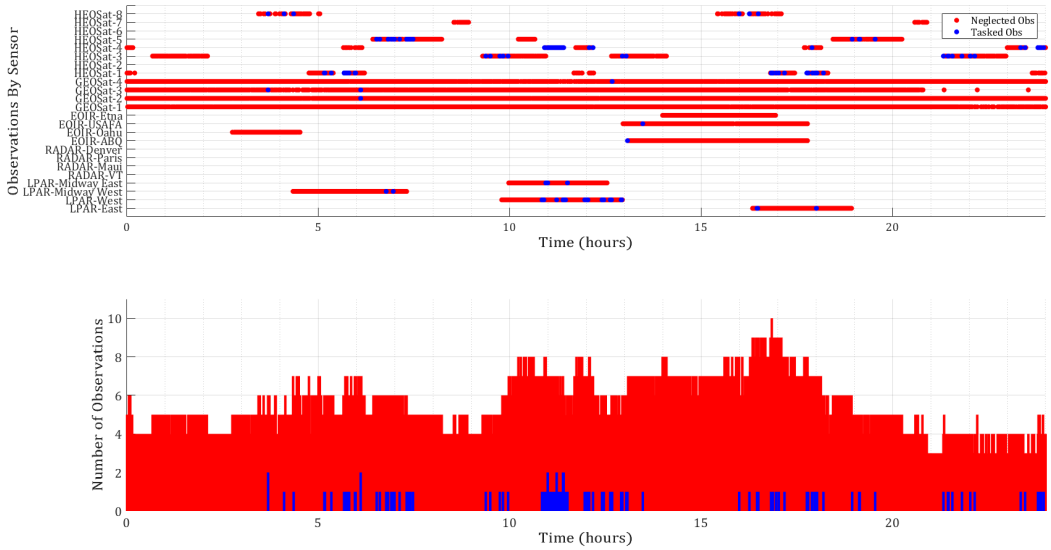

Figure C.6: Nominal/FIG-Only MEOMnvr-1 Observations

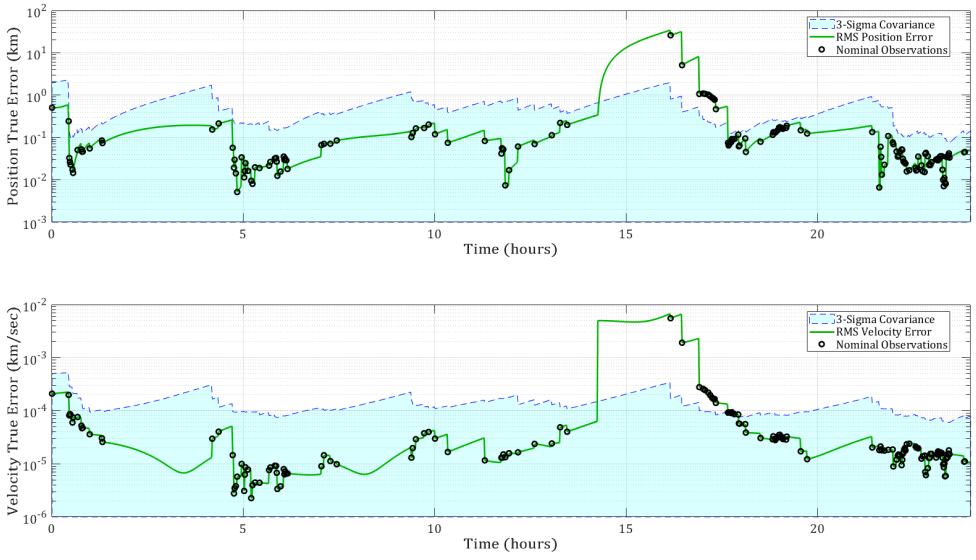

Figure C.7: Nominal/FIG-Only MEOMnvr-2 Track

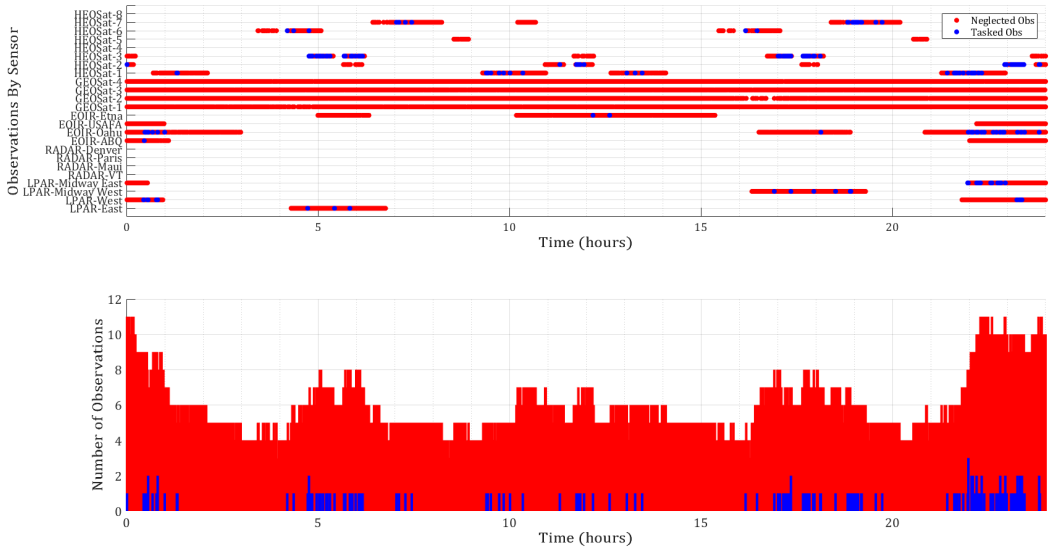

Figure C.8: Nominal/FIG-Only MEOMnvr-2 Observations

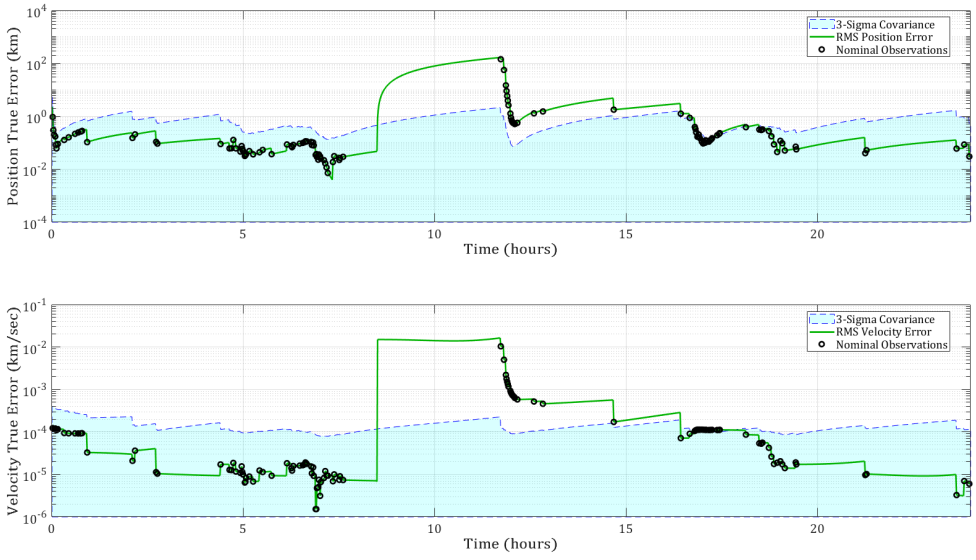

Figure C.9: Nominal/FIG-Only GEOMnvr-1 Track

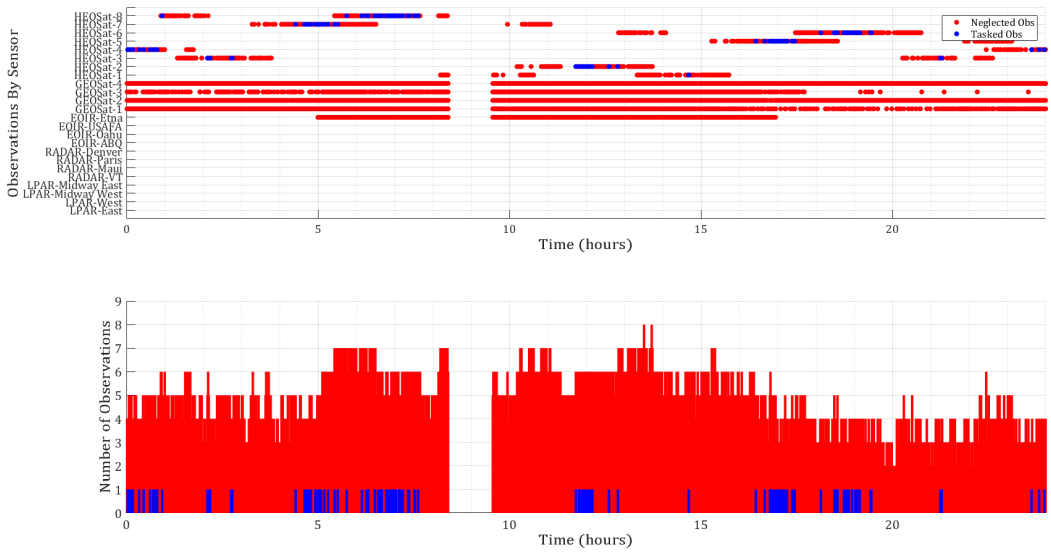

Figure C.10: Nominal/FIG-Only GEOMnvr-1 Observations

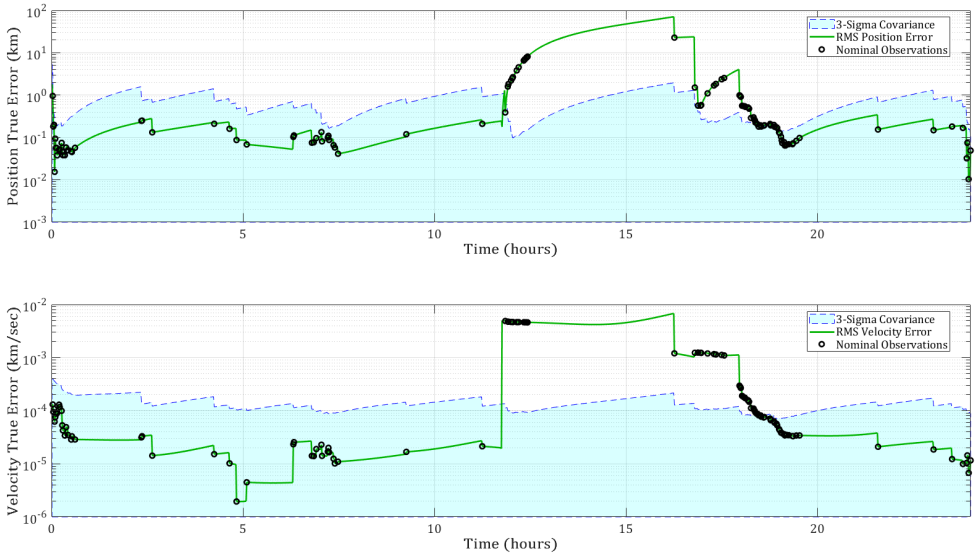

Figure C.11: Nominal/FIG-Only GEOMnvr-2 Track

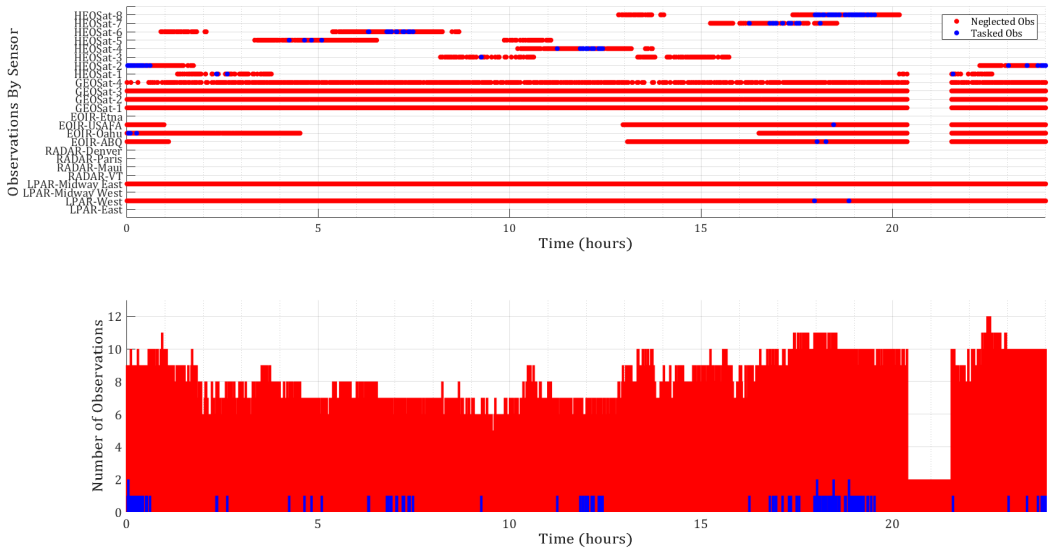

Figure C.12: Nominal/FIG-Only GEOMnvr-2 Observations

C.2 No Adaptive Estimation & Continuous POMDP

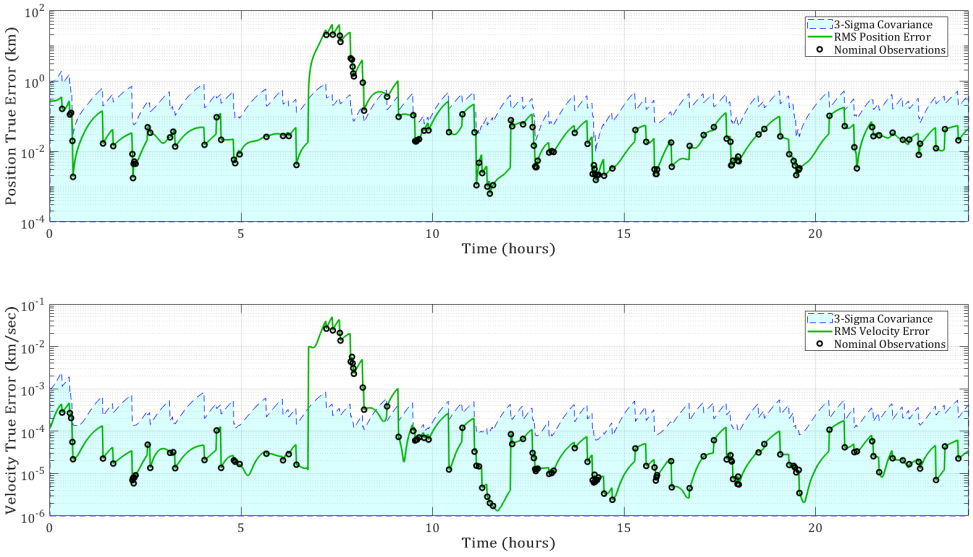

Figure C.13: Nominal/Continuous LEOMnvr-1 Track

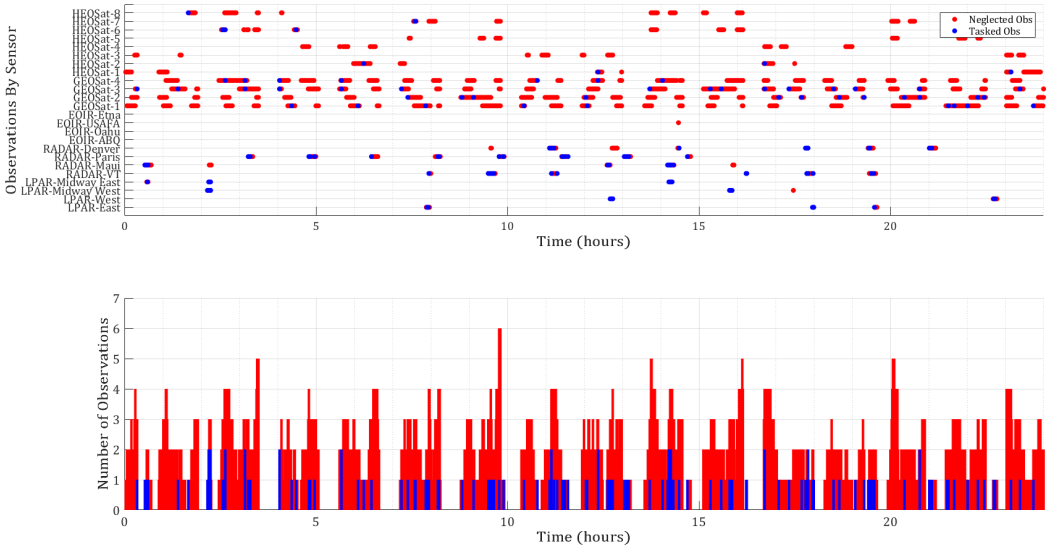

Figure C.14: Nominal/Continuous LEOMnvr-1 Observations

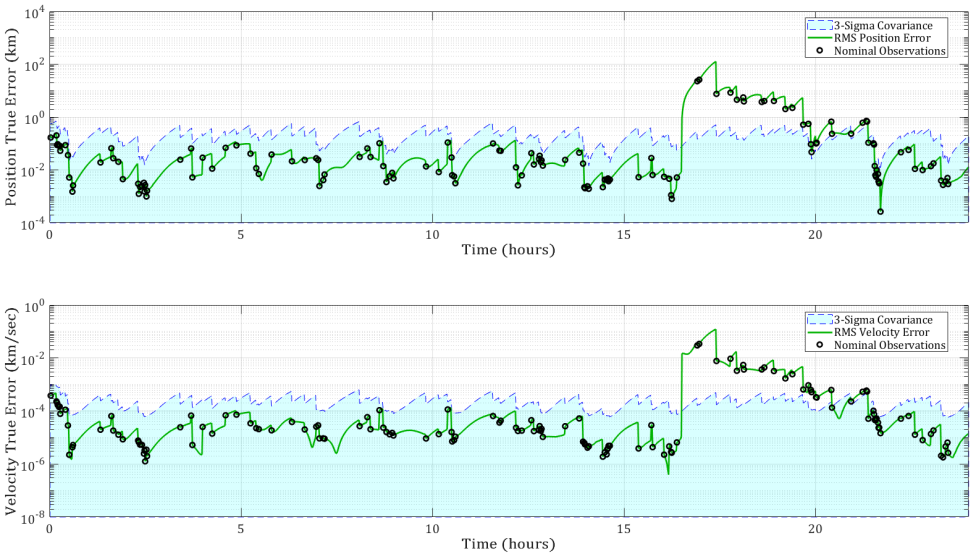

Figure C.15: Nominal/Continuous LEOMnvr-2 Track

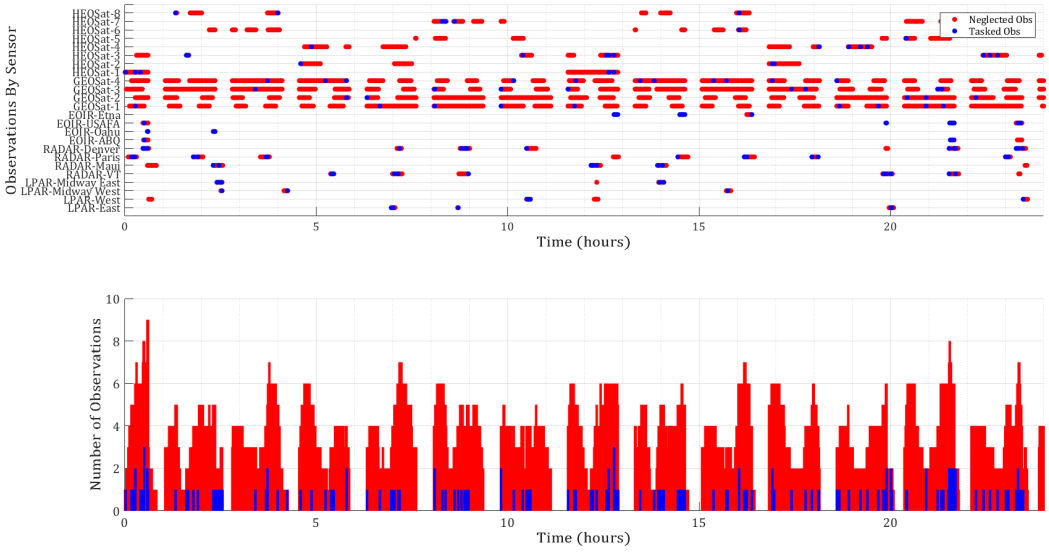

Figure C.16: Nominal/Continuous LEOMnvr-2 Observations

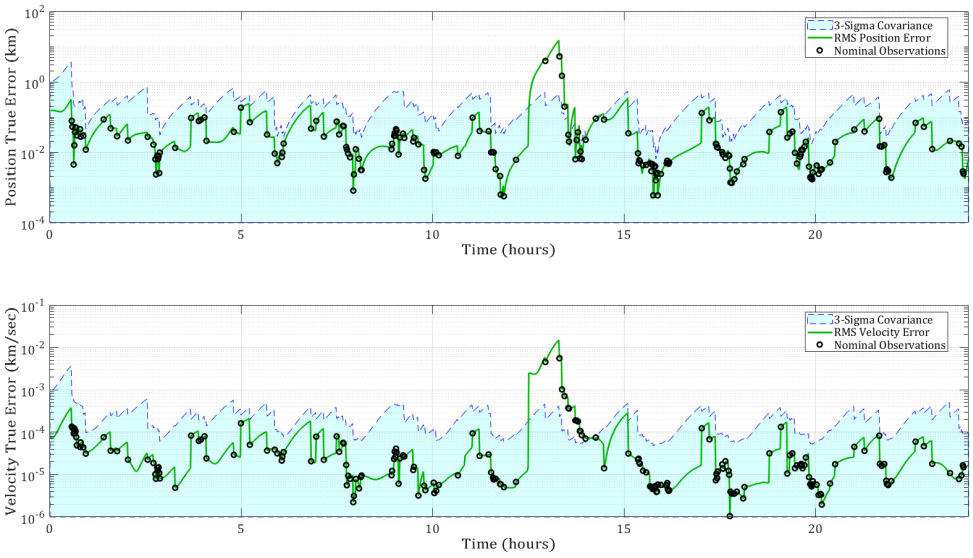

Figure C.17: Nominal/Continuous LEOMnvr-3 Track

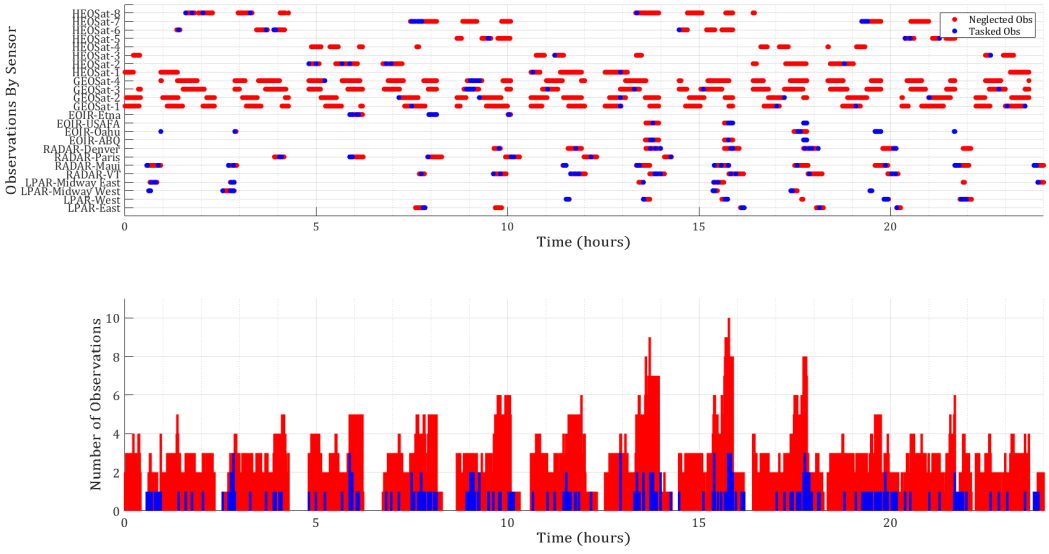

Figure C.18: Nominal/Continuous LEOMnvr-3 Observations

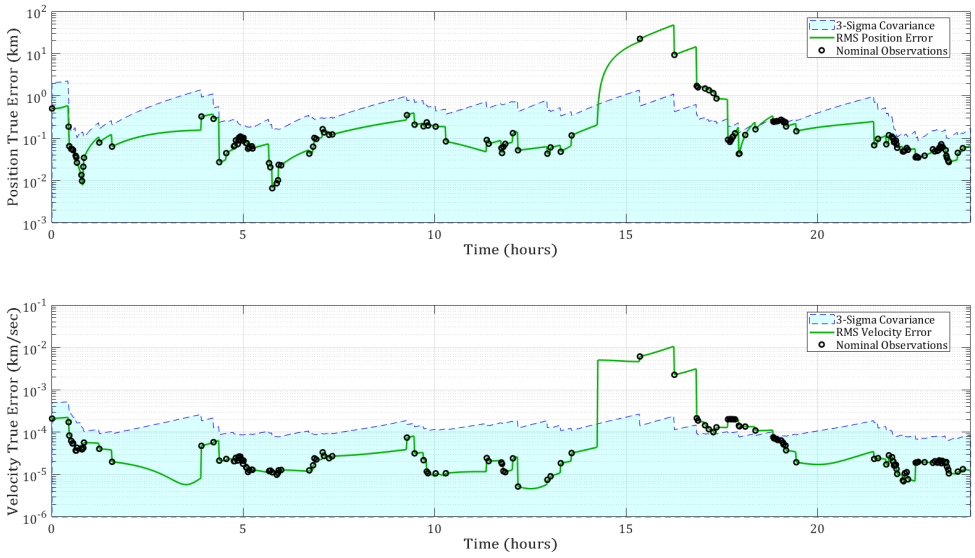

Figure C.19: Nominal/Continuous MEOMnvr-2 Track

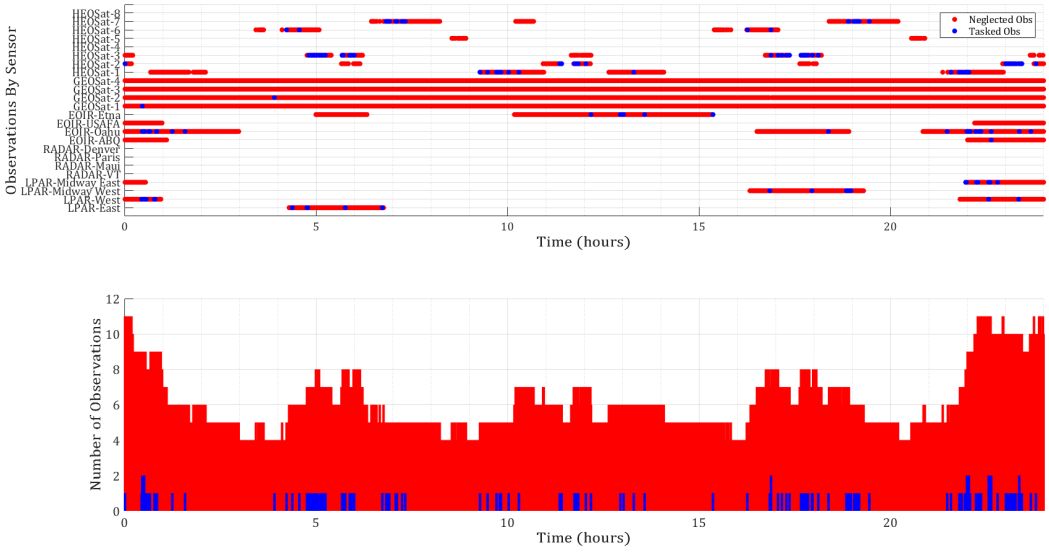

Figure C.20: Nominal/Continuous MEOMnvr-2 Observations

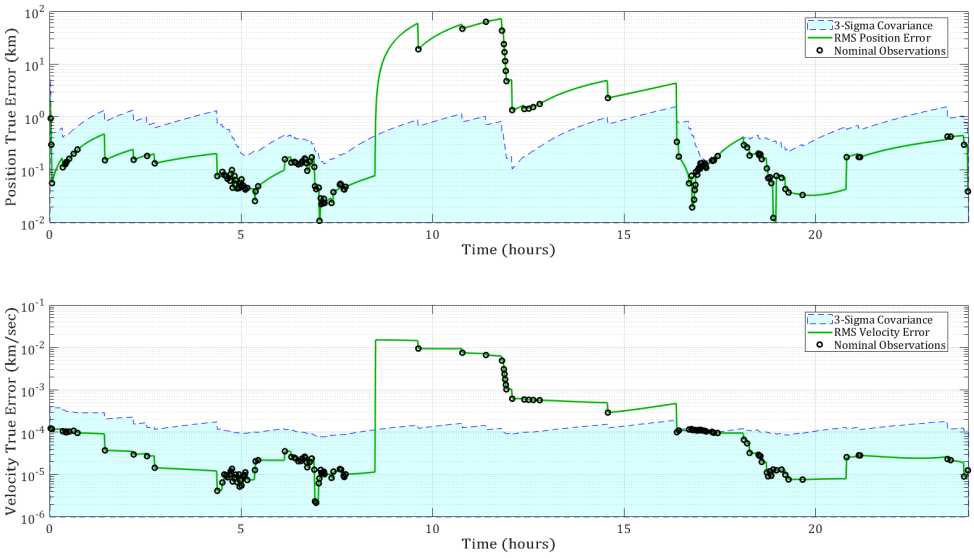

Figure C.21: Nominal/Continuous GEOMnvr-1 Track

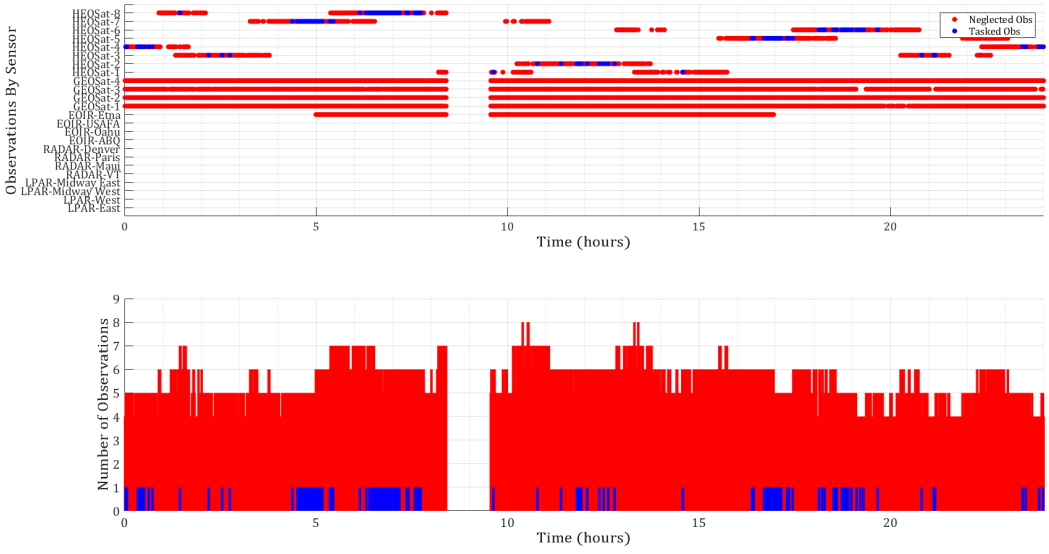

Figure C.22: Nominal/Continuous GEOMnvr-1 Observations

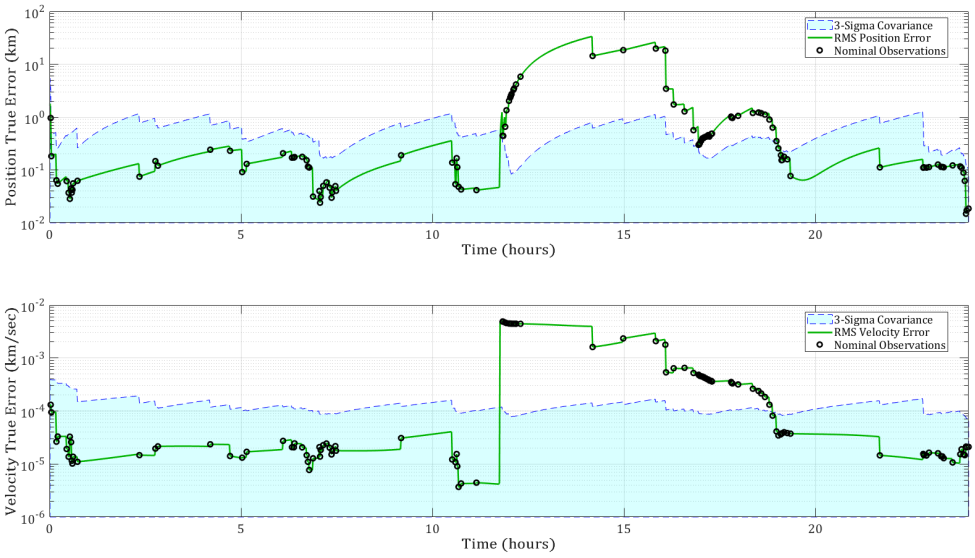

Figure C.23: Nominal/Continuous GEOMnvr-2 Track

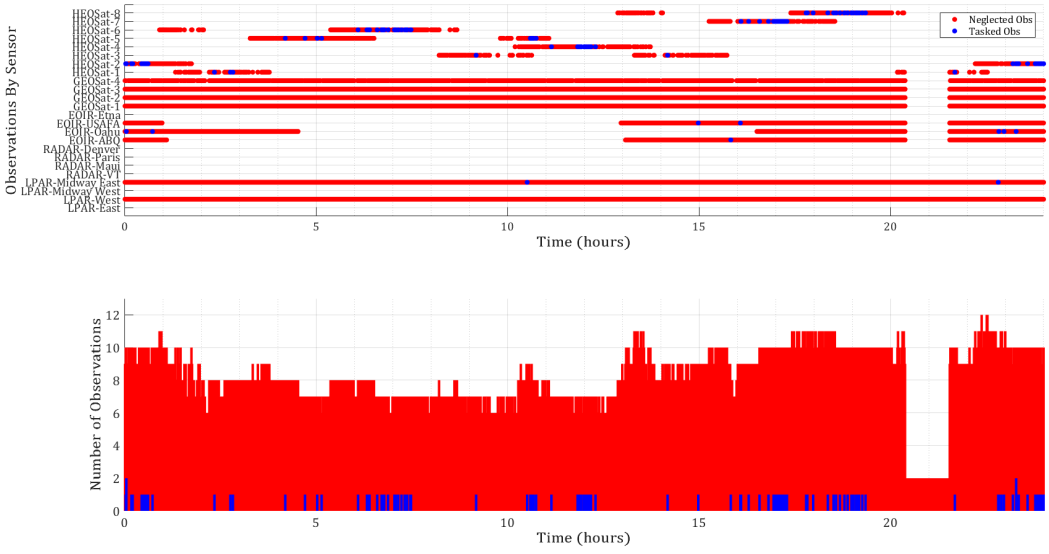

Figure C.24: Nominal/Continuous GEOMnvr-2 Observations

C.3 No Adaptive Estimation & Constrained POMDP

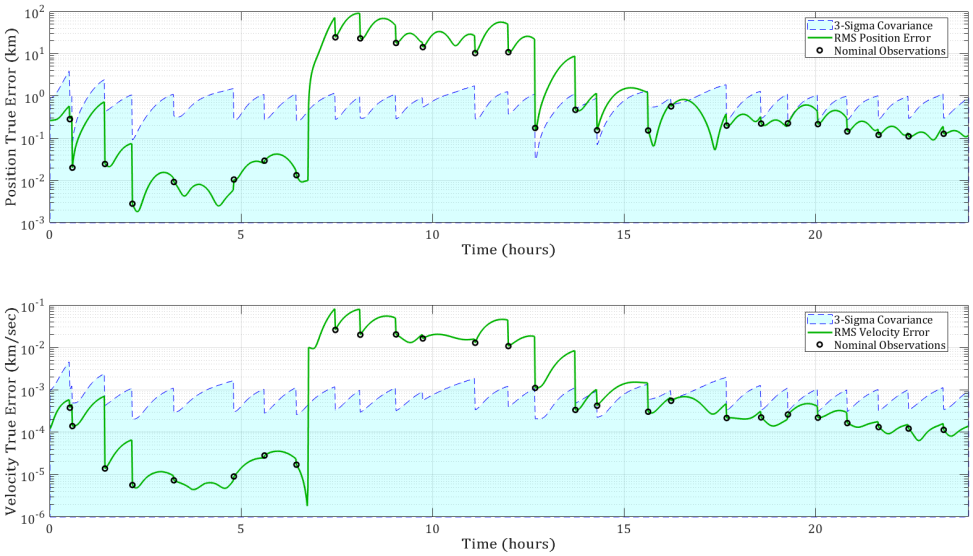

Figure C.25: Nominal/Constrained LEOMnvr-1 Track

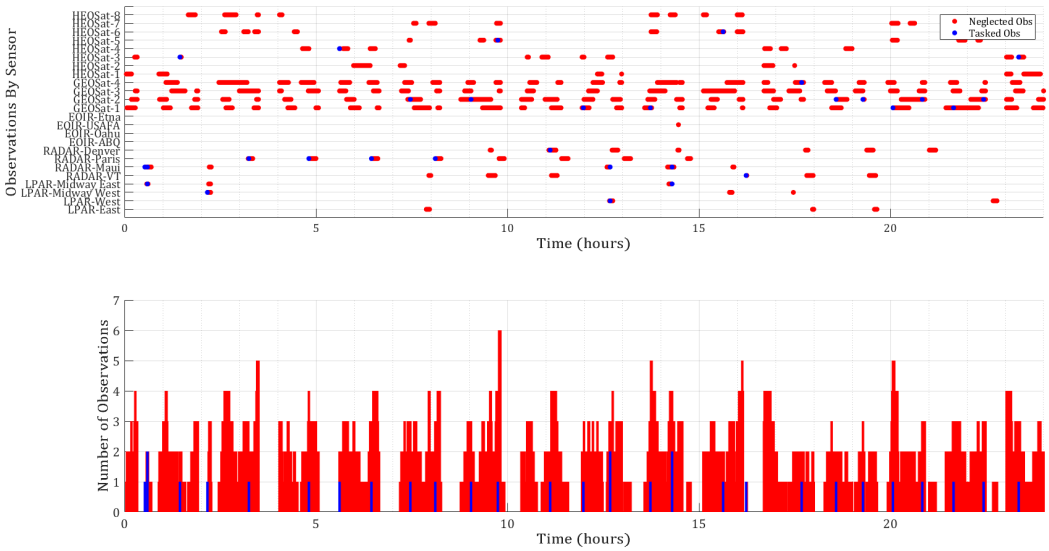

Figure C.26: Nominal/Constrained LEOMnvr-1 Observations

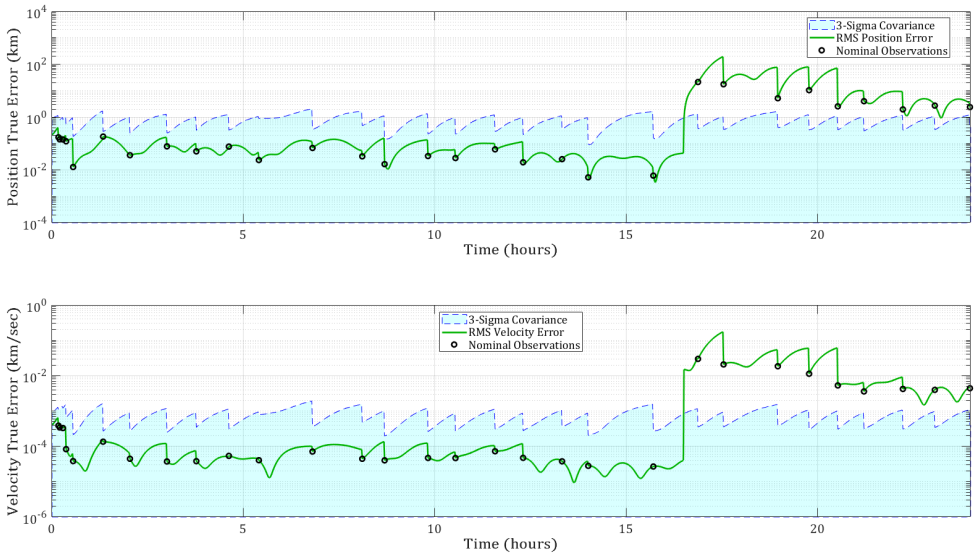

Figure C.27: Nominal/Constrained LEOMnvr-2 Track

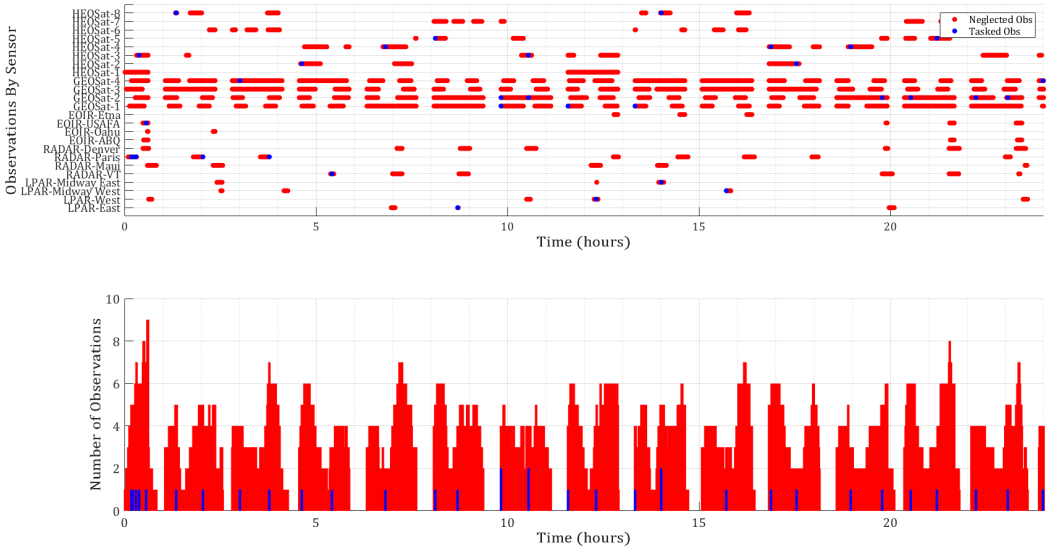

Figure C.28: Nominal/Constrained LEOMnvr-2 Observations

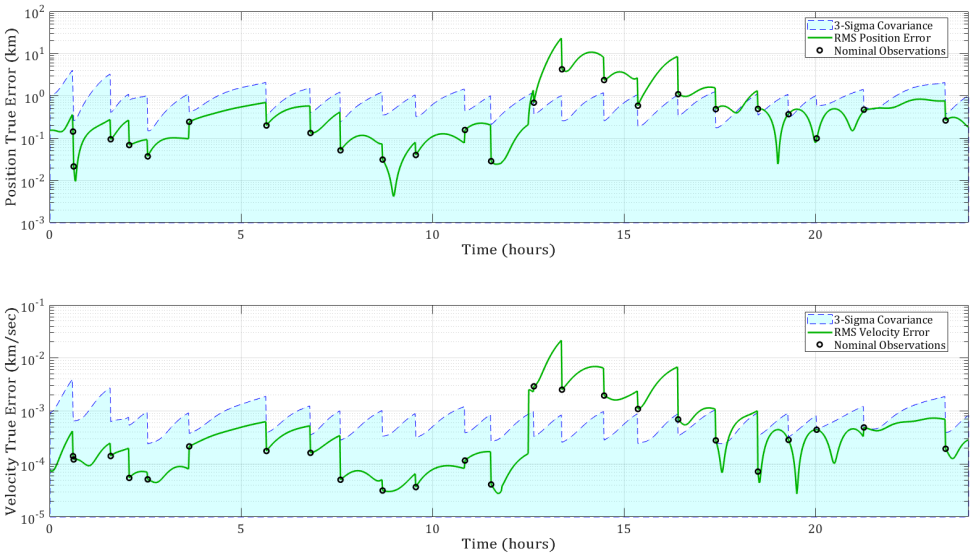

Figure C.29: Nominal/Constrained LEOMnvr-3 Track

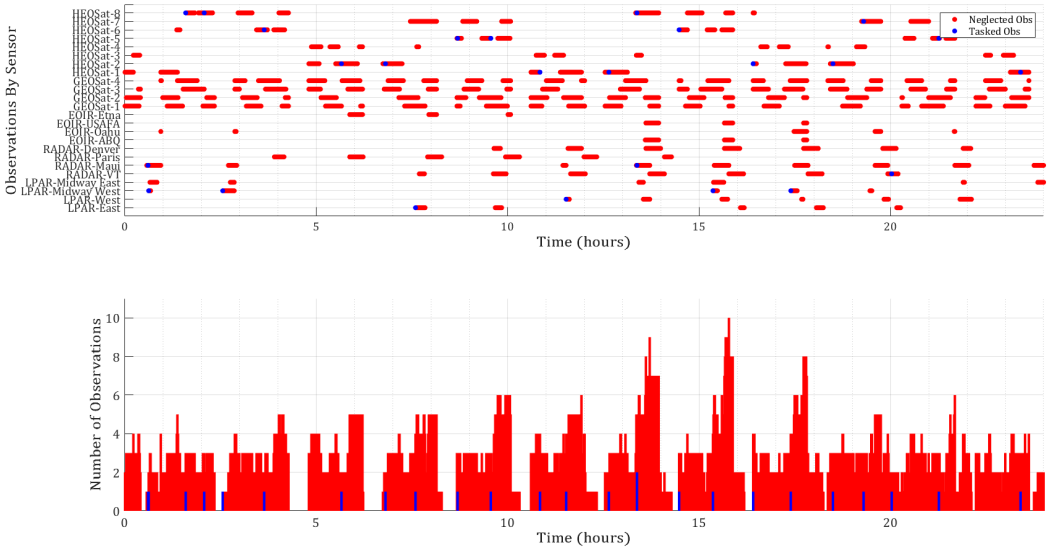

Figure C.30: Nominal/Constrained LEOMnvr-3 Observations

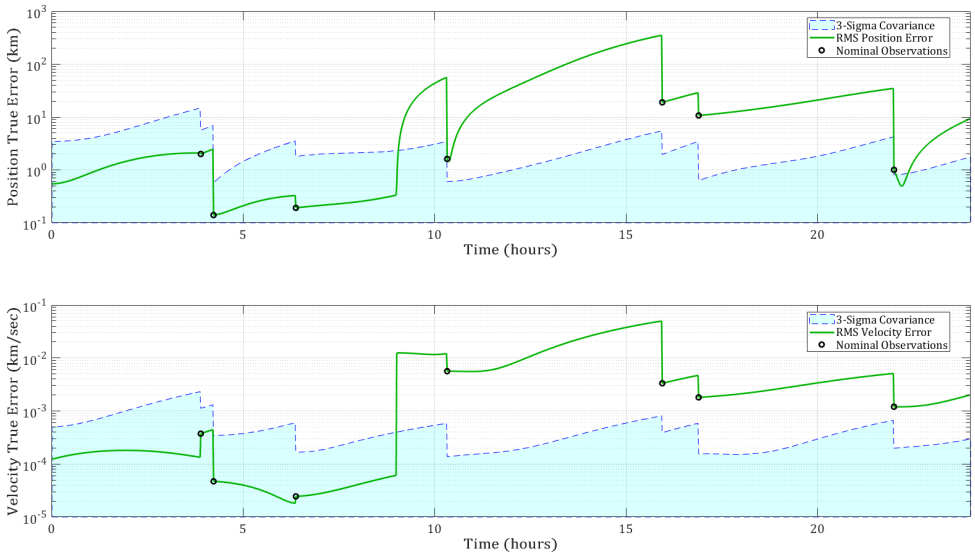

Figure C.31: Nominal/Constrained MEOMnvr-1 Track

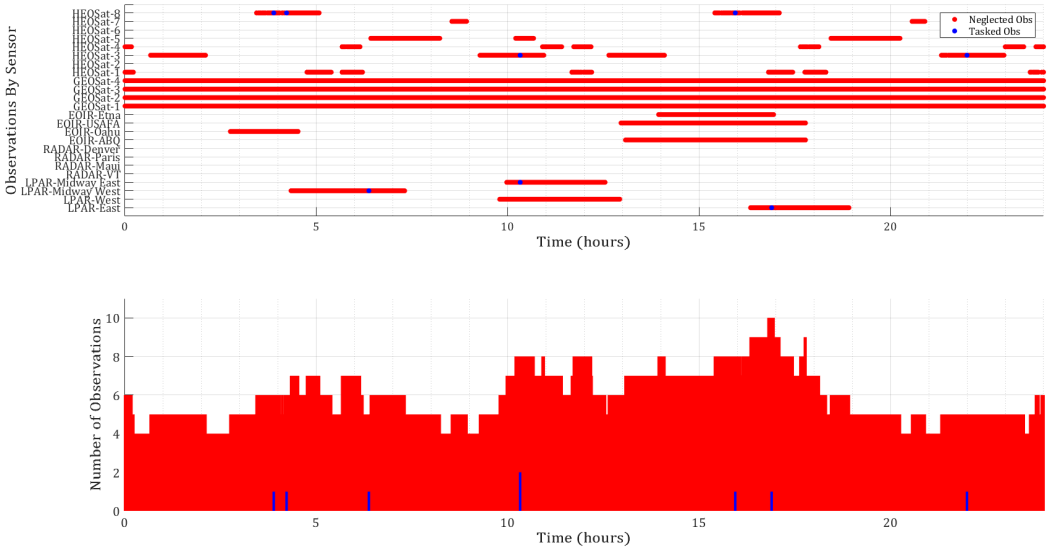

Figure C.32: Nominal/Constrained MEOMnvr-1 Observations

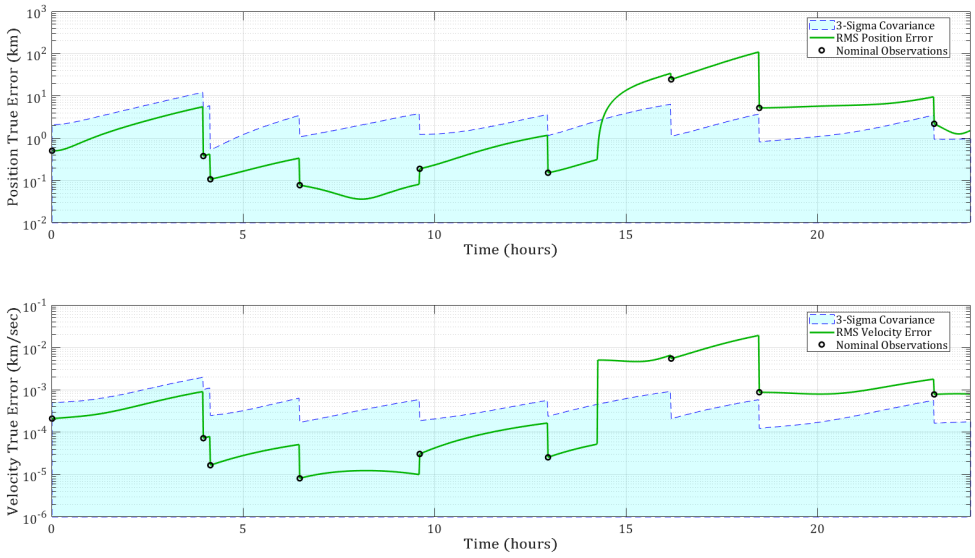

Figure C.33: Nominal/Constrained MEOMnvr-2 Track

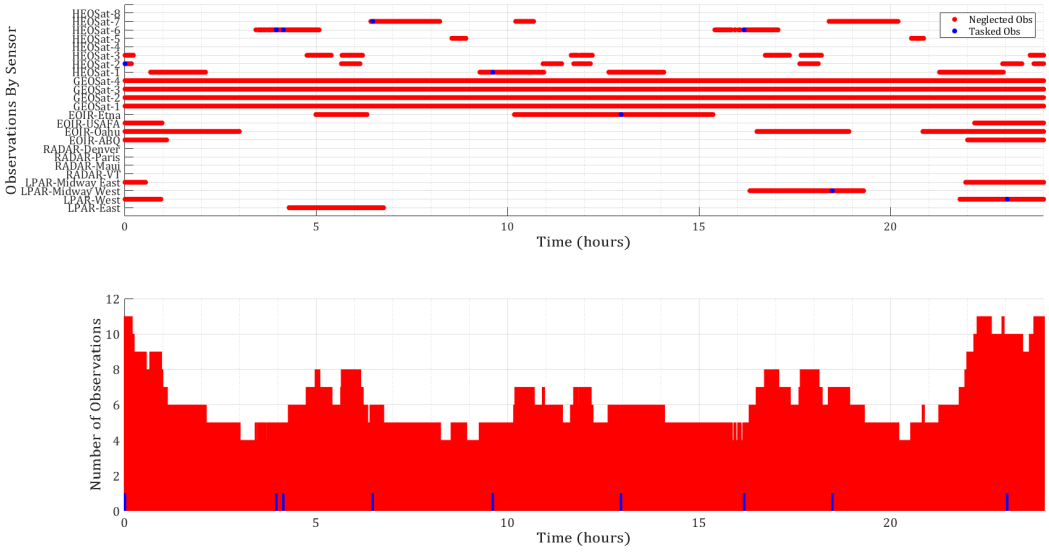

Figure C.34: Nominal/Constrained MEOMnvr-2 Observations

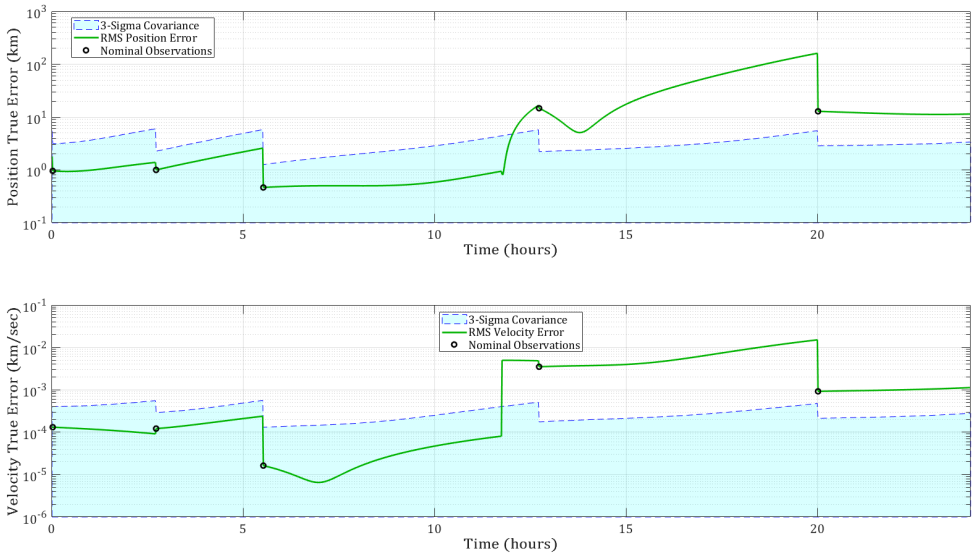

Figure C.35: Nominal/Constrained GEOMnvr-2 Track

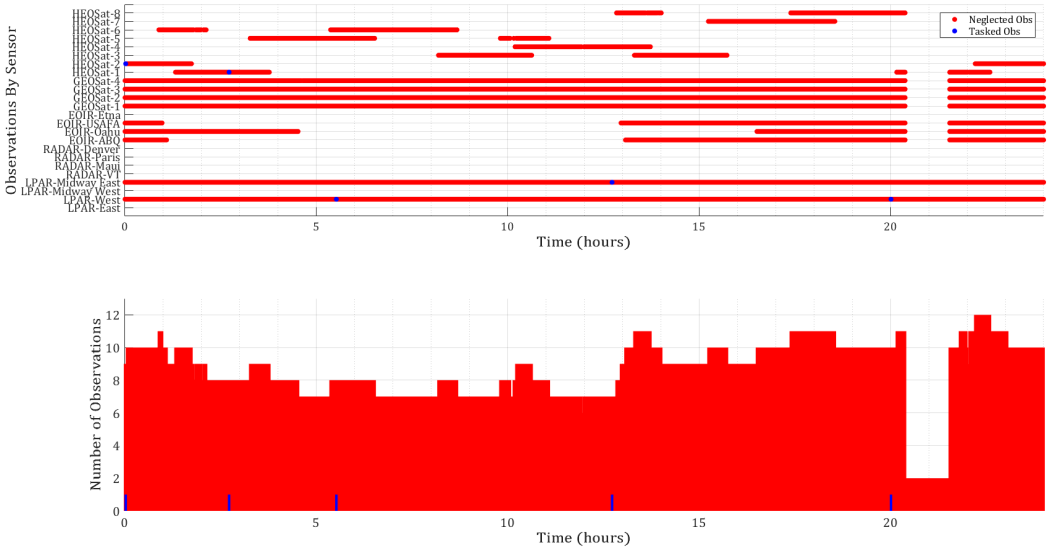

Figure C.36: Nominal/Constrained GEOMnvr-2 Observations

C.4 Covariance Inflation & FIG-Only POMDP

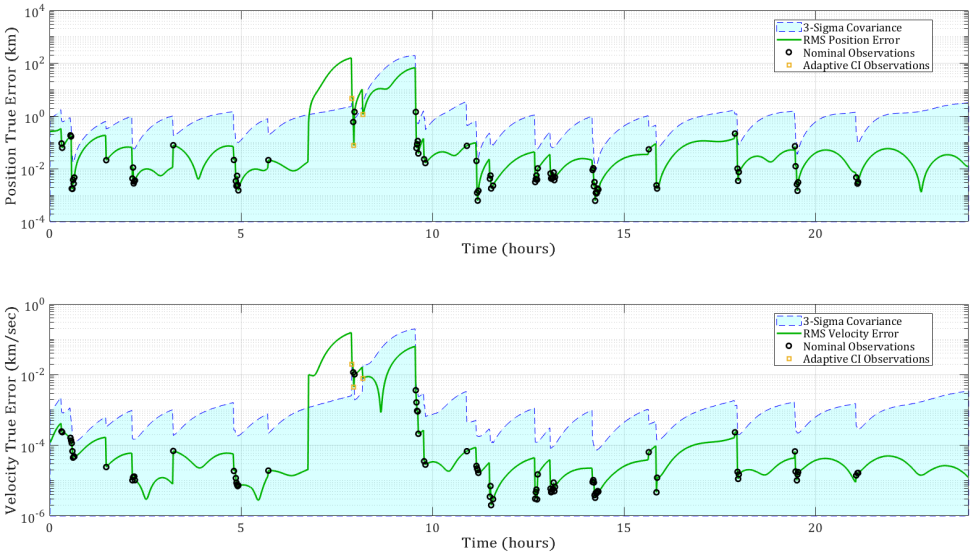

Figure C.37: Inflation/FIG-Only LEOMnvr-1 Track

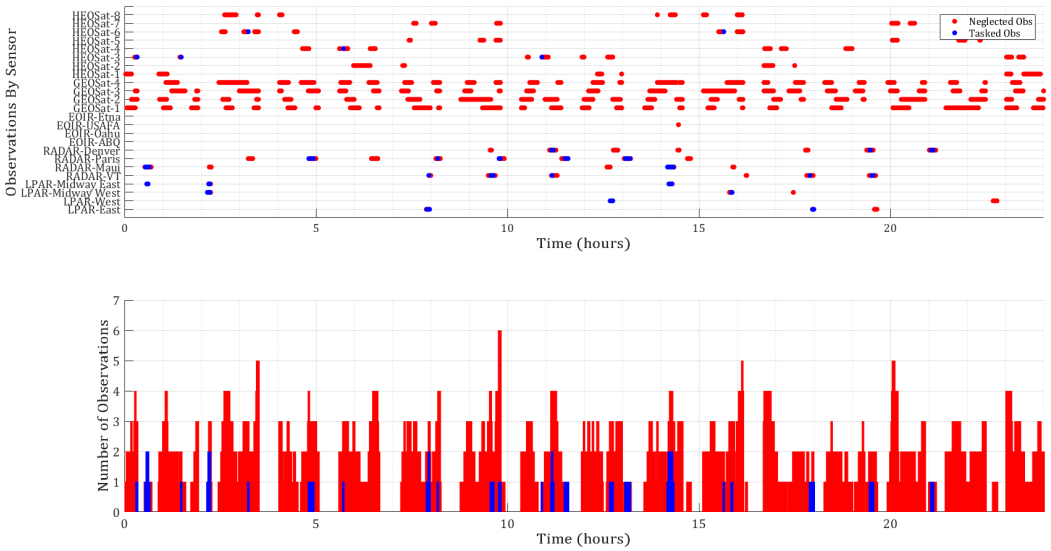

Figure C.38: Inflation/FIG-Only LEOMnvr-1 Observations

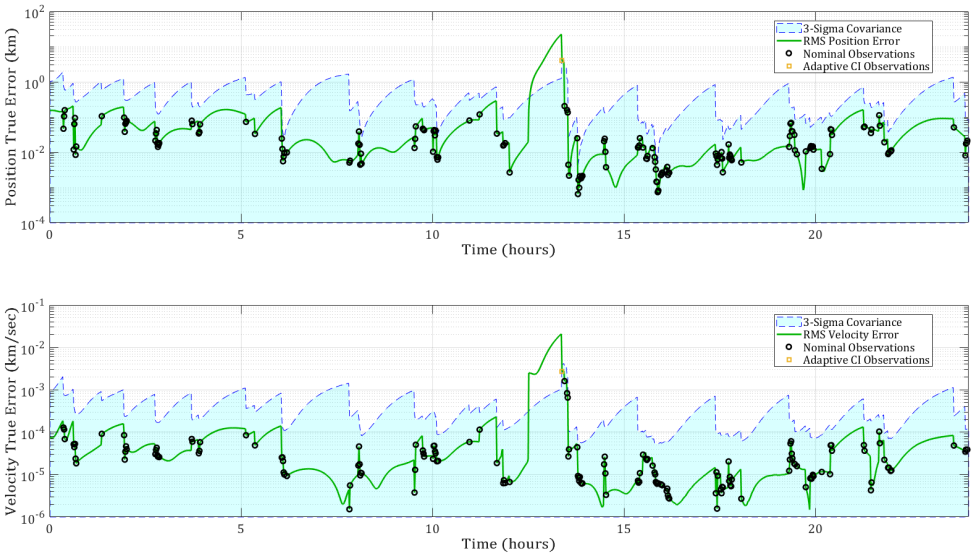

Figure C.39: Inflation/FIG-Only LEOMnvr-3 Track

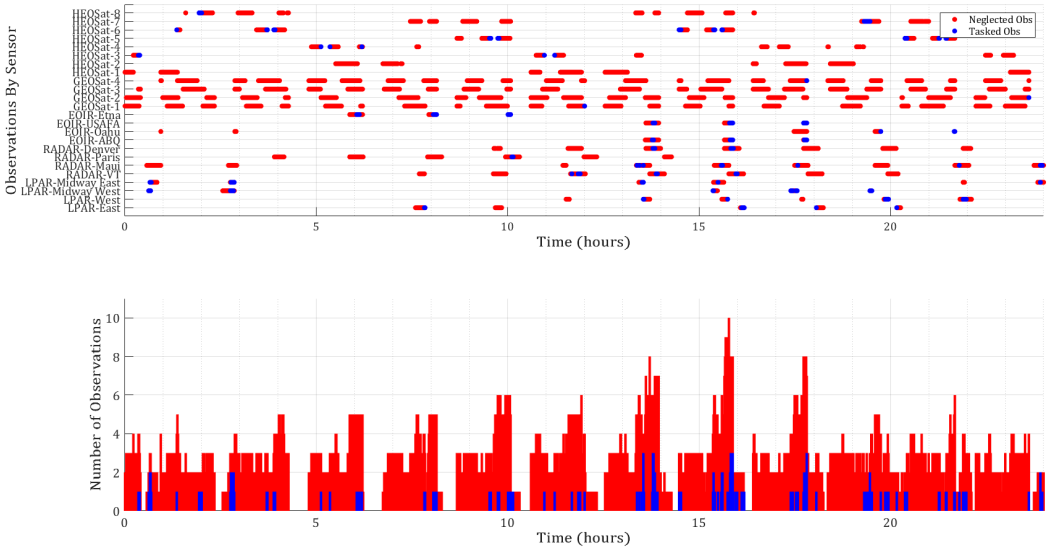

Figure C.40: Inflation/FIG-Only LEOMnvr-3 Observations

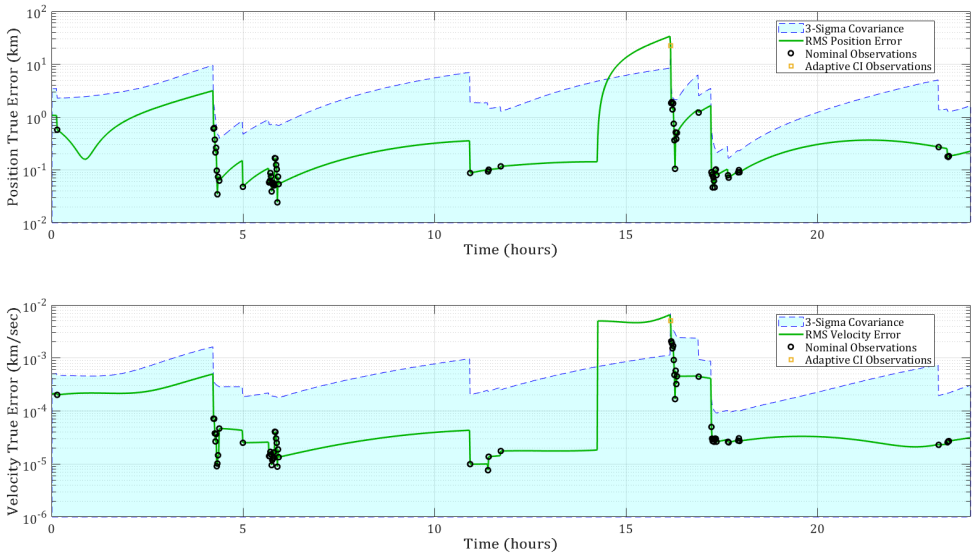

Figure C.41: Inflation/FIG-Only MEOMnvr-2 Track

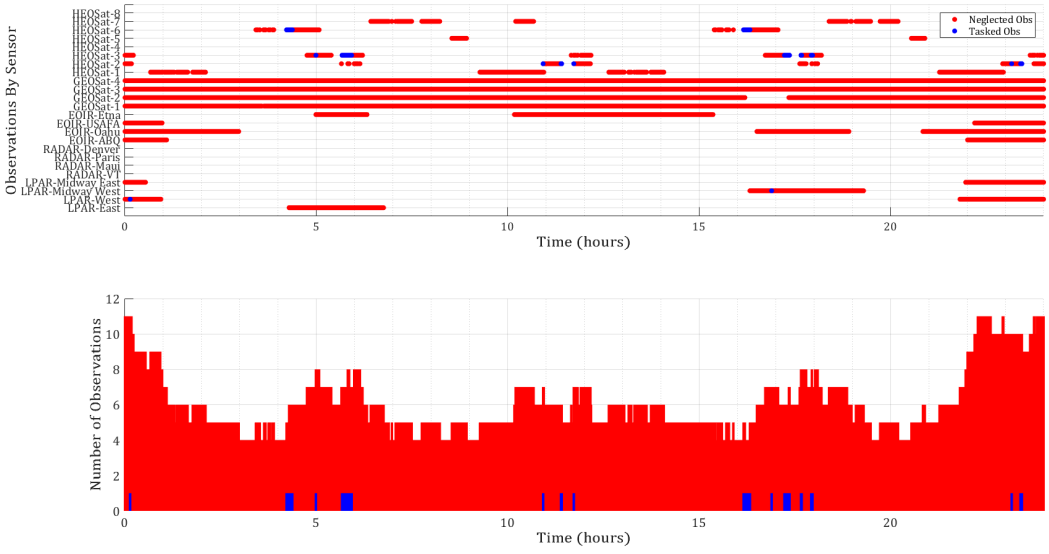

Figure C.42: Inflation/FIG-Only MEOMnvr-2 Observations

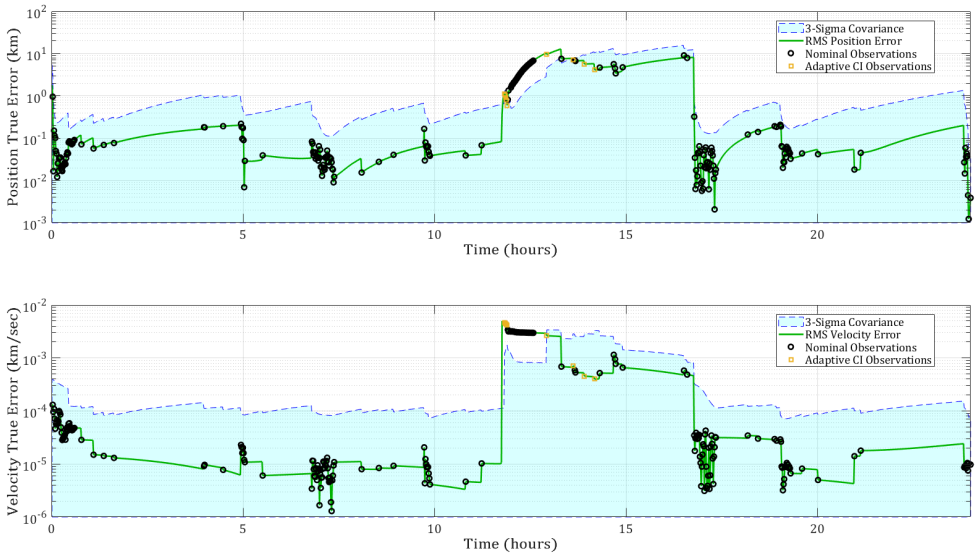

Figure C.43: Inflation/FIG-Only GEOMnvr-2 Track

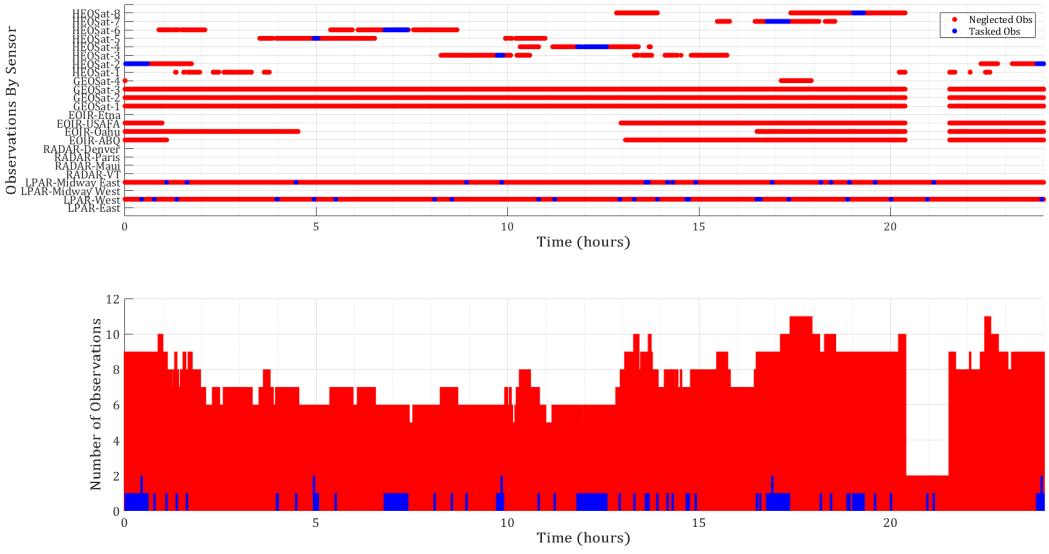

Figure C.44: Inflation/FIG-Only GEOMnvr-2 Observations

C.5 Shotgun SMM & Continuous Observation POMDP

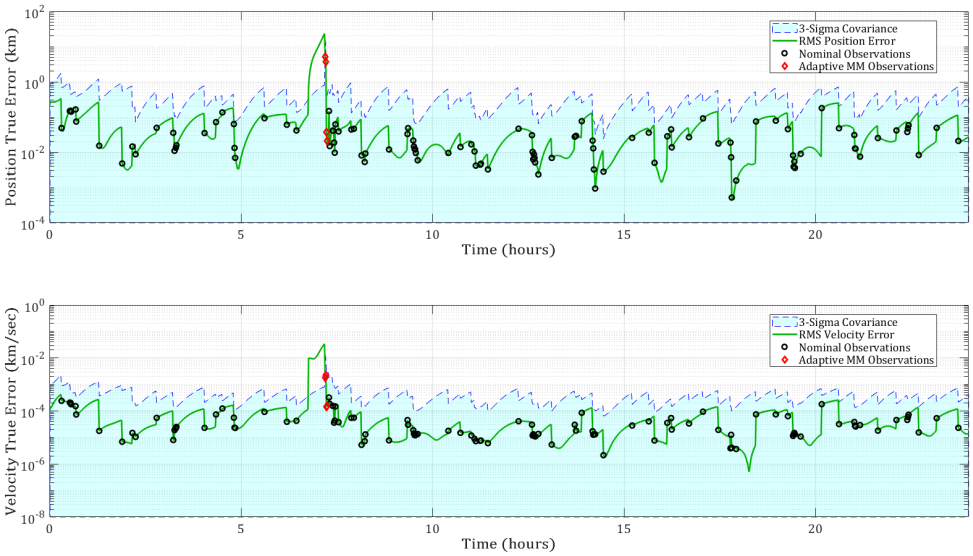

Figure C.45: Shotgun SMM/Continuous LEOMnvr-1 Track

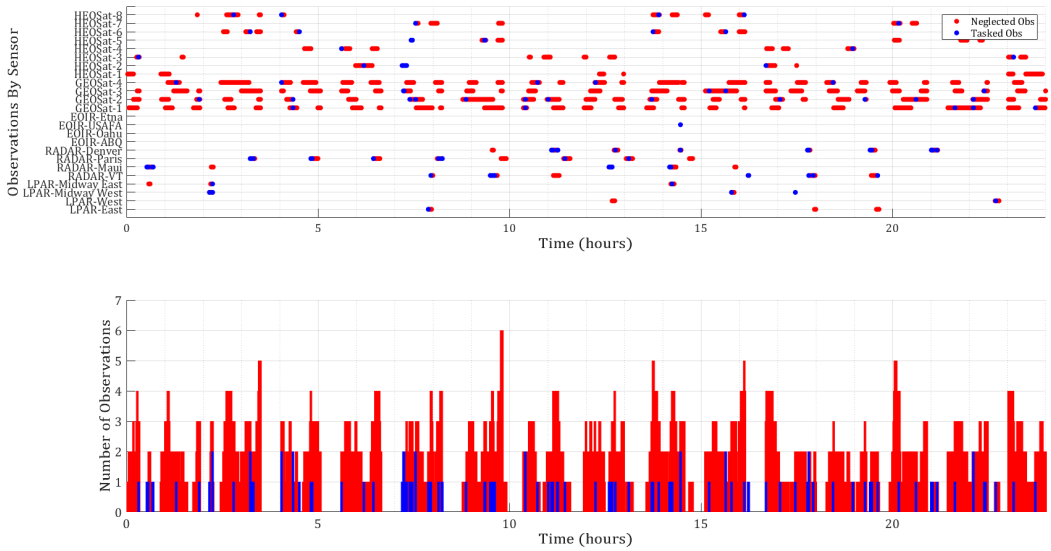

Figure C.46: Shotgun SMM/Continuous LEOMnvr-1 Observations

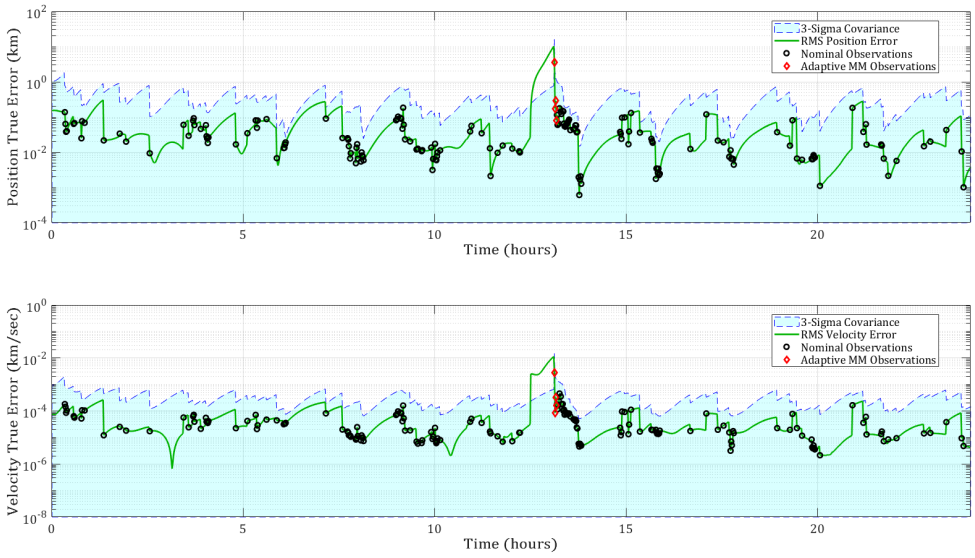

Figure C.47: Shotgun SMM/Continuous LEOMnvr-3 Track

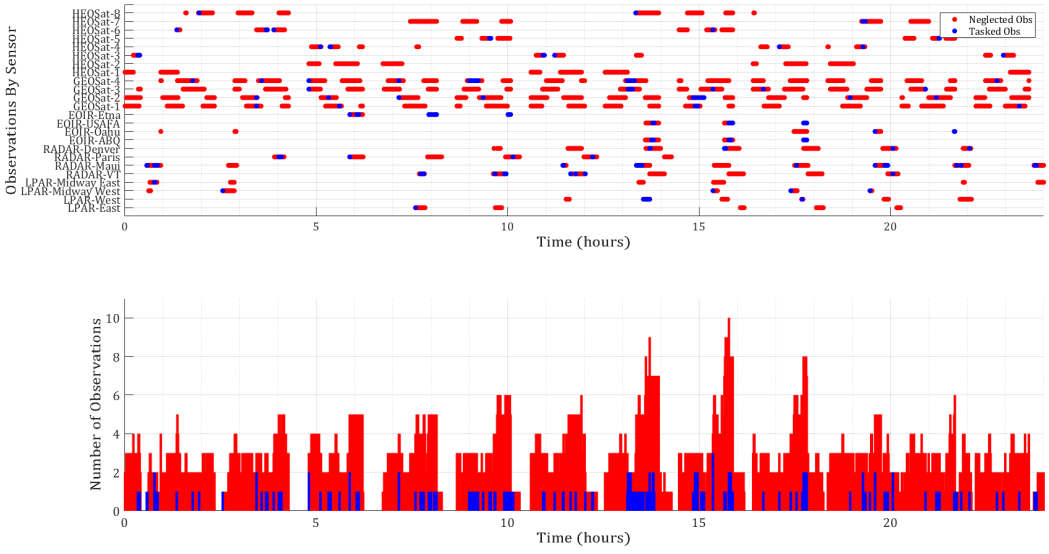

Figure C.48: Shotgun SMM/Continuous LEOMnvr-3 Observations

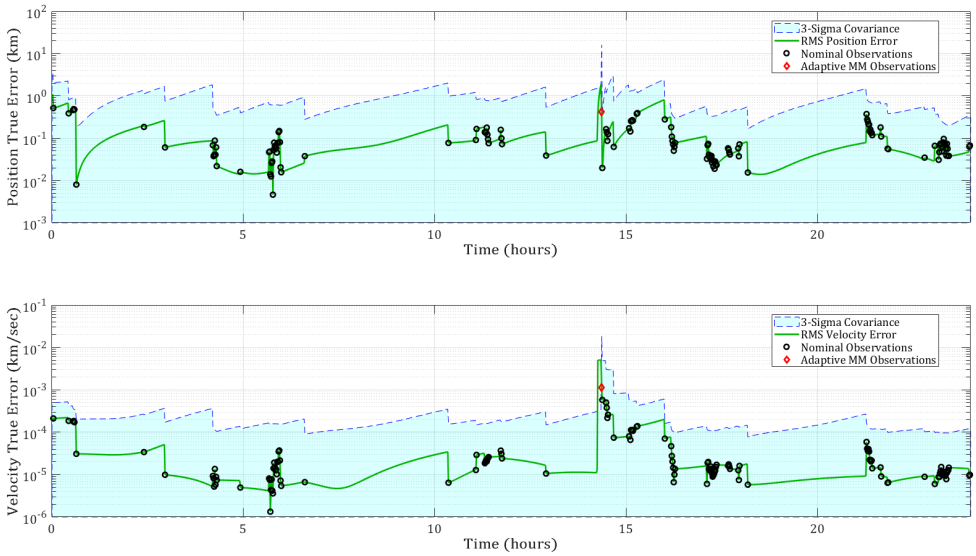

Figure C.49: Shotgun SMM/Continuous MEOMnvr-2 Track

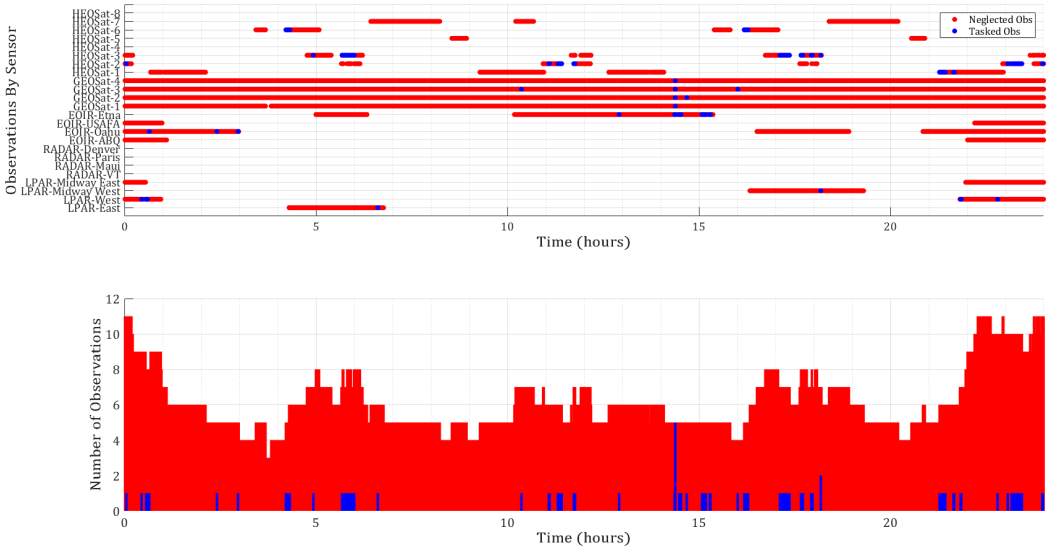

Figure C.50: Shotgun SMM/Continuous MEOMnvr-2 Observations

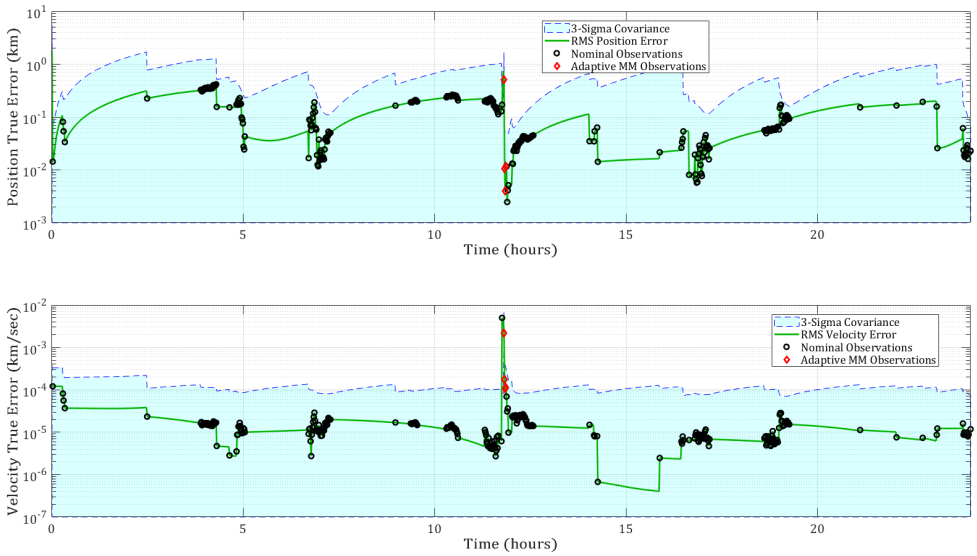

Figure C.51: Shotgun SMM/Continuous GEOMnvr-2 Track

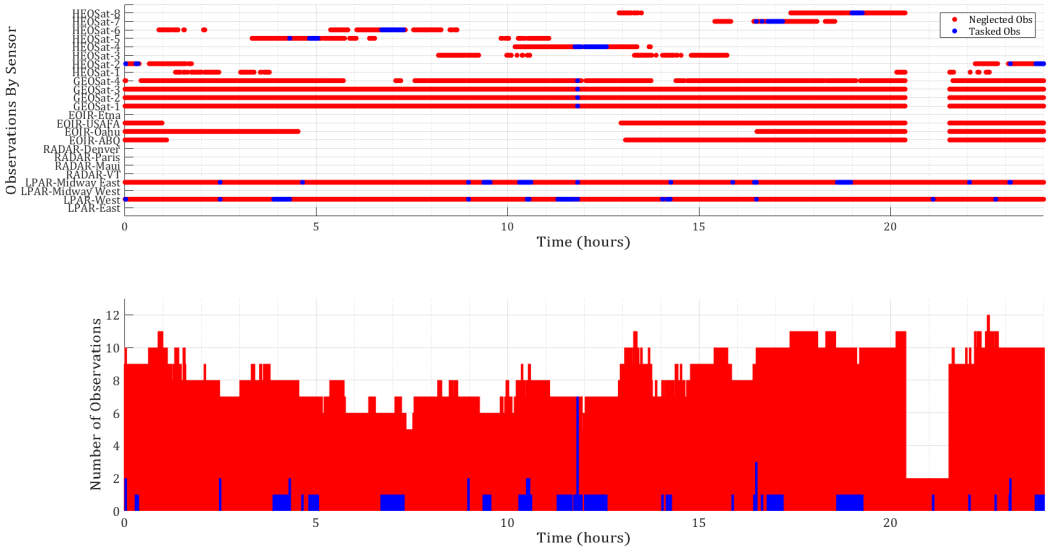

Figure C.52: Shotgun SMM/Continuous GEOMnvr-2 Observations

C.6 Lambert SMM & Constrained Observation POMDP

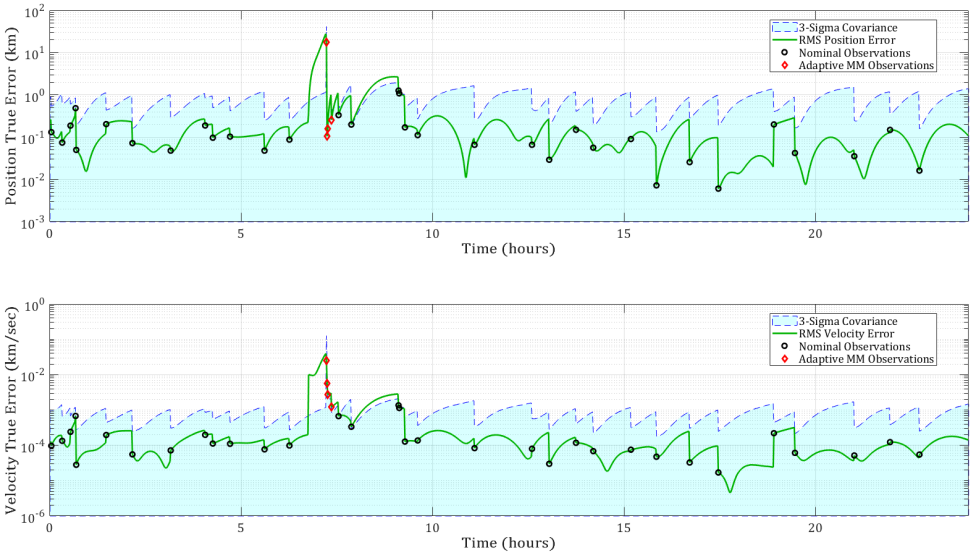

Figure C.53: Lambert SMM/Constrained LEOMnvr-1 Track

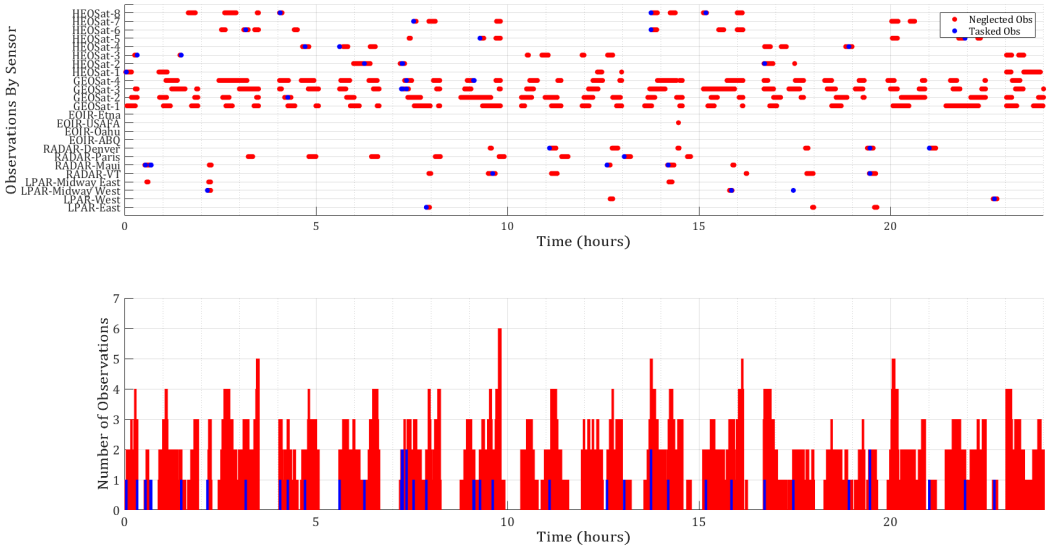

Figure C.54: Lambert SMM/Constrained LEOMnvr-1 Observations

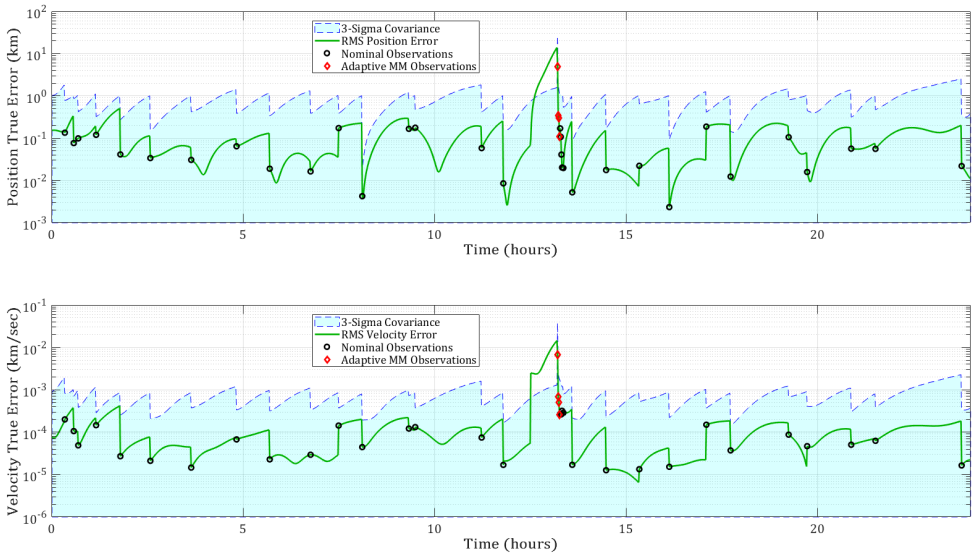

Figure C.55: Lambert SMM/Constrained LEOMnvr-3 Track

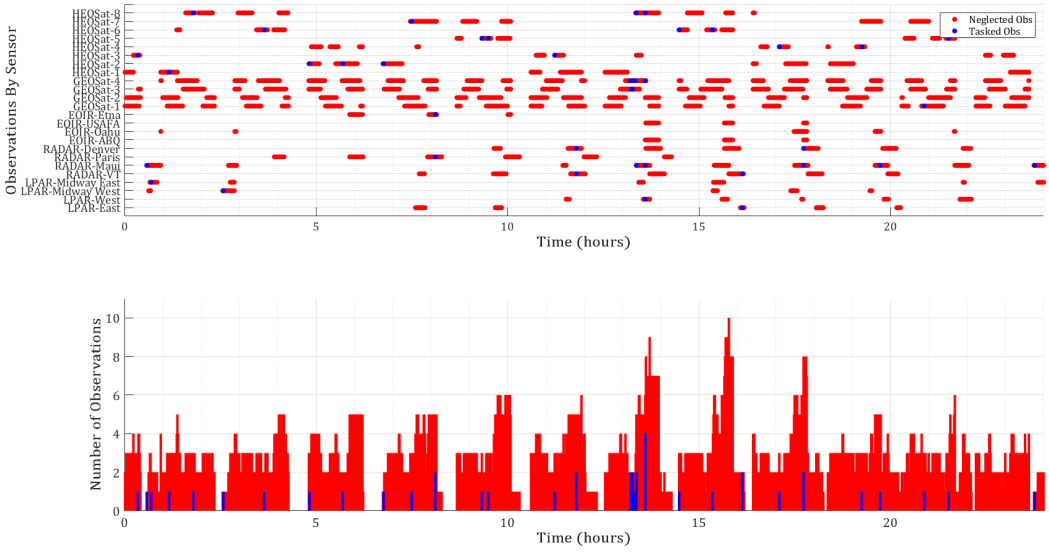

Figure C.56: Lambert SMM/Constrained LEOMnvr-3 Observations

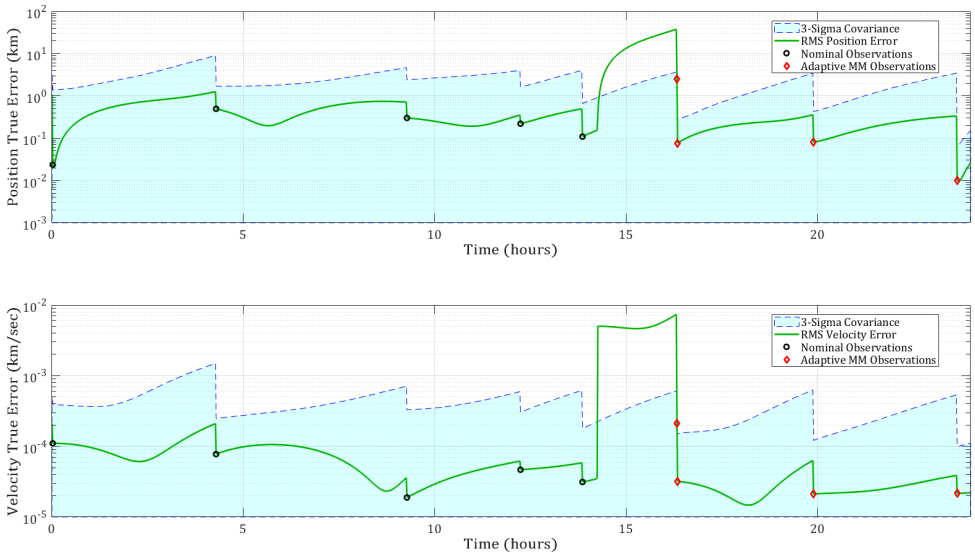

Figure C.57: Lambert SMM/Constrained MEOMnvr-2 Track

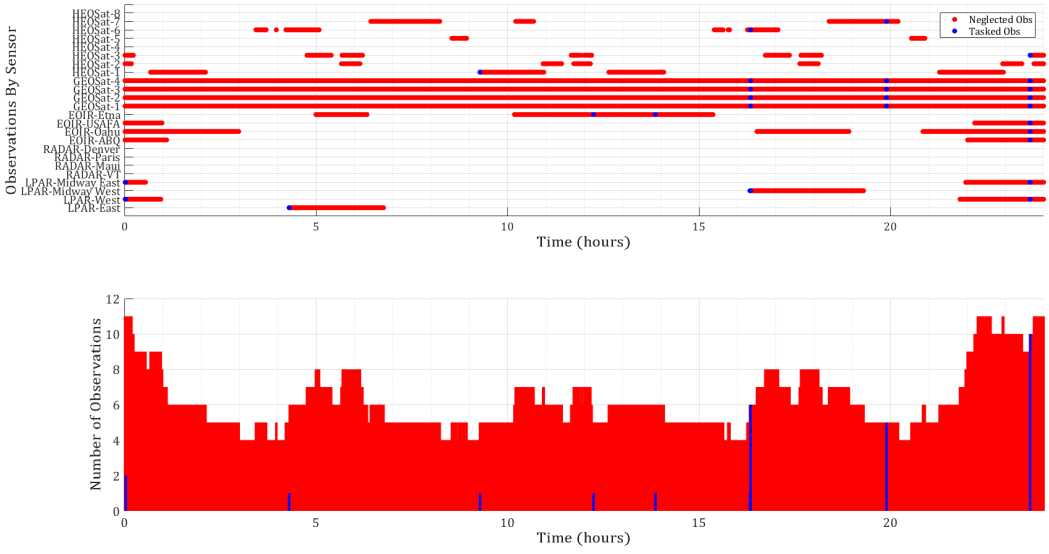

Figure C.58: Lambert SMM/Constrained MEOMnvr-2 Observations

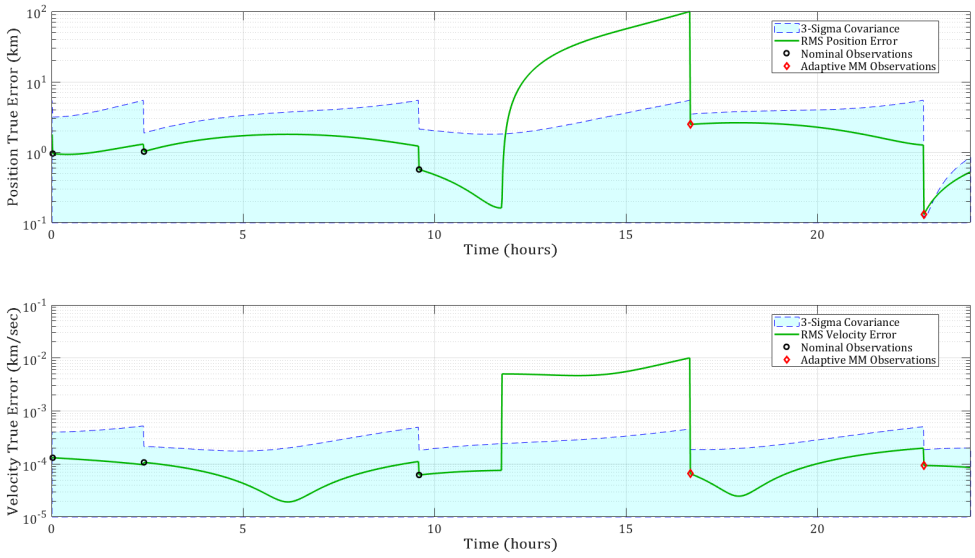

Figure C.59: Lambert SMM/Constrained GEOMnvr-2 Track

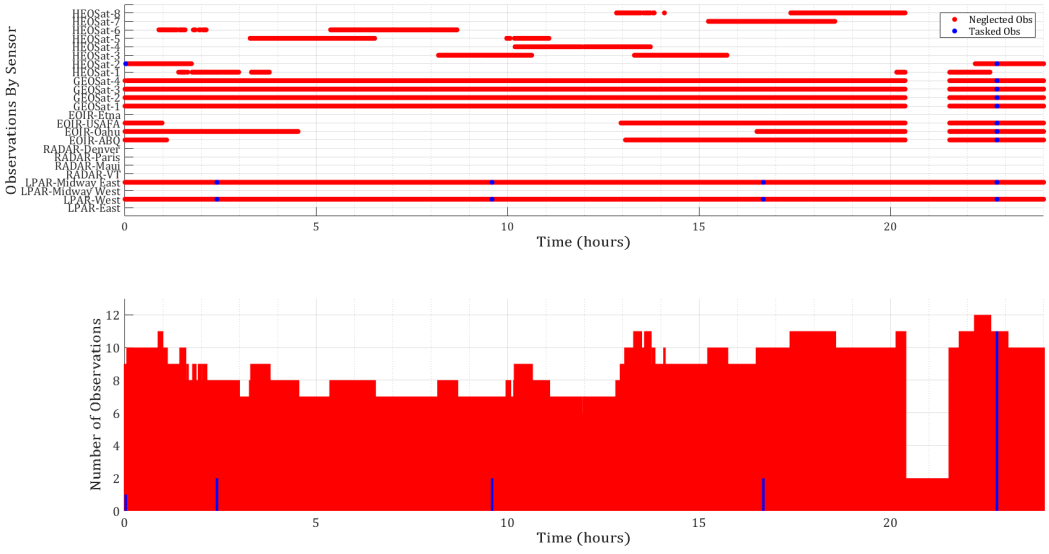

Figure C.60: Lambert SMM/Constrained GEOMnvr-2 Observations

C.7 Lambert GPB1 & Constrained Observation POMDP

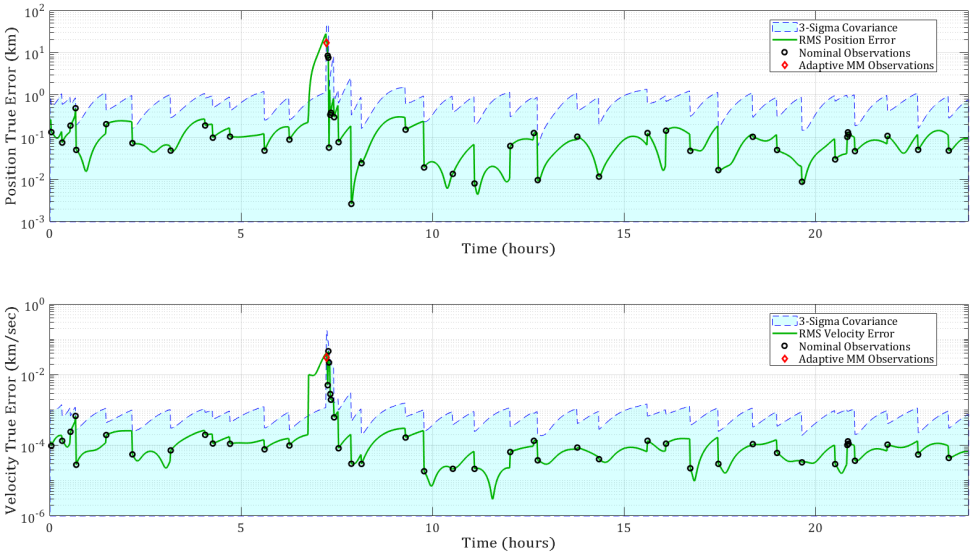

Figure C.61: Lambert GPB1/Constrained LEOMnvr-1 Track

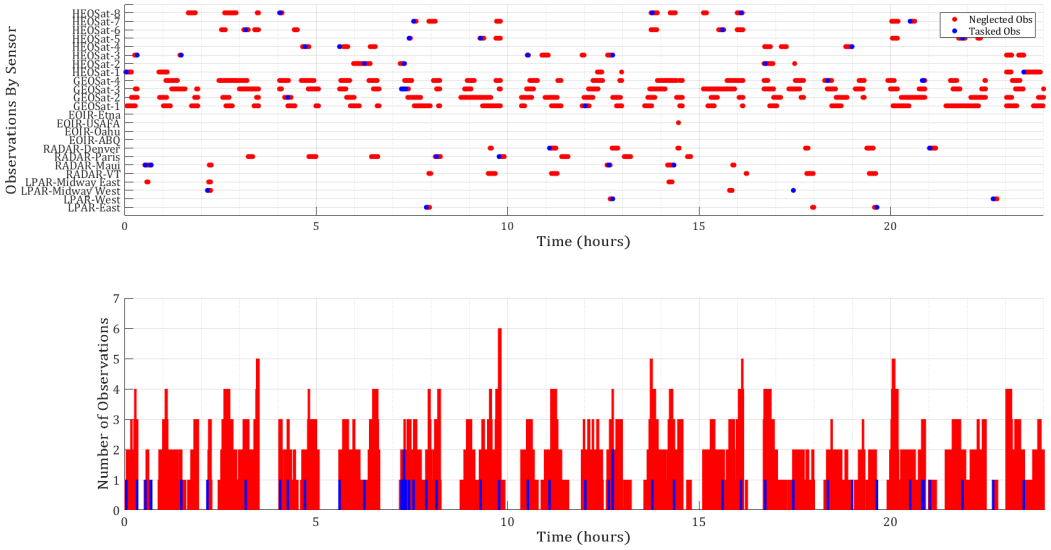

Figure C.62: Lambert GPB1/Constrained LEOMnvr-1 Observations

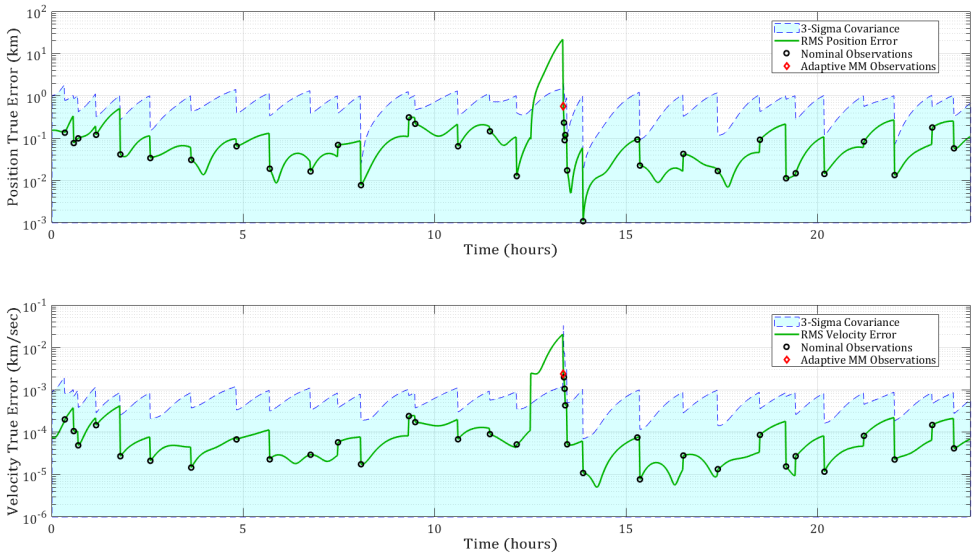

Figure C.63: Lambert GPB1/Constrained LEOMnvr-3 Track

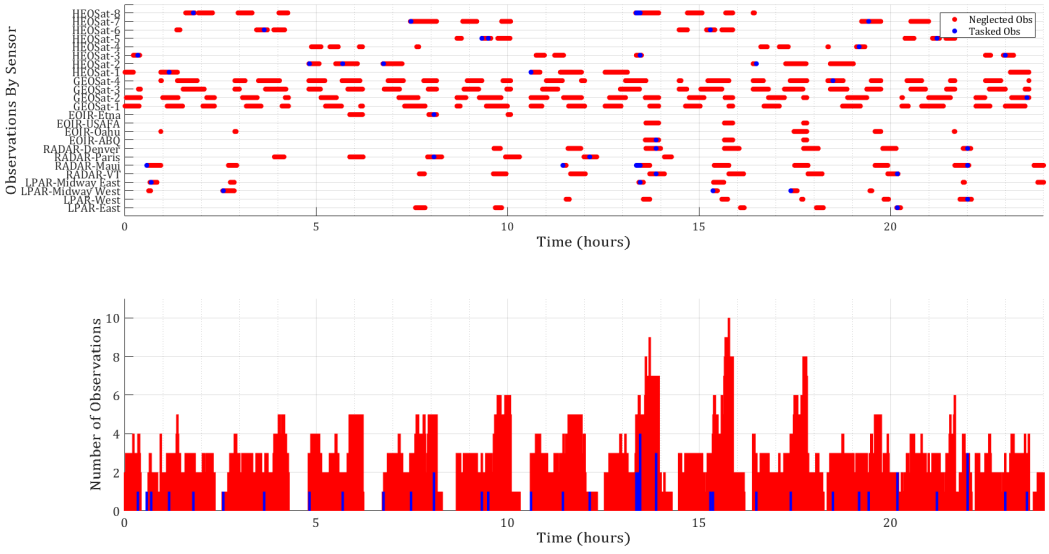

Figure C.64: Lambert GPB1/Constrained LEOMnvr-3 Observations

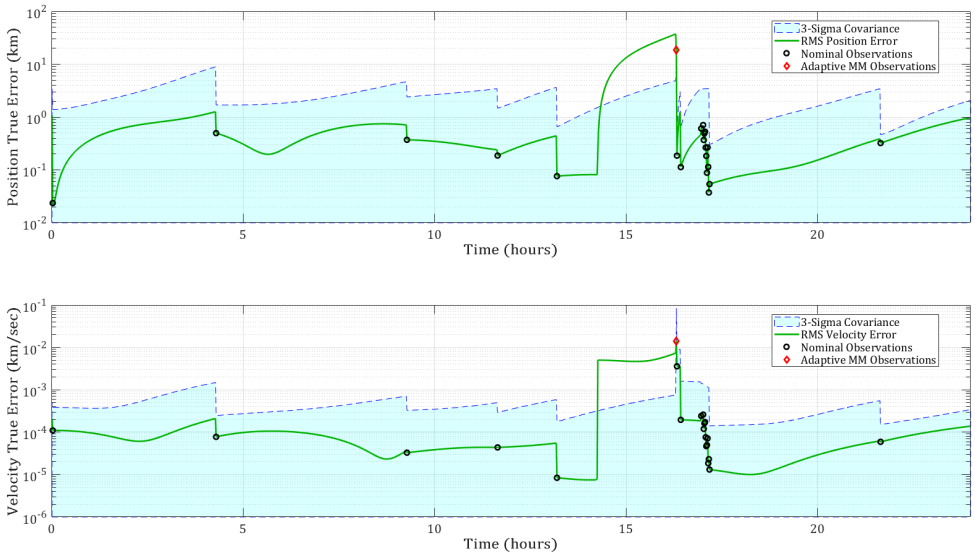

Figure C.65: Lambert GPB1/Constrained MEOMnvr-2 Track

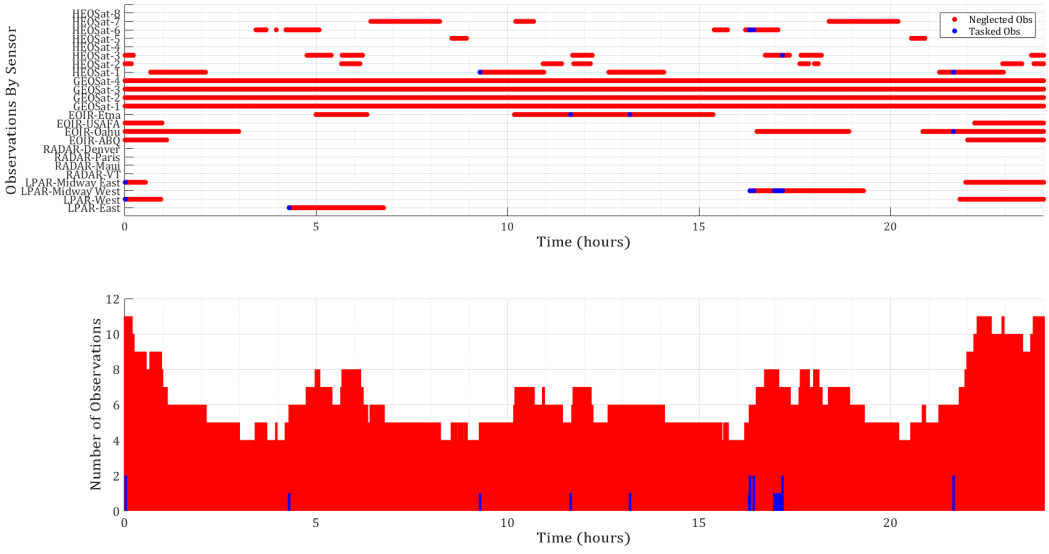

Figure C.66: Lambert GPB1/Constrained MEOMnvr-2 Observations

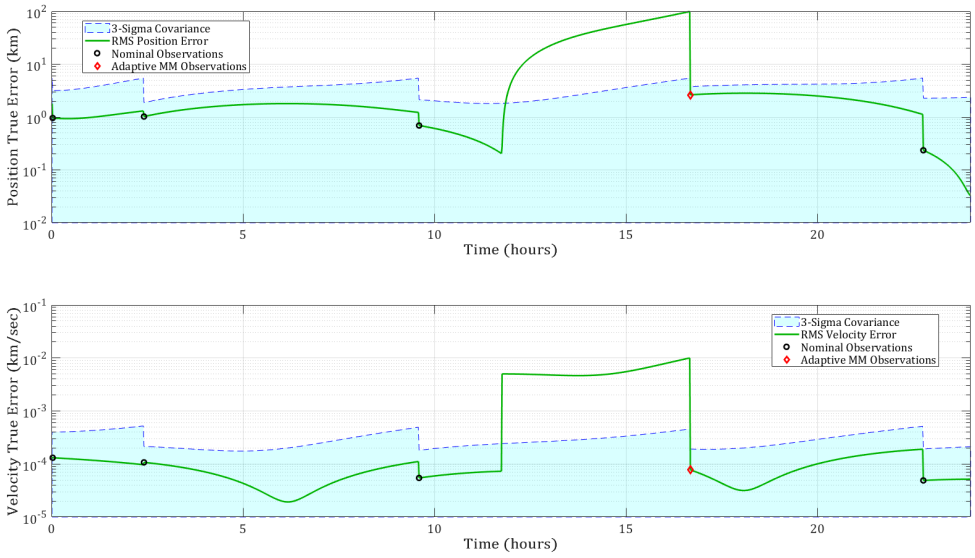

Figure C.67: Lambert GPB1/Constrained GEOMnvr-2 Track

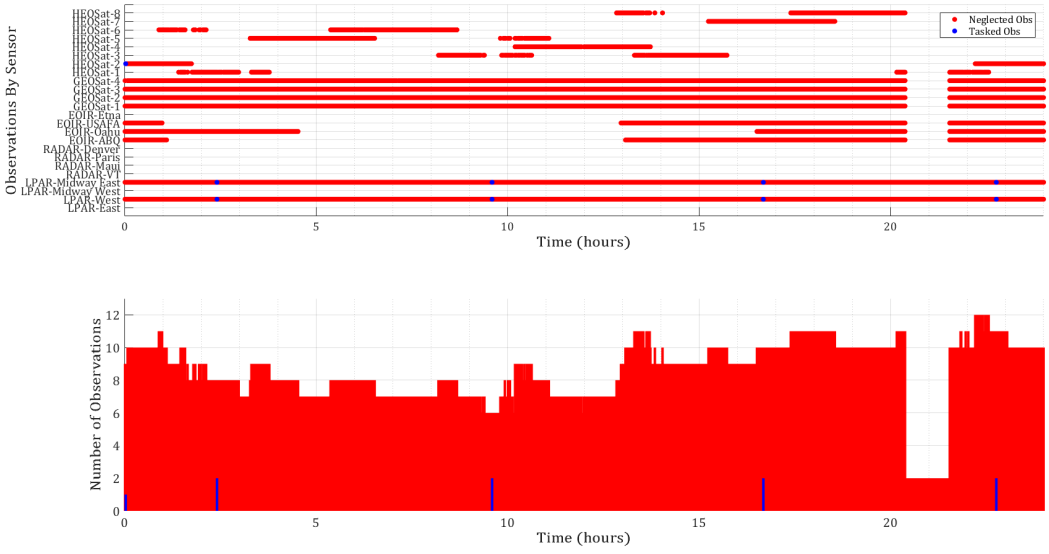

Figure C.68: Lambert GPB1/Constrained GEOMnvr-2 Observations

Bibliography

[1] Department of Defense and Director of National Intelligence, "National Security Space Strategy: Unclassified Summary," tech. rep., Department of Defense, 2011.

[2] Committee for the Assessment of the U.S. Air Force's Astrodynamic Standards, "Continuing Kepler's Quest: Assessing Air Force Space Command's Astrodynamics Standards," tech. rep., The National Academies Press, Washington, D.C., 2012.

[3] U.S. Strategic Command, "Joint Publication 3-14: Space Operations," tech. rep., Department of Defense, Washington, D.C., 2013.

[4] D. A. Vallado and J. D. Griesbach, "Simulating Space Surveillance Networks," in *AAS/AIAA Astrodynamics Specialist Conference*, vol. 142, pp. 1–19, American Astronautical Society, August 2011.

[5] F. Hoots, "Keeping Track: Space Surveillance for Operational Support," *Crosslink*, vol. 16, pp. 22–27, 2015.

[6] U.S. Air Force Space Command, "Space Based Space Surveillance," 2017. Accessed 14 June 2017.

[7] U.S. Air Force Space Command, "Geosynchronous Space Situational Awareness Program," 2017. Accessed 14 June 2017.

[8] M. Wasson, "Space Situational Awareness in the Joint Space Operations Center," in *AMOS Tech Conference*, pp. 1–2, AMOS, 2011.

[9] T. Blake, "Space Domain Awareness (SDA)," in *AMOS Tech Conference*, pp. 1–15, AMOS, 2011. AMOS 11-Blake.

[10] Committee on National Security Space Defense and Protection, "National Security Space Defense and Protection: Public Report," tech. rep., The National Academies Press, Washington, D.C., 2016. 10.17226/23594.

[11] E. Pawlikowski, D. Loverro, and T. Cristler, "Space: Disruptive Challenges, New Opportunities, and New Strategies," *Strategic Studies Quarterly*, vol. 6, pp. 27–54, 2012.

[12] *MPS-120: Innovative Propulsion Solutions for SmallSats.*

[13] R. Masse, R. A. Spores, S. Kimbrel, M. Allen, E. Lorimor, P. Myers, and C. McLean, "GPIM AF-M315E Propulsion System," in *AIAA/SAE/ASEE Joint Propulsion Conference*, Propulsion and Energy Forum, pp. 1–12, AIAA, July 2015.

[14] *MPS-130: Innovative Propulsion Solutions for SmallSats.*

[15] T. C. Co and J. T. Black, "Responsiveness in Low Orbits using Electric Propulsion," in *AIAA Guidance, Navigation, and Control Conference*, AIAA SciTech, pp. 1–23, AIAA, August 2012.

[16] D. J. Showalter and J. T. Black, "Responsive Theater Maneuvers via Particle Swarm Optimization," *AIAA Journal of Spacecraft and Rockets*, vol. 51, pp. 1976–1985, December 2014.

[17] A. M. Leigh and J. T. Black, "Navigation Solution to Maneuver a Spacecraft Relative to Multiple Satellites and Ground Locations," *Acta Astronautica*, vol. 109, pp. 1–13, May 2015.

[18] A. Rogers, C. Woolsey, and R. McGwier, "Nonlinear Tracking of Optimal Maneuvers in Spacecraft Formations," in *American Control Conference*, pp. 5859–5864, IEEE, 2015. 10.1109/ACC.2015.7172258.

[19] K. M. Nastasi, D. J. Thomas, K. Tetreault, I. Elliott, and J. T. Black, "Real-Time Optimal Control & Tracking of Autonomous Micro-Satellite Proximity Operations," in *AIAA SPACE 2016*, AIAA SPACE Forum, pp. 1–14, American Institute of Aeronautics and Astronautics, 2016.

[20] D. J. Thomas, K. Tetreault, K. Mott, I. Elliott, R. Scheible, E. Ohriner, K. M. Nastasi, and J. T. Black, "Real-Time On-board Estimation & Optimal Control of Autonomous Micro-Satellite Proximity Operations," in *AIAA Aerospace Science Meeting*, AIAA SciTech Forum, pp. 1–16, American Institute of Aeronautics and Astronautics, 2017.

[21] G. Roesler, "Robotic Servicing of Geosynchronous Satellites (RSGS) Proposers Day," May 2016.

[22] T. Harrison, K. Johnson, and T. G. Roberts, "Space Threat Assessment 2018," tech. rep., Center For Strategic & International Studies, Washington, D.C., 2018.

[23] R. Reesman and A. Rogers, "Getting in Your Space: Learning from Past Rendazvous and Proximity Operations," *Aerospace Corp. Policy Papers*, pp. 1–13, May 2018.

[24] C. M. A. Baird, "Maintaining Space Situational Awareness and Taking It to the Next Level," *Air & Space Power Journal*, vol. 27, pp. 50–72, October 2013.

[25] M. K. Kalandros, L. Trailovic, L. Y. Pao, and Y. Bar-Shalom, "Tutorial on Multisensor Management and Fusion Algorithms for Target Tracking," in *American Control Conference*, pp. 638–652, IEEE, July 2004.

[26] M. E. Liggins, D. L. Hall, and J. Llinas, *Handbook of Multisensor Data Fusion: Theory and Practice*. The Electrical Engineering and Applied Signal Processing Series, Boca Raton, FL: CRC Press, 2 ed., 2009.

[27] J. L. Crassidis and J. L. Junkins, *Optimal Estimation of Dynamic Systems*. Boca Raton, FL: CRC Press, 2 ed., 2012.

[28] G. M. Goff, J. T. Black, J. A. Beck, and J. Hess, "A Dynamic Sensor Tasking Strategy for Tracking Maneuvering Spacecraft Using Multiple Models," in *AIAA Guidance, Navigation, and Control Conference*, AIAA SciTech, pp. 1–21, American Institute of Aeronautics and Astronautics, 2016. DOI:10.2514/6.2016-1859.

[29] K. M. Nastasi and J. T. Black, "Dynamically Tracking Maneuvering Spacecraft with a Globally-Distributed, Heterogeneous Wireless Sensor Network," in *AIAA SPACE and Astronautics Forum and Exposition*, AIAA SPACE Forum, pp. 1–23, American Institute of Aeronautics and Astronautics, 2017.

[30] K. M. Nastasi and J. T. Black, "An Autonomous Sensor Management Strategy for Monitoring a Dynamic Space Domain with Diverse Sensors," in *AIAA Information Systems-AIAA Infotech @ Aerospace*, AIAA SciTech Forum, pp. 1–29, American Institute of Aeronautics and Astronautics, 2018.

[31] D. Thomas, K. M. Nastasi, K. Schroeder, and J. T. Black, "Autonomous, Multi-Phenomenology Space Domain Sensor Tasking & Adaptive Estimation," in *21st International Conference on Information Fusion*, pp. 1–8, IEEE, July 2018.

[32] Y. Bar-Shalom, X. R. Li, and T. Kirubarajan, *Estimation with Applications to Tracking and Navigation: Theory, Algorithms, and Software*. New York: John Wiley & Sons, Inc., 2001.

[33] D. A. Vallado, *Fundamentals of Astrodynamics and Applications*. Hawthorne, CA: Microcosm Press, 4 ed., 2013.

[34] B. D. Tapley, B. E. Schutz, and G. H. Born, *Statistical Orbit Determination*. Boston, MA: Elsevier Academic Press, 2004.

[35] R. Kalman, "A New Approach to Linear Filtering and Prediction Problems," *Journal of Basic Engineering*, vol. 82, pp. 35–45, March 1960.

[36] L. A. McGee and S. F. Schmidt, "Discovery of the Kalman Filter as a Practical Tool for Aerospace and Industry," Tech. Rep. 86847, NASA Ames Research Center, 1985.

[37] S. Julier, J. Uhlmann, and H. F. Durrant-Whyte, "A New Method for the Nonlinear Transformation of Means and Covariances in Filters and Estimators," *IEEE Transactions on Automatic Control*, vol. 45, pp. 477–482, March 2000.

[38] S. J. Julier and J. K. Uhlmann, "Unscented Filtering and Nonlinear Estimation," *Proceedings of the IEEE*, vol. 92, no. 3, pp. 401–422, 2004.

[39] M. L. Psiaki, "The Blind Tricyclist Problem and a Comparative Study of Nonlinear Filters," *IEEE Control Systems Magazine*, vol. 33, no. 3, pp. 40–54, 2013.

[40] D.-J. Lee and K. T. Alfriend, "Sigma Point Filtering for Sequential Orbit Estimation and Prediction," *AIAA Journal of Spacecraft and Rockets*, vol. 44, no. 2, pp. 388–398, 2007.

[41] E. A. Wan and R. van der Merwe, *Kalman Filtering and Neural Networks*, ch. The Unscented Kalman Filter, pp. 221–282. New York: John Wiley & Sons, Inc., 2001.

[42] K. J. DeMars, *Nonlinear Orbit Uncertainty Prediction and Rectification for Space Situational Awareness*. PhD thesis, The University of Texas At Austin, 2010.

[43] G. M. Goff, *Orbit Estimation of Non-Cooperative Maneuvering Spacecraft*. PhD thesis, Air Force Institute of Technology, 2015.

[44] P. S. Williams, *Coupling Between Nonlinear Estimation and Dynamic Sensor Tasking Applied to Satellite Tracking*. PhD thesis, Pennsylvania State University, 2012.

[45] Y. Wu, D. Hu, M. Wu, and X. Hu, "Unscented Kalman Filtering for Additive Noise Case: Augmented versus Nonaugmented," *IEEE Signal Processing Letters*, vol. 12, pp. 357–360, May 2005.

[46] S. Lee and I. Hwang, "State-Dependent Adaptive Estimation for Impulsively Maneuvering Spacecraft Tracking," in *AIAA SciTech Forum*, pp. 1–13, AIAA, 8 January 2016 2016.

[47] S. Lee and I. Hwang, "Interacting Multiple Model Estimation for Spacecraft Maneuver Detection and Characterization," in *AIAA Guidance, Navigation, and Control Conference*, AIAA SciTech Forum, pp. 1–9, AIAA, January 2015.

[48] N. Adurthi, M. Majji, and P. Singla, "Conjugate Unscented Transformation Based Orbital State Estimation and Sensor Tasking for Efficient Space Surveillance," in *AIAA/AAS Astrodynamics Specialist Conference*, pp. 1–15, AIAA, August 2014.

[49] P. S. Williams, D. B. Spencer, and R. S. Erwin, "Coupling of Estimation and Sensor Tasking Applied to Satellite Tracking," *AIAA Journal of Guidance, Control, and Dynamics*, vol. 36, pp. 993–1007, August 2013.

[50] H. C. Ko and D. J. Scheeres, "Maneuver detection with event representation using thrust fourier coefficients," *AIAA Journal of Guidance, Control, and Dynamics*, vol. 39, no. 5, pp. 1080–1091, 2016.

[51] Z. J. Folcik, P. J. Cefola, and R. I. Abbot, "GEO Maneuver Detection for Space Situational Awareness," *Advances in Astronautical Sciences*, vol. 129, pp. 1–27, 2007.

[52] A. D. Jaunzemis, M. V. Mathew, and M. J. Holzinger, "Control Cost and Mahalanobis Distance Binary Hypothesis Testing for Spacecraft Maneuver Detection," *AIAA Journal of Guidance, Control, and Dynamics*, vol. 39, pp. 2058–2072, September 2016.

[53] Y. Chan, A. Hu, and J. Plant, "A Kalman Filter Based Tracking Scheme with Input Estimation," *IEEE Transactions on Aerospace and Electronic Systems*, vol. AES-15, pp. 237–244, March 1979.

[54] G. M. Goff, D. Showalter, J. T. Black, and J. A. Beck, "Parameter Requirements for Noncooperative Satellite Maneuver Reconstruction Using Adaptive Filters," *AIAA Journal of Guidance, Control, and Dynamics*, vol. 38, pp. 361–374, March 2015.

[55] Y. Bar-Shalom and K. Birmiwal, "Variable Dimension Filter for Maneuvering Target Tracking," *IEEE Transactions on Aerospace and Electronic Systems*, vol. AES-18, pp. 621–629, September 1982.

[56] T. S. Lee, "Theory and Application of Adaptive Fading Memory Kalman Filters," *IEEE Transactions on Circuits and Systems*, vol. 35, no. 4, pp. 474–477, 1988.

[57] Y. Wang, S. Sun, and L. Li, "Adaptively robust unscented kalman filter for tracking a maneuvering vehicle," *AIAA Journal of Guidance, Control, and Dynamics*, vol. 37, no. 5, pp. 1696–1701, 2014.

[58] D.-J. Lee and K. T. Alfriend, "Adaptive Sigma Point Filtering for State and Parameter Estimation," in *AIAA/AAS Astrodynamics Specialist Conference and Exhibit*, pp. 1–21, AIAA, August 2004.

[59] V. M. Moreno and A. Pigazo, eds., *Adaptive Unscented Kalman Filter and Its Applications in Nonlinear Control*, ch. 1, pp. 1–25. Vienna, Austria: I-Tech, 2009.

[60] D. Magill, "Optimal Adaptive Estimation of Sampled Stochastic Processes," *IEEE Transactions on Automatic Control*, vol. 10, no. 4, pp. 434–439, 1965.

[61] H. A. Blom and Y. Bar-Shalom, "The Interacting Multiple Model Algorithm for Systems with Markovian Switching Coefficients," *IEEE Transactions on Automatic Control*, vol. 33, no. 8, pp. 780–783, 1988.

[62] Y. Bar-Shalom, K.-C. Chang, and H. A. Blom, "Tracking a Maneuvering Target Using Input Estimation Versus the Interacting Multiple Model Algorithm," *IEEE Transactions on Aerospace and Electronic Systems*, vol. AES-25, no. 2, pp. 296–300, 1989.

[63] W. Blair and Y. Bar-Shalom, "Tracking Maneuvering Targets With Multiple Sensors: Does More Data Always Mean Better Estimates?," *IEEE Transactions on Aerospace and Electronic Systems*, vol. 32, no. 1, pp. 450–456, 1996.

[64] G. M. Goff, J. T. Black, and J. A. Beck, "Tracking Maneuvering Spacecraft with Filter-Through Approaches Using Interacting Multiple Models," *Acta Astronautica*, vol. 114, pp. 152–163, October 2015.

[65] G. M. Goff, D. Showalter, J. T. Black, and J. A. Beck, "Orbit Estimation of a Continuously Thrusting Spacecraft Using Variable Dimension Filters," *Journal of Guidance, Control, and Dynamics*, vol. 38, pp. 2407–2420, December 2015.

[66] S. Lee, J. Lee, and I. Hwang, "Maneuvering Spacecraft Tracking via State-Dependent Adaptive Estimation," *AIAA Journal of Guidance, Control, and Dynamics*, vol. 39, pp. 2034 – 2043, September 2016.

[67] R. Fonod and T. Shima, "Multiple Model Adaptive Evasion Against a Homing Missile," *AIAA Journal of Guidance, Control, and Dynamics*, vol. 39, no. 7, pp. 1578–1592, 2016.

[68] B. Gao, S. Gao, Y. Zhong, G. Hu, and C. Gu, "Interacting Multiple Model Estimation-Based Adaptive Robust Unscented Kalman Filter," *International Journal of Control, Automation, and Systems*, vol. 15, no. 5, pp. 2013–2025, 2017.

[69] V. Krishnamurthy, *Partially Observed Decision Processes From Filtering to Controlled Sensing*. Cambridge, UK: Cambridge University Press, 2016.

[70] A. J. V. Alvarez and R. S. Erwin, *An Introduction to Optimal Satellite Range Scheduling*, vol. 106 of *Springer Optimization and Its Applications*. Springer International Publishing, 1 ed., 2015.

[71] B. Ristic, S. Arulampalam, and N. Gordon, *Beyond The Kalman Filter: Particle Filters for Tracking Applications*. Boston, MA: Artech House, 2004.

[72] P. S. Williams, D. B. Spencer, R. S. Erwin, and K. J. DeMars, "The Effects of Uncertainty Estimation on Dynamic Sensor Tasking," in *AIAA/AAS Astrodynamics Specialist Conference*, Guidance, Navigation, and Control and Co-located Conference, pp. 1–19, American Institute of Aeronautics and Astronautics, 2012. 10.2514/6.2012-4808.

[73] H. Kantz and T. Schreiber, *Nonlinear Time Series Analysis*. Cambridge, UK: Cambridge University Press, 1997.

[74] A. Wolf, J. B. Swift, H. L. Swinney, and J. A. Vastano, "Determining Lyapunov Exponents from a Time Series," *Physica D: Nonlinear Phenomena*, vol. 16, pp. 285–317, July 1985.

[75] F. Rauf and H. M. Ahmed, "Calculation of Lyapunov Exponents through Nonlinear Adaptive Filters," in *IEEE International Symposium on Circuits and Systems*, pp. 1–4, IEEE, 1991.

[76] W. Schmaedeke, "Information Based Sensor Mangement," in *Signal Processing, Sensor Fusion, and Target Recognition II*, vol. 1955, pp. 156–164, SPIE, September 1993.

[77] V. V. Kulkarni and L. Y. Pao, "A Sensor Management Protocol for Tracking with Diverse Sensors," in *American Control Conference*, pp. 5015–5020, IEEE, June 2005.

[78] Y. Fu, Q. Ling, and Z. Tian, "Distributed Sensor Allocation for Multi-Target Tracking in Wireless Sensor Networks," *IEEE Transactions on Aerospace and Electronic Systems*, vol. 48, pp. 3538–3553, October 2012.

[79] N. Adurthi, P. Singla, and T. Singh, "Optimal Information Collection for Nonlinear systems - An Application to Multiple Target Tracking and Localization," in *American Control Conference*, pp. 3864–3869, IEEE, 2013.

[80] S. Hariharan, Z. Zheng, and N. B. Shroff, "Maximizing information in unreliable sensor networks under deadline and energy constraints," *IEEE Transactions on Automatic Control*, vol. 58, no. 6, pp. 1416–1429, 2013.

[81] V. Krishnamurthy and D. V. Djonin, "Structured Threshold Policies for Dynamic Sensor Scheduling - A Partially Observed Markov Decision Process Approach," *IEEE Transactions on Signal Processing*, vol. 55, pp. 4938–4957, October 2007.

[82] V. Krishnamurthy, M. Maskery, and G. Yin, "Decentralized adaptive filtering algorithms for sensor activation in an unattended ground sensor network," *IEEE Transactions on Signal Processing*, vol. 56, no. 12, pp. 6086–6101, 2008.

[83] G. K. Atia, V. V. Veeravalli, and J. A. Fuemmeler, "Sensor Scheduling for Energy-Efficient Target Tracking in Sensor Networks," *IEEE Transactions on Signal Processing*, vol. 59, pp. 4923 – 4937, October 2011.

[84] J. A. Fuemmeler and V. V. Veeravalli, "Energy efficient multi-object tracking in sensor networks," *IEEE Transactions on Signal Processing*, vol. 58, no. 7, pp. 3742–3750, 2010.

[85] Y. Sarkale and E. K. Chong, "Orchestrated Management of Heterogeneous Sensors Incorporating Feedback from Intelligence Assets," in *SPIE Defense + Security*, vol. 9474, May 2015.

[86] A. Zatezalo, A. El-Fallah, R. Mahler, R. Mehra, and J. Brown, "Dispersed and Disparate Sensor Management for Tracking Low Earth Orbit Satellites," in *Signal Processing, Sensor Fusion, and Target Recognition*, vol. 7336, pp. 1–12, SPIE, May 2009.

[87] R. S. Erwin, P. Albuquerque, S. K. Jayaweera, and I. Hussein, "Dynamics Sensor Tasking for Space Situational Awareness," in *American Control Conference*, pp. 1153–1158, IEEE, 2010.

[88] K. Hill, P. Sydney, R. Cortez, K. Hamada, D. Nishimoto, K. Luu, and J. Paul W. Schumacher, "Dynamics tasking of networked sensors using covariance inflation," in *AMOS Tech Conference*, pp. 1–11, AMOS, September 2010.

[89] T. A. Hobson and I. V. L. Clarkson, "Sensor-Scheduling Simulation of Disparate Sensors for Space Situational Awareness," in *AMOS Tech Conference*, pp. 1–10, AMOS, September 2011.

[90] N. Adurthi, P. Singla, and M. Majji, "Conjugate Unscented Transform Based Approach for Dynamic Sensor Tasking and Space Situational Awareness," in *American Control Conference*, pp. 5218–5223, IEEE, 2015.

[91] A. J. Vazquez and R. S. Erwin, "Optimal Fixed Interval Satellite Range Scheduling," in *International Conference on Operations Research and Enterprise Systems*, pp. 401–408, ESEO, 2014.

[92] A. J. Vazquez and R. S. Erwin, "On The Tractability of Satellite Range Scheduling," *Springer Optimization Letters*, vol. 9, pp. 311–327, February 2015.

[93] U.S. Air Force Space Command, "Ballistic Missile Early Warning System," 2017. Accessed 14 June 2017.

[94] U.S. Air Force Space Command, "COBRA DANE Radar," 2017. Accessed 14 June 2017.

[95] U.S. Air Force Space Command, "PAVE PAWS Radar System," 2017. Accessed 14 June 2017.

[96] M. Graham and S. Bocquet, "Modelling a C-Band Space Surveillance Radar using Systems Tool Kit," tech. rep., Joint Operations Division, Defense Science and Technology Organisation, Victoria, Australia, 2013.

[97] W. Rees, *Physical Principles of Remote Sensing*. Cambridge, UK: Cambridge University Press, 3 ed., 2013.

[98] J. B. Campbell and R. H. Wynne, *Introduction to Remote Sensing*. New York, NY: Guilford Press, 5 ed., 2011.

[99] U.S. Air Force Space Command, "Ground-Based Electro-Optical Deep Space Surveillance," 2017. Accessed 14 June 2017.

[100] I. Molotov, V. Agapov, Z. Khutorovsky, V. Titenko, V. Rumyantsev, V. Biryukov, N. Minikulov, M. Gulyamov, B. Abdulloev, S. Andrievsky, S. Kashuba, V. Kashuba, R. Inasaridze, T. Phiralishvili, V. Ayvazian, Y. Ivashchenko, I. Korobtsev, T. Tsukker, and V. Tergoev, "Faint High Orbit Debris Observations with ISON Optical Network," in *AMOS Tech Conference*, pp. 1–10, AMOS, September 2009.

[101] P. M. Cunio and B. R. Flewelling, "Space Analysis and Research Centers (SpARCs) for SSA Data and Analytics," in *Space Traffic Management Conference*, pp. 1–8, Embry-Riddle Aeronatical University, 2016.

[102] F. K. Chun, R. D. Tippets, M. E. Dearborn, K. C. Gresham, R. E. Freckleton, and M. W. Douglas, "The U.S. Air Force Academy Falcon Telescope Network," in *AMOS Tech Conference*, pp. 1–8, AMOS, September 2014.

[103] G. H. McCall and J. H. Darrah, "Space Situational Awareness: Difficult, Expensive - and Necessary," *Air & Space Power Journal*, vol. 28, pp. 6–16, December 2014. Senior Leader Perspective.

[104] R. Byrne, M. Griesmeyer, R. Schmidt, J. Shaddix, and D. Bodette, "Benefits of a Geosynchronous Orbit (GEO) Observation Point for Orbit Determination," in *AMOS Tech Conference*, pp. 1–10, AMOS, September 2011.

[105] J. R. Wertz, D. F. Everett, and J. J. Puschell, *Space Mission Engineering: The New SMAD*. The Space Technology Library, Hawthorne, CA: Microcosm Press, 2011.

[106] X. R. Li and Y. Zhang, "Numerically robust implementation of multiple-model algorithms," *IEEE Transactions on Aerospace and Electronic Systems*, vol. 36, no. 1, pp. 266–278, 2000.

[107] A. Miele, M. Ciarcia, and J. Mathwig, "Reflections on the Hohmann Transfer," *Springer Journal of Optimization Theory and Applications*, vol. 123, pp. 233–253, November 2004.

[108] *Falcon 9 Launch Vehicle: Payload User's Guide*, 2 ed., October 2015.

[109] *Atlas V Launch Services User's Guide*. Centennial, CO, 11 ed., March 2010.

[110] R. R. Bate, D. D. Mueller, and J. E. White, *Fundamentals of Astrodynamics*. New York: Dover Publications, Inc., 1971.

[111] L. Sullivan and W. W. LaMorte, "Summarizing Data: InterQuartile Range (IQR)," 2016.

[112] K. J. DeMars, I. I. Hussein, C. Frueh, M. K. Jah, and R. S. Erwin, "Multiple-Object Space Surveillance Tracking Using Finite-Set Statistics," *AIAA Journal of Guidance, Control, and Dynamics*, vol. 38, pp. 1741–1756, September 2015.

[113] R. Linares and R. Furfaro, "Dynamic Sensor Tasking for Space Situational Awareness via Reinforcement Learning," in *AMOS Tech Conference*, pp. 1–10, AMOS, September 2016.